Electronically induced phenomena: low temperature aspects (Preface)

Electronic excitations of insulators and semiconductors initiate a complex sequence of transport and relaxation processes involving both the electronic and the nuclear subsystem. Under certain conditions they may result in a diversity of dramatic changes of the local atomic arrangements of bulk materials as well as of surfaces and interfaces. These effects are based on a concentration of the electronic excitation energy within a volume of the order of a unit cell as a result of localization. From the point of view of condensed matter theory, investigations of electronically induced phenomena are of great importance for elucidating the problem of nonradiative transitions in solids and the physics of nonequilibrium processes.

A fundamental understanding of the mechanisms and elementary steps of these transport and relaxation processes may open new ways for many novel technological applications, including electronically induced reactions on the atomic scale in material and surface sciences, micro- and nanoelectronics, photochemistry, and biology. This promises, on the one hand, to avoid troublesome irradiation-induced deterioration and damage of materials and devices, and on the other hand, to produce benefits from material modification induced by electronic excitations and from finding approaches to the use of these techniques to full potential. Material modification via excitation of the electronic subsystem is a topic of active current research covering a variety of materials including insulators, semiconductors, molecular systems such as biomolecules, HTSCs, and others.

The electronically induced processes give rise to a diversity of microscopic phenomena such as mass diffusion, charge transport, defect formation, bond breaking and bond creation, and desorption of different species from surfaces (molecules, fragments, and atoms, either neutral or charged). In all these cases the dynamical processes in the excited states, their interplay, and the conversion of electronic energy into kinetic energy of the lattice atoms are of primary importance. Very often these phenomena are used as an efficient tool for studies of solids, adsorbed layers, and clusters. Considering the high current interest in nanoparticles, the investigation of electronically induced phenomena in these structures is particularly promising.

The most efficient experimental approach is a combined employment of selective excitation and selective analysis techniques. Impressive progress has been made using narrow-bandwidth synchrotron radiation and short laser pulses. Tunable light in a wide spectral range has opened new avenues for detailed studies of processes induced by excitations in the excitonic range, in the range of band-to-band transitions, and in the inner-shell region. The pulse structure of synchrotron radiation has made it possible to combine energy- and time-resolved measurements. Recent progress in laser technology has enabled researchers to investigate fast dynamics by pump and probe techniques on a femto- and picosecond time scale. The photon stimulated desorption (PSD) is investigated for a wide spectral range from infrared (IR) through vacuum ultraviolet (VUV) to x rays, with registration of ions, neutrals, and metastables. Electron-stimulated desorption (ESD), and especially its angularly resolved variation ESDIAD (electron stimulated desorption ion angular distribution), provide interesting information on the dynamics and the directions of chemical bonds. Electron-ion coincidence techniques (EICO) link the primary excitation and the products, enabling an unambiguous analysis of the electronic evolution. The high potential of studies of electron transport in condensed matter was demonstrated by the muon spin relaxation (μSR) technique. Scanning microscopy (STM and AFM) and the spectrocopic techniques related to them allow an unsurpassed view of the microscopic details of surfaces in real space.

Low-temperature studies are of considerable importance for gaining a better insight into the mechanisms of electronically induced phenomena, since they allow one to minimize the influence of thermally stimulated processes. Moreover, there exists a special group of low-temperature solids, the van der Waals condensates. Mainly wide band-gap insulators with weak interparticle interaction, they are accepted as unique model systems for unveiling elementary steps of the electronic evolution, including transport, localization, and coupling to the nuclei. This is why this special issue is devoted to electronically induced phenomena occuring at low temperatures and in cryogenic systems.

The paper by Bargheer and Schwentner is focused on mass transport in rare gas solids studied by ultrafast spectroscopy. The theoretical article by Ratner deals with the energy transport properties of two-atom excitons and holes. Electron transport phenomena in cryogenic solids and liquids are explored by Eshchenko *et al.* by advanced μSR techniques, while the paper by Lastapis *et al.* concentrates on electron transport on semiconductor surfaces studied by STM techniques. Bass and Sanche review reactions induced by slow electrons in cryogenic films of molecular systems, including species of biophysical interest. The effect of electron irradiation on structure and bonding of SF_6 is the topic of the contribution of Faradzhev *et al.* Soft landing of size-selected clusters in cryogenic layers is investigated by Lau *et al.* Bond breaking by excitation of deep core levels monitored by ion desorption from a number of condensed and adsorbed molecules is reviewed by Baba. The article of Mase *et al.* reports on the potential of the EICO technique for the investigation of electronically induced bond breaking in condensates and physisorbates. The paper by Arakawa *et al.* concerns the metastable particles desorption from rare gas solids. The authors were able to measure absolute yields of the metastable atoms. The formation of biexcitons in Ne layers condensed on a metal substrate is explored by Wiethoff *et al.* in PSD experiments. The paper by Savchenko *et al.* concentrates on the creation of permanent lattice defects via excitonic mechanisms.

1063-777X/2003/29(3)/2/$24.00

Though a single issue cannot cover all aspects of the research, we do hope to give the reader a brief overview of the current research in this field and to show to some extent the development of a basis for the controlled modification of lattice structures and for implementing surface-sensitive technological processes.

P. Feulner
E. Savchenko

Particle transport phenomena in low-temperature solids (Review)

M. Bargheer and N. Schwentner*

Institut für Experimentalphysik, Freie Universität Berlin Arnimallee 14, 14195 Berlin, Germany
(Submitted November 11, 2002)
Fiz. Nizk. Temp. **29**, 225–236 (March 2003)

We review different approaches to measure the transport of F atoms and ions in rare-gas matrices and compare the experimental results to simulations. Static measurements on sandwich structures and co-doped matrices yield rather long travel ranges beyond 2 nm, in accord with early classical simulations which predict a channeling of the F atoms in rare gas matrices. Nonadiabatic simulations show a rapid energy loss, fast nonadiabatic dynamics, and only short travel ranges of typically 1 unit cell. The rapid energy loss, fast nonadiabatic transitions and the time scale for direct dissociation (~250 fs) are verified by femtosecond pump–probe experiments. It remains a challenge to account for the long-range migration when nonadiabatic processes are allowed in simulations, and to measure the long-distance flights directly by ultrafast spectroscopy. © *2003 American Institute of Physics.* [DOI: 10.1063/1.1542437]

1. INTRODUCTION

The transport of low-energy neutral atoms and ions through atomic and molecular layers is of importance in diverse areas such as radiation physics and chemistry, deposition by beams, electrochemistry, and chemistry in matrices. This overview tries to tie together theoretical predictions with a set of experimental data from different techniques. It turns out that transport is a significant challenge for theoretical treatment. We therefore focus our attention on the transport of small atoms and ions through solid rare-gas films, a subject most amenable to theoretical simulations. The interaction of the migrating particles with the rare-gas lattice atoms is expected to be strong, and from a mechanistic point of view a small particle size should support migration. The size of an external particle in a lattice is best characterized by the separation of the minimum energy in the pair potential. The pair potentials for a set of neutral atoms with respect to the interaction with Kr atoms, scaled to the Kr–Kr Lennard-Jones potential, are taken from a recent review[1] and displayed in Fig. 1. From the chosen selection it turns out that F atoms have the smallest size of the ground-state atoms and it may be surprising that even H atoms are considerably larger according to this consideration. Only oxygen atoms in the excited ^1D state appear smaller; however, here we intend to deal only with ground-state atoms or ions. Therefore the particles of choice for long range migration are F atoms together with F^+ and F^- ions, and we restrict this overview exclusively to those. Information on other particles can be obtained from Ref. 1 and the literature cited therein. Concerning the term transport, we also intend to restrict ourselves. There is a large body of information on thermally activated migration. The onset of this process at temperatures of 25 K in Ar and 15 K in Kr is shown in Fig. 2 for F atoms. In this article only the migration of ''hot'' F atoms with kinetic energies well above these thermal energies will be considered. The kinetic energy originates typically from photodissociation of an F-containing molecule, and the topic of interest is the range of this nonequilibrium particle until it comes to rest due to a sequence of scattering events. Therefore the experiments are in general carried out at temperatures well below the thermal threshold. However, care has to be taken that unintentional local heating is also avoided.

Classical simulations date back to 1984, and they predict a very interesting, quite long-range motion for F atoms in Ar

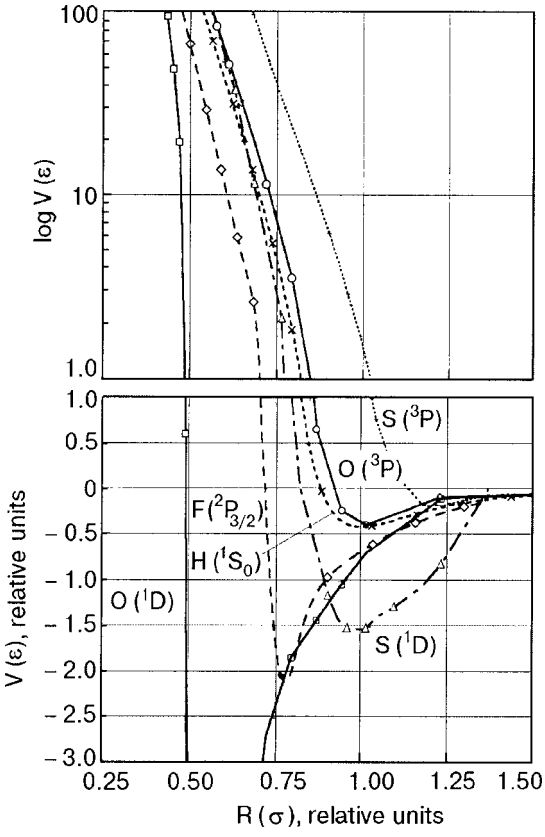

FIG. 1. The sizes of atoms, as discerned from pair potentials with Kr, scaled to the Kr–Kr Lennard–Jones parameters. The lowest energy surface from each of the spin–orbit terms is shown, and the curves are shifted to have a common dissociation limit at zero. The diatomic states corresponding to the various atomic terms are RgX ($^3\Pi$) for X=O(^3P) and S(^3P), RgX($1\,^1\Sigma^+$) for X=O(^1D), S(^1D), and H($^1S_0$), RgX($I_{1/2}$) for X=F($^2P_{3/2}$). The figure is reproduced from Ref. 1.

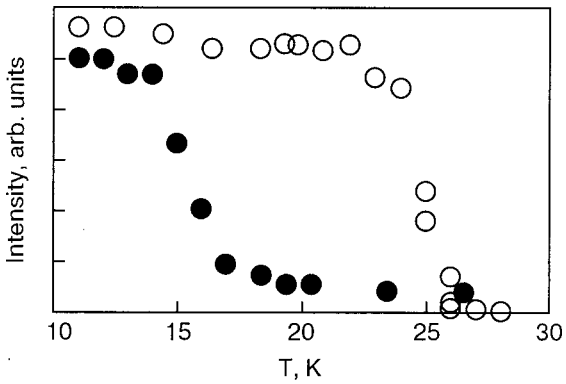

FIG. 2. Fluorescence intensities from RgF excimers after complete dissociation of F_2/Ar 1:4000 (○) and of F_2/Kr 1:3000 (●) by irradiation at 248 nm. The fluorescence is excited with 193 nm in the Ar and 275 nm in the Kr matrix. Heating the samples at a rate of 0.5 K/min yields the thresholds for thermal recombination, indicated by the step in the excimer fluorescence intensity. Figure taken from Ref. 26.

crystals.[2] Some trajectories showed a motion along ''channels'' for several lattice constants and one may associate a ''channeling'' known for energetic particles.[3] The further improvements in theory will be sketched in Sec. 2. The inclusion of nonadiabatic processes and more advanced potential energy surfaces seems in general to increase the interaction with the lattice and to reduce the range. Therefore it remains a challenge for experiment to separate out the channeling type of motion with a long free path between large-angle scattering events, in contrast to the diffusive type of motion with a hopping from site to site and without essential angular correlation.

A ''gedanken'' experiment using a particle beam of well-defined momentum and recording in transmission the change in energy and direction as the thickness of a rare-gas film is varied monolayer (ML) by monolayer would require a free standing film. The escape experiments described in Sec. 3.1 employ dissociation of molecules well oriented on a single crystalline substrate surface, and the penetration of the resulting F ions through the overlaying rare-gas films is measured.[4] The transmission of the ions already decays to zero at a rare-gas coverage of 1 (2.5) ML for F^+ (F^-) ions, indicating a very strong interaction of the ions with the rare-gas, while for neutral atoms the detection problem remains unsolved. Therefore, sandwich type of experiments are designed in which F atoms are generated by photodissociation of F_2 in a surface layer. They are sent through a spacer layer with variable thickness, and the penetrating ones are recorded in a substrate layer.[5] The discussion of these experiments in Sec. 3.2 will reveal a moderate penetration depth in Ar of the order of 2 nm, or 8 to 9 monolayers. However, the angular information is no longer available. It will be emphasized that assuming a diffusive or channeling type of motion would lead to rather different average length of travel for the same penetration depth.

Another body of information will be considered in Sec. 3.3, in which the transport of F fragments between dopants in a rare-gas film is studied. Statistical doping is attempted in these experiments, which therefore involve averaging over spatial separations. Rather long ranges of migration are found in several of these experiments. The problem of the spatial averaging and perhaps of multiple excitations, which also showed up in the sandwich experiments, will be addressed. This type of experiment, is essential, however, since it leads into the very heart of chemical applications in the framework of matrix isolation spectroscopy.[6,7] The formation of a high density of F-containing compounds can be optimized with these studies. A variety of solid-state rare-gas excimer lasers with extraordinary high excimer density and thus gain have been realized in this way.[8,9]

A promising new avenue is presented in Sec. 4 by studying the cage escape of F atoms with femtosecond time resolution.[10] The very first results indicate that it will be possible to follow the F atom migration from site to site. Finally, a combination of the time-resolved experiment with spatial information proposed in Sec. 5 may lead in the near future to a complete characterization of transport in the spirit of the ''gedanken'' experiment.

2. SIMULATIONS

In a strictly classical molecular dynamics calculation one F_2 molecule was placed at the center of a cell of 365 Ar atoms with the fcc lattice structure.[2] Cage exit probabilities were studied at 4 and 12 K within an excess energy range of 0.5 to 2.8 eV. Inspection of the finally populated sites for 50 trajectories at 12 K showed that 5 F atoms had left the cell. All these trajectories revealed a wiggly motion along a lattice diagonal (110 direction) without sidesteps, as demonstrated in Fig. 3. One such trajectory was observed at 2 eV excess energy and four at 2.8 eV. An extrapolation of the path beyond the boundary of the cell according to the calculated small energy loss of 0.5 eV/nm resulted in a total travel length of ~3 nm, or 12 monolayers. This fascinating long-range and channeled motion stimulated further simulations and experimental investigations. The summation of pair potentials and the relevance of nonadiabatic processes are points of concern, because the interaction of an $F(^2P_{3/2})$ atom with a rare-gas atom involves a ground state $X_{1/2}$ and

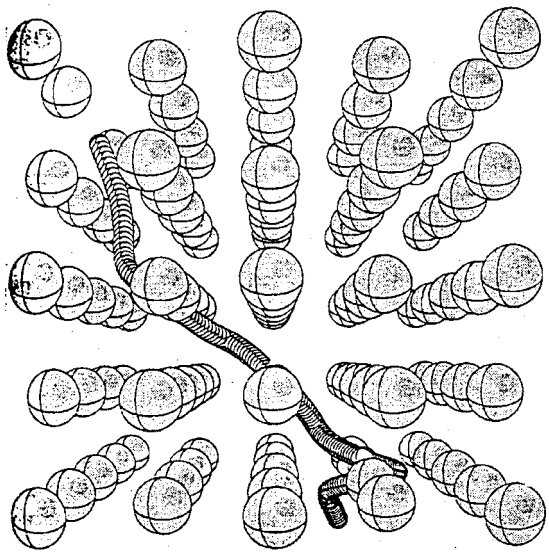

FIG. 3. Result of the earliest classical simulation of an F fragment traveling along the 110 direction after dissociation of F_2 with an excess energy of $E=2.8$ eV. The sample cell contains 365 Ar atoms at $T=12$ K and the F fragment finally leaves the cell. Figure taken from Ref. 2.

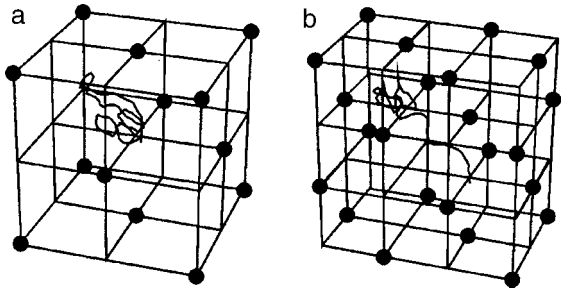

FIG. 4. Two typical adiabatic trajectories for the dissociation of Kr_2F in a Kr matrix. The path of the F atom is shown: a) no cage exit, b) direct cage exit with stabilization in the O_h interstitial site. The figures are reproduced from Ref. 13, and no trajectories with longer range were reported.

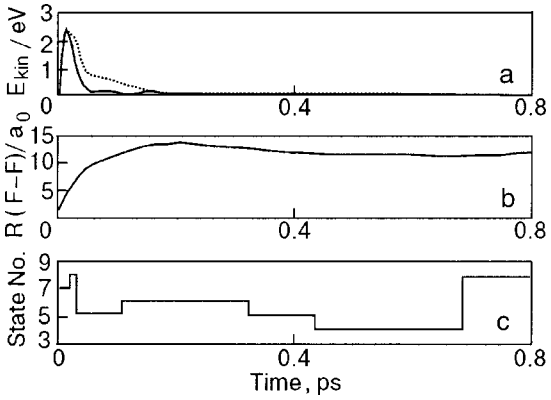

FIG. 5. Direct dissociation of F_2 in an Ar_{54} cluster equilibrated at 8 K and excited with 4.9 eV excess energy. The nonadiabatic calculations demonstrate a) rapid energy loss within 0.2 ps, b) direct cage exit to the nearest interstitial site at 10 a_0, and c) rapid hopping among the quantum states (numbered from the ground state=1 to the most repulsive valence state =36) associated with the F_2 molecule. The figures are taken from Ref. 15.

an excited $I_{3/2}$ potential. Running half of the trajectories in a similar slab of Kr on the $X_{1/2}$ potential energy surface and half on the $I_{3/2}$ resulted in a better agreement with the experiment as to the simulated cage exit probabilities versus excess energy than did assuming very rapid electronic relaxation to the $X_{1/2}$ surface.[11] Relying still on additive pair potentials and including nonadiabatic processes in a semiclassical way by Tully's surface hopping method showed, however, that reorientation of the *p* orbitals proceeds very fast in Kr on a time scale below 100 fs.[12,13] The method was applied to study the migration of F atoms induced by the radiative dissociation after emission of $Kr_2^+F^-$ to the repulsive ground state.[13] The F atoms acquire a kinetic energy of only about 0.2 eV, and the heating of the cage due to the Kr–Kr repulsions is included. A significant and fast energy loss by nonadiabatic transitions was observed which substantially shifted the distribution of final distances of the F atoms from the initial position to smaller values. Exclusion of these nonadiabatic contributions resulted in a large probability for cage exit to different sites next to the original F atom position (see Fig. 4), but no F atoms excursions beyond one unit cell were reported. A very instructive statistical treatment of the barrier height distribution from additive pair potentials was applied to F_2 dissociation with orbital alignment and cage exit in Ar and Kr (Ref. 4). Parallel alignment of the *p*-hole to the cage wall corresponds to much lower barrier heights. If it is assumed that this favorable orientation yields qualitative agreement with the measured cage exit probabilities, however, the simulated absolute values are lower by a factor of two, and long-range migration was not addressed.

Finally, a major effort was undertaken to go beyond the summation of pair potentials and to diagonalize the Hamiltonian for the molecular electronic states in the solid-state environment. The potential energy surfaces of 36 electronic states and the nonadiabatic couplings between them were derived from the diatomics-in-molecules approach for F_2 at the center of a cluster of 54 Ar atoms.[15] Excitation with 4.6 eV and 6.53 eV was considered. All trajectories of the high-energy excitation lead to dissociation and direct exit from the cage. The example in Fig. 5 illustrates the fast release of kinetic energy (Fig. 5a) and the manifold of nonadiabatic transitions (Fig. 5c) on a subpicosecond time scale. The F atom leaves the cage (Fig. 5b), but the F–F amplitude remains between 10 and $15a_0$ and the F fragments do not leave the cluster itself on the 1–2 ps time scale of the simulations. Thus the question of long-range migration is still open. Inclusion of charge transfer contributions by the diatomics-in-ionic-systems method,[16] for example, may weaken the interaction strength of the F atom with the lattice. Femtosecond experiments discussed in Sec. 4 allow to follow the fragment motion in real time and provide a more direct way of comparison with the simulations. In essence, it remains to the experiment to settle the contributions of long-range trajectories to migration.

3. ESCAPE AND TRANSPORT EXPERIMENTS

3.1. Transmission through rare-gas overlayers at surfaces

The transmission of low-energy ions through thin films is studied in a long-standing effort in relation to the depth of origin of secondary ions. The subject is covered in this volume by the contribution of Madey and a review by Akbulut *et al.*[17] Here we include only a brief account on the transmission of F^- and F^+ ions through rare-gas films[4] because it is interesting to compare the ion properties with those of neutral atoms. A saturation coverage of PF_3 is condensed on a Ru (0001) surface in a way that it exhibits a $(\sqrt{3}\times\sqrt{3})R30°$ low-energy electron diffraction pattern and an azimuthally ordered F^+ and F^- electron stimulated desorption ions angular distribution pattern. Monolayer-by-monolayer growth of rare-gas layers on top of the PF_3 molecules has been verified.[4] F^+, F^- and F_2^- are desorbed by bombardment with 300 eV electrons. The attenuation of the F^+ and the F^- yield with Kr and Xe coverage is displayed in Fig. 6. F^+ ions desorb with a mean kinetic energy of ~4 eV, and F^- ions have a peak kinetic energy of 0.7 eV. The attenuation for F^+ is very efficient, and one monolayer blocks the transmission completely. The effect is attributed to elastic scattering and charge transfer. A small contribution of large angle scattering is in favor of charge transfer contributions. F_2^- attenuation is similarly strong.

The initial increase in F^- yield originates mainly from a suppression of neutralization which occurs near the substrate. Attenuation is once more quite efficient and the F^- ions are blocked for film thicknesses between 2 and 2.5 monolayers. Elastic scattering seems to be the dominant attenuation process. The longer range compared to F^+ is at-

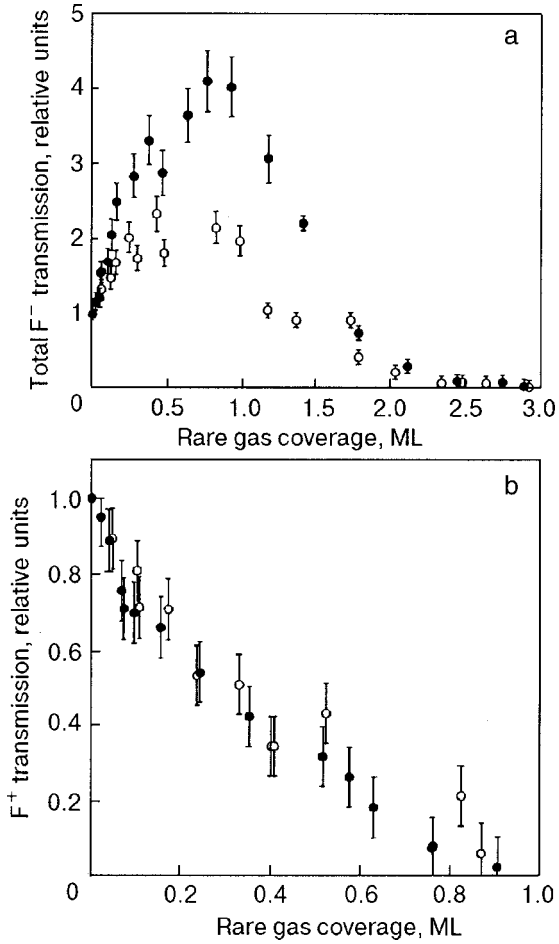

FIG. 6. Plot of the total ion yield generated by electron bombardment of PF_3/Ru(0001) as a function of Kr (○) and Xe (●) overlayer coverage. The data are normalized to unity for the clean surface value. The figures are reproduced from Ref. 4. a) The F^- yield first increases with rare gas coverage, but the transmission decays to zero for 2.5 ML coverage. b) The F^+ transmission decays linearly to zero for 1 ML coverage.

tributed to the specific layering in an fcc structure which provides channels perpendicular to the surface until completion of the third layer. The measured angular distribution is in accord with the necessity to direct the escaping F^- ions into the channel direction.

In summary, a severe attenuation for the ions is obtained in the escape experiments. However, some type of channeling seems to occur for F^- ions in the thickness regime of 2 monolayers. For a small fraction of O^+ even longer penetration up to 5 or 6 monolayers, was observed.[18] Most interesting would be escape measurements for neutral F atoms, which are most likely also present in these experiments. The neutral atoms are more difficult to detect.

3.2. Sandwich film structures

In an alternative approach the transport of neutral F atoms through an Ar spacer layer of variable thickness is studied in a stack of three rare-gas films. The inset in Fig. 7 shows a scheme of the sandwich-like structure.[19] 30 to 40 nm of Kr are condensed on a MgF_2 substrate. The thickness of an Ar spacer layer on top of the Kr film is varied from sample to sample between 0 and 100 nm. Finally the structure is closed by an F_2 doped Ar film typically 5 nm thick.

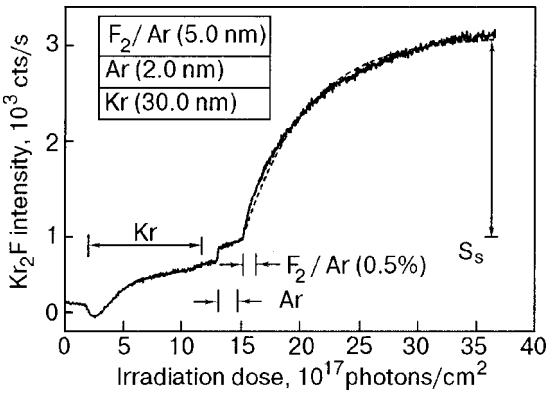

FIG. 7. Intensity dependence of Kr_2F fluorescence at 444 nm for irradiation with 10.15 eV during sandwich condensation. The inset shows the sandwich structure. The background of 1000 cts/s is due to the Kr detection layer and the Ar spacer layer only. Upon condensation of the F_2/Ar (0.5%) layer, the emission grows and saturates at the signal level S_s. For more detailed discussion see Ref. 19.

The thickness of each layer is carefully controlled by a quartz microbalance. The compactness of the Ar spacer layer is verified by the suppression of surface excitons from the Kr film and the structural quality is optimized by condensation rate and temperature.[19] The F_2 molecules are dissociated using synchrotron radiation with a photon energy of 10.25 eV, thus delivering on average a kinetic energy of 4.3 eV to each F atom. The F atoms generated in the top layer which reach the Kr film are recorded by the characteristic $Kr_2^+F^-$ fluorescence. The emission intensity for irradiation during the formation of the stack is displayed in Fig. 7. Besides some background during Kr and Ar condensation, a pronounced increase upon condensation of the F_2/Ar top layer is observed which continues even after completion of the top layer. The increase is attributed to the dissociation of the F_2 content. A fraction of the formed F atoms penetrates through the Ar spacer and contributes to the emission. The saturation after prolonged irradiation indicates complete F_2 dissociation and the maximal amount of F atoms which can be kicked by the dissociation process through the spacer layer of Ar. Plotting the saturation values S_s for a set of samples versus the Ar spacer thickness d yields a rather monoexponential decrease of the probability for penetration, as shown in Fig. 8. The derived penetration depth d_0 varies between 2.3 and 2.8 nm for two different sets of data, indicating a mean penetration for a $1/e$ attenuation of 10 monolayers.[19] Thus a much larger penetration depth is observed for neutral F atoms compared to ions. The value is of the order of magnitude proposed by the very first classical simulations, and it challenges the more advanced calculations. For further consideration one has to distinguish between the penetration depth d_0 measured in this experiment, the average length of travel s_0, and the mean free path l between scattering events. The penetration depth measurement does not directly tell whether the migration is diffusive or predominantly rectilinear due to channeling. In any case, d_0 is a lower limit for s_0. For diffusive motion with short l one would obtain a much larger s_0 compared to the measured d_0. The parallel geometry in the sandwich structure also imposes some constraints. For a predominant rectilinear migration with exponential damping, it turns out that only a rather narrow cone of tra-

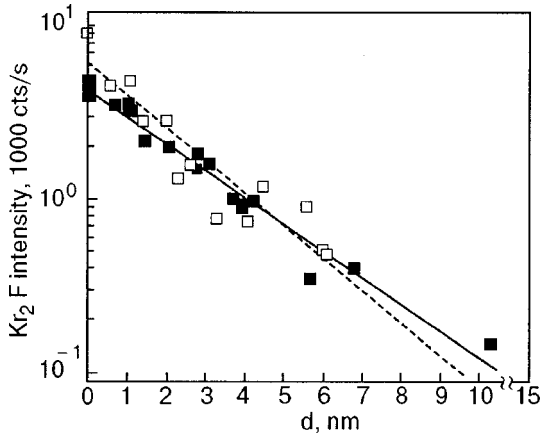

FIG. 8. Saturation value S_s of the Kr_2F fluorescence intensity as a function of the Ar-spacer layer thickness d for two data sets. The solid and dashed line are exponential fits to the data with decay constants (mean penetration depth) $d_0 = 2.8$ and 2.3 nm, respectively. For a detailed discussion of the experiment see Ref. 19.

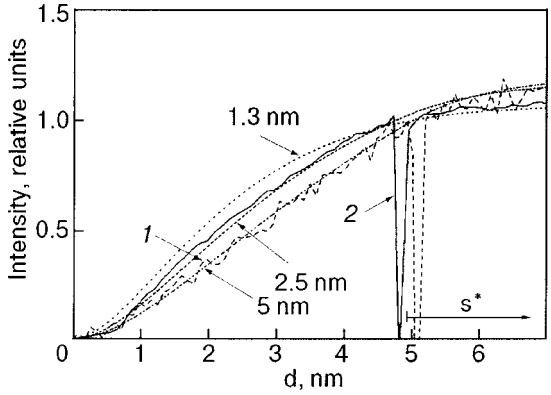

FIG. 9. Normalized measured Kr_2F emission intensity during deposition (up to the dip in the spectra) and for prolonged irradiation. The spacer layers are 5.6 (curve *1*) and 1.1 (curve *2*) nm thick. The assumed penetration depths $d_0 = 1.3$, 2.5 and 5 nm for the modeled curves are indicated. For a detailed discussion of the model the reader is referred to Ref. 21.

jectories directed normal to the layers contributes significantly to the signal. The decomposition of d_0 into s_0 and l is not yet unique. A reasonable estimate which is consistent with the measured d_0 yields $s_0 = 7$ nm and $l = 0.9$ nm. Thus for a mean free path l of three monolayers between large energy loss and large angle scattering events, one obtains an average length of travel of the order of 7 nm, or 28 monolayers. For an extreme diffusive motion with l as small as the nearest neighbor separation an upper limit of $s_0 = 17$ nm is derived.

The detection of the F atoms in the Kr layer is in itself interesting. It is surprisingly efficient. The high sensitivity originates from exciting excitons in the Kr film, which transfer their energy to the F atoms.[20] By investigating the dependence of the F emission and Kr emission on the Kr film thickness and by modeling the spectral dependence, it was possible to derive the migration properties of the excitons and the transfer efficiencies. Indeed, 10% of the available light flux can be funneled to a small content of F atoms of only 1/100 of monolayer by optimizing the experiment. In addition, the Kr emission intensity can be used to normalize the detection efficiency, and an improved set of data was obtained with $d_0 = 2.5$ nm (Ref. 20).

The rise in the signal in Fig. 7 during the deposition of the top layer contains independent information on d_0. If the F_2 molecules are dissociated efficiently during the layer-by-layer growth, then those generated later on have to cross the distance between the actual surface and the interface between the Ar/F_2 film and the Ar spacer film before they enter into the Kr layer. Thus this rise corresponds to a penetration depth measurement for a single sample with a continuously variable spacer thickness.[21] Figure 9 displays the measured rise and its simulation with different d_0 values. Once more, d_0 between 2 and 2.5 nm is obtained. It is important, however, that now a check of consistency for each sample is possible between the rise according to Fig. 9 and the attenuation by the pure Ar spacer according to Fig. 8. In this way a reliable $d_0 = 2.1$ nm corresponding to 8 or 9 monolayers was established.[21] This value is close to the earlier results and is consistent with the discussion in terms of s_0 and l. In addition, it was found that several samples yield a significant penetration probability for rather large spacer thickness of the order of 10 nm. The effect was attributed to multiple excitation of the F atoms induced by impurities. Prolonged irradiation allows the crossing of large thicknesses by this unintentional multistep excitation. The effect has to be kept in mind as a source for overestimation of d_0 in related experiments.

3.3. Multiply doped films and crystals

This subject has been reviewed recently[1] and some main results are summarized briefly. The realization of a high-gain solid-state excimer laser was based on the formation of a high density of XeF in Kr, Ar, and Ne matrices.[22,23] The XeF centers are prepared by F_2 dissociation and transport of the F fragments to the Xe dopants. It was immediately recognized that the F atoms undergo long-range migration.[24] A systematic study of the migration properties was carried out by shuttling F atoms between Xe and Kr dopants in an Ar crystal.[25] The kinetic energy of the F atoms of $\sim$0.5 eV was acquired by emission of the KrF and XeF exciplexes to the repulsive ground state. An average length of travel of 5 to 8 nm or 10–15 lattice constants was derived from the shuttling kinetics, assuming a statistical distribution of the dopants. The bimolecular recombination of F atoms in Ar crystals was recorded via the bleaching of the $Ar_2^+F^-$ emission in an analogous study, and an average length of travel of 7 nm was obtained for an estimated kinetic energy of 0.7 eV (Ref. 26). For Kr crystals co-doped with F_2 and Xe it was observed that the F atoms migrate an average length of (8 ± 4) nm in the case of a kinetic energy of 2.4 eV, while they remain localized below 1.9 eV (Ref. 27).

The high mobility of F atoms was exploited quite early to establish new photochemical reactions in matrices.[7,28,29] This field is very active, and a major improvement is achieved by a combination of ESR and IR analysis with optical spectroscopy.[30–33] A quantitative study of the migration lengths was done[34] using the kinetics in the addition reactions of F to CO and O_2 (Ref. 34). A comparison of vapor-deposited matrices with results from free-standing crystals shows a dramatic increase, from 0.7–1.4 nm in the

films to (14 ± 6) nm in the crystals. The influence of the morphology on the observed migration length must be strongly emphasized. There is long-standing experience in the art of sample preparation. The condensation of films especially has to be carried out with optimization of the condensation temperature and rate to avoid porous or disordered structures.[1] Therefore the preparation and structure of the films studied in Secs. 3.1 and 3.2 was carefully controlled. In summary, the results from the multiply doped samples emphasize a considerable average length of travel of neutral F atoms, typically of the order of 5 to 10 nm for samples with good structural quality. The results are compatible with those from Sec. 3.2, since the penetration depth d_0 yields a lower bound for the average length of travel s_0, and estimates for s_0 fall into this range. Some of the values for small kinetic energies in multiply doped samples appear to be rather close to the upper limit. The method of multiple doping has to deal with the statistical averaging and with a possible deformation of the lattice in the vicinity of the dopants. This provided motivation to investigate sandwich structures with transport through a pure spacer layer. It is quite satisfying that both methods yield a consistent and quite large average length of travel.

4. FEMTOSECOND PUMP–PROBE SPECTROSCOPY

Femtochemistry allows one to follow the intermediates in a photochemical reaction on a molecular time scale.[35] The method is therefore well suited for studying the recombination dynamics in the matrix cage as well as cage exit and presumably migration. ClF molecules have been established as a good source to follow the dynamics of F atoms in matrices.[36] Emission from the bound A' state of ClF to the ground state allows to record the remaining concentration of ClF molecules. The quantum yield for permanent dissociation of ClF in Ar, i.e., cage-exit of the F fragment without geminate or non-geminate recombination, was measured to be 5%. In Kr matrices the decay of the ClF concentration is an order of magnitude faster.

A prerequisite is that the sample composition be approximately constant over the whole pump–probe scan. In the case of ClF in Ar, the dissociation efficiency is sufficiently small. In Kr matrices, the fluorescence from the excimer states Kr^+F^- leads to a mobilization of the F fragments and can be used to prepare a convenient equilibrium[37] in the reaction $ClF+Kr \rightleftharpoons Cl+KrF$. The femtosecond experiments are carried out in this equilibrium, which slowly decays because F atoms are expelled from the laser focus by sequential reexcitation. The F fragments accumulate in a ring around the laser focus. This can be verified by translating the sample perpendicularly to the laser beam (focal diameter of 100 μm) after several minutes of irradiation. Whereas the Kr^+F^- fluorescence in the original spot has decayed significantly, it increases when the ring around this focus is probed. Thus the F fragments are transported over this macroscopic length scale by successive reexcitation. A detailed description of the equilibrium and F transport will be given elsewhere.[10]

To apply ultrafast spectroscopy, both the pump- and the probe transition must lie in a spectral range which is accessible with femtosecond laser sources. The dynamics of the ClF molecule itself can be conveniently followed by probing to the Cl^+F^- manifold with $\lambda_{probe}<320$ nm. The dissociated F fragments can be monitored by exciting the Kr^+F^- excimer with an ultrafast pulse at $\lambda_{probe}<270$ nm.[37] The formation of Ar^+F^- from F fragments in Ar requires much shorter wavelengths ($\lambda\sim210$ nm) which are at present not easily accessible with femtosecond lasers. This problem can be circumvented by co-doping the Ar matrix with Kr or Xe.

The recombination dynamics of ClF—as opposed to cage exit—is studied by preparing a vibrational wave packet near the inner turning point on the repulsive limb of the B

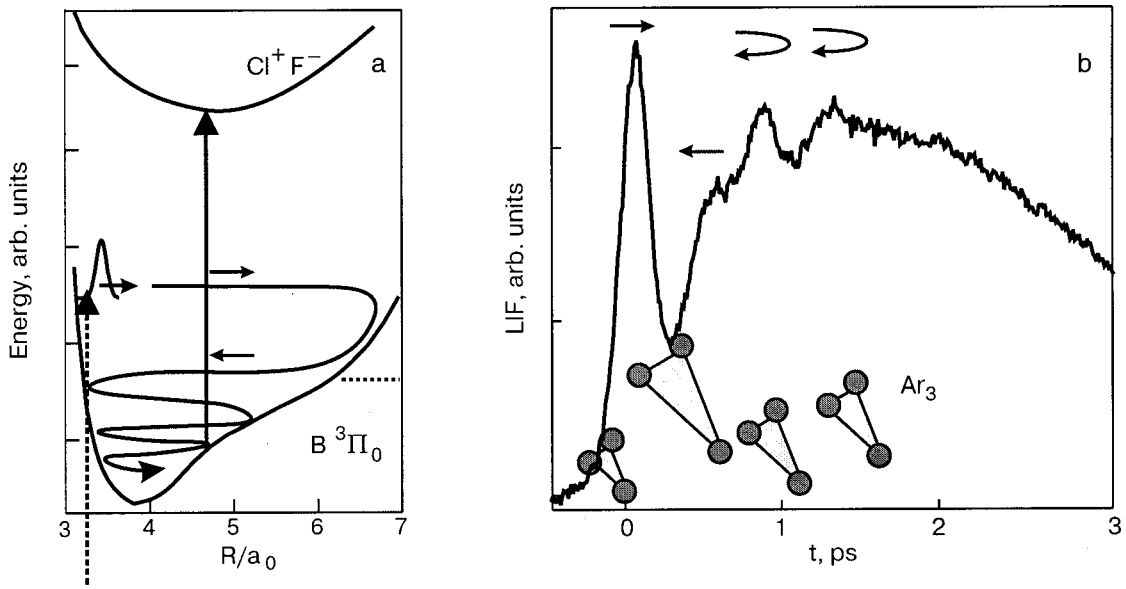

FIG. 10. a) Scheme of the wave packet dynamics with the probe window indicated by the vertical arrow at $R_{win}=4.8\,a_0$ that yields the pump–probe spectrum in panel b. The wave packet is excited (dashed vertical arrow) above the gas phase dissociation limit (dotted line) and loses energy in the B state due to interaction with the cage. b) fs-pump–probe spectrum with $\lambda_{pump}=387$ nm and $\lambda_{probe}=319$ nm. The arrows above the peaks indicate how the wave packet passes through the window. Further discussion of the wave packet dynamics can be found in Ref. 38.

state with a short laser pulse according to the scheme in Fig. 10a. The passage of the wave packet through the spatial region of a delayed probe pulse leads to excitation to the ionic ClF states. The intensity of the emission from the ionic states versus the time delay thus monitors the time sequence of passages through the probe window. The measured time course[38] in Fig. 10b displays the outward motion of the wave packet (→), the return from the outer turning point (←), and the subsequent oscillations (↔). Analysis of the spectrum shows that the wave packet loses most of its kinetic energy during the long-lasting outer bow in the first collision with the cage,[38] in accord with the simulation.[15] The recombining wave packet does not reach out so far due to the energy loss, and in the next passages it is caught near the outer turning point. The wave packet can be scattered with skewed angles from the matrix cage. If an aligned ensemble of excited ClF molecules is prepared by photoselection with a polarized pump beam, probing the polarization dynamics shows that the bond direction is tilted within few oscillations on a timescale of 1.2 ps.[39] This ultrafast reorientation by scattering and recombination has to be well distinguished from the usual rotation, which even in the free molecule would lie in the 100 ps range. The dynamics of nonradiative transitions between electronic states was investigated via the spin flip from a repulsive singlet state to bound triplet states. These nonradiative transitions are surprisingly fast, and 40% to 50% of the final triplet population is already reached after the wave packet returns from its first encounter with the cage, i.e., in about 500 fs.[40] This result agrees very well with the simulations.[15]

Initial results on cage exit and localization of the wave packet in a neighboring cage are presented below, while a detailed description will be given elsewhere.[10] ClF in Kr is excited with a sequence of two fs-pulses with a duration of approximately 100 fs at the wavelengths $\lambda_1 = 387$ nm and $\lambda_2 = 270$ nm. The fluorescence from the $Kr_2^+F^-$ excimer (lifetime ~150 ns) is recorded as a function of the time delay between the two fs-pulses. The 270 nm pulse probes all F atoms that have been accumulated in the course of the experiment. To detect a fs-pump–probe signal of the hot escaping F atoms, it is necessary to employ a differential technique that subtracts the strong background from these accumulated F atoms. Figure 11 shows the resulting $Kr_2^+F^-$ fluorescence as a function of time delay between the pulses at λ_1 and λ_2. Care is taken to accurately determine the time zero when the two pulses overlap "*in situ*" by a FROG-cross correlation.[41] The interpretation of the spectrum for positive time delays $t > 0$ is straightforward. The pump pulse $\lambda_1 = 387$ nm excites ClF to its bound $^3\Pi$ state beyond the dissociation limit (cf. Fig. 12a). After approximately 250 fs, a first maximum in the signal indicates that the F atoms have arrived at the nearest interstitial site (O_h). Here $\lambda_2 = 270$ nm excites the "hot" KrF to Kr^+F^-, which leads to the $Kr_2^+F^-$ configuration and emission after structural rearrangement. This time agrees very well with the prediction for direct cage exit from the simulations[15] and corresponds to a straight flight of the F atom through the triangular window of Kr atoms, as indicated by the solid arrow in Fig. 12b. The signal keeps rising in the first 2 ps and is essentially constant for 100 ps. The assignment of the structures after the first peak requires further experimental and theoretical effort, since they originate from both delayed cage exit and migration of the F fragments within the matrix. For positive time delays the signal is linearly dependent on the intensity of both pulses, in accord with the scheme in Fig. 12a.

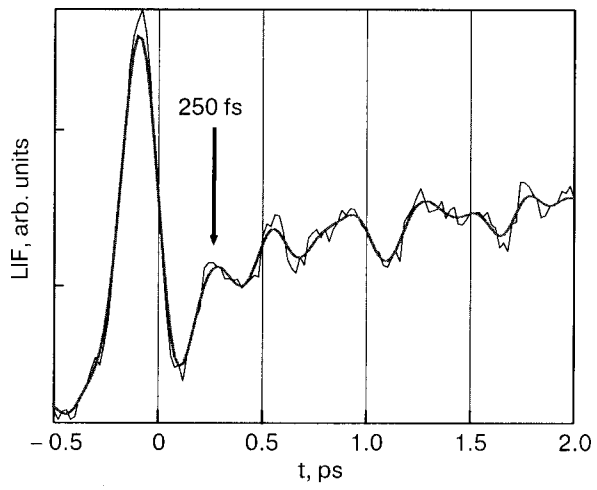

FIG. 11. Normalized Kr_2F fluorescence intensity for ClF/Kr (1/1000) at $T = 5$ K as a function of the time delay t between two fs pulses at $\lambda_1 = 387$ nm and $\lambda_1 = 270$ nm. The process that leads to the formation of the $Kr_2^+F^-$ exciplex is indicated in Fig. 12a for positive time delays and in Fig. 12c for negative time delay t. For $t > 0$ the fs-pump–probe spectrum measures the ultrafast direct cage exit of F in Kr. After $t = 250$ fs the first F atoms have reached the nearest interstitial site.

For negative time delays, the $\lambda_2 = 270$ nm pulse takes the role of the pump pulse, and a two-photon transition with $\lambda_1 = 387$ nm is used as a probe. The peak at $t = -50$ fs depends quadratically on the intensity of the $\lambda_2 = 387$ nm probe pulse. Figure 12c shows the corresponding pump–probe scheme. The pulse at $\lambda_2 = 270$ nm excites ClF to its repulsive $^1\Pi$ state. After 50 fs, while the Cl–F is stretching on the $^1\Pi$ surface, an efficient two-photon transition at $\lambda_2 = 387$ nm transfers the wave packet to the ion-pair manifold Cl^+F^-. This is consistent with the potential energy diagram of ClF (Ref. 42) and with the fact that only one peak is observed at negative time delays, since vibrational and nonadiabatic decay to $^3\Pi$ prohibit another excitation when the wave packet returns. After absorption of λ_1 and λ_2 in this time ordering, the wave packet travels towards larger $Cl^+ - F^-$ distances on the ionic manifold (Fig. 12c). The F^- ion may reach a nearest-neighbor cage, as indicated in Fig. 12b by the solid arrow, and show the same fluorescence from $Kr_2^+F^-$ after relaxation within the excimer state. The experiment demonstrates that the F^- ion can overcome the barrier for cage exit within the ionic manifold, however, the pump–probe delay contains no information on the dynamics of the cage exit of the F^- ion, as the time between the pump and probe pulse is spent on the valence states. Here it may be more appropriate to call λ_1 the pump pulse and λ_2 the control pulse, which determines the yield for F^- cage exit.

5. CONCLUSION

Fluorine ions have rather small penetration depths (Sec. 3.1). The transmission of F^+ through Kr and Xe films is near zero for one monolayer. The damping to a transmission of

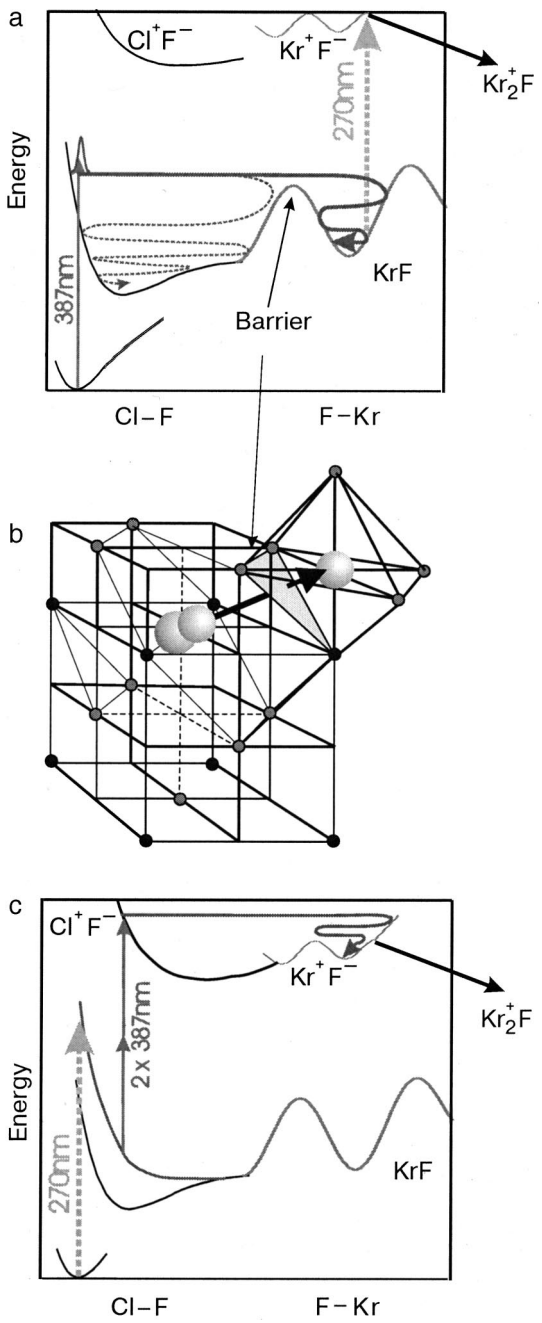

FIG. 12. a) Scheme for the pump–probe spectrum in Fig. 11 for $t>0$. The pump pulse $\lambda_1=387$ nm prepares a wave packet on the bound $^3\Pi$ state of ClF. The F atom leaves the cage, overcoming the barrier and can be probed by $\lambda_2=270$ nm to form the Kr^+F^- excimer. b) ClF molecule on a single substitutional site of the Kr fcc lattice. The arrow indicates the direction of the F atom's cage exit. c) Scheme explaining the peak at $t=-50$ fs in Fig. 11. $\lambda_2=270$ nm prepares a wave packet on the repulsive $^1\Pi$ state of ClF. A two photon resonance after 50 fs transfers the wave packet to the ionic Cl^+F^- manifold. F^- exit, rearrangement, and relaxation lead to the $Kr_2^+F^-$ excimer.

$1/e$, which is used throughout the paper as the definition of penetration depth and average length of travel, occurs already for a half monolayer.

The experimental evidence for neutral F atoms, in contrast, yields much larger penetration depths. The early studies of multiply doped Ar crystals are described by the reaction cross sections with other particles on the track of the mobile F atom (Sec. 3.3). Therefore the derived track length corresponds to the number of visited sites and is correlated with the average length of travel s_0. Considerations of multiply visited sites, etc., were not included in the evaluation of the kinetics. These measurements, carried out by several groups for various reaction partners, consistently yield an average length of travel on the order of $s_0=7$ to 10 nm in well-ordered Ar samples. It was shown that the average length of travel may be reduced to 1 nm in disordered matrices. The interpretation of the multiple-doping experiments could be questioned concerning the assumed statistical distribution of dopants and a modification of the F mobility by lattice deformations in the vicinity of the dopants. In addition, the kinetic energy was provided by a rather intense laser excitation that dissociates F_2 molecules, and the locally deposited energy could mobilize previously generated F atoms that are trapped in the vicinity. This unintentional reexcitation can enlarge the observed length of travel.

Therefore, the penetration depth d_0 of F atoms through an Ar film of well-defined thickness was determined in the sandwich experiments (Sec. 3.2). In this way the excitation region is separated from the transport region, the transport region is spatially well defined, and lattice distortions by dopants are avoided. In carefully prepared and characterized Ar films, a penetration depth of around 2 to 3 nm was observed in several independent measurements. Multiple excitations were excluded according to the spectroscopy. This assumption and the consistency of the data were checked by monitoring the penetration kinetics during growth of the top layer, which delivers the F atoms by F_2 dissociation. Slowing down the deposition rate in such a way that most of the F_2 molecules are dissociated on the actual surface before it is covered by the next monolayer allows one to decide whether F atoms are remobilized after completion of the film. In several samples remobilization indeed occurred and was attributed to unintentional impurities. Sorting out the well-behaved samples resulted once more in a penetration depth between 2 and 2.5 nm.

To compare the penetration depth d_0 with the average length of travel s_0 from the multiply doped samples, the different geometries have to be taken into account. The penetration depth d_0 corresponds to a vertical and straight path through the spacer layer. The isotropic angular distribution of the initial momentum of the F atoms leads to a corresponding average length of travel s_0 significantly larger than the measured d_0, even for straight trajectories. A diffusive type of motion enlarges s_0 further, and a realistic estimate of $s_0=7$ nm was derived from the d_0 values. This is at the lower limit of the range derived from the multiple doping experiment and consistent within the error bars. Thus the experiments show that F atoms provided with several eV of kinetic energy travel more than 2 nm in Ar matrices, i.e., at least 8 monolayers.

If we contrast the experimental findings with the calculations (Sec. 2), we arrive at a severe discrepancy. The very first molecular dynamics simulations looked promising and predicted long-range trajectories which exceed the chosen size of the cluster. Advanced calculations, which treat the interaction of the F atom's *p*-orbital with the matrix in more detail and include nonadiabatic transitions among the electronic surfaces, yield much shorter travel ranges. Improve-

ments of the potentials by using the DIM method did not resolve the problem. All of the more recent high-level calculations predict cage exit only to neighboring sites and no long-range mobility at all.

On the other hand, these simulations deliver a swarm of trajectories on the femtosecond time scale. The recombination dynamics of ClF molecules in Ar, studied in a first set of femtosecond pump-probe experiments, agrees well with the predictions of the DIM-trajectory simulations on F_2 as far as the very fast energy loss and the redistribution in the manifold of electronic states are concerned (Sec. 4). Finally, the cage exit dynamics of the F fragment, measured in ClF-doped Kr samples, shows a time for direct cage exit to the next site within 250 fs, in good agreement with the predictions. It seems that the discrepancies between experiment and high level simulations are on a rather subtle level that allows for a convincing prediction of the short-time dynamics (up to 1 ps) but precludes correct simulation of the migration.

Thus it is up to a monitoring of the migration process itself by femtosecond spectroscopy to pin down where the demonstrated deviation between experiment and simulations occurs. This may be accomplished, e.g., by combining femtosecond spectroscopy with co-doped matrices.

This collection of results was obtained in long-standing collaborations with the groups of Prof. V. A. Apkarian, Prof. B. Gerber, Prof. J. Manz, and Prof. H. Gabriel.

*E-mail: nikolaus.schwentner@physik.fu-berlin.de

[1] V. A. Apkarian and N. Schwentner, Chem. Rev. **99**, 1481 (1999).
[2] R. Alimi, R. B. Gerber, and V. A. Apkarian, J. Chem. Phys. **92**, 3551 (1990).
[3] V. Biryukov, Nucl. Instrum. Methods Phys. Res. B **53**, 202 (1991).
[4] N. Sack, M. Akbulut, T. Madey, P. Klein, H. Urbassek, and M. Vicanek, Phys. Rev. B **54**, 5130 (1996).
[5] C. Bressler and N. Schwentner, Phys. Rev. Lett. **76**, 648 (1996).
[6] E. Misochko, A. Akimov, and C. Wight, Chem. Phys. Lett. **274**, 23 (1997).
[7] C. Bressler, W. Lawrence, and N. Schwentner, J. Chem. Phys. **105**, 1318 (1996).
[8] G. Zerza, G. Sliwinski, and N. Schwentner, Appl. Phys. B **55**, 331 (1992).
[9] G. Zerza, F. Knopp, R. Kometer, G. Sliwinski, and N. Schwentner, *UV-VIS Solid State Excimer Laser XeF in Crystalline Argon*, in Solid State Laser II, SPIE **1410**, 202 (1991).
[10] M. Bargheer and N. Schwentner, in preparation.
[11] R. Alimi, R. B. Gerber, and V. A. Apkarian, Phys. Rev. Lett. **66**, 1295 (1991).
[12] A. Krylov and R. Gerber, Chem. Phys. Lett. **231**, 395 (1994).
[13] A. Krylov, R. Gerber, and V. Apkarian, Chem. Phys. **189**, 261 (1994).
[14] K. S. Kizer and V. A. Apkarian, J. Chem. Phys. **103**, 4945 (1995).
[15] M. Y. Niv, M. Bargheer, and R. B. Gerber, J. Chem. Phys. **113**, 6660 (2000).
[16] M. Ovchinnikov and V. A. Apkarian, J. Chem. Phys. **110**, 9842 (1999).
[17] M. Akbulut, N. Sack, and T. Madey, Surf. Sci. Rep. **28**, 177 (1997).
[18] N. Sack, M. Akbulut, and T. Madey, Phys. Rev. B **51**, 4585 (1995).
[19] C. Bressler, M. Dickgiesser, and N. Schwentner, J. Chem. Phys. **107**, 10268 (1997).
[20] M. Dickgiesser and N. Schwentner, J. Phys. Chem. A **104**, 3743 (2000).
[21] M. Dickgiesser and N. Schwentner, J. Chem. Phys. **113**, 8260 (2000).
[22] M. Frankowski, G. Sliwinski, and N. Schwentner, J. Low Temp. Phys. **122**, 443 (2001).
[23] M. Frankowski, G. Sliwinski, and N. Schwentner, in *Proceedings*, Laser Physics and Applications **3724**, 362 (1999).
[24] N. Schwentner and V. Apkarian, Chem. Phys. Lett. **154**, 413 (1989).
[25] H. Kunttu, J. Feld, R. Alimi, A. Becker, and V. Apkarian, J. Chem. Phys. **92**, 4856 (1990).
[26] H. K. J. Feld and V. A. Apkarian, J. Chem. Phys. **93**, 1009 (1990).
[27] H. Kunttu, E. Sekreta, and V. A. Apkarian, J. Chem. Phys. **94**, 7819 (1991).
[28] M. Jacox, Rev. Chem. Intermed. **6**, 77 (1985).
[29] R. Perutz, Chem. Rev. **85**, 77 (1985).
[30] I. Goldschleger, E. Misochko, A. Akimov, and C. Wight, J. Mol. Spectrosc. **205**, 269 (2001).
[31] E. Misochko, A. Akimov, and C. Wight, J. Phys. Chem. A **103**, 7972 (1999).
[32] E. Misochko, A. Akimov, I. Goldschleger, and C. Wight, Fiz. Nizk. Temp. **26**, 981 (2000) [Low Temp. Phys. **26**, 727 (2000)].
[33] E. Misochko, A. Akimov, I. Goldschleger, and C. Wight, J. Chem. Phys. **116**, 10318 (2002).
[34] E. Misochko, A. Akimov, and C. Wight, Chem. Phys. Lett. **293**, 547 (1998).
[35] A. H. Zewail, J. Phys. Chem. A **104**, 5660 (2000).
[36] M. Bargheer, P. Dietrich, and N. Schwentner, J. Chem. Phys. **115**, 149 (2001).
[37] M. Bargheer, Ultrafast Photodynamics in Condensed Phase, Shaker, Aachen (2002), ISBN 3-8322-0814-3.
[38] M. Bargheer, J. Pietzner, P. Dietrich, and N. Schwentner, J. Chem. Phys. **115**, 9827 (2001).
[39] M. Bargheer, M. Gühr, and N. Schwentner, J. Chem. Phys. **117**, 5 (2002).
[40] M. Bargheer, M. Y. Niv, R. B. Gerber, and N. Schwentner, Phys. Rev. Lett. **89**, 108301 (2002).
[41] M. Bargheer, K. Donovang, P. Dietrich, and N. Schwentner, J. Chem. Phys. **111**, 8556 (1999).
[42] A. B. Alekseyev, H. Liebermann, R. J. Buenker, and D. B. Kokh, J. Chem. Phys. **112**, 2274 (2000).

This article was published in English in the original Russian journal. Reproduced here with stylistic changes by AIP.

Coherent motion and anomalous transport properties of exciton and hole polarons with intrinsic vibrational structure

A. M. Ratner*

B. Verkin Institute for Low Temperature Physics and Engineering of the National Academy of Science of Ukraine, 47 Lenin Ave., Kharkov, 61103, Ukraine
(Submitted June 25, 2002)
Fiz. Nizk. Temp. **29**, 237–249 (March 2003)

It is shown that intrinsic vibrational degrees of freedom, inherent in two-atom exciton and hole polarons, drastically affect their transport properties in wide-band dielectrics (rare-gas solids and alkali halides). A fast excitonic energy transport and a comparatively high hole mobility, experimentally observed and attributed to two-site polarons tightly bound with the lattice, cannot be explained by the conventional theory of small-radius polarons that predicts their negligibly weak diffusion, exponentially small in the ratio of the binding energy to temperature. The theory developed below with allowance for the intrinsic vibrational structure of two-site polarons describes qualitatively a large relevant set of experimental data which seem anomalous from the viewpoint of the conventional theory. [DOI: 10.1063/1.1542438]

INTRODUCTION

In dielectrics with broad exciton and hole bands, formed by a strong exchange interaction, the most stable excitonic and hole states are known to be of a two-site type (two neighboring atoms, strongly brought together, form a quasi-molecule with the exchange binding growing sharply with decreasing interatomic distance). Such two-atom electronic excitations with an intrinsic vibrational degree of freedom are inherent and distinctly observed in the electronic spectra of rare-gas solids[1] and alkali-halide crystals[2] (these classes of dielectrics have common features of electronic structure, outlined at the beginning of Sec. 1).

Such two-atom excitations are usually treated as polaronic states tightly bound with the lattice. In the theory of polarons, the energy of this binding is identified with the separation Δ of the polaron level from the bottom of the corresponding band. For the classes of dielectrics mentioned, the separation Δ is of the scale of 1 eV.

However, the transport properties of such two-site excitations cannot be described satisfactorily within the conventional polaronic theory.[3–6] For a strongly bound polaron, the latter predicts an exponentially small diffusion coefficient

$$D = D_0 \exp(-U_{\text{act}}/T_{\text{eff}}), \tag{1}$$

where the activation energy U_{act} is close to Δ and T_{eff} stands for an effective temperature (expressed in energy units) which at low temperatures makes allowance for the lattice zero-vibration energy. This inference of the theory drastically contradicts experimental evidence (analyzed in Secs. 5 and 6) of a fast transport of charge and especially energy by two-site polarons.

The physical reason for this discrepancy consists in the following. The conventional theory considers the hopping of a polaron devoid of intrinsic structure. Such a polaron, staying near a lattice site A, causes lattice deformation around it and a corresponding lowering of the polaron level by an amount $\Delta \approx U_{\text{act}}$. The electron or hole localized at site A at a deep level E_A can go over to a neighboring site B only under a fluctuation of its lattice surroundings strong enough to lower the level of the electronic state localized at site B down to E_A. The energy of such a lattice deformation is found to be close to Δ, as described by Eq. (1). Such a simple notion is not applicable to a two-site polaron: its intrinsic degree of freedom enables it to move continuously together with the deformation cloud maintaining the polaronic state. In other words, the lattice deformation around a new position of a two-site polaron is mainly produced not by thermodynamic fluctuations but by the continuous motion of the polaron itself.

In the present paper, the theory of the continuous motion and transport properties of two-site polarons is developed and qualitatively compared with experiment as applied to rare-gas and alkali-halide crystals. First, in Sec. 1, it is shown that a fast transport in these dielectrics is conditioned by some features of their electronic spectrum, viz., the exchange nature of the exciton and hole bands and their anisotropic structure, entailing one-dimensional translational motion. As a result, the energy barrier impeding the translational motion is sharply diminished as compared to a structureless polaron with the same binding energy Δ.

In the next Sections, 2, 3, and 4, such one-dimensional motion of two-site excitations is explored, depending on the main factors dictating their character, viz., the vibrational energy of a two-atom quasi-molecule and the height of the ''residual'' energy barrier. In the case of a high vibrational energy, much exceeding the barrier height and temperature, the translational motion has a coherent directional character (Sec. 3), but under thermodynamic equilibrium (Sec. 4) the translational motion aquires a diffusive character, and transport is slowed down by several orders of magnitude compared to the former case. In Secs. 5 and 6 a qualitative comparison with experiment is carried out as applied to these two cases.

1. CONTINUOUS ONE-DIMENSIONAL MOTION OF POLARONS WITH INTRINSIC DEGREES OF FREEDOM

This manner of translational motion is to a large degree conditioned by a feature of the electronic spectrum of rare-gas or alkali-halide crystals. In the case of a rare-gas crystal, the system of excitonic bands occupies the upper part of the dielectric gap (more than 10 eV wide) and originates from the Rydberg atomic excited states $ns^2np^5(n+1)s$. A significant bandwidth of about 1 eV is due to a rather strong exchange interaction between an excited atom and adjacent ground-state ones. On the other hand, this strong exchange results in the existence of two-site excitonic states. A two-site exciton is formed on adjacent atoms which are brought together, providing a much stronger attractive exchange interaction than for regular lattice sites. Such a two-atom quasi-molecule with a bond energy of about 1 eV is quite similar (judging from spectroscopic data) to the corresponding excimer molecule in the gas phase.[1] In a crystal, the vibrational levels of such a quasi-molecule turn to narrow subbands practically covering the energy extent of all excitonic bands.[7,8]

The dispersion law of excitons or holes is determined by the interatomic overlap of excited states $ns^2np^5(n+1)s$, which mainly coincides with the overlap of the *np*-hole states ns^2np^5 centered at adjacent sites. This overlap is largest in the direction of the *p*-state axis and gives rise to a sharply anisotropic excitonic dispersion law.[9] Actually, a free exciton or hole moves in the direction of the minimal effective mass, which coincides with the axis of the *np*-hole and dictates the axis direction of a two-site exciton or hole polaron.

The outlined picture holds qualitatively for alkali halide crystals with large anions and small cations (e.g., NaI, NaCl, and KI). The exciton and hole states (free or self-trapped) formed in the sublattice of closed-shell anions are similar to those of rare-gas solids. These electronic excitations, associated with the anion sublattice, cannot be noticeably affected by small cations with a very high ionization potential.

The translational motion of two-site excitons and holes is described by the same equations and has the same qualitative features (a distinction in their behavior, caused by essentially different lifetimes, will be considered in Secs. 3 and 4). So far this distinction does not manifest itself, and we will speak, for definiteness, about holes.

Let us trace the qualitative features of the motion of a two-site self-trapped hole (also called a two-atom ionized quasi-molecule) in a rare-gas crystal. The molecular ion consists of two identical rare-gas atoms A and B with a common shared *px*-hole in their outer shell (the *x* axis coincides with the axis of the atomic *P* state). These atoms are brought together by a strong exchange interaction conditioned by the hole. The exchange potential, mainly proportional to the overlap of the *px* states centered at the points A and B, strongly diminishes with an increase of the angle between the *x* axis and the AB direction.[9] So, the hole forming the quasi-molecule AB is polarized in the *x* direction, coincident with the quasi-molecule axis AB. The translational motion of the hole is conditioned by the exchange interaction between the atoms A, B and other atoms. Since this exchange is significant only for adjacent atoms lying on the same axis *x*, the motion of a two-site hole is of a one-dimensional character (which is evidenced experimentally; see Sec. 6, Item 2). Below we will consider the motion of such a hole along the atomic chain, with allowance being made for its static three-dimensional surroundings. The same relates to two-site excitons as well.

The nontrivial phenomena under consideration are conditioned by a nonpair exchange interaction of atoms among which a hole is distributed.[9,10] Such an exchange is described by the usual exchange Hamiltonian

$$\mathcal{H}=\sum_{n=1}^{N} E_0 a_n^+ a_n - \sum_{n=1}^{N-1} V(x_{n+1}-x_n) \times (a_n^+ a_{n+1} + a_n a_{n+1}^+). \tag{2}$$

Here E_0 is the site hole level, a_n^+ is the creation operator for a hole on the nth atom, $-V(x)$ is the negative exchange energy, strongly dependent on the interatomic distance x, and x_n is the coordinate of the nth atom counted along the chain. The hole is generally distributed among several atoms, as described by the eigenfunction of the Hamiltonian (2)

$$\Psi=\sum_n c_n\varphi_n, \quad \sum_n |c_n|^2=1, \tag{3}$$

where $|c_n|^2$ is the portion of the hole at the nth site, and

$$\varphi_n = a_n^+ \Psi_{\text{ground}} \tag{4}$$

is the corresponding site state of the crystal (Ψ_{ground} is its ground state).

The same Hamiltonian (2) also describes an exciton, with the sole difference that the operator a_n^+ in Eqs. (2), (4) creates an atomic excitation instead of a hole at the nth site. Therefore, all of the inferences drawn below in this Section and in Sec. 2 pertain to holes and excitons to the same degree.

The lowest eigenvalue of the Hamiltonian (2) for arbitrary fixed positions of the atoms is

$$W=E_0-\max\left\{\sum_n V(x_{n+1}-x_n)c_n c_{n+1}\right\}, \quad \sum_n |c_n|^2=1 \tag{5}$$

(the energy is minimized with respect to the set $\{c_n\}$). If the occupation numbers c_n were fixed, the quantity (5) as a function of atomic coordinates would be the sum of pair potentials $V(x_{n+1}-x_n)$ multiplied by fixed coefficients. But in fact the occupation numbers c_n depend substantially on $V(x_{n+1}-x_n)$ and, hence, on x_n; therefore, the hole energy (5) cannot be reduced to the sum of pair potentials. This circumstance is of fundamental importance: it results in a substantial lowering of the energy barrier that impedes translational motion (within the pair potential approach, this barrier is found to be much higher and the translational motion much slower).[7,8]

For a periodic chain consisting of N atoms, the minimum of energy (5) is achieved at $c_n=N^{-1/2}$, which corresponds to the lowest band state.

We consider the opposite case of a tightly bound polaronic state with a hole localized near two adjacent atoms brought together (they are numbered, for definiteness, by indices $n=2$ and 3). For this pair of atoms, the exchange multiplier $V(x_3-x_2)$ in (5) strongly exceeds the rest of the mul-

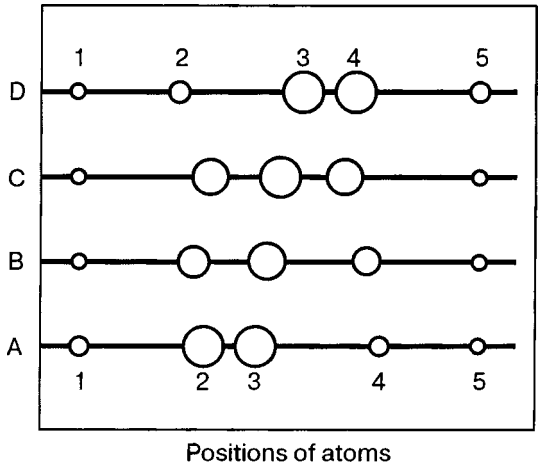

FIG. 1. Translational motion of a two-site self-trapped hole via its continuous redistribution among atoms, shown by circles (the areas of the circles indicate the portion of the hole on the atoms). The hole sequentially passes the states A, B, C, D without overcoming a significant barrier. This scheme relates to a two-site exciton as well.

tipliers $V(x_{n+1}-x_n)$; hence, the energy (5) is minimized at $c_2=c_3\approx 2^{-1/2}$, the rest of the coefficients c_n being much less. Such a state labeled by A is shown in Fig. 1, where the areas of the circles denote the portion of the hole, $|c_n|^2$, localized on the atoms. Let us trace the change from the state A to a similar state D with the hole shifted by one chain period, first keeping to the traditional notion and then with allowance for the nonpair exchange interaction.

Within the traditional notion,[3–6] the state A turns immediately to the state D: the hole hops by one lattice period from the atomic pair (2,3) to the pair (3,4). To make such a hop possible, an adjacent atom 4 (devoid of a hole until the hop occurs) must be moved towards atom 3 strongly enough to reduce the distance (4,3) down to the distance (3,2). The energy of such a deformation nears the binding energy, so that the hopping rate is described by Eq. (1).

If the nonpair exchange interaction is taken into account, the picture becomes quite different: the initial state A turns to the final state D through a continuous sequence of intermediate states (B, C...) in the following way. To minimize energy (5), atom 4, when moving towards the pair (2,3), gets a portion of hole that increases with decreasing separation (4,3) (as shown by the varying areas of the circles). Thus, the distribution of the hole among atoms follows their motion continuously (not by a jump as within the conventional scheme). This sharply diminishes the energy barrier B to be overcome when changing from the initial state A to the final state D.

Nevertheless, the height of the ''residual'' energy barrier essentially influences the translational motion of a two-site hole that, in view of its long lifetime, moves in thermodynamic equilibrium with the lattice and occupies rather low vibrational levels comparable with the barrier height. Unlike a hole, a two-site exciton, during its short lifetime, comparable with the time of vibrational relaxation, occupies high vibrational levels. As long as the vibrational energy much exceeds the barrier height, a two-site exciton moves in a coherent directional way practically irrespective of the barrier.

For this reason, the barrier is of great importance only for the motion of holes. In the next Section, the barrier is investigated as applied to two-site holes, but the results obtained are pertinent to two-site excitons as well.

2. ENERGY BARRIER FOR TRANSLATIONAL MOTION

To obtain the barrier, let us introduce the total adiabatic potential of an N-atom chain containing one hole:

$$W_{\rm tot}(x_1,\ldots,x_N)=W(x_1,\ldots,x_N)+\sum_{n=1}^{N-1}u_0(x_{n+1}-x_n)+\sum_{n=1}^{N}\sum_{\mathbf{R}}u_0(|\mathbf{r}_n-\mathbf{R}|). \quad (6)$$

The total potential consists of the hole energy (5) [first term on the right-hand side of Eq. (6)] and the sum of the pairwise ground-state interatomic potentials u_0 taken along the chain (second term) as well as between every chain atom (with coordinates $\mathbf{r}_n$) and the immovable lattice atoms not belonging to the chain (with coordinates $\mathbf{R}$). To find the barrier, one has to continuously change from the state A to the state D (see Fig. 1) via reducing the distance (4,3), the rest of interatomic distances being adjusted to the minimum of the total potential (6) at a given separation (4,3). Such a trajectory in the space $(x_1,\ldots,x_N)$ inevitably passes a symmetric configuration C (Fig. 1) that provides an extremum of $W_{\rm tot}$. Usually a two-site hole state A or D is assumed to be stable, that is

$$W_{\rm tot}({\rm C})>W_{\rm tot}({\rm A}). \quad (7)$$

If the condition (7) is met, the barrier height should be defined as

$$B=W_{\rm tot}({\rm C})-W_{\rm tot}({\rm A})=W_{\rm tot}({\rm C})-W_{\rm tot}({\rm D}). \quad (8)$$

Below, the barrier definition (8) will be used without restriction (7), a negative B being understood in the meaning of the energy separation between the stable three-atom state C and unstable two-atom state A or D.

To calculate the barrier (8) for a real crystal, it is necessary to reconstruct the total potential (6). It contains, besides the ground-state potential u_0 which is known to good accuracy,[9] the resonance contribution (5) defined through the exchange potential $V(x)$, mainly proportional to the interatomic overlap integral $J(x)$ (x is the interatomic distance). The dependence $J=J(x)$ can be derived approximately from the ground-state repulsion potential that, on one hand, is in the main proportional to $J(x)^2$ and, on the other hand, is known to decrease with increasing x nearly as $\exp(-12x/l)$ (l is the interatomic distance in the ideal lattice)[9]. Thus, the exchange potential V can be approximated in the form

$$V(x)=V_0\exp\left\{q\,\frac{l-x}{l}+\gamma\left(\frac{l-x}{l}\right)^2\right\},\quad q\approx 6. \quad (9)$$

Here we have allowed for a small quadratic term influencing the barrier. The pre-exponential factor V_0 (close to 0.24 eV for solid krypton) can be derived from the width of the hole band formed in the ideal lattice ($V=V_0$ at $x=l$).

Below, the parameters q, γ, and $V_0=0.24$ eV are taken for solid krypton. For hole states, there are no spectroscopic

TABLE I. Barrier height (8) for solid krypton calculated using the exchange potential (9) with different q and γ for lattice periods 0.5812 and 0.5850 nm related to the temperatures 80 and 110 K, respectively.

q	γ	B, K	
		T=80 K	T=110 K
5.66	0.07	473	410
5.76	0.06	386	308
5.865	0.05	288	196
5.97	0.04	168	60
6.08	0.03	38	−84
6.22	0.02	−62	−199
6.36	0.01	−192	−343
6.51	0	−335	−500

data to derive the exchange interaction parameters q and γ. But q and γ can be derived for the lowest two-site excitonic state via fitting the corresponding luminescence spectrum (energy position and half-width) with experiment. Note that the exchange interaction, resulting from a p-hole in the valence shell, cannot noticeably differ for the hole and exciton: the p-electron is completely removed in the former case or carried over to a large-radius Rydberg state in the latter. Making use of this, let us fit the required parameters q and γ with the two-site exciton luminescence band of solid krypton. The fitting can be carried out with nearly the same accuracy with q varying in the range 6 ± 0.5 and the corresponding values of γ given in Table I as a function of q.

For every set (q, γ), Table 1 presents the barrier (8) calculated with the exchange potential (9) for two lattice parameters 0.5812 and 0.5850 nm related to temperatures of 80 and 110 K, respectively.[11] (Note that the lattice parameter, appearing in the last term of Eq. (6), influences the barrier in an essential way. It grows with a decrease of the distance between chain atoms and the nearest lattice atoms lying beyond the chain.) Table 1 demonstrates a high sensitivity of the barrier to the exchange potential parameters as well as to the lattice period (its thermal increase by 0.7% lowers the barrier by about 100 K). The point is that the potential (6), whose maximum creates the barrier, is formed by the sum of positive and negative quantities with a scale of 1 eV, which exceeds the characteristic height of the barrier by about two orders of magnitude. A slight variation of a separate summand causes a significant relative variation of the barrier.

As will be shown below, the barrier height influences the hole motion in an essential and nontrivial way (the specific way of realizing the barrier is of much less importance).

Song[12] has estimated the barrier B for a two-site hole quasi-molecule in solid argon within the approximation of pair potentials. The interaction between the atoms of the quasi-molecule (atoms 2, 3 in Fig. 1, state A) and between every atom of the quasi-molecule and an adjacent atom not belonging to it (the pairs 1,2 and 3,4) was described by the same potential, which was assumed to be independent of the hole distribution between these atoms. As a result, it was found that the barrier height does not exceed 0.05 eV $=600$ K, which agrees in order of magnitude with Table I.

3. DIRECTED TRANSLATIONAL MOTION OF A TWO-SITE POLARON (EXCITON) ON HIGH VIBRATIONAL LEVELS

Due to its short lifetime, comparable with the vibrational relaxation time, a two-site exciton dwells on high vibrational levels during a significant part of its existence. The directed translational motion, possible only on high vibrational levels, manifests itself in an anomalously fast energy transport.

Even within the one-dimensional model (set forth in Sec. 1) a rigorous quantum-mechanical description of such a complicated phenomenon seems unrealistic. Below, only the electronic subsystem will be considered in a quantum-mechanical way; the lattice motion will be described classically in the adiabatic approximation. The latter is justified since the separation between the lowest level of the Hamiltonian (2) and the rest of its levels greatly exceeds both T and the vibrational frequencies of the chain (expressed in energy units). Within this model, the lattice is represented by an N-atom chain (its length is chosen large enough that the calculation results are independent of N). The rest of the lattice atoms are assumed to be placed strictly at their sites and are taken into account by the last term in the total potential (6).

Keeping to the adiabatic scheme within the one-dimensional model, let us first consider the lowest excitonic state formed at arbitrary fixed positions of N atoms. The energy W of this state is given by Eq. (5). According to a standard procedure, the partial derivatives of the right-hand side of Eq. (5), added to the sum $W\Sigma c_n^2$, should be taken with respect to the coefficients c_n and equated to zero. This results in the system of linear homogeneous equations

$$\begin{aligned} &V(x_2-x_1)c_2-Wc_1=0,\\ &V(x_{n+1}-x_n)c_{n+1}+V(x_n-x_{n-1})c_{n-1}-Wc_1\\ &\quad=0 \quad (1<n<N),\\ &V(x_N-x_{N-1})c_{N-1}-Wc_N=0. \end{aligned} \tag{10}$$

Let D be the N-order determinant of this equation system. The excitonic energy $W(x_1,\ldots,x_N)$ at arbitrary fixed positions, $x_1,\ldots,x_n$, of the chain atoms can be obtained from the equation

$$D(W,x_1,\ldots,x_N)=0. \tag{11}$$

Of the N roots of this determinant, the lowest one corresponds to the self-trapped excitonic state and is separated by a large gap from all the other roots, which belong to a slightly distorted excitonic band. The least root is identified with W. Substituting W into (6), we obtain the total adiabatic potential W_{tot} of the N-atom system with a self-trapped exciton.

The classical motion of the system of N atoms with the nonpair potential (6) is described by the equation

$$M_0\frac{d^2x_n}{dt^2}+\frac{\partial W_{\text{tot}}(x_1,\ldots,x_N)}{\partial x_n}=0 \tag{12}$$

with the atom mass M_0.

Equation (12) was solved numerically for solid krypton under the following conditions. At the initial time $t=0$, a two-site quasi-molecule with the vibrational energy E_{vib}

arose on two adjacent atoms arbitrarily chosen inside the atomic chain. In the course of motion, the electronic excitation is distributed among 4 atoms (as shown in Fig. 1). The nonequilibrium vibrational energy, concentrated within this four-atom complex, is maintained at the given level $E_{\rm vib}$ via a weak continuous input of energy. The rest of the atoms are in equilibrium with the lattice at a given constant temperature T. In the course of motion, the total average kinetic energy of all atoms of the chain (except the above four-atom complex) was maintained at the level $(N-4)T/2$ via a very slow injection or removal of heat. Simultaneously the dispersion of this kinetic energy as a function of time was maintained at a proper level of $(N-4)^{1/2}T/2$ (to that end, every atom of the chain received weak random augmentations to its momentum with the frequency of lattice vibrations).

The computer solution of Eqs. (11), (12) exhibits some general features. The strongest resonance bond, formed between two atoms with the numbers L and $L+1$, comprises more than half the electronic excitation (this means that $c_L^2+c_{L+1}^2>0.5$); the excitation is concentrated practically completely on four atoms $(L-1,L+1,L+2)$. The vibrational energy of this four-atom complex decreases slowly (by about 1% per period) in the course of thermal relaxation. Note that in the corresponding quantum-mechanical system the vibrational relaxation occurs substantially (by two orders of magnitude) more slowly in view of the relevant conservation laws and complicated phase relations between different vibrational wave functions.[9] This circumstance was taken into account by a weak steady input of energy into the four-atom complex, which maintained its vibrational energy at the initial level.

The character of the motion is determined by the parameters $E_{\rm vib}$ and T. Numerical analysis of Eqs. (11), (12) shows that the translational motion of the four-atom complex can occur either in a diffusive way (through random translational shifts, one of which is shown in Fig. 1) or in a coherent directional way (through sequential shifts matched in phase with one another). The directional motion takes place at a high vibrational energy $E_{\rm vib}$ and a low temperature; in the opposite case, the self-trapped exciton moves in a random diffusive way. The picture is practically independent of the barrier height B as long as $B \ll E_{\rm vib}$. The boundary between these types of motion in the $E_{\rm vib}$-versus-T plane is shown in Fig. 2.

Figure 3 shows the motion of the exciton center of weight

$$x_c=\sum_{n=1}^{N}|c_n|^2x_n \quad \left(\sum_{n=1}^{N}\left|c_n\right|^2=1\right) \tag{13}$$

at different points of the $E_{\rm vib}$-versus-T plane. The figure demonstrates that the motion of a two-site exciton changes its character in a similar way with increasing vibrational energy at a constant temperature (Fig. 3a) or with decreasing temperature at a constant vibrational energy (Fig. 3b). The directional motion of an exciton is quite stable on the right-hand side of the boundary indicated in Fig. 2, whereas on the left-hand side directional motion can be realized during short time intervals in a random way due to fluctuations.

At any temperature, the stability of the coherent translational motion of the self-trapped exciton depends strongly on its vibrational energy. This seems quite natural since this translational motion is coupled with the vibrations of the four-atom complex.

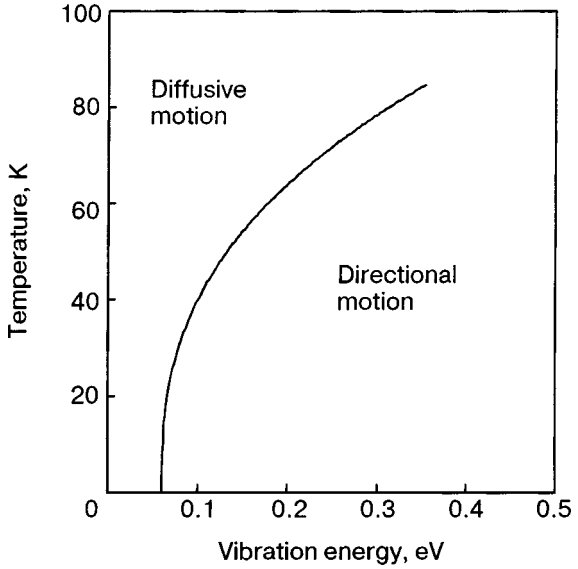

FIG. 2. Regions of the diffusive and directional motion of a two-site exciton in the plane temperature versus vibrational energy.

The directional motion velocity, $V=dx_c/dt$, is found to be of the scale of the sound velocity in the crystal. This is easy to understand: a longitudinal elastic wave, coupled with electronic excitation, propagates in the crystal in basically the same way as ordinary sound. As can be seen from Fig. 3a, V grows with $E_{\rm vib}$. The directional motion velocity was found to be proportional to $E_{\rm vib}^{1/2}$ and practically independent of temperature and barrier height (at $E_{\rm vib}=0.63$ eV, V coincides with the longitudinal sound velocity in solid krypton, equal to 1.37×10^5 cm/s).

4. DIFFUSIVE MOTION OF A TWO-SITE POLARON (HOLE) IN THERMODYNAMIC EQUILIBRIUM WITH THE LATTICE

Unlike short-lived excitons (with a lifetime of about 1 ns), two-site hole polarons during measurement of their mobility have a long lifetime (more than 1 μs),[13] exceeding the vibrational relaxation time by 3 or 4 orders of magnitude. Therefore, a self-trapped hole moves under conditions of thermodynamic equilibrium with the lattice. Such motion was investigated by solving Eqs. (11), (12) in a way described in Sec. 3, but without the input of energy into the four-atom complex to maintain its vibrational energy at a given level. Under such conditions the hole polaron motion is of a random diffusive character, so that the hole mobility μ is connected with the hole diffusion coefficient D by the known Einstein relation

$$\mu=\frac{De}{T}=\frac{e}{2Tt}\sum_{t_j\leqslant t}(\Delta x_j)^2, \tag{14}$$

where e is the electron charge, T is the temperature in energy units, Δx_j stands for the random shift of the center of weight of the hole at the instant of time t_j, and the summation extends over all statistically independent shifts occurring during time t.

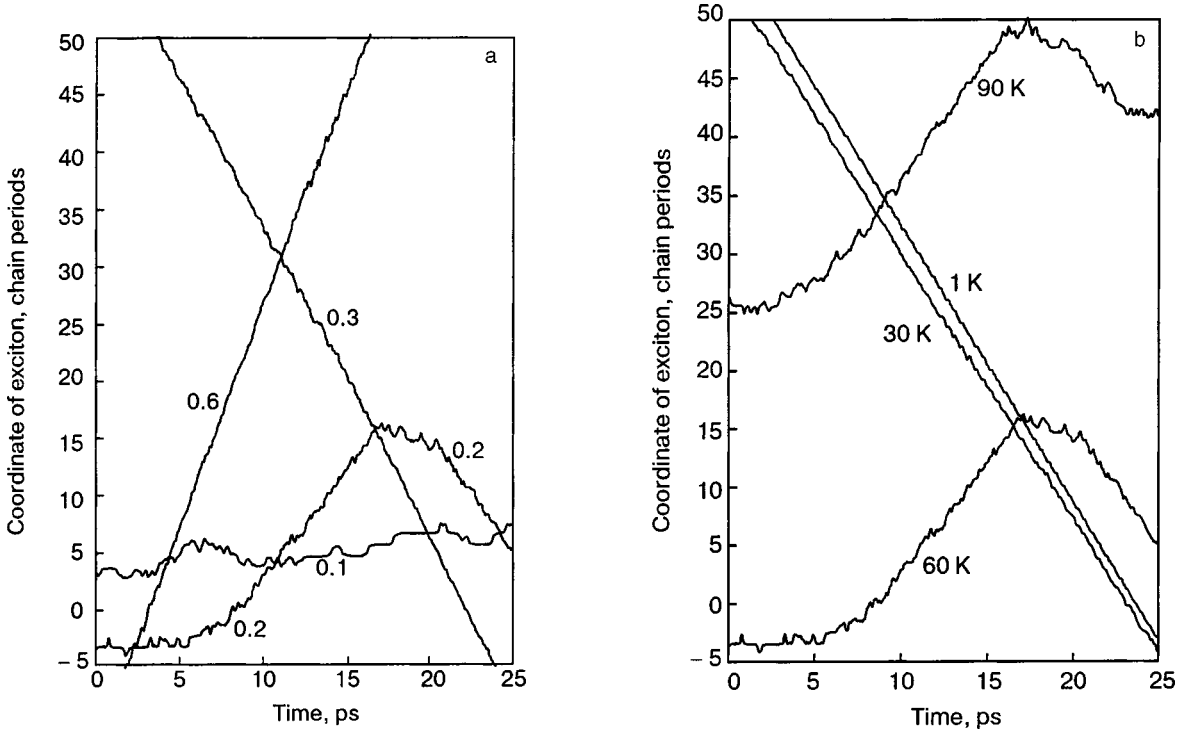

FIG. 3. Typical fragments of the motion of the exciton center of weight calculated by solving Eqs. (11), (12). The exciton coordinates in units of the chain period (ordinate axis) and time (abscissa axis) are relative to an arbitrary origin. The figure shows how the character of motion changes: (a)—with increasing vibrational energy (indicated in the figure in eV) at a constant temperature equal to 60 K; (b)—with decreasing temperature (indicated in the figure) at a constant vibrational energy equal to 0.2 eV. The directional motion is quite stable on the right of the boundary presented in Fig. 2 and arises in a random fluctuation way on the left of the boundary.

To evaluate the diffusion coefficient D with sufficient accuracy, the diffusional motion of a hole was traced for a time of about 5 ns; during this time, about 700 squared chain periods are accumulated in the sum (14).[11]

Unlike an exciton occupying a high vibrational level, the equilibrium motion of a self-trapped hole essentially changes its character depending on the barrier height B, as is demonstrated in Fig. 4. As can be seen from the figure, for a high barrier $B=386\ \mathrm{K}=4.8\ T$ (upper curve in Fig. 4), a hole participates in motion of two sharply different types: high-frequency vibrations with a small amplitude (merged into a thick line on the reduced scale of the figure) and random transnational shifts by one chain period, which look like hops on the scale used. Note that in fact such ''hops'' occur in a continuous way, as shown in Fig. 1. For a lower barrier, ''hops'' by several ($M=2,3...$) chain periods become possible (the meaning of such ''multiple hops'' will be explained below). In Fig. 4, every ''hop'' is marked by the number M indicating the distance of hopping in units of the chain period or, more briefly, the hopping multiplicity.

As the barrier lowers, the distinction between transnational shifts (''hops'') of the hole and its vibrational motion is blurred. Along with usual high-frequency vibrations, low-frequency ones appear with amplitudes enhanced up to the chain period l. Such low-frequency vibrations can result (but not inevitably) in a transnational shift according to the scheme of Fig. 1; their large period (up to 10 ps) corresponds to a small variation of the adiabatic potential W_{tot} when changing between the states B and C near the top of a low barrier.

It is easy to understand why the vibrational motion is

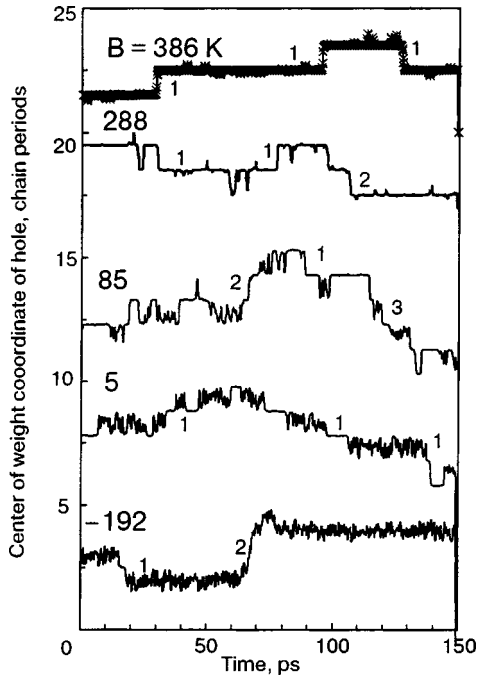

FIG. 4. Typical fragments of the diffusional motion of the center of weight of a hole in thermodynamic equilibrium with the lattice at $T=80$ K, calculated for different barriers (whose height is indicated in kelvins by the large numerals). Random transnational shifts (hole ''hops'') are marked by small numerals indicating the hopping distance in units of the chain period. As the barrier B is lowered in the region $B<T$, the vibrational motion of the hole develops at the expense of its transnational motion (therefore, as can be seen from Fig. 5, diffusion is not monotonously enhanced as the barrier is lowered).

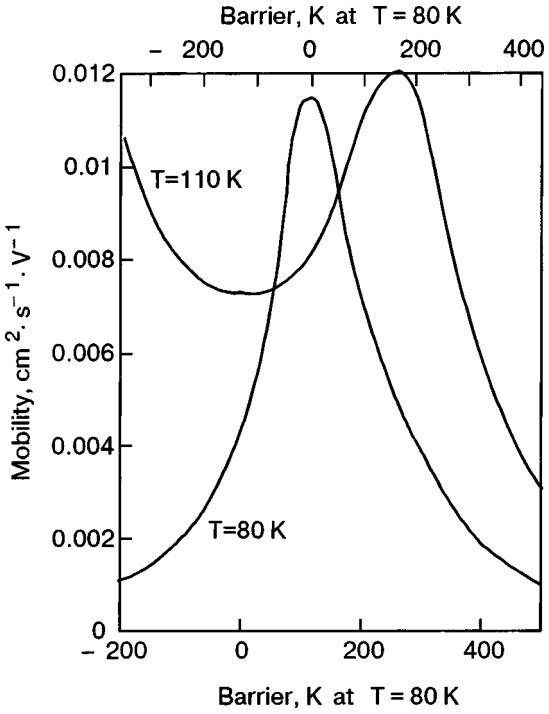

FIG. 5. Two-site hole mobility calculated for solid krypton as a function of the barrier height B at $T=80$ and 110 K (B varies noticeably with temperature due to thermal expansion, which is allowed for by two scales of barrier, related to 80 and 110 K).

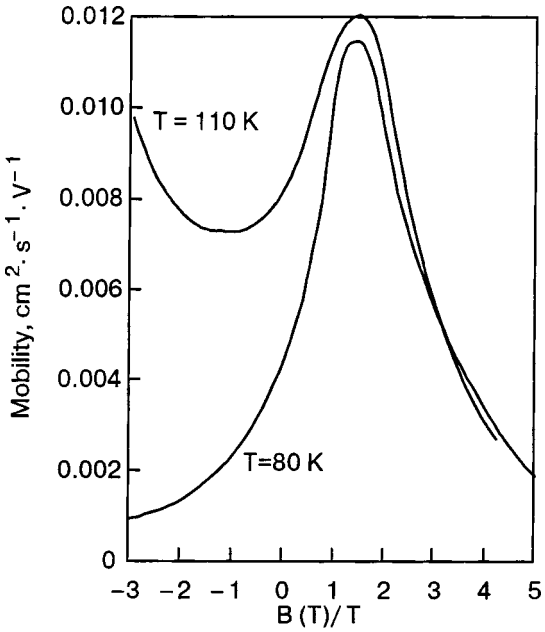

FIG. 6. The same results as in Fig. 3 presented versus the reduced variable $B(T)/T$ for $T=80$ and 110 K. Note that in the region $B>T$, where the ''hopping'' has an activational character, the mobility actually depends only on the reduced variable B/T.

well pronounced only in the case of a low barrier. Of interest are vibrations of a few atoms (the atoms 2, 3, 4 in Fig. 1) among which the hole is distributed. Such vibrations are accompanied by overcoming the barrier in both directions. For a high barrier ($B \gg T$), a noticeable motion of the hole is made possible by a strong short-lived thermodynamic fluctuation during which the system has enough time to pass the barrier only in one direction; such motion looks like a series of random independent hops (quite distinct at $B=386$ K $=4.8\,T$). As the barrier is lowered somewhat ($B=288$ K $=3.6\,T$), the fluctuation lifetime becomes sufficient to pass the barrier one time sequentially in both directions, which results in single-period vibrations with an amplitude near the chain period; such vibrations do not contribute to the mobility (14). When the barrier decreases and disappears ($B=85$ and 5 K), the vibrational motion of the hole becomes most developed and occurs in the form of a long sequence of aperiodic oscillations interrupted by comparatively infrequent ''hops''. In the absence of the barrier, the vibrational motion predominates over hopping; this is the reason why the mobility at a given T achieves its maximum value not in the absence of the barrier but at $B \approx 1.5\,T$ (see Figs. 5 and 6).

In order to compare the theory with an experiment[13] performed for solid krypton in the interval $80\ \mathrm{K} < T < 110$ K, computer calculations of the mobility with the use of Eqs. (11), (12) were carried out for solid krypton at the temperatures $T=80$ and 110 K (the analysis of these results, made below, permits one to extend their temperature range). For these fixed values of temperature, Fig. 5 presents the mobility μ (in units of $\mathrm{cm^2 s^{-1} V^{-1}}$) as a function of barrier height B. It should be recalled (see Sec. 2) that B varies noticeably with temperature due to thermal expansion. In Fig. 5, this is allowed for by two scales of barrier, related to 80 and 110 K. Nearly the same results (but with a large statistical straggling) were obtained via direct calculation of the mobility with the use of Eq. (12) complemented by an electrostatic term describing the hole charge in a weak external electric field.

Along with this, it is interesting to trace how the mobility depends on B/T irrespective of the way of varying the barrier (by varying the interatomic potentials or the lattice period). To that end, Fig. 6 presents the same results as in Fig. 5 in the coordinate μ versus the reduced variable $B(T)/T$ for $T=80$ K and 110 K. As can be seen from Fig. 6, in the region $B>T$, where the ''hopping'' has an activational character, the mobility actually depends only on the reduced variable B/T. Thus, the part of the curve to the right of the maximum gives the temperature dependence of the mobility in the range of lower temperatures for a positive barrier.

The absolute values of the mobility presented in Fig. 5 agree in order of magnitude with experiment[13] (see Sec. 6) but are systematically underestimated by almost a factor of four in comparison with the experimental data. The physical reason for this quantitative discrepancy, to all appearance, is connected with underestimation of the multiple hopping of self-trapped holes.

As was shown in Sec. 3, a two-site polaron on a high vibrational level simultaneously with vibrational motion participates in the directed transnational motion which is realized through sequential shifts correlated in phase. A short-time motion of such a type can occur also under conditions of thermodynamic equilibrium with the lattice when a strong fluctuation brings the vibrational energy of the four-atom complex (on average equal to $4T$) to a critical level necessary for the directed translational motion. Such fluctuational enhancement of E_{vib} gives rise to a short-lived coherent elastic wave coupled with the hole. To all appearances, the

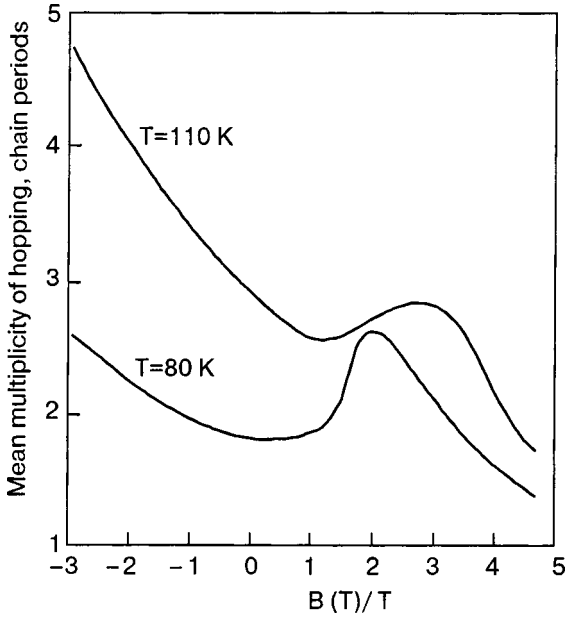

FIG. 7. Mean distance of hopping in units of the chain periods (hopping multiplicity), calculated at $T=80$ K and 110 K.

model of one-dimensional chain underestimates the lifetime of such a fluctuational elastic wave. Indeed, the lattice atoms not belonging to the chain but adjacent to it are assumed to be immovable, whereas in fact they are involved in this elastic wave, thus enhancing the total mass of the atoms involved and the stability of the wave. The underestimation of the hopping multiplicity within the one-dimensional model entails a corresponding underestimation of the mobility (quadratic in the multiplicity). This seems to be a reason for the above-mentioned quantitative discrepancy between the theory and experiment.

Let us consider multiple hops in more detail and introduce the hopping multiplicity M, equal to the total length of a hop in units of the chain period. As can be seen from Fig. 4, where all hops are marked by numbers indicating their length M, multiple hops with $M=2$ or 3 occur comparatively often. Hops with greater M (up to 10) occur more seldom but they contribute noticeably to the hole mobility (14). If the number of M-fold hops is denoted by ν_M, their contribution to mobility is proportional to $w_M=\nu_M M^2$. The mean multiplicity of hopping should be defined via averaging M over hops with the weights w_M:

$$\langle M\rangle=\frac{\Sigma_M w_M M}{\Sigma_M w_M}=\frac{\Sigma_M \nu_M M^3}{\Sigma_M \nu_M M^2}. \tag{15}$$

The mean multiplicity of hopping, calculated according to (15), is shown in Fig. 7 for two temperatures as a function of $B(T)/T$. Note that multiple hopping, due to its fluctuational nature, is rapidly enhanced with increasing temperature.

5. QUALITATIVE COMPARISON WITH EXPERIMENT. ENERGY TRANSPORT BY TWO-SITE EXCITONS

Let us, first, adduce the available spectroscopic evidence for a predominant role of two-site excitons in energy transfer to impurity centers in wide-band dielectrics and, second, explain the experimental data on fast energy transport realized by two-site excitons.

Energy transfer from excitons to neutral impurity centers has been observed by many authors in dielectrics of various types. The character of the excitonic state responsible for the energy transfer depends on the specific band structure of the dielectric crystal. Experimental data for wide-band dielectrics of the type considered provide evidence that energy transport is realized not by free excitons but by two-site excitonic polarons.

5.1. Energy transport in alkali halide crystals

The assumption of energy transfer by free excitons should be discarded for the following reason. Usually impurity levels lie below the bottom $E_{\rm bot}$ of the lowest exciton band. An exciton, before it can transfer its energy to such an impurity center, first must achieve $E_{\rm bot}$ via thermal relaxation. The quantum yield of creating excitons at the band bottom can be estimated from the quantum yield of the free-exciton luminescence, $Y_{\rm free}$ (in crystals of the type considered, the radiative decay of excitons is possible only at the band bottom, where the exciton quasi-momentum goes to zero). For all the alkali halides examined,[17] $Y_{\rm free}$ is of the order of 10^{-2}. Such a low quantum yield of the photoproduction of free excitons cannot provide efficient energy transfer to the impurity centers observed spectroscopically.[14–16] But even after an exciton has reached the band bottom, the transfer of its energy to an impurity atom must be preceded by localization in a shallow potential well near the impurity center; this is impeded by the rather small effective mass of a free exciton.[9]

On the other hand, an efficient energy transfer to thallium impurity centers, present in a very low concentration of 10^{-6} to 10^{-5}, has been observed in KI(Tl), RbI(Tl), and NaI(Tl) crystals under excitation below the bottom of the lowest excitonic band.[14–16] In this excitation energy region, two-site excitons are created with a high efficiency, but free excitons cannot be generated at all (which is confirmed by the zero quantum yield of free-exciton luminescence measured for pure KI, RbI, and NaI under excitation below $E_{\rm bot}$; Ref. 17). Moreover, the efficiency of the energy transfer to the impurity did not grow as the excitation frequency was changed from a value below $E_{\rm bot}$ (where $Y_{\rm free}=0$) to any value lying inside the band (where $Y_{\rm free}\sim 0.01$).[14]

Consider now the rate of energy transport realized by two-site excitons. The efficiency of the energy transfer to impurity centers can be characterized by the ratio $Y_{\rm imp}/Y_{\rm host}$, where $Y_{\rm imp}$ is the intensity of impurity luminescence and $Y_{\rm host}$ is the luminescence intensity of two-site excitons formed in the host crystal. The ratio $Y_{\rm imp}/Y_{\rm host}$ has been measured spectroscopically for the alkali halide crystals KI, RbI, and NaI weakly doped with thallium.[14–16] According to Refs. 14–16, efficient energy transfer to the impurity ($Y_{\rm imp}/Y_{\rm host}\approx 1$) at $T=5$ K is achieved for KI(Tl), RbI(Tl), and NaI(Tl) at the concentrations $n=1.5\times 10^{16}$, 3×10^{16}, and 5×10^{17} cm^{-3}, respectively. Let us show that the coherent directional motion of self-trapped excitons with the velocity V, investigated in Sec. 3, provides such an efficient energy transfer to the impurity, described by the relation

$$Y_{\text{imp}}/Y_{\text{host}} \approx Vt\sigma n \sim 1. \tag{16}$$

Here $t \approx 1$ ns stands for the vibrational relaxation time and σ is the cross section of the exciton localization near an impurity ion; the velocity V of the directional motion of two-site self-trapped excitons is taken equal to the longitudinal sound velocity in the crystal, near 2×10^5 cm/s.

The value of σ is determined by the interaction of an exciton with an impurity ion, described (in atomic units) by the van der Waals potential

$$U(R) = -\alpha_{\text{imp}}\langle r^2\rangle R^{-6}, \tag{17}$$

where $\langle r^2\rangle$ is the squared state radius of the site exciton, and α_{imp} stands for the positive difference between the polarizability of the impurity atom (molecule) and that of the substituted lattice atom.[9] A two-site exciton, moving along the anion chain, can be localized near an impurity atom lying at a distance R from the chain if $|U(R)| > T$. This gives the estimate (in atomic units):

$$\sigma = \pi R^2 \sim \pi\left(\frac{\alpha_{\text{imp}}\langle r^2\rangle}{T}\right)^{1/3}. \tag{18}$$

With realistic values of the parameters: $\langle r^2\rangle = 150$, $\alpha_{\text{imp}} = 40$ (Refs. 9 and 18) at $T = 5$ K, the estimate (18) gives $\sigma = 2300$ a.u. $= 6.3\times10^{-14}$ cm^2. For KI(Tl), RbI(Tl), and NaI(Tl), the right-hand side of Eq. (16) takes on the values 0.4, 0.6, and 6, respectively. Thus, the fast energy transfer to an impurity, observed in Refs. 14–16, is explained qualitatively by directional motion of two-site excitons. (In view of the rather weak dependence of the trapping cross section (18) on the parameters, the choice of the latter cannot influence this conclusion.)

Experiment shows[14–16] that the ratio $Y_{\text{imp}}/Y_{\text{host}}$ decreases rapidly with increasing temperature, especially above 30 K. The observed temperature dependence of $Y_{\text{imp}}/Y_{\text{host}}$ is too strong to be described by Eqs. (16) and (18) with a constant V and should be attributed mainly to the temperature destruction of the coherent directional regime of the two-site exciton motion (see Sec. 3).

5.2. Energy transport in rare-gas crystals

For rare-gas crystals, the free-exciton mechanism of energy transfer should be discarded in view of the following experimental fact. The luminescence quantum yield Y_{imp} of a very weak impurity grows sharply with an increase of the excitation photon energy E near the point E_g of the dielectric gap width.[19,20] This energy dependence of Y_{imp} cannot mirror the E dependence of the free-exciton photoproduction efficiency, which is of opposite character (a photon with $E < E_g$ inevitably generates a free exciton, whereas an electron and hole, generated at $E > E_g$, do not necessarily recombine in the form of a free exciton.)[8,21]

However, this feature of the excitation spectrum can be easily understood in terms of the vibrational spectrum of two-site excitons, assuming that they are responsible for the energy transfer to impurities.[8,20] Indeed, a photon with $E > E_g$ generates an electron–hole pair. The hole is very rapidly self-trapped, turning into a two-site molecular ion. The latter, after recombination with an electron, becomes a two-site exciton related to a high excited atomic state (close to the ionization level) with a very large state radius $\langle r\rangle$. (Ref. 9). Due to the large $\langle r\rangle$, this excited state is strongly attracted to impurity centers by its van der Waals potential (17). On the other hand, a two-site exciton, occupying a high vibrational level (extended to a narrow subband), is a very heavy band particle;[7] the large $\langle r\rangle$ in combination with a large effective mass provides a high probability for a two-site exciton to be localized near an impurity center even at a very low impurtiy concentration. A two-site exciton, localized on a high vibrational level, remains pinned at the same impurity center during vibrational relaxation, after which the exciton energy is transferred to the impurity. Under such conditions, a fast directional motion of two-site excitons provides an extremely efficient energy transfer to impurities. Note that the high motion velocity of two-site excitons, derived in Sec. 3 within the classical approach with allowance for a nonpair exchange potential, is consistent with the large effective mass of the two-site exciton subbands derived quantum-mechanically within the approach of a pairwise exchange potential (this seeming contradiction was elucidated in Ref. 10).

Quite a different relaxation picture takes place when a photon with $E < E_g$ turns to a free exciton (such optical transitions are partly allowed in a real crystal with lattice defects).[22] The generated exciton persists in a free state during the relaxation through the upper part of the exciton band where the free and two-site states are not mixed.[9] Unlike a two-site exciton, which can be localized on any vibrational level near an impurity center, a free exciton cannot be trapped inside the band on a impurity level lying below the band bottom, since this electronic transition requires a too strong jump-wise heat release. Only in the lower part of the band is the free exciton mixed with two-site states[7] and can be localized near an impurity center; but the localization probability is low because of a comparably small state radius.

6. QUALITATIVE COMPARISON WITH EXPERIMENT. MOBILITY OF TWO-SITE HOLES

6.1. Rare-gas crystals

The mobility of two-site holes in rare-gas crystals was measured experimentally[13] in a vicinity of the triple point, where the structural perfection of the samples was high enough to make such measurements possible. Table II presents the temperature change of the mobility of self-trapped holes in rare-gas crystals measured in the temperature interval $T_1 < T < T_2$ (Ref. 13). Both the experimental values of the mobility and its observed temperature behavior strongly contradict the law (1) with activation energy $U_{\text{act}} \approx \Delta \sim 1$ eV. The conventional equation (1) predicts a negligibly small mobility and its highly sharp dependence on T. The observed mobility is comparatively high and its temperature variation is found to be weak (and even practically absent for krypton). This can be reconciled with (1) only by substituting a very small binding energy E_b. (Ref. 13). These values of E_b (given in the next-to-last column of Table II) differ strongly from the true binding energy estimated from spectroscopic data and given in the last column. (The spectroscopic estimate of E_b (Ref. 1) is related to the corresponding

TABLE II. Brief summary of experimental data on the self-trapped hole mobility μ in rare-gas crystals measured in the temperature interval $T_1<T<T_2$ near the triple point.[13] The next-to-last column gives the polaron binding energy E_b found in Ref. 13 by fitting Eq. (1) with the experimental dependence $\mu=\mu(T)$; the last column presents an independent realistic estimate of E_b from spectroscopic data.[1] Note that the conventional theory, making no allowance for the intrinsic structure of a self-trapped hole,[3–6] cannot explain a weak temperature dependence of μ, drastically contradicting Eq. (1) with the true binding energy $E_b\sim 1$ eV.

Crystal	T_1	T_2	$\mu(T_1)$	$\mu(T_2)$	E_b, eV	
	K		in units 0.01 $cm^2\cdot V^{-1}\cdot s^{-1}$		from $\mu(T)$ [13]	spectroscopically
Ne	18	25	0.2	1.05	0.024	>1.9
Ar	71	83	1.2	2.3	0.07	>1.2
Kr	84	113	4.0 ± 0.5	4.0 ± 0.5	0.04	>0.9
Xe	110	160	3.2	1.8	0.005 to 0.02	>0.7

two-site excitonic state; it turns into the self-trapped hole after ionization, which can only enhance the binding energy.[9])

As was shown in Sec. 4, these contradictions are naturally eliminated by taking into account the intrinsic vibrational structure of two-site hole polarons. Figure 5 shows that, depending on the barrier height, the calculated mobility can either grow or diminish somewhat with increasing temperature. This inference, as well as the absolute values of the mobility obtained, are in qualitative agreement with the experimental data listed in Table II.

6.2. Alkali-halide crystals

As was already mentioned in Sec. 1, the anion sublattice of an alkali-halide crystal has a spectrum of electronic excitations similar to that of the corresponding rare-gas crystal (the electronic configuration of the anion, e.g., I^- or Cl^-, is identical with that of the corresponding rare-gas atom Xe or Ar, respectively). The spectrum of electronic excitations of the cation (Na^+, K^+ etc.) sublattice lies much higher and cannot interfere with the spectrum of the anion sublattice. In particular, a stable self-trapped state of an anion hole has the form of a two-site quasi-molecule similar to that formed in rare-gas crystals.

However, as regards the manner of motion of self-trapped holes, alkali-halide crystals exhibit a distinction from rare-gas solids. As was mentioned in Sec. 2, lattice atoms lying beyond the chain hamper the motion of the chain atoms to some degree, so that the lattice surroundings of the chain heighten the barrier. In alkali-halide crystals, the effect of the lattice surroundings on the barrier depends on the separation, d_{AC}, of an anion from the nearest cation, or, more exactly, on the ratio of d_{AC} to the distance d_{AA} between adjacent anions within the chain. The barrier height grows with a decrease of the ratio d_{AC}/d_{AA} and, quite naturally, with an increase of the cation-to-anion size ratio.

Such an effect of the lattice surroundings on the barrier B is illustrated by Table III, based on the experimental data of Ref. 2. The lowest barrier of about 0.1 eV was observed for the case of the largest anion I^- and the smallest cation Na^+. Although Cs^+ significantly exceeds Na^+ in size, the barrier remains almost the same for CsI due to a greater ratio $d_{AC}/d_{AA}=3^{1/2}/2$ for the body-centered cell (for a rare-gas crystal, the corresponding ratio equals unity). The barrier increases gradually on account of a decrease of the anion size in the sequence CsI - CsBr - CsCl and rises sharply (despite a decrease of the cation size) when changing to the KCl crystal, with a smaller d_{AC}/d_{AA} ratio. The difference in B between KCl and NaI manifests itself in a sharp difference in mobility (10^{-3} $cm^2\cdot s^{-1}\cdot V^{-1}$ for NaI and 10^{-10} $cm^2\cdot s^{-1}\cdot V^{-1}$ for KCl).[2]

Along with this, Table III contains data related to the reorientation of the hole axis, i.e., changing of the hole polarization direction.[2] These data provide evidence for a one-dimensional character of the two-site hole motion (stated in Sec. 1). The motion of a hole along the anion chain is accompanied by conservation of its polarization direction (parallel to the chain). A hole changes its direction of motion (escaping to another chain intersecting the former one) simultaneously with changing of the polarization direction. So the distance (in units of the chain period), traveled by a hole along the chain before hopping to another chain, can be estimated as

$$\frac{P_{\text{transl}}}{P_{\text{reor}}}\sim\exp\left(\frac{B_{\text{reor}}-B}{T}\right), \tag{19}$$

where P_{transl} and B denote the rate and barrier height for the hole translational motion, and P_{reor} and B_{reor} are those for the hole axis reorientation.

As is seen from Table III, B_{reor} exceeds B by about 1000 K, which provides a predominant motion of a hole within the same chain with infrequent hops between different chains. The difference $B_{\text{reor}}-B$ is negative only for KCl which drops out of the scheme developed, being nearer to the conventional notion; but even for KCl, P_{transl} has been found to exceed P_{reor} at least by an order of magnitude.[2] In Ref. 2 a

TABLE III. Height of the barrier for transnational motion B and axis reorientation B_{reor} of two-site self-trapped holes in alkali halides according to the experimental data of Ref. 2. d_{AC} is the separation of an anion from the nearest cation and d_{AA} is that between adjacent anions.

Crystal	NaI	CsI	CsBr	CsCl	KCl
d_{AC}/d_{AA}	0.707	0.866	0.866	0.866	0.707
B, eV	0.1	0.13	0.20	0.24	0.57
B_{reor}, eV	0.18	0.20	0.37	–	0.54

general conclusion for alkali halides was reached that the number of translational hops of a two-site hole greatly exceeds the number of reorientation hops.

The author is thankful to A.N. Ogurtsov and E.V. Savchenko for helpful discussions. This work was carried out within the project DFG No. 436 UKR 113/55/0.

*E-mail: Ratner@ilt.kharkov.ua

[1] I. Ya. Fugol', Adv. Phys. **27**, 1 (1978).
[2] E. D. Aluker, D. Yu. Lusis, and S. A. Chernov, *Electronic Excitations and Radioluminescence of Alkali Halide Crystals*, Riga Zinatne, Latvia (1979) (in Russian).
[3] T. Holstein, Ann. Phys. (N.Y.) **8**, 343 (1959).
[4] D. Emin and T. Holstein, Ann. Phys. (N.Y.) **53**, 439 (1969).
[5] D. Emin, Phys. Rev. B **3**, 1321 (1971).
[6] D. Emin, Phys. Rev. B **4**, 3639 (1971).
[7] A. M. Ratner, J. Lumin. **81**, 271 (1999).
[8] A. M. Ratner, Phys. Lett. A **265**, 411 (2000).
[9] A. M. Ratner, Phys. Rep. **269**, 197 (1996).
[10] A. M. Ratner, Phys. Lett. A **291**, 165 (2001).
[11] A. M. Ratner, Phys. Lett. A **298**, 422 (2002).
[12] K. S. Song, Can. J. Phys. **49**, 26 (1971).
[13] P. G. Le Comber, R. J. Loveland, and W. E. Spear, Phys. Rev. B **11**, 3124 (1975).
[14] M. Tomura, O. Fujii, and H. Nishimura, J. Phys. Soc. Jpn. **41**, 194 (1976).
[15] H. Nishimura, T. Kubota, and M. Tomura, J. Phys. Soc. Jpn. **42**, 175 (1977).
[16] H. Nishimura and M. Tomura, J. Phys. Soc. Jpn. **39**, 390 (1976).
[17] H. Nishimura and T. Yamano, J. Phys. Soc. Jpn. **51**, 2947 (1982).
[18] P. Gombas, *Theorie und Losungsmethoden des Mehrteilchenproblems der Wellenmechanik*. Basel, (1950).
[19] M. Haevecker, M. Runne, and G. Zimmerer, *Electron Spectr. Related Phenomena* **79**, 103 (1996).
[20] A. N. Ogurtsov, A. M. Ratner, E. V. Savchenko, V. Kisand, and S. Vielhauer, J. Phys.: Condens. Matter **12**, 2769 (2000).
[21] D. Varding, I. Reimand, and G. Zimmerer, Phys. Status Solidi B **185**, 301 (1994).
[22] A. M. Ratner, Phys. Lett. A **269**, 245 (2000).

This article was published in English in the original Russian journal. Reproduced here with stylistic changes by AIP.

Excess electron transport in cryoobjects

D. G. Eshchenko*

Institute for Nuclear Research, Moscow 117312, Russia

V. G. Storchak

Russian Research Centre, "Kurchatov Institute" 46 Kurchatov Sq., Moscow 123182, Russia

J. H. Brewer

Canadian Institute for Advanced Research and Department of Physics, University of British Columbia, Vancouver, B.C., Canada V6T 2A3

S. P. Cottrell and S. F. J. Cox

ISIS Facility, Rutherford Appleton Laboratory, Oxfordshire OX11 OQX, United Kingdom
(Submitted February 19, 2002)
Fiz. Nizk. Temp. **29**, 250–262 (March 2003)

Experimental results on excess electron transport in solid and liquid phases of Ne, Ar, and solid N_2–Ar mixture are presented and compared with those for He. The muon spin relaxation technique in frequently switching electric fields was used to study the phenomenon of delayed muonium formation: excess electrons liberated in the μ^+ ionization track converge upon the positive muons and form Mu (μ^+e^-) atoms. This process is shown to be crucially dependent upon the electron's interaction with its environment (i.e., whether it occupies the conduction band or becomes localized in a bubble of tens of angstroms in radius) and upon its mobility in these states. The characteristic lengths involved are 10^{-6}–10^{-4} cm, and the characteristic times range from nanoseconds to tens of microseconds. Such a microscopic length scale sometimes enables the electron to spend its entire free lifetime in a state which may not be detected by conventional macroscopic techniques. The electron transport processes are compared in: liquid and solid helium (where the electron is localized in a bubble); liquid and solid neon (where electrons are delocalized in the solid, and the coexistence of localized and delocalized electron states in the liquid was recently found); liquid and solid argon (where electrons are delocalized in both phases); orientational glass systems (solid N_2–Ar mixtures), where our results suggest that electrons are localized in an orientational glass. This scaling from light to heavy rare gases enables us to reveal new features of excess-electron localization on a microscopic scale. Analysis of the experimental data makes it possible to formulate the following tendency of the muon end-of-track structure in condensed rare gases. The muon–self-track interaction changes from isolated-pair (muon plus the nearest track electron) in helium to multipair (muon in the vicinity of tens of track electrons and positive ions) in argon. [DOI: 10.1063/1.1542439]

1. INTRODUCTION

The investigation of electronic conduction in condensed rare gases (CRG) is of a great fundamental and practical interest. Rare-gas solids (RGS) and liquids (RGL) form a group of cryosystems and cryoliquids characterized by very weak van der Waals interatomic interactions. The forbidden gap of CRG is extremely wide (about 10–20 eV). From a fundamental point of view a condensed rare gas is a prototypic ideal dielectric and a good object to test various theoretical approaches to the excess-electron transport in insulators. Rare-gas liquids represent relatively simple disordered materials, and the study of the excess-electron transport in these systems is of considerable importance for general understanding of the electronic properties of noncrystalline solids.

On the other hand, condensed rare gases are frequently used as insulators in high-voltage devices, and the processes leading to electric breakdown are certainly determined by the transport of the charge carriers in these substances. An electronic conduction in rare gas liquids is of special interest because of their employment in high-energy physics experiments as working media for ionization chambers and other particle detection systems.[1] The excess-electron transport in insulators is of great practical interest as it may cause electrical breakdown even in wide-gap insulating materials subjected to high electric field. These materials are used in a large number of applications ranging from power generation equipment to microelectronic devices. Nonpolar cryocrystals are used as moderators to produce ultralow energy muon beams.[2] The yield of ultralow energy muons could be connected with end-of-track electron transport to the low-energy muon. Therefore studying of the mechanisms of electron transport in solid and liquid rare gases and cryosystems is of primary importance in condensed matter physics.

TABLE I. Low-field electron mobility in condensed He, Ne, Ar, Kr, and Xe (Ref. 3).

Rare gas	Triple point, K	Electron mobility, $cm^2/V{\cdot}s$	
		in solid	in liquid
^{4}He	–	10^{-5*}	0.019^{**}
Ne	25	600	0.0016
Ar	84	1000	475
Kr	116	3600	1800
Xe	161	4000	1900

Note: $*T=2$ K, $V_{mol}=20$ cm^3; $**T=4.2$ K.

Electron transport in condensed rare gases has been studied extensively for over forty years. The majority of results on the motion of charges have been obtained using the time-of-flight (TOF) technique. In this technique the drift velocity achieved by a group of charges in an electric field is estimated by the drift length divided by the traveling time.

The time-of-flight results[3] for low-field electron mobility in condensed He, Ne, Ar, Kr, and Xe are summarized in Table I.

One can notice a huge difference between light and heavy CRG. In heavy CRG (Ar, Kr, and Xe) the electron mobilities were found to be of the same order of magnitude as those in conventional semiconductors ($\sim 10^3$ cm^2 V^{-1} s^{-1}), implying the existence of extended delocalized electron states (band states).[3,4] Low electron mobility in light RGL has been interpreted[3] as arising from electron localization in a ''bubble.'' These bubbles are rather macroscopic objects. In liquid He the radius of the bubble is about 10–20 Å.[5] Such bubbles form because of the Pauli exclusion principle: a space is opened up around the excess electron by a strong short-range repulsive exchange interaction between it and the electrons of the host atoms, which is opposed by a weak long-range attractive interaction (caused by the polarizability of the host atoms), pressure–volume interaction, and surface tension. Electron bubbles are also formed in solid helium.[6]

With increasing atomic number the polarizability of rare gases grows, making the delocalized state energetically preferable. Liquid neon (ℓ-Ne) represents a borderline case where theoretical calculations[5] failed to make definite predictions of the excess-electron state. However, early time-of-flight experiments[7,8] revealed only low-mobility negative carriers in liquid Ne, which were identified as stable-electronic bubbles. Recent TOF experiments in *high electric fields* have revealed a peculiar situation in which both localized and short-lived ($\tau \sim 10^{-9}$ s) delocalized electron states exist.[9]

Bubble formation is not the only mechanism of electron localization in cryosystems. One of the possible channels for localization of a particle is through its interaction with lattice excitations (phonons, librons, magnons, etc.). In a dissipative environment[10] the lattice excitations can be represented as a bath of harmonic oscillators; interaction with this environment causes a crossover from coherent quantum tunneling to incoherent hopping dynamics, when the particle ''dressed'' with the lattice excitations can be effectively thought of as a polaron.

At low temperatures, the environmental excitations are frozen out. In this case, conventional understanding suggests that the only possible channel for particle localization is the introduction of crystal disorder, which thus may dramatically change the transport properties of a solid. A well-known example is the spatial localization of electron states near the Fermi level in a disordered metallic system, which leads to a transition into a dielectric state (the Anderson transition).[11] The concept of Anderson localization suggests that the wave function of a particle in a random potential may change qualitatively if the randomness becomes large enough. Coherent tunneling of a particle is possible only between levels with the same energy (e.g., between equivalent sites); in the case of strong randomness, states with the same energy may be too distant (spatially separated) for tunneling to be effective.

In metals, however, electron–electron interactions dramatically modify the density of states at the Fermi level, leading to the formation of a Coulomb pseudogap.[12] To observe the effects of disorder on electron transport without the complications of electron–electron interactions, one must therefore study electron dynamics in a disordered *insulating* host.[13] Orientational glasses formed by random mixtures of molecular (N_2, CH_4, CD_4) and atomic (Ar, Kr) species[14] offers a unique opportunity for such studies.

There is one basic drawback of TOF measurements. In such experiments the drift length between electrodes is macroscopic (typically $>10^{-2}$ cm). This macroscopic length makes it very difficult to measure the mobilities in cryocrystals at temperatures significantly lower the melting temperature. With decreasing temperature, the amplitude of the recorded current drops drastically.[3] The thermal expansion of cryocrystals results in the generation of internal strengths and defects, which can trap electrons. Moreover, the thermal expansion may result in the loss of direct contact between the electrodes and crystal. The use of special flexible electrodes[4,15] enabled measurement of the electron mobility down to 66 K in solid Ar (triple point $T_3=84$ K), while no experimental TOF data have been obtained at lower temperatures. In liquids, where the electrode–sample contact is good, the drift velocity measurements are influenced by the presence of electron-attaching impurities. If the attaching time is comparable with the drift times, it is difficult to extract the drift time from the shape of the damping current signal.

1.1. Delayed muonium formation

The techniques of muon spin rotation/relaxation/resonance (μSR)[16] are in intensive use as a powerful tool providing valuable information on various chemical and solid-state physical phenomena. In such experiments a beam of high-energy (several MeV) muons is injected into the sample. In many substances the muon can pick up an electron to form a hydrogenlike muonium (Mu$\equiv \mu^+ e^-$) atom. Muon and muonium signals are well resolved in experiments due to the big difference of muon/muonium gyromagnetic ratios: $\gamma_{Mu}/\gamma_{\mu^+} \sim -103$; $\gamma_{\mu^+}=13.55$ kHz/G. Usually two different ways of muonium formation are distinguished—prompt and delayed. According to the first approach muo-

nium is formed under the slowing down of an energetic muon. During slowing down to an energy of a few tens of keV, the inelastic muon scattering mainly involves the production of excitations and ionizations. At lower energies, the muon undergoes cycles of electron capture and subsequent electron loss. When the last such collision leaves atomic muonium in its neutral charge state, the muonium is said to have been formed promptly.[17] When the muon thermalizes in condensed matter as the positive ion, it leaves behind an ionization track of liberated electrons and ions. In many hosts (see the recent review[18]) some of the excess electrons generated in this track can reach the stopped muon within the time scale of the muon lifetime ($\tau_\mu \sim 2.2\times 10^{-6}$ s) and form muonium. The essential point of this delayed muonium formation (DMF) scenario is that at time zero the electrons and muon are spatially separated. This circumstance made it possible to create an experimental procedure[19] to distinguish delayed and prompt muonium formation. DMF is sensitive to a relatively weak (up to tens of kV/cm) external electric field which prohibits muon-electron recombination and diminishes the ''delayed'' muonium fraction, while to affect the prompt muonium formation electric fields of about atomic value are required.

1.2. DMF and μSR signal

To compare experiments on muonium formation measured at different magnetic fields it is convenient to analyze the general expression for the muon polarization function $P(t)$, which is the experimental value of interest in the μSR spectrum:

$$N(t)=N_{\rm norm}\exp(-t/\tau_\mu)(1+aP(t))+N_0, \tag{1}$$

where $N(t)$ is the number of muon decays registered during the time interval $[t-\delta t/2, t+\delta t/2]$ after the muon stops (δt is the time per chanel for the data acquisition system), $N_{\rm norm}$ is a normalization constant, $\tau_\mu = 2.197\times 10^{-6}$ s is the muon lifetime, N_0 is the background signal, and a (usually about 0.2–0.22) is the apparatus asymmetry. If $n(t)$ is the probability of muonium formation at the time t (where $\int_0^\infty n(t)dt$ is muonium fraction), then the polarization function will be:

$$P(t)=1/2\int_0^t n(t')\cos(\omega_\mu t'+\omega_{\rm Mu}(t-t'))dt' + \left(1-\int_0^t n(t')dt'\cos\omega_\mu t\right). \tag{2}$$

The first term in (2) is the signal from all muoniums formed up to the time t, including the phase shift in the muon state (the constant 1/2 appears because only the triplet spin state of muonium is seen,[14] and the second term is the muon signal. From Eq. (2) it is clear how to extract *muon fraction* from the experimental signal. The muon fraction is $1-\int_0^\infty n(t)dt$, or the amplitude of the *nonrelaxing signal at the muon frequency*. The correct procedure for extracting the muon fraction is to fit the experimental spectrum by an expression which contains the nonrelaxing signal at the muon frequency. Of course this procedure is valid if there is no other reason for muon relaxation (such as magnetic impurities, radical formation, etc.), but it has been shown to be applicable for CRG.

The muonium fraction can be extracted from the experimental spectrum easily only in the case of ''short'' muonium formation (the time scale of muonium formation $\tau_{\rm delay}$ is less than the muon lifetime). Then *in the limit of low magnetic fields* the muonium fraction tends to the amplitude of the fitting at the muonium frequency. In *high transverse magnetic fields*, where the muonium signal [the first term in (2)] is very small, the amplitude of the relaxing signal at the muon frequency is equal to the muonium fraction (and is twice as big as the amplitude of the muonium signal in the limit of low magnetic field).

1.3. DMF as a tool to study microscopic electron transport

The mechanism of DMF is critically dependent on the *electron mobility* and, as the characteristic muon–track-electron distances are about 10^{-6}–10^{-4} cm, represents a ready-to-use technique for electron mobility measurements on a microscopic scale.[20] Measurements of the *electric* field dependences of both the Mu and diamagnetic fractions provide information on the characteristic distance $R_{\rm char}$ between the μ^+ and its radiolysis electrons. Due to the well known dephasing effect, the time scale of Mu formation τ is readily determined by measurements of the *magnetic* field dependence of the Mu precession amplitude.[21,22] If the muonium formation time happened to be bigger than the time resolution of μSR spectrometer, τ can be estimated directly from the dumping rate of the diamagnetic fraction.[19,22] Taking an appropriate model of muon–electron recombination, one can estimate the microscopic mobility from $R_{\rm char}$ and τ. In a simple case (viscous motion of the track electron nearest to the muon under the Coulomb attraction) this estimate is:

$$b=\frac{R_{\rm char}^3\varepsilon}{3e\tau}, \tag{3}$$

where b is the mutual electron–muon mobility, and ε is the dielectric constant of the medium.

The advantages of the μSR technique were demonstrated in an experiment with solid nitrogen,[20] where, in contradiction to the TOF experiments, delocalized electrons were identified in α nitrogen (at $T=20$ K). In β nitrogen (at $T=59$ K) both techniques give close estimates of the excess-electron mobility; μSR experiments[23] have found a *delocalized* electron state in liquid Ne, which is consistent with recent TOF measurements.[9]

2. END-OF-TRACK STRUCTURE

In a lot of substances, DMF can be artificially divided into two stages. The first stage is the slowing down of an energetic muon which is accompanied by the production of energetic free electrons and other excitations of the medium. In this stage the track products are hot (out of thermal equilibrium with the medium). The time scale of the first stage is less than 10^{-10} s. The second stage is the recombination of the track products and muonium formation itself due to the recombination of the muon with one of the track electrons and has an unlimited time scale. From this point of view, first stage prepares ''initial'' conditions for the second. This in-

cludes initial spatial and momentum distributions of the electrons, cations, and muon just after the end of the muon slowing down process.

To calculate initial track structure the cross sections of all elastic and inelastic track processes must be known. For high muon energies (above about 35 keV, where the velocity of the muon exceeds that of the electrons bound in the molecules of the target) the initial track structure can be calculated using the Bethe[24] theory to describe the inelastic scattering of the muon. Unfortunately the cross sections for lower energies of muon scattering are unknown. Due to the big muon-to-electron mass ratio the angular scattering is not essential at high muon energies, and the track is linear along initial muon momentum. At low muon energies muon angular scattering could play a significant role. Nevertheless, experiments[18] reveal asymmetric dependences of the muon (muonium) fraction versus the direction of the external electric field. This can be interpreted as the track products being asymmetrical around the slowed down muon or the scattering of muon at low energies being incompletely randomized. According to the multipair track model[25,26] the initial structure of the final part of muon track is a linear chain of cations (with the muon at the end) surrounded by a cloud of electrons. In this model the influence of external electric field on muonium formation is asymmetric. At positive fields (the direction of external electric field coincides with the initial muon momentum) we pull track electrons away from the muon, diminishing muonium formation. At negative fields we move ''early'' track electrons towards the muon, and, in the first approximation, muonium formation should not be sensitive to a ''weak'' electric field.

As will be shown later, this simplified model is a good start to understanding muonium formation in CRG and other condensed gases. There are three characteristic distances in this model: the distance between cations in the chain R_+, the distance between the last cation and the muon R_μ, and the rms distance from the scattered electron to the parent cation R_e. The fact that in CRG at zero electric field the muonium fraction is big[18] or the probability of muon-electron recombination is high implies that $R_e > R_+$ and $R_e > R_\mu$. It means that for *all* CRG under consideration the muon is inside its own track. Otherwise an electron will rather recombine with one of the positive ions. The number of electrons involved in muonium formation at zero and positive fields will be $N_e \sim R_e/R_+$. The characteristic fields for suppression of muonium formation will be of the order of $E_{\mathrm{char}_+} \sim e/\varepsilon R_e R_+$.

At negative fields muonium formation is sensitive to the flux of ''early'' track electrons and one should expect the track motion to be different at fields higher than $E_{\mathrm{char}_-} \sim e/\varepsilon R_+^2$, where one can neglect interactions between anions.

Details of the track motion in different CRG will be discussed in the corresponding Sections.

3. EXPERIMENTAL DETAILS

Experiments in condensed He are described elsewhere[19,22,27] (see Table II). Experiments in condensed Ne, Ar, and N_2-Ar were performed at the M13 spin-polarized surface muon beam line at TRIUMF and at the EMU pulsed spin-polarized muon beam line at ISIS (Rutherford Appleton Laboratory). In both laboratories we used similar sample cells. The front and back sides of the brass sample cell (22 mm inner diameter for the TRIUMF setup and 35 mm inner diameter for ISIS, and 5 mm thick) are glued with 0.1 mm titanium windows. This thickness is small enough to estimate the stopping of surface muons (momentum$\approx$28 MeV/c) in the entrance foil within a few percent. The muon beam was collimated down to 9 mm in the TRIUMF experiments. At ISIS the spot size of muon beam is about 20 mm; therefore essentially all the muons were stopped in the samples at both laboratories.

TABLE II. Muonium fraction in condensed He,[27] Ne, and Ar.

Rare gas	Muonium fraction	
	in solid	in liquid
^{4}He	0	0,92*
Ne	0,80	0,80**
Ar	0,90	0,90

Note: *$T > 0.8$ K; **$T = 25$ K.

Windows are glued through 0.5 mm kapton layers (with inner diameter 0.5 mm less than the diameter of the cell) by epoxy and supported by brass flanges. Such a construction enables one to apply high voltage (up to tens of kV) on any window and was tested at a pressure of 10 atm at room temperature. To produce the temperature gradient required for crystal growth at the top and at the bottom of sample space there are special copper plates (0.5 mm thick). The bottom plate is connected to the cold finger of the cryostat. The top plate is placed at a capillary insert which is connected to a gradient heater. Both plates are attached to the cell body with a small gap (about half a millimeter). This enables good thermal contact to the bulk of the solid CRG sample as the temperature is lowered.

We used standard high-purity (impurity content$\leqslant 10^{-5}$) gases. Samples were condensed from big ballast volumes by cooling the cell. Crystallization of the samples was done by steady lowering of the base temperature with open ballast volume (constant-pressure regime). Typical crystal growth times were about one hour; the temperature gradients were about 0.5 K per sample length.

Muon experiments in solid condensed gases are associated with some experimental difficulties. First—in spite of the high electrical strength of bulk solid condensed gases, upon lowering of the temperature below the melting point, thermal cracks in the sample and the low equilibrium vapor pressure of the gas result in the appearance of ''easy paths'' for electrical breakdown of the sample. To increase the maximum electrical strength of our solid condensed-gas samples we added some pressure (up to 1 atm) of He gas into the cell just after the cooling below melting point. Unfortunately this procedure is effective only at temperatures below the superfluid λ transition $T_\lambda = 2.17$ K, where a superfluid film can penetrate into all the sample cracks. At higher temperatures, the procedure of He gas filling helps to increase the breakdown voltage by about a factor of two. In solid neon we succeeded in increasing the maximum electric field up to 12

kV/cm, which is still less than the maximum electric field in liquid neon ($E_{max} \sim 33$ kV/cm).

Our first attempts to increase the range of the electric field were accompanied by a huge scatter in the experimental data. Now we understand that this problem is connected with the sample–electrode interface. The incoming muon beam eventually produces radiation damage in the sample, in particular, it generates free carriers (electrons and ions). If there is a barrier for the electrons to pass through the electrode–sample gap (which is probably formed under the cooling of the sample) under the influence of external electric field, it will result in the accumulation of space charge near the sample surface. This charge screens the external electric field inside the sample (if it does not cancel it completely), which may diminish (if not cancel) the effect under study.

The time scale of this screening will depend upon the free carrier generation rate in the bulk of the sample and on the electrical properties of the sample–electrode connection. For a typical muon flux at accelerators, the time scale range from tens of minutes to seconds. As the typical time for collecting the necessary statistics in one spectrum is about one hour, the screening effect can mask the effect of electric field. To avoid this difficulty we have developed a special technique of μSR measurements in alternating electric fields.[28] If the frequency of the alternating field is higher than the inverse time of the screening charge accumulation near the sample surface, the value of the internal electric field in the sample tends to the applied external electric field. For example, in solid Ne for an incoming muon beam intensity of about 3×10^4 s^{-1} the switching period should not exceed 5 seconds.

4. RESULTS AND DISCUSSION

4.1. Liquid and solid helium

To present a complete picture of the end-of-track processes in CRG, we start from a reproduction of the μSR results in condensed helium,[19,22,29] where the features of DMF are seen most cleanly.

The main reason for this is a unique property of liquid helium—the phenomenon of superfluidity. The mobility of the charge carriers is relatively low ($b_+ = 0.05$ cm^2 V^{-1} s^{-1} for cations and $b_- = 0.03$ cm^2 V^{-1} s^{-1} for anions) in normal helium[30] at 4.2 K. The spectrum of elementary excitations in superfluid helium has a characteristic threshold, which causes an exponential increase of the mobility[31] as the temperature is reduced below the lambda point $T_\lambda = 2.17$ K ($b_+ = 1700$ cm^2 V^{-1} s^{-1} for cations and $b_- = 155$ cm^2 V^{-1} s^{-1} for anions at 0.6 K). This circumstance gives a unique opportunity to examine various models of track motion by scaling the mobility over five orders of magnitude. Moreover, by adding a small amount of ^{3}He one can regularly diminish the mobilities at low temperatures $T < 0.8$ K (where the mobilities are determined by the scattering on ^{3}He impurities) keeping the other parameters (temperature, etc.) unchanged. Unfortunately, the behavior of cations and anions in helium is outstanding in comparison with other CRG (especially heavy CRG). First, the charges are extremely heavy: electrons form "bubbles" with a hydrodynamic mass of about 200 helium atoms, and positive charges form "snow balls" of about 40–60 helium atoms.[32] Second, in all the temperature interval in the liquid the mobility of the anions is bigger than the mobility of the cations, while in solid heavy CRG the mobility of the anions is negligible in comparison with the mobility of the light delocalized electrons.

This fact will result in the breakdown of the linear structure of the track-anion chain. If we suppose $R_e > R_+$ and $R_e > R_\mu$, then just after the slowing-down process (when the electrons have formed bubbles and the positive helium atoms and, probably, the muon have formed snowballs) the main interaction between the charges will be the strong plus–plus repulsion. For example, the muon will feel a high repulsive force from the nearest positive ion or even (if $R_+ < R_\mu$) group of R_e/R_+ ions in the direction roughly parallel to the primary muon beam. Muon–positive ion repulsion can explain the origin of the "initial" muon snowball momentum MV_L (where $M \sim 40 m_{He}$ is the mass of the snowball, $V_L \sim 6\times10^3$ cm/s is the Landau velocity) required to explain the decrease of the muonium fraction at temperatures $T < 0.7$ K in pure ^{4}He (Ref. 19).

Repulsion of the light and mobile anions will in a short time interval cause all the distances between all the charges to become the same order of magnitude, about R_e. Then the process of muonium formation will continue in a long (in comparison with plus–plus repulsion) recombination of μ^+ and e^- in a simple Coloumb potential.

Note that a single muon—electron pair will also arise if the hot excited muonium decays far away from the other track (the muon—electron pair is far from the track from the very beginning of the track recombination). A minor problem with this scenario is the difficulty of explaining asymmetry of the muon—electron initial position, which is readily obtained in the multipairs model.

Combining all we have mentioned above we can conclude that the longest part of the muon–electron interaction in liquid helium can be written as a simple Coloumb attraction between the muon and the nearest electron, no matter what is the origin of this pair. This approach made it possible to draw a qualitative (and sometimes a quantitative) description of muonium formation in helium.[19] Let r_0 be the typical distance between the muon and electron and $b = b_+ + b_-$ be the sum of the mobilities of the charges. The mobility of the muon is assumed to be the same as that of "heavy" positive charges.[31] In normal helium the mobility of charges is low and the equation of mutual muon–electron motion seems to be a viscous one. In this case the time of muonium formation is $\tau = \varepsilon r_0^3/3be$. The forming muoniums reduce the free muon fraction. In high transverse magnetic fields (where only muon precession signal is seen) this muonium formation causes apparent muon relaxation $\lambda \propto \tau^{-1}$, and the polarization function is directly connected with the number of free muons. Using the relaxation rate in normal helium $\lambda = 0.06\ \mu$s^{-1} and taking $b \simeq 0.08$ cm^2 V^{-1} s^{-1}, one can estimate the typical value for the muon–electron distribution in liquid helium: $r_0 \simeq (3be/\lambda)^{1/3} = 7\times10^{-5}$ cm.[19] Note that Onsager length $R_c = (e^2/k_b T\varepsilon) \sim 10^{-4}$ cm at helium temperatures is much longer than r_0, so the diffusion in Mu formation is not important. As to the amplitude of muonium precession $a_{Mu}(H)$, in normal He only a small fraction of the

pairs manage to recombine during the time of the precession signal formation $\tau(H)\sim 1/(\gamma_{\mathrm{Mu}}H)\sim 10^{-7}$ s for $H=0.4$ G, and the Mu precession amplitude is small. To obtain more ''visible'' muonium one should diminish the time of mutual muon–electron motion and use low magnetic fields. After entering the superfluid phase, a_{Mu} (0.4) begins to increase with decreasing temperature (accompanied by exponential growth of the mobility). When b becomes 10^3 times that in normal helium, the most distant pairs manage to converge during the time τ (0.4), and the amplitude of muonium precession achieves its maximum value, which corresponds to a muonium fraction of 92%. This takes place at $T=0.7-0.85$ K in pure ^{4}He. Under further lowering of the temperature in pure ^{4}He a_{Mu} drops and tends to a constant of about 0.8 of the maximum value. This behavior can be explained by taking into account the initial momentum of the muon snowball[19] and the ballistic motion (due to the extremely low drag force) of this snowball around the nearest electron at temperatures $T<0.7$ K. If during the slowing down process μ^+ forms a snowball at a velocity higher than $M/m_\mu V_L\sim 2.4\times 10^6$ cm/s (where $M/m_\mu\sim 400$ is the snowball-to-muon mass ratio) or the snowball acquires momentum due to the repulsion from track cations in the first stage of track motion (see the speculation in the previous paragraph), then all the muons with positive energy $MV_L^2/2-e^2/r_i\varepsilon>0$ (where r_i is the ''initial'' muon–electron distance) will escape muonium formation. A corresponding estimate of the ''critical'' value r_c (all the muons with initial conditions $r_i<r_c$ will definitely recombine with the electron) gives $r_c=2e^2/\varepsilon MV_L^2\sim 6\times 10^{-5}$ cm, which is comparable with the typical muon–electron distance estimated from the rate of muonium formation in normal helium, $r_0\sim 7\times 10^{-5}$ cm. The real motion of charges in superfluid helium is far from the classical ballistic regime. If under the influence of the electric field a charge exceeds the critical Landau velocity it will (within a time scale 10^{-13} s) emit roton(s), diminish its speed,[33] and follow a new trajectory with a reduced energy. That is why a significant fraction of muon snowballs will form muonium even when the initial energy is positive. In a mixture ^{4}He+0.2% ^{3}He, where because of scattering on ^{3}He impurities the low-temperature anion mobility cannot exceed 20 $\mathrm{cm^2\,V^{-1}\,s^{-1}}$, the motion of a muon snowball is of a viscous nature, and there is no peculiarity in the temperature dependence of the muonium fraction.[19]

The most powerful tool for studying muonium formation is experiment in electric fields. An external electric field prevents recombination of track charges, diminishes the muonium fraction, and increases the muon fraction.

The electric field dependence of the double amplitude of muonium precession divided by the apparatus asymmetry in a diluted mixture—^{4}He+0.2% ^{3}He ($T=0.5$ K), measured in *low magnetic field* $H=0.4$ G,[19] is represented in Fig. 1 by open circles. Under such conditions this normalized amplitude tends to the muonium fraction (see Sec. 1.2 DMF and μSR signal), at least 90% of the muons recombine, forming Mu in less than 10^{-7} s, and the double amplitude of muonium precession a_{Mu} in zero electric field is close to its limiting value $a_{\mathrm{Mu}}^{\max}=0.2$ (Ref. 22)—the apparatus asymmetry.

At high temperatures close to the λ point, the time of muonium formation in liquid helium is about 5×10^{-6} s and

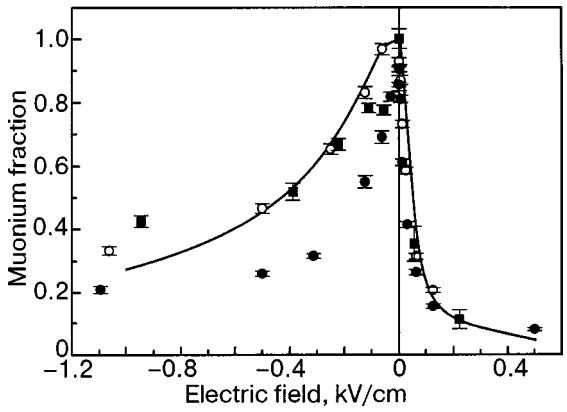

FIG. 1. Electric field dependences of the muonium fraction in liquid helium: ^{4}He+0.2% ^{3}He at $T=0.5$ K (open circles); pure ^{4}He at $T=1.7$ K (solid squares); pure ^{4}He at $T=0.7$ K (solid circles). The direction of electric field coincides with the initial momentum of the muon beam. The solid line represents the best fit of the viscous model to the data at $T=0.5$ K in the mixture (see the text).

the amplitude of muonium signal is low even at fields $H=0.4$ G. To represent the muonium fraction at $T=1.7$ K, the amplitude of the relaxing signal at the *muon* frequency divided by the apparatus asymmetry is plotted in Fig. 1 by solid squares. One can notice that in spite of the huge difference of the mobilities of the charges at these temperatures ($b=20$ $\mathrm{cm^2\,V^{-1}\,s^{-1}}$ at 0.5 K and $b=0.2$ $\mathrm{cm^2\,V^{-1}\,s^{-1}}$ at 1.7 K) the electric field dependences of the muonium fractions are very similar. This behavior suggests a similar distribution of the track products (or, in other words, the same initial electron–muon distribution function) in all the temperature interval 0.5–4.2 K in the ^{4}He+0.2% ^{3}He mixture. The case of a mixture is very important as the main mechanism of muon cluster scattering at low temperature is governed by impurity (^{3}He) atoms with momentum $p_i\sim(m_3kT)^{1/2}$. Therefore the mean path between collisions of a cluster, $L=\Delta pb/e\sim 3\times 10^{-7}$ cm (where $\Delta p\sim p_i$ is the change of cluster momentum in a single collision), is small in comparison with the typical length in the problem. Then the motion of muon cluster will be of the ''viscous'' type—the direction of the cluster motion will coincide with the direction of an electric field which acts on it. For any given configuration of electric field (internal track field plus external field) it will result in the separation of the space of initial electron–muon pairs into two regions. In the first region, where the lines of electric field strength end at the muon, the muon will form muonium. In the second, where the lines of electric field strength go to infinity, the muon will escape muonium formation. In the case of a single electron–muon interaction, the muon will recombine if

$$r<(e/E\varepsilon)^{1/2}\cos(\vartheta/2), \tag{4}$$

where r and ϑ are spherical coordinates (the vector $\vartheta=0$ coincides with the direction of the external electric field), and will be withdrawn by the external field otherwise. The solid line in Fig. 1 represents the best fit of the calculated [using criterion (4)] normalized muonium amplitude to the measured values at $T=0.5$ K in a ^{4}He+0.2% ^{3}He mixture. The initial mutual muon–electron distribution function was sought in the form of a three-dimensional Gaussian:[19]

$$p(\mathbf{r}) = (2\pi)^{-3/2}\sigma_x^{-1}\sigma_{yz}^{-2} \times \exp\left[\frac{-(x-a)^2}{2\sigma_x^2}\right]\exp\left[\frac{-(y^2+z^2)}{2\sigma_{yz}^2}\right], \quad (5)$$

where x is parallel to the external electric field, the point $(a,0,0)$ is the center of the muon–electron distribution, σ_x and σ_{yz} are the corresponding standard deviations of the initial muon–electron position. The best fit gives $a = 4 \times 10^{-5}$ cm (the maximum of muons density is shifted forward in the direction of p_μ with respect to the electrons), $\sigma_x = 4 \times 10^{-5}$ cm, and $\sigma_{yz} = 2 \times 10^{-5}$ cm.

In pure helium at low temperatures an electric field has a stronger effect than in the mixture. The electric field dependence of the normalized muonium amplitude in pure ^{4}He is represented in Fig. 1 by solid circles. This difference is apparently due to the high mobility ($b_+ \simeq 200$ cm^2 V^{-1} s^{-1}) of the particles in pure helium. Under these conditions the viscous approach to the muon cluster motion is not valid (the mean free path becomes comparable with the dimension of the problem) and one should take into account the initial momentum of the cluster. In the case when μ^+ starts with velocity pointing away from e^-, the muon can go very far away from the electron. For an initial distance $r_0 > 2e^2/mv_L^2 \simeq 5 \times 10^{-5}$ cm (where the kinetic energy of the cluster is greater than the potential electrostatic energy) the maximum charge separation will amount to $r_{\max} \sim r_{(0)} + v_L mb/e \simeq 2 \times 10^{-4}$ cm, and the effect of the field will be seen already at the magnitude $E > e/r_{\max}^2 \simeq 5$ V/cm.

The mobilities of the charges are extremely low ($b < 10^{-5}$ cm^2 V^{-1} s^{-1}) in solid helium.[34] This is the reason for the *complete absence* of muonium signal in solid ^{4}He.[29] Moreover, the muon signal shows no damping—$\lambda_{\text{muon}} < 0.004 \times 10^{-6}$ s^{-1}, which means a high limit of the muonium formation time of about $\tau \sim 10^{-4}$ s^{-1}.

As a conclusion of this Section we will summarize the main features of muonium formation in condensed helium: high relative mobility of positive ions leads to the breakdown of the linear structure of the muon track and results in a ''single pair'' regime of muon–nearest-electron attraction; in a wide range of the charges' mobilities (until the viscous limit of the track motion is valid) the mutual ''initial'' distribution of the track products is independent of temperature; the low mobilities of ions in solid helium prohibit muonium formation.

4.2. Liquid and solid neon

Muon spin rotation experiments in solid Ne[18,35] revealed a near-maximum value of the muonium precession signal, which is natural in view of the high electron mobility in solid Ne (see Table I). Electric field experiments in solid Ne show a great change in the muonium/diamagnetic signals, though the characteristic fields are almost ten times bigger than those for liquid He. Our recent experimental data—diamagnetic signal versus electric field dependence in solid Ne near the melting point ($T = 22$ K) is plotted in Fig. 2 by the solid circles. One can notice a significant asymmetry in the influence of electric fields (in this article, the positive sign of electric field coincides with initial muon beam momentum), which means that the electron density is shifted to the direction opposite to the initial muon momentum. High characteristic electric fields can be explained by multipair structure of the muon track in solid neon (see Sec. 2, End-of-track structure). In this case the intrinsic electric field on the electron will be $E_{\text{char}} \sim e/\varepsilon R_+ R_e$, where R_+ is the distance between cations in the chain and R_e is the square average distance from the scattered electron to the parent cation. This field is R_e/R_+ times bigger than the single-pair Coulomb interaction.

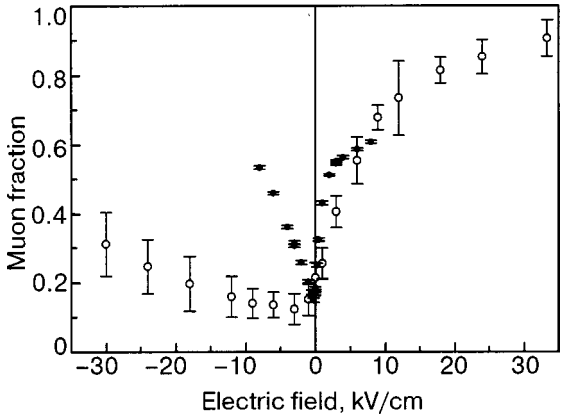

FIG. 2. Electric field dependences of muon fraction in liquid Ne at $T = 25$ K (open circles) and solid Ne at $T = 22$ K (solid circles). The direction of electric field coincides with the initial momentum of muon beam.

The experimental μSR signal is very sophisticated in liquid neon. It contains the signal at the muonium frequency and a two-component (relaxing and nonrelaxing) diamagnetic signal. The essential feature of the muonium signal is that it is in contradiction with the envelope of the diamagnetic signal. The amplitude of the muonium precession is *much higher* than expected from Eq. (2). It looks like it corresponds to a short process in comparison with the damping rate of the diamagnetic signal or even in comparison with the time resolution of the apparatus.

There could be two possibilities for this behavior—prompt muonium or ''fast'' DMF. In the experiment with solid neon, due to the limited electric strength of the samples we achieved only *partial* recovery of diamagnetic signal (see Fig. 2). That is why from the solid-phase data it is unclear whether the whole muonium signal is delayed or if some part of this signal comes from prompt muonium. It is very unlikely that the cross sections for charge exchange processes are different in solid and liquid Ne, and the prompt fraction (if any) should be the same in both phases. The fact that all the signals in the liquid depend on external electric field and the complete suppression of the muonium signal at high positive fields implies a *track* origin of the muonium signal in liquid Ne. It has been proposed[23] that electron states localized in bubbles and delocalized in the conduction band coexist in liquid neon. In high magnetic fields $H > 1/\tau_{\text{loc}}\ \gamma_{\text{Mu}}$ (where τ_{loc} is the characteristic time for muon–electron recombination with an electron in the bubble state), fast delocalized electrons give the main contribution to the muonium precession amplitude. Muonium formation due to the arrival of slow localized electrons is seen in the relaxation of the diamagnetic signal. The coexistence of localized

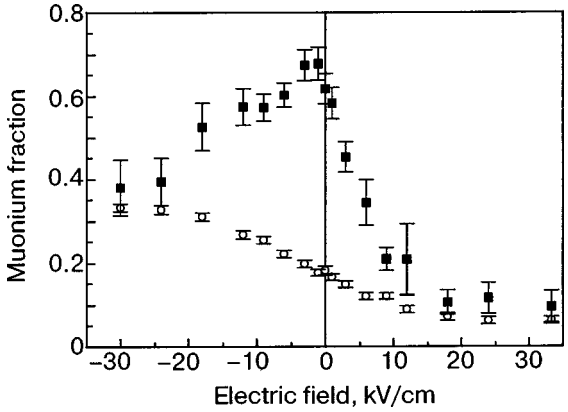

FIG. 3. Electric field dependences of the muonium fractions in liquid Ne at 25 K formed by: delocalized electrons (open circles); localized electrons (solid squares). The direction of the electric field coincides with the initial momentum of the muon beam.

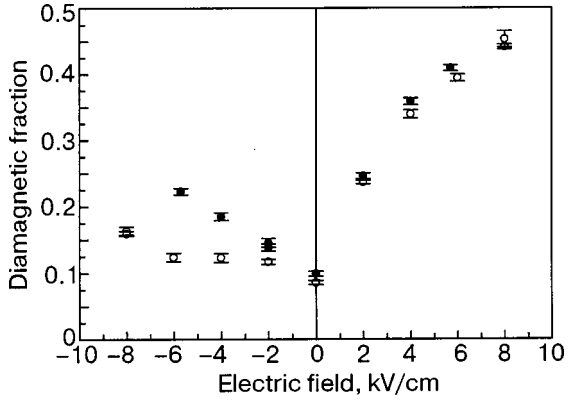

FIG. 4. Electric field dependences of the muon fraction in liquid Ar at $T=84$ K (open circles) and solid Ar at $T=78$ K (solid circles). The direction of the electric field coincides with the initial momentum of the muon beam.

and delocalized electrons in liquid neon has also been observed by time-of-flight measurements.[9]

The electric field dependences of the normalized (to the apparatus asymmetry) amplitudes of twice the muonium signal $2A_{\mathrm{Mu}}$ (circles) and of the relaxing diamagnetic signal A_{rel} (squares) in liquid Ne at $T=25$ K are plotted in Fig. 3. The sum of these two signals is the muonium fraction versus the electric field. The ratio $A_{\mathrm{Mu}}/A_{\mathrm{rel}}$ is the fraction of delocalized electrons versus the electric field. It can be shown that this ratio is an *increasing function* of the external electric field. Unfortunately we cannot plot the probability of delocalization as a function of the electric field acting on the electron. This ''true'' electric field is the external electric field plus the intrinsic track electric field, and we can only estimate the second term.

For comparison with solid Ne the normalized amplitude of the nonrelaxing diamagnetic signal as a function of the external electric field in liquid neon is plotted in Fig. 2 by the open circles. This value reflects the fraction of muons which escapes recombination. One can notice a huge difference between liquid and solid Ne. In the liquid in negative fields the free muon fraction changes little (at fields up to -10 kV/cm it is practically constant), while in positive fields the slope of the curve in the solid is bigger than in the liquid.

A possible explanation of the peculiarities mentioned above could be the following. The weak dependence in the liquid implies that the characteristic muon–electron distance is shorter in the liquid. In both substances the excess track electrons are initially delocalized and moving rapidly away from the ionization centers where they were created. Then the electrons lose their energy in collisions with the media atoms. In the solid the electrons remain delocalized up until the recombination with muons (or other positive centers). In the liquid, with decreasing electron velocity the probability for the electron, to be localized in a ''bubble'' is increased.[9] This implies that the mean square distance between the delocalized electron and its parent ion is shorter in the liquid or that the intrinsic track electric fields are bigger in liquid neon and the dependence of the free muon fraction on the external electric field is flatter.

At negative fields we pull ''early'' track electrons to the muon. The free diamagnetic asymmetry seems to be the result of the two tendencies. The higher the field, the lower the probability for the muon to recombine with any individual electron but the higher the probability of finding an additional track electron. If the second tendency dominates, the probability of muonium formation tends to unity and, in this sense, is independent of electric field.

Unless specially prepared, a solid CRG sample (excluding solid He, which anneals easily) has a polycrystalline structure with a characteristic grain size[3] of about $10^{-5}-10^{-4}$ cm. If electrons are scattered or captured by polycrystalline defects, only electrons within some critical distance (about the crystallite size) will reach a muon. The number of these electrons will be $N_{\mathrm{neg}}=R_{\mathrm{cr}}/R_{+}$, where R_{cr} is the crystallite size and R_{+} is the distance between ionizations at the final stage of muon track. One should expect the negative part of the E-field dependences to be sensitive to the quality of the crystal. In the liquid crystalline-like defects are absent, the amount of electrons involved in muonium formation is bigger, and the probability of muonium formation with ''early'' electrons is higher.

As a summary of this Section, the end-of-track processes in solid and liquid neon are very different. In solid Ne, muonium is formed as a result of muon recombination with delocalized electrons. In the liquid a muon can recombine with a delocalized or localized electron. Localization of initially free track electrons in the liquid results in high (in comparison with solid Ne) internal electric fields.

4.3. Liquid and solid argon

Electrons are delocalized in both solid and liquid argon (see Table I), and one should expect the end-of-track processes in condensed argon to be similar to those in solid Ne. Electric-field dependences of the free muon fractions in liquid argon at $T=84$ K (open circles) and solid argon at $T=78$ K (solid circles) are presented in Fig. 4. The data were obtained from μSR measurements in switching electric fields. The switching time is 10 s. One can notice the practical coincidence of the experimental points in liquid and solid argon at positive fields and a significant difference at high negative fields. At negative fields the points in the liquid are lower than the points in the solid. Moreover, in spite of using the technique of electric field measurements in switching fields, the points at negative fields in the solid were

''sample dependent.'' Switching helps to remove random scatter from the data but maintains the different slopes of the negative part of the curve measured under ''different'' conditions. The data represented in Fig. 4 were obtained just after the crystallization of the sample. After few hours of annealing the data change to lower values closer to the points in the liquid.

The peculiarities mentioned above can be explained in the framework of a multipair structure of the muon track. The explanation is analogous to that in condensed neon with the simplification that the electrons are delocalized in both phases of Ar. Then the characteristic track distances seem to be close in solid and liquid argon.

If we suppose both the characteristic distance between the positive ions R_+ and the distance from the last track ionization to the stopped muon R_μ to be less than the rms distance from the scattered electron to the parent ion R_e, then at positive fields, when we pull track electrons from the muon, the number of particles involved in muonium formation will be R_e/R_+. If R_e is bigger than the crystallite size of the solid sample, muonium formation will be similar in the solid and liquid phases.

At negative fields we push ''early'' track electrons towards the muon, and muonium formation is sensitive to the quality of the sample. In the solid the scattering or even trapping of track electrons at crystalline imperfections diminishes the flux of early electrons, and the probability of muonium formation is lower than in the liquid. Annealing of crystalline defects will result in an increase of electron flux to the muon, and the probability of muonium formation at negative fields tends to the value in the liquid, where crystalline defects are absent.

From the argon data we can estimate the number of electrons involved in muonium formation in condensed Ne. In condensed Ar the muon fraction at zero field is less than that in solid Ne. The respective values measured in the same experimental chamber at TRIUMF are $A_{\mu_{\mathrm{Ar}}}=0.076(3)$ and $A_{\mu_{\mathrm{Ne}}}=0.177(6)$. At the final stage of the muon track, as we have μ^+ one additional positive particle, the probability for the muon to escape recombination will be $A_\mu=1/(N+1)$, where N is the number of electrons (or positive ions) involved in muonium formation in zero electric field. This gives a rough estimate for the number of electrons: $N_{e_{\mathrm{Ne}}} \sim 1/(A_{\mu_{\mathrm{Ne}}}-A_{\mu_{\mathrm{Ar}}})\sim 10$. Unfortunately we cannot do an analogous estimate for condensed Ar, as some unknown part of the muon signal comes from the thermal shields, chamber windows, etc. The low value of the muon fraction at zero field in Ar suggests that the number of electrons involved in muonium formation $N_{e_{\mathrm{Ar}}}$ is bigger than $N_{e_{\mathrm{Ne}}}$. As an alternative estimate of N_e is $N_e \sim R_e/R_+$, this ratio is bigger for condensed Ar. On the other hand, the characteristic electric field for suppression of muonium formation at positive fields is $E_{\mathrm{char}} \propto e/\varepsilon R_+ R_e$. These fields are close for Ar and solid Ne. Combining all we have said and taking $E_{\mathrm{char}} \sim 4-10$ kV/cm, we can estimate: $R_{+_{\mathrm{Ne}}} \sim 1.5-2\times 10^{-6}$ cm, $R_{e_{\mathrm{Ne}}} \sim 1.5-2\times 10^{-5}$ cm, $R_{e_{\mathrm{Ar}}} > R_{e_{\mathrm{Ne}}}$, and $R_{+_{\mathrm{Ar}}} < R_{+_{\mathrm{Ne}}}$.

Due to excess electron delocalization in both phases the end-of-track processes in the liquid and solid (near the triple point) Ar are very similar. The low value of the muon fraction in zero electric field suggests a multipair structure of the muon track. The number of particles involved in muonium formation is some tens.

4.4. Electron localization in a disordered insulating host

Most of our understanding of electron transport in solids is modeled on nearly perfect crystalline materials, but even in this limit disorder plays a crucial role.[36] The most familiar phenomenon governing electron transport in disordered *metals* is ''Anderson localization:'' [11] The introduction of sufficiently strong disorder into a metallic system causes spatial localization of electron states near the Fermi level and thus drives a transition to an insulating state. To observe the effects of disorder on electron transport without the complications of electron–electron interactions, we studied electron dynamics in a disordered *insulating* host.[13]

Orientational glasses formed by random mixtures of molecular (N_2,CH_4,CD_4) and atomic (Ar, Kr) species[14] offers a unique opportunity for such studies. One of the best-studied orientational glass systems is the N_2-Ar mixture.[37] Pure N_2 has two low-pressure crystalline forms, the hexagonal close-packed (hcp) high-temperature phase and the cubic $Pa3$ (fcc) low-temperature phase. Despite intrinsic geometrical frustration, pure N_2 undergoes a first-order phase transition to a long-range periodic orientationally ordered α phase below $T_{\alpha\beta}=35.6$ K; the high temperature β phase is orintationally disordered.

Solid $(N_2)_{1-x}Ar_x$ is obtained by simply cooling liquid mixtures, as nitrogen and argon are completely miscible. As the Ar concentration x is increased, the hcp-to-fcc transition temperature decreases. Above the critical Ar concentration $x_c \approx 0.23$, the hcp lattice appears to be stable down to $T=0$. The dynamical orientational disorder of the high-T phase eventually freezes into a static pattern of randomly oriented N_2 molecules, the *orientational glass*.[37]

Being a mixture of insulators, the N_2-Ar system has a very large energy gap (~ 10 eV), so that even at high temperature the ambient density of free electronic states is exponentially low. Experimental study of electron transport in this system therefore requires that the empty conduction band be ''injected'' with free carriers, ideally in low enough concentrations that electron–electron interactions can be safely ignored. The ionization of molecules and/or atoms by high-energy charged particles (e.g. positive muons) offers just such a source of free carriers.

Figure 5 depicts the temperature dependences of the asymmetries (amplitudes) of the various signals in solid $(N_2)_{1-x}Ar_x$ for $x=0$, 0.09, 0.16, and 0.25. At high temperature (above about 40 K), all the mixtures have roughly the same Mu and μ_D asymmetries as pure N_2. At low temperatures, however, adding argon causes dramatic changes. In pure N_2 below about 30 K there is a large Mu signal and a small μ_D signal, indicating efficient DMF; as Ar is added there is a progressively larger μ_D signal, indicating reduced DMF, until at $x=0.25$ there is only a small Mu signal.

In solid N_2 muonium formation has been shown[38,39] to proceed via two channels: the thermal DMF process outlined above and the epithermal *prompt* process which takes place prior to the μ^+ thermalization and is therefore independent of temperature, electron mobility, etc. The small,

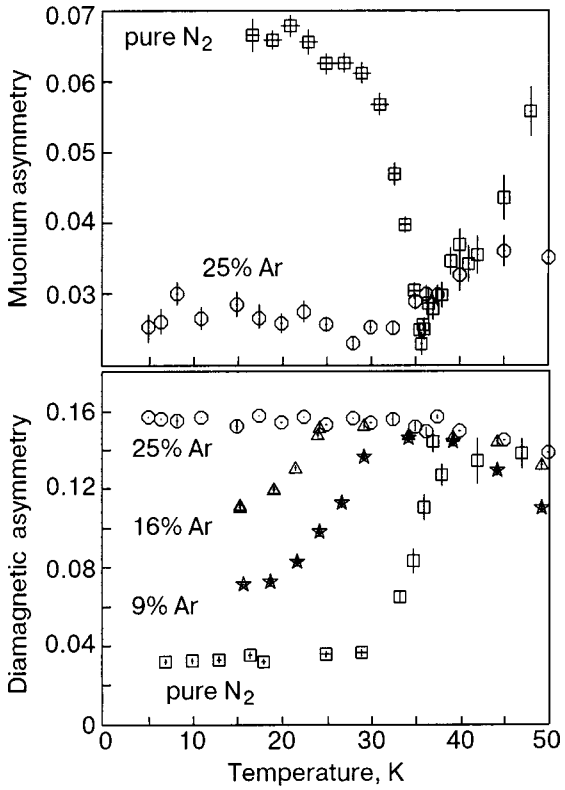

FIG. 5. Temperature dependences of muonium (top, $H \approx 5$ G) and net diamagnetic (bottom, $H \approx 100$ G) signal amplitudes in pure solid nitrogen (squares) and solid $(N^2)_{1-x}Ar_x$ (circles: $x=0.25$; triangles: $x=0.16$; stars: $x=0.09$).

temperature-independent Mu amplitude in the $x=0.25$ sample (see Fig. 5) is the same as the *prompt* Mu amplitude in pure solid nitrogen,[39] suggesting a complete absence of DMF in the orientational glass.

The hypothesis that Mu formation in the $x=0.25$ mixture is essentially all via the *prompt* channel at 20 K is further supported by the observation that A_{Mu} and A_D for that sample do not depend on an externally applied electric field, as is seen in Fig. 6. Both amplitudes show significant electric field dependence in pure N_2 at 20 K, from which the characteristic muon–electron distance is estimated to be about 5×10^{-6} cm;[38,39] about the same value of the muon–electron distance is estimated for solid Ar, which exhibits almost 100% DMF.[18] The absence of DMF at this length scale at low temperature in the $x=0.25$ mixture suggests that electrons are *localized* in an orientational glass.[13]

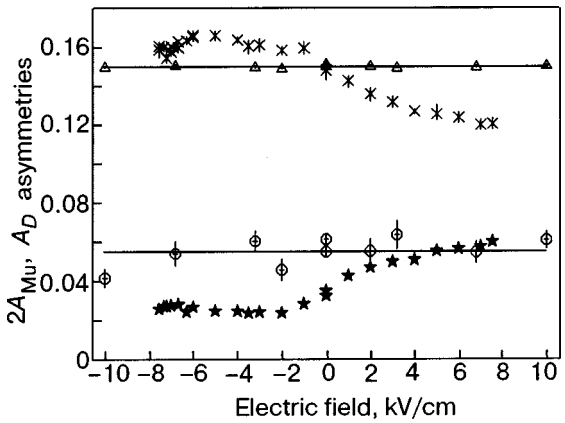

FIG. 6. Electric field dependences of $2A_{\mathrm{Mu}}$ and A_D in pure solid nitrogen (crosses and stars, respectively) and in solid 75% N_2 + 25% Ar (circles and triangles, respectively) in a transverse magnetic field $H=36$ G at $T=20$ K. The muonium amplitudes are doubled to compensate for the 50% depolarization of Mu by hyperfine oscillations.[16]

5. CONCLUSIONS

Scaling from light to heavy CRG enabled us to reveal new features of end-of-track motion in these substances.

We have shown that the unique properties of liquid helium—large relative mobility and light relative mass of the positive ions—make it outstanding in comparison with other condensed gases.

In solid Ne and Ar (where electrons are delocalized and light) the track seems to be a linear chain of anions terminating in a muon and surrounded by a cloud of electrons. The number of electrons involved in muonium formation is about ten in solid Ne and probably bigger in solid Ar. From a comparison of Ne and Ar data we can estimate the distance between track anions to be about 10^{-6} cm and the rms distance between the electron and parent anion to be about 10^{-5} cm.

The slight difference between muonium formation in liquid and solid Ar (electrons are delocalized in both phases) could be attributed to the presence of crystalline defects in the solid.

In liquid Ne the muon can recombine with delocalized or localized electrons. Localization of the initially free track electrons in the liquid results in high (in compression with solid Ne) internal electric fields. External electric fields prevent electron localization.

We have demonstrated a dramatic effect of orientational disorder on electron transport in an insulator. In contrast to electron *delocalization* in the orientationally ordered phase of α-N_2, electrons appear to be *localized* in the orientational glass $(N_2)_{0.75}Ar_{0.25}$.

This work was supported by the Canadian Institute for Advanced Research, the Natural Sciences and Engineering Research Council of Canada, the National Research Council of Canada, and the Engineering and Physical Sciences Research Council of the United Kingdom. Two of us (V.G.S. and D.G.E.) were also supported by the INTAS Foundation (through grant 97-30063), the Royal Society (through the International Award), and NATO (through grant PST CLG.977687). We would like to thank Prof. V. N. Gorelkin for helpful discussions. D.G.E. and V.G.S. also express their gratitude to Profs. S. T. Belyaev, V. P. Martemyanov, and V. A. Matveev for constant support.

*Email: eshchenko@a120.inr.troitsk.ru

[1] R. A. Muller, S. E. Derenzo, G. Smadja, D. B. Smith, R. G. Smits, H. Zaklad, and L. W. Alvarez, Phys. Rev. Lett. **27**, 532 (1971).
[2] E. Morenzoni, F. Kottmann, D. Maden, B. Matthias, M. Meyberg, Th. Prokscha, Th. Wutzke, and U. Zimmermann, Phys. Rev. Lett. **72**, 2793 (1994).
[3] W. E. Spear and P. G. Le Comber, in *Rare Gas Solids*, edited by M. L. Klein and J. A. Venables, Academic Press, New York (1977), p. 1119.
[4] L. S. Miller, S. Howe, and W. E. Spear, Phys. Rev. **166**, 871 (1968).

[5] B. E. Springett, J. Jortner, and M. H. Cohen, J. Chem. Phys. **48**, 2720 (1968).
[6] A. T. Golov and L. P. Mezhov-Deglin, JETP Lett. **56**, 514 (1992).
[7] L. Bruschi, G. Mazzi, and M. Santini, Phys. Rev. Lett. **28**, 1504 (1972).
[8] R. J. Loveland, P. G. Le Comber, and W. E. Spear, Phys. Rev. B **6**, 3121 (1972).
[9] Y. Sakai, W. F. Schmidt, and A. Khrapak, Chem. Phys. **164**, 139 (1992).
[10] A. O. Caldeira and A. J. Leggett, Phys. Rev. Lett. **46**, 211 (1981); Ann. Phys. (N.Y.) **149**, 374 (1983).
[11] P. W. Anderson, Phys. Rev. **109**, 1492 (1958).
[12] N. F. Mott, *Metal-Insulator Transitions*, Taylor and Francis, London (1974).
[13] V. Storchak, D. G. Eshchenko, J. H. Brewer, G. D. Morris, S. P. Cottrell, and S. F. J. Cox, Phys. Rev. Lett. **85**, 166 (2000).
[14] U. T. Hochli, K. Knorr, and A. Loidl, Adv. Phys. **39**, 405 (1990).
[15] H. Schnyders, S. A. Rice, and L. Meyer, Phys. Rev. Lett. **15**, 187 (1965).
[16] A. Schenck, *Muon Spin Rotation: Principles and Applications in Solid State Physics*, Adam Hilger, Bristol (1986); S. F. J. Cox, J. Phys. C **20**, 3187 (1987); J. H. Brewer, in *Encyclopedia of Applied Physics* **11**, VCH, New York (1995), p. 23.
[17] M. Senba, J. Phys. B **21**, 3093 (1988); *ibid.* **22**, 2027 (1989); *ibid.* **23**, 1545 (1990).
[18] V. G. Storchak, J. H. Brewer, and D. G. Eshchenko, Appl. Magn. Reson. **13**, 15 (1997).
[19] D. G. Eshchenko, Ph.D. thesis, Kurchatov Institute, Moscow, 1996 (in Russian).
[20] V. Storchak, J. H. Brewer, and G. D. Morris, Phys. Rev. Lett. **75**, 2384 (1995).
[21] P. W. Percival, E. Roduner, and H. Fischer, Chem. Phys. **32**, 353 (1978); D. C. Walker, *Muon and Muonium Chemistry*, Cambridge Univ. Press (1983); F. M. Jacobsen, Hyperfine Interact. **32**, 501 (1986); O. E. Mogensen and P. W. Percival, Radiat. Phys. Chem. **28**, 85 (1986).
[22] E. Krasnoperov, E. Meilikhov, R. Abela, D. Herlach, E. Morenzoni, F. Gygax, A. Schenck, and D. Eshchenko, Phys. Rev. Lett. **69**, 1560 (1992).
[23] V. Storchak, J. H. Brewer, and G. D. Morris, Phys. Rev. Lett. **76**, 2969 (1996).
[24] M. Inokuti, Rev. Mod. Phys. **43**, 297 (1971).
[25] V. M. Gorelkin and L. P. Kotova, Hyperfine Interact. **65**, 841 (1990).
[26] L. D. A. Siebbeles, S. M. Pimblott, and S. F. J. Cox, J. Chem. Phys. **111**, 7493 (1999); Physica B **289–290**, 404 (2000).
[27] E. P. Krasnoperov, E. E. Meilikhov, D. G. Eshchenko, D. Herlach, E. Morenzoni, U. Zimmermann, F. N. Gygax, and A. Schenck, Hyperfine Interact. **87**, 1011 (1994).
[28] D. G. Eschenko, V. G. Storchak, and G. Morris, Phys. Lett. A **264**, 226 (1999).
[29] E. P. Krasnoperov, E. E. Meilikhov, C. Baines, D. Herlach, G. Solt, U. Zimmermann, and D. G. Eshchenko, Hyperfine Interact. **97/98**, 347 (1996).
[30] A. J. Dahm and T. M. Sanders, J. Low Temp. Phys. **2**, 199 (1970).
[31] F. Reif, L. Meyer, Phys. Rev. **119**, 1164 (1960).
[32] K. P. Atkins, Phys. Rev. **116**, 1339 (1959).
[33] T. Ellis, P. V. E. McClintock, R. M. Bowley, and D. R. Allum, Philos. Trans. R. Soc. London **296**, A1425, 581 (1980).
[34] A. J. Dahm, ''*Charge motion in solid helium*,'' in *Progress in Low Temperature Physics*, Vol. IX, North-Holland, Amsterdam (1985), p. 9.
[35] E. P. Krasnoperov, E. E. Meilikhov, A. N. Ponamarev, V. Yu. Pommyakushin, D. G. Eshchenko, V. N. Duginov, V. A. Zhukov, T. N. Mamedov, and V. G. Olshevskij, JETP Lett. **59**, 749 (1994).
[36] N. F. Mott and E. A. Davis, *Electron Processes in Non-Crystalline Materials*, Clarendon Press, Oxford (1979).
[37] J. A. Hamida, E. B. Genio, and N. S. Sullivan, J. Low Temp. Phys. **103**, 49 (1996).
[38] V. Storchak, J. H. Brewer, and G. D. Morris, Phys. Rev. Lett. **75**, 2384 (1995).
[39] V. Storchak, J. H. Brewer, G. D. Morris, D. J. Arseneau, and M. Senba, Phys. Rev. B **59**, 10559 (1999).

This article was published in English in the original Russian journal. Reproduced here with stylistic changes by AIP.

Low-temperature electron transport on semiconductor surfaces

M. Lastapis, D. Riedel, A. Mayne, K. Bobrov, and G. Dujardin*

Laboratoire de Photophysique Moleculaire, Batiment 210, Universite Paris-Sud, 91405 Orsay Cedex, France

(Submitted October 2, 2002)
Fiz. Nizk. Temp. **29**, 263–269 (March 2003)

The low-temperature electron transport on semiconductor surfaces has been studied using an ultrahigh-vacuum, variable temperature scanning tunneling microscope (STM). The STM $I(V)$ spectroscopy performed at various temperatures has made it possible to investigate the temperature dependence (300 K to 35 K) of the surface conductivity of three different semiconductor surfaces: highly doped *n*-type Si(100), *p*-type Si(100), and hydrogenated C(100). Low temperature freezing of specific surface electronic channels on the highly doped *n*-type Si(100) and moderately doped *p*-type Si(100) surfaces could be achieved, whereas the total surface conductivity on the hydrogenated C(100) surface can be frozen below only 180 K. © *2003 American Institute of Physics.* [DOI: 10.1063/1.1542440]

1. INTRODUCTION

The operation of nanoscale electronic devices requires an efficient electronic decoupling from the substrate on which the devices have been built.[1] This can be best achieved either on insulating or on low-temperature semiconducting substrates. For example, the electronic transport of gold nanowires deposited on a Si(111) surface has been recently measured at low temperature (4 K).[1] At such a low temperature, all the measured current flows through the gold nanowire as long as the applied bias voltage is within the silicon electronic band gap. Indeed, the electronic channels through the silicon surface whose energies are located within the band gap are assumed to be frozen at such a low temperature. Low temperature semiconductor surfaces have several advantages over insulators. First, they can still be conducting at low temperature, when sufficiently doped.[2] This allows the use of experimental surface techniques requiring some surface conductivity, such as scanning tunneling microscopy (STM). Second, the preparation of high-quality surfaces having few defects at the atomic-scale is much easier for semiconductors.

The low-temperature electron transport properties of *bulk* semiconductors are rather well understood,[2] mainly in terms of the decreased number of free carriers. However, when dealing with *surface* properties, the situation is much more complicated. Indeed, the interface between the semiconductor and the vacuum can produce specific surface (or subsurface) electronic states inducing charges or holes confined at the surface,[3,4] which may completely modify the low-temperature electron transport properties.

The low-temperature electron transport properties of semiconductor surfaces have never been investigated before at the atomic scale, except for a recent study of the Ge(111) surface.[5] In this paper, we report the temperature dependence of the electron transport properties of three different semiconductor surfaces: highly doped *n*-type Si(100), STM *p*-type Si(100), and hydrogenated C(100). We used STM $I(V)$ spectroscopy performed at various temperatures to explore the conductivity of these surfaces. The observed behavior is very different in these three cases. It will be shown that specific surface conductivity channels can be frozen at low temperature for highly doped *n*-type Si(100) and *p*-type Si(100), whereas the surface conductivity is completely frozen at low temperature for hydrogenated C(100).

2. EXPERIMENTAL

The electron transport properties of semiconductor surfaces have been measured in an ultrahigh-vacuum (UHV) chamber (base pressure 2×10^{-11} torr) using a variable temperature scanning tunneling microscope (STM). The sample can be cooled down to 30 K using a helium liquid-flow cryostat.

Three types of semiconductor samples have been studied:

– *highly doped n-type* Si(100): the silicon sample ($6\times2\times0.1$ mm) was *n* doped with arsenic (bulk resistivity of 0.004 to 0.007 $\Omega\cdot$cm). Clean and well-ordered Si(100)$-(2\times1)$ reconstructed surfaces were obtained by first outgassing for at least 12 hours at 700 °C in UHV before flashing to 1080 °C to remove the oxide layer. The duration of each flash was adjusted so that the pressure remained below 1×10^{-9} torr (usually$<2\times10^{-10}$ torr).

– *p-type* Si(100): the silicon sample ($6\times2\times0.25$ mm) was *p* doped with boron (bulk resistivity 0.7 to 1.3 $\Omega\cdot$cm). Clean and well-ordered Si(100)$-(2\times1)$ reconstructed surfaces were obtained as described before.

– *hydrogenated* C(100): the diamond sample ($6\times1\times0.2$ mm) is a natural single crystal of (100) orientation. It is a weakly boron *p*-type doped sample. Prior to insertion into the UHV chamber, the diamond sample was saturated *ex situ* with hydrogen in a microwave hydrogen plasma at 800 °C for 1 hour. Details on the hydrogenation procedure can be found elsewhere.[6] Clean and well-ordered hydrogenated C(100)$-(2\times1)$:H surfaces were obtained by outgassing in UHV for a few minutes at 300 °C to remove any physisorbed species from the surface.

During the STM experiments, the edges of the sample

were sandwiched between two molybdenum plates to which the voltage was applied.

Experiments were performed as follows at a given sample temperature between 30 K and 300 K. The sample surface was first imaged at a constant tunnel current with the STM. For some samples and some temperatures, no tunnel current could be established between the STM tip and the sample. In such cases, the STM tip crashed on the surface. Where STM imaging was possible, the STM tip was located at fixed positions across the surface, and $I(V)$ spectroscopy curves were recorded at a fixed tip-surface distance.

3. RESULTS AND DISCUSSIONS

Before we discuss the results, one should note that the $I(V)$ STM spectroscopy curves are usually considered to be due only to the STM junction conductivity. Indeed, the conductance between the electronic surface states located under the STM tip and the sample metallic holder to which the voltage is applied is assumed to be very high. In such a case, the $I(V)$ curves only reflect the coupling between the surface electronic states of the tungsten tip with those of the sample surface.[3] However, at low temperature, where the resistivity of the semiconductor sample can no longer be neglected, the analysis of the $I(V)$ curves is more complicated. The measured I/V conductivity is the combination of the STM junction conductivity itself, the coupling between the electronic surface states of the sample and the electronic channels through the sample and the conductivity of these electronic channels as far as the sample molybdenum holders. At this point, the electronic channels through the sample can be either surface or bulk electronic channels.

3.1. Highly doped *n*-type Si(100)

The highly doped *n*-type Si(100) surface could be easily imaged with the STM at any temperature between 30 K and 300 K under usual sample voltage ($V=-1.5$ V) and tunnel current ($I=0.5$ nA) conditions (see Fig. 1). This is not surprising since such a highly doped silicon sample is known to have an almost constant conductivity in this temperature range.[2] More astonishing are the $I(V)$ curves recorded as a function of temperature (Fig. 2). As seen in Fig. 2b, the dI/dV curve at 300 K shows a narrow band gap of about 0.2 eV, whereas the dI/dV curve at 35 K shows a band gap of about 1 eV, i.e., equal to the bulk electronic band gap of silicon.[3] This temperature effect cannot be explained by any freezing of the bulk conductance since such a highly doped silicon sample is known to have a bulk conductivity which is almost constant between 300 K and 35 K.[2] A similar opening of the surface band gap at low temperature has been observed previously on the Ge(111) surface.[5] It has been assigned to low-temperature freezing of specific surface electronic channels whose energies are located within the electronic bulk band gap.[5] Recent measurements of the total surface conductivity of the Si(100) surface[7] have shown that, on the contrary, the surface conductivity increases at low temperature. One cannot completely rule out that the conductivity of the specific surface electronic channels whose energies are located within the bulk band gap would decrease at low temperature while the total surface conductivity would increase. However, such an explanation seems very unlikely. Therefore, another explanation needs to be considered as illustrated in Fig. 3. At room temperature, the tunnel current flowing through occupied surface states located within the bulk band gap requires some transport of electrons from the bulk conduction band (CB) to the occupied surface states (SS). This can be achieved by a combination of two effects, (*i*) the electron transport through the energy barrier of the upward surface band, bending caused by the "pinning" of the surface states at the Fermi level,[3] and (*ii*) the release of electron energy to reach the lower-lying surface states. This latter effect would require some coupling between electrons and phonons. Considering that the transmission over the energy barrier as well as the phonon population are thermally activated, both effects are expected to be much less efficient

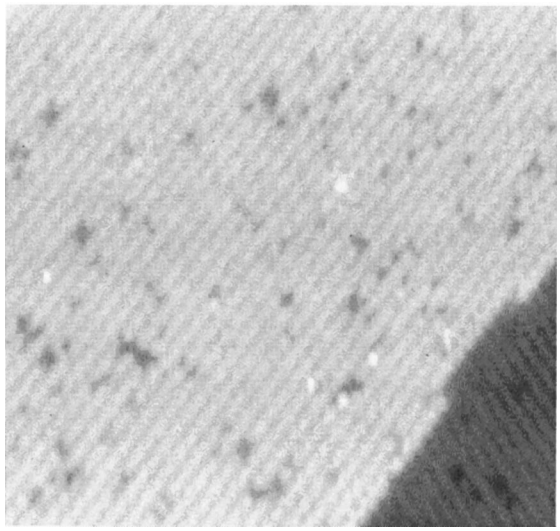

FIG. 1. Scanning tunneling microscope topography (390 Å by 240 Å) of the highly doped *n*-type Si(100)-2×1 surface, recorded at 35 K. The sample voltage is $V_S=-1.5$ V and the tunnel current $I=0.5$ nA.

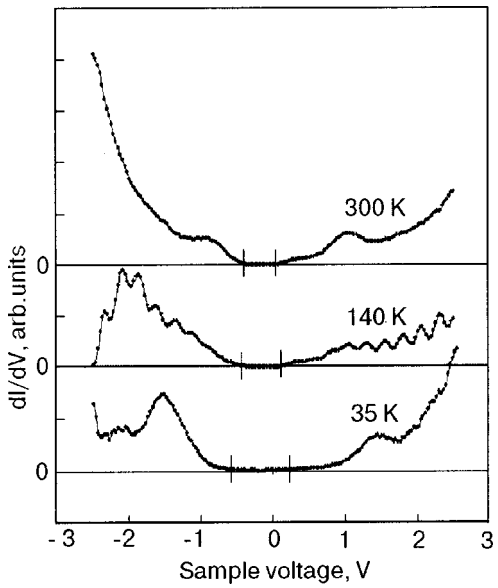

FIG. 2. dI/dV curves recorded on the highly doped *n*-type Si(100)$-(2\times1)$ surface at various temperatures. The scanning conditions for recording these curves are $V_S=-1.5$ V and $I=0.5$ nA.

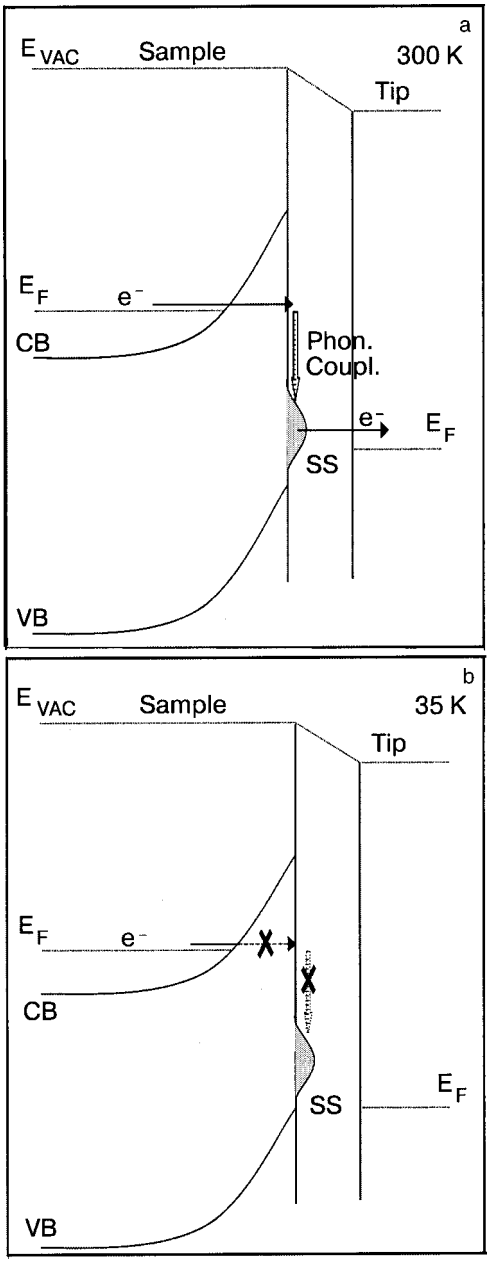

FIG. 3. Schematic energy diagram of electrons flowing from the highly doped *n*-type Si(100)$-(2\times1)$ sample to the STM tip. At 300 K (a), the thermal energy can (i) activate the transport of electrons from the sample Fermi level E_F through the subsurface barrier due to the upward band-bending, and (ii) activate the coupling with phonons and surface states (SS). At 35 K (b), the loss of thermal activation freezes the electron current.

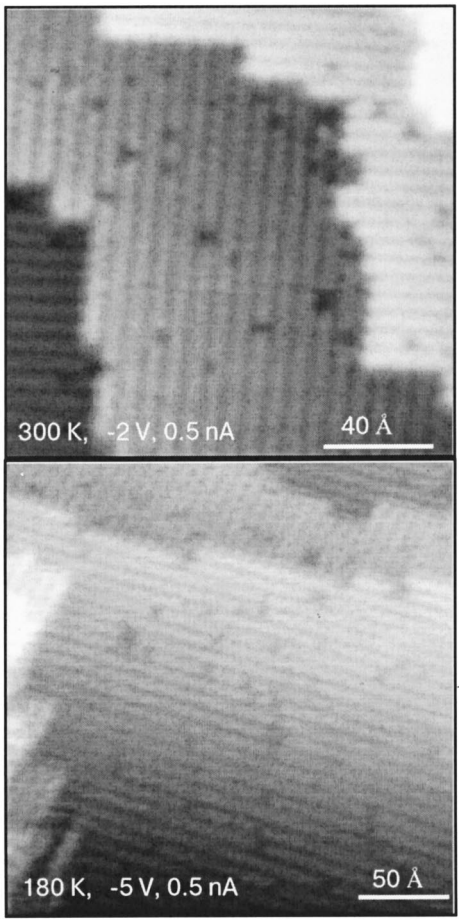

FIG. 4. Scanning tunneling microscope topographies of the *p*-type Si(100) surface at 300 K (top — 160×160 Å) and 180 K (bottom — 250×250 Å).

at low temperature, thus explaining the freezing of the electronic channels through the surface states located within the bulk band gap.

3.2. *p*-type Si(100)

At room temperature, the *p*-type Si(100) sample shows a STM topography and $I(V)$ spectroscopy curves similar to those for the highly doped *n*-type Si(100) (see Fig. 4). However, as soon as the sample temperature is lowered to about 180 K, both the STM topography and $I(V)$ curves are markedly modified. At 180 K, stable STM topographies with atomic resolution can hardly be obtained. At room temperature, STM topographies could easily be obtained at relatively small negative (-2 V, $I=0.5$ nA) sample voltages. At 180 K, STM topographies could be obtained only at high negative sample voltages (-5 V, $I=0.5$ nA) (see Fig. 4) and were found to be very unstable, suggesting some local charging occurring after a few minutes of tunneling. The $I(V)$ curves are also strongly modified (see Fig. 5), with a much reduced conductivity at negative sample voltages. At 35 K, it was impossible to obtain any STM topography at any negative sample voltage, and the $I(V)$ curves show a weak conductivity extending at even larger negative sample voltages (see Fig. 5). The conductivity is zero for sample voltages between -3 V and $+1$ V.

These results are somewhat surprising, since they cannot be simply ascribed to the temperature dependence of the bulk conductivity of *p*-type Si(100). Indeed, from 300 K to 180 K, the conductivity of the sample is considered to increase.[2] Obviously this cannot explain the shift from -2 V to -5 V of the sample voltage for imaging, since this shift (associated with a tunnel current of 0.5 nA) would correspond to a spreading resistance of 6×10^9 Ω. In fact, these results can be well understood by considering a tip-induced band-bending as shown schematically in Fig. 6. The ''pinning'' of the surface states at the Fermi level produces a downward band-bending.[3] At negative sample bias, charge carriers (h^+, holes) are prevented from flowing from the tip to the sample by the downward band-bending of the valence bands. At

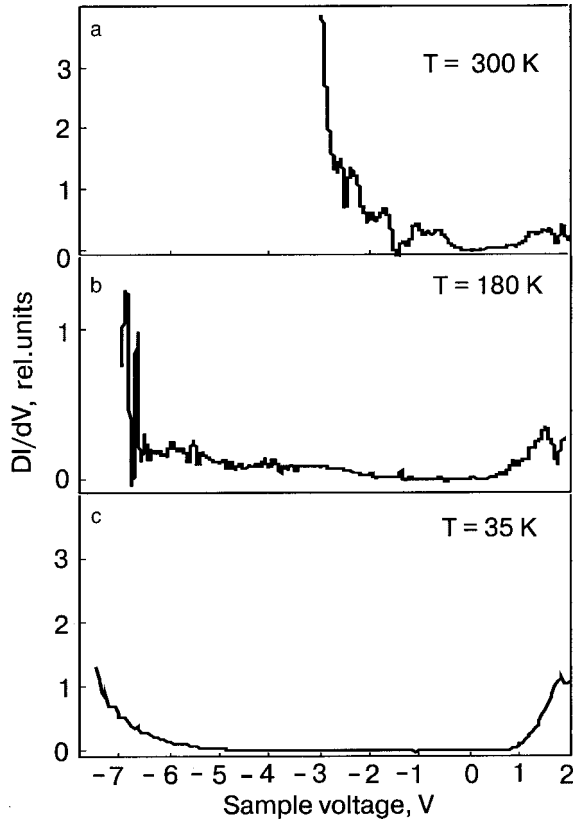

FIG. 5. dI/dV curves recorded on the p-type Si(100)-2×1 surface at various temperatures. The scanning conditions for recording these curves are (a) -2 V, 0.5 nA; (b) -6 V, 0.5 nA; (c) -7 V, 0.5 nA.

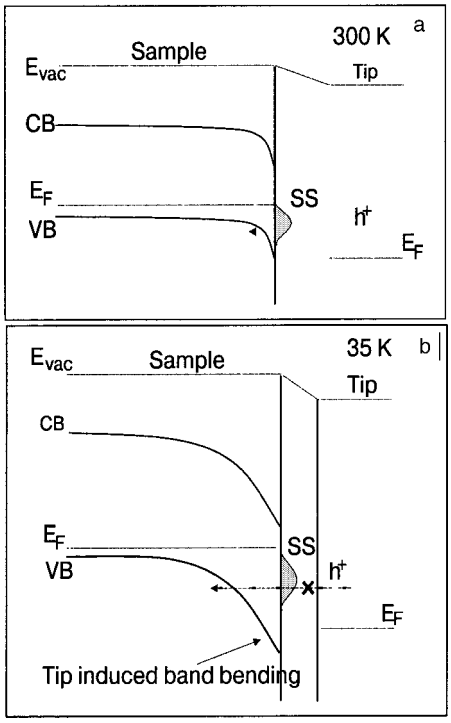

FIG. 6. Schematic energy diagram of electrons showing the flow of positive holes (h^+) from the STM tip to the p-type Si(100) sample. At 300 K (a), the thermal energy can activate the transport of holes through the energy barrier due to the surface state induced band bending. At 35 K (b), the tip induced band bending is too large to allow the flow of hole current.

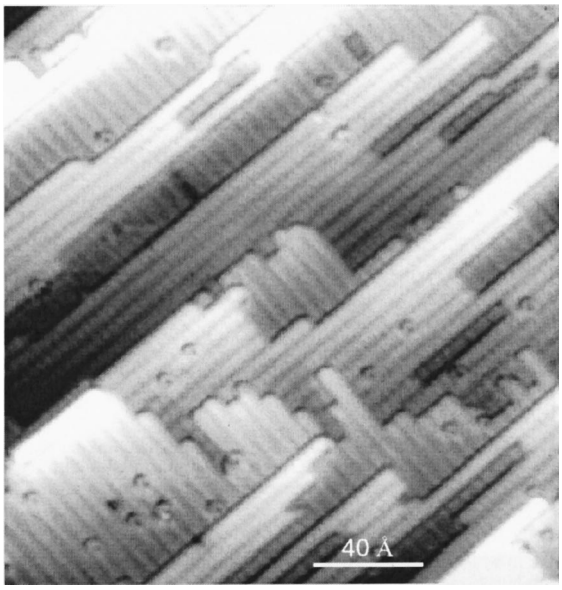

FIG. 7. 175×175 Å statement topography of the diamond C(100)-2×1 surface recorded at room temperature ($V_S=+1.5$ V, $I=1.5$ nA).

room temperature, the holes can acquire enough thermal energy to overcome this energy barrier. However, at low temperature the hole transport through this energy barrier is frozen. Since the conductivity decreases, the STM tip tends to approach the surface to maintain the tunnel current constant. As a consequence, the electric field between the STM tip and the surface is strongly increased, inducing a more pronounced downward band bending as shown in Fig. 6. This explains the large shift from -2 V (300 K) to -5 V (180 K) for imaging the surface as well as the shape of the $I(V)$ curves (Fig. 5). One should also mention here the possible influence of the surface states on the penetration of the electric field into the silicon sample. Indeed, the reduced charge population of the surface states at low temperature may decrease the screening effect and thus facilitate the penetration of the electric field produced by the tip. This tip-induced band-bending was not observed for the previously studied n-type sample due to its high concentration of dopants, which prevents the electric field from penetrating inside the sample.

3.3. Hydrogenated C(100)

At room temperature, the hydrogenated C(100) diamond surface can be imaged at the atomic scale with the STM at both positive ($V=+1.5$ V, $I=1$ nA) (see Fig. 7) and negative ($V=-1.5$ V, $I=1$ nA) sample bias. The corresponding $I(V)$ curve is shown in Fig. 8. When lowering the sample temperature, the I/V conductivity decreases, especially at positive sample bias (see Fig. 8), so that below 180 K no STM imaging is possible any more. Around 150 K, the $I(V)$ curve becomes ''metallic'' in form, i.e., linear. For temperatures below 150 K, no tunneling current could be established whatever the sample bias. This behavior is quite different from the two previous cases of the silicon surface and requires a specific explanation.

The clean natural (weakly doped) C(100) diamond surface is known to be insulating.[8] However, when hydroge-

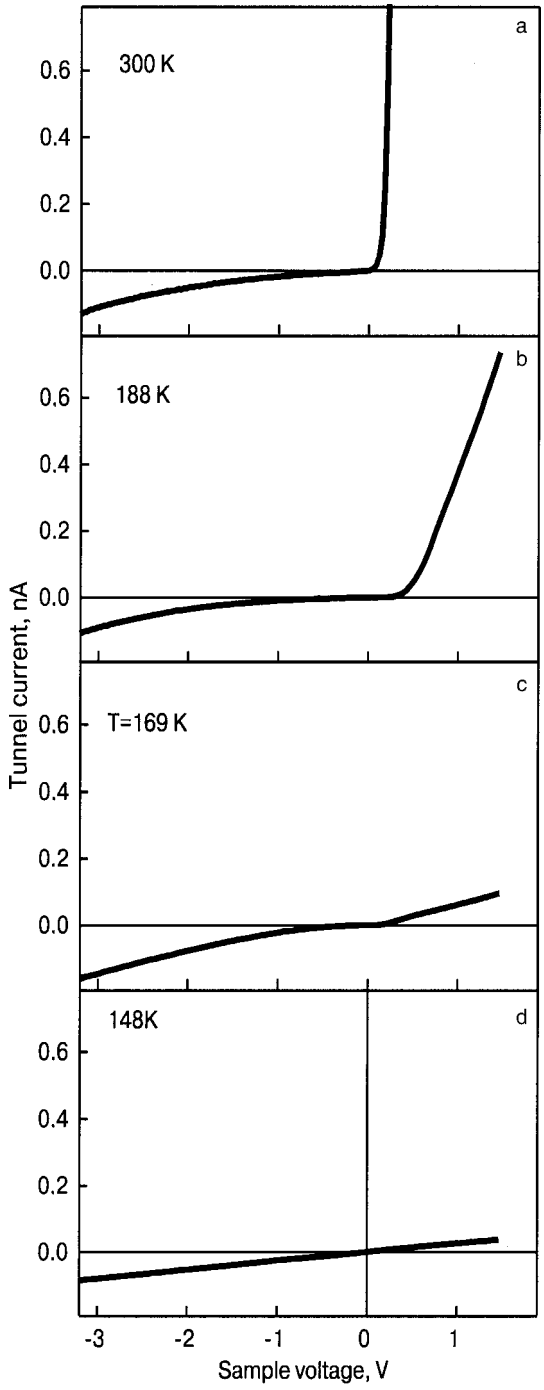

FIG. 8. $I(V)$ curves recorded on the diamond C(100)$-(2\times1)$ surface as a function of the temperature. The scanning conditions for recording these curves are $V_S=-2$ V, $I=0.1$ nA.

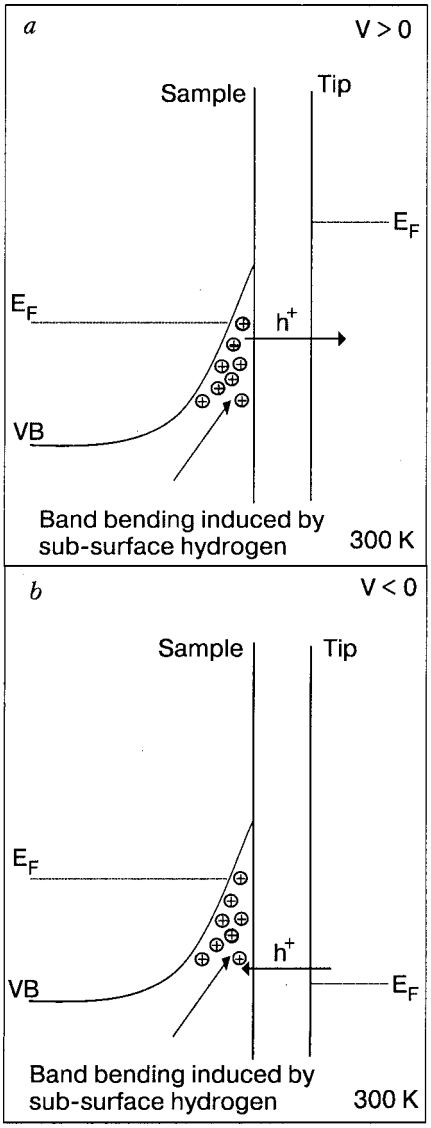

FIG. 9. Schematic energy diagram of electrons showing the flow of positive holes (h^+) for two polarities of the voltage on the diamond C(100)$-(2\times1)$ surface.

nated, the C(100) diamond surface becomes conductive and STM imaging in the usual tunneling mode can be performed.[9] It has been demonstrated recently[9] that this surface conductivity requires the presence both of hydrogen atoms on the surface and of subsurface oxygen and hydrogen. These subsurface species, which are produced during the preparation procedure of the hydrogenated sample, result in an upward surface band-bending (see Fig. 9) and a concentration of holes in the subsurface region. As is seen in Fig. 9, this enables a flow of holes at both negative and positive sample bias. With decreasing sample temperature the activation of the subsurface species as dopants should decrease rapidly if their activation energy is high enough, of the order of 0.6 eV. This explains the much reduced surface conductivity. Around 150 K, the subsurface conductivity is so low that the STM tip needs to be in full contact with the sample, thus leading to a ''metallic'' $I(V)$ curve. In summary, the freezing of the subsurface conductivity explains why the hydrogenated diamond surface becomes fully insulating below 150 K.

4. CONCLUSIONS

Investigating the low-temperature conductivity of semiconductor surfaces with the STM is a very interesting problem, since a large variety of phenomena can be encountered.

For highly doped *n*-type Si(100), lowering the sample temperature down to 35 K enables the freezing of the electronic channels whose energies are within the bulk band gap. Other electronic channels (outside the bulk band gap) seem to be accessible at low temperature, enabling the STM im-

aging of the sample down to 35 K. Due to the high concentration of dopants, tip-induced surface band-bending can be neglected.

For moderately doped *p*-type Si(100), the surface band-bending also freezes electronic channels at negative sample voltages. This effect is amplified by tip-induced surface band-bending, which at low temperature freezes all the electronic channels from -2 V down to -5 V at 35 K.

For hydrogenated C(100), the surface conductivity is due to the presence of sub-surface species (oxygen and hydrogen). The whole surface conductivity is strongly dependent on the temperature, since below 180 K the hydrogenated C(100) surface becomes fully insulating.

These three examples offer an interesting range of applications for nanoelectronics. The highly doped *n*-type Si(100) surface can be advantageously used at low temperature to decouple the electronic channels of a nanoscale device from the substrate only in the energy range located within the bulk band gap. The advantage is that the substrate is still conducting and STM imaging can still be performed at such a low temperature (35 K). The hydrogenated C(100) surface can be used, below room temperature at $T=180$ K, to fully decouple the electronic channels of a nanoscale device from the substrate. However, in this case, the substrate is completely insulating and STM imaging is no longer possible. The moderately doped *p*-type Si(100) surface offers another potentially interesting application, where surface tip-induced-band bending can be used at low temperature (35 K) to freeze all the electronic channels across the surface whose energy is between -5 V and $+1$ V.

We wish to thank the European IST-FET ''Bottom-up-Nanomachines'' (BUN) and the European ''Atomic and Molecular Manipulation; a new tool In Science and Technology'' (AMMIST) network.

*E-mail: gerald.dujardin@ppm.u-psud.fr

[1] U. Ramsperger, T. Uchihashi, and H. Nejoh, Appl. Phys. Lett. **78**, 85 (2001).
[2] S. M. Sze, *Physics of Semiconductor Devices*, Wiley, New York (1981) p. 26.
[3] J. A. Stroscio and R. M. Feenstra, in *Scanning Tunneling Microscopy*, edited by J. A. Stroscio and W. J. Kaiser, Academic Press, New York (1993), p. 27.
[4] W. Mönch, *Semiconductor Surfaces and Interfaces*, Springer-Verlag, Berlin (1993), p. 15.
[5] G. Dujardin, A. J. Mayne, and F. Rose, Phys. Rev. Lett. **89**, 36802 (2002).
[6] K. Bobrov, H. Shechter, M. Folman, and A. Hoffman, Diamond Relat. Mater. **7**, 170 (1998).
[7] K. Yoo and H. H. Weitering, Phys. Rev. Lett. **87**, 026802 (2001).
[8] K. Bobrov, A. J. Mayne, and G. Dujardin, Nature (London) **413**, 616 (2001).
[9] K. Bobrov, A. J. Mayne, G. Comtet, G. Dujardin, L. Hellner, and A. Hoffman (in preparation).

This article was published in English in the original Russian journal. Reproduced here with stylistic changes by AIP.

Reactions induced by low energy electrons in cryogenic films (Review)

A. D. Bass* and L. Sanche**

Department of Nuclear Medicine and Radiobiology, University of Sherbooke Sherbooke, Quebec, I1H5N4, Canada

(Submitted December 13, 2002)
Fiz. Nizk. Temp. **29**, 270–285 (March 2003)

We review recent research on reactions (including dissociation) initiated by low-energy electron bombardment of monolayer and multilayer molecular solids at cryogenic temperatures. With incident electrons of energies below 20 eV, dissociation is observed by the electron stimulated desorption (ESD) of anions from target films and is attributed to the processes of dissociative electron attachment (DEA) and to dipolar dissociation. It is shown that DEA to condensed molecules is sensitive to environmental factors such as the identity of co-adsorbed species and film morphology. The effects of image-charge induced polarization on cross sections for DEA to CH_3Cl are also discussed. Taking as example, the electron-induced production of CO within multilayer films of methanol and acetone, it is shown that the detection of electronic excited states by high-resolution electron energy loss spectroscopy can be used to monitor electron beam damage. In particular, the incident energy dependence of the CO indicates that below 19 eV, dissociation proceeds via the decay of transient negative ions (TNI) into electronically excited dissociative states. The electron-induced dissociation of biomolecular targets is also considered, taking as examples the ribose analog tetrahydrofuran and DNA bases adenine and thymine, cytosine and guanine. The ESD of anions from such films also show dissociation via the formation of TNI. In multilayer molecular solids, fragment species resulting from dissociation, may react with neighboring molecules, as is demonstrated in anion ESD measurements from films containing O_2 and various hydrocarbon molecules. X-ray photoelectron spectroscopy measurements reported for electron-irradiated monolayers of H_2O and CF_4 on a Si—H passivated surface further show that DEA is an important initial step in the electron-induced chemisorption of fragment species. [DOI: 10.1063/1.1542441]

1. INTRODUCTION

The interactions of electrons of energies less than ~20 eV with the constituent atoms and molecules of condensed matter are of considerable interest since low-energy electrons generated within and at the surface of condensed media are implicated in a variety of processes ranging from the aging of dielectrics under high voltage[1] and friction-induced damage to lubricants[2] to nano-lithography (for example, see Ref. 3). Interest also lies in their use to study catalytic reaction intermediates by their dissociative interaction with organic molecules.[4] Motivation for the authors' research derives essentially from the large numbers of low-energy secondary electrons generated within biological systems by irradiation with high-energy primary particles (e.g., therapeutic x rays).[5] What role (if any) do these secondary electrons play in the genotoxic effects of radiation? Attempting to answer this question, we have adapted techniques from gas-phase electron-scattering experiments for use with thin solid targets. In a typical experiment an energy-selected beam of electrons is incident from vacuum onto a solid film, and a variety of analytical techniques are then used to determine the mechanisms by which electronic energy is absorbed. These techniques may include surface spectrocopies, such as high-resolution electron energy loss (HREELS), x-ray photoelectron spectroscopy (XPS), or measurements of particle desorption or of charge accumulation within the film. Experimental systems studied include simple vapor-deposited atomic and molecular solids, molecules physisorbed on ordered metal and semiconductor surfaces, organic self-assembled monolayers and complex biomolecules such as DNA. Various aspects of this work, as applied to dielectric aging,[1] electron microscopy,[6] radiation track calculations[7] and particle desorption[8] have been described elsewhere. Here we will discuss principally results reported within the past 6 years that demonstrate electron-induced chemical changes, including dissociation, in condensed phase systems. As a further restriction on our discussion, all the target systems presented, whether thin molecular solids or adsorbate/substrate systems, require cryogenic stabilization. We stress that while cooling to temperatures of between 15 K and 100 K allows preparation of films under ultrahigh-vacuum (UHV) conditions, cryogenic conditions also limit vibrational excitation of the molecular constituents in the solid targets and help ensure that the observed electron-scattering effects are dominated by the interaction of electrons with the majority of molecules in their vibrational ground state.

The structure of this paper is as follows: In Sec. 2 we introduce various theoretical concepts, such as negative ion resonances, which are required to explain low-energy electron scattering in condensed matter. In Sec. 3 we briefly describe the experimental methods. In Sec. 4 we present recent results on electron-induced dissociation in several systems,

including condensed halomethanes, acetone, and methanol and simple organic molecules of biological significance. In Sec. 5 we discuss simple reactions, including ion scattering, that succeed electron-induced dissociation.

2. ELECTRON-SCATTERING PHENOMENA

Studies of electron-molecule scattering and attachment in the gas phase have a long history, dating back to the experiments of James Franck and Gustav Hertz in 1914.[9] Subsequent research has shown how at low energies (i.e., below ~20 eV), the cross sections for electron–molecule scattering are often dominated by the transient localization of the electron on the molecule, in what is often termed a ''resonance.'' [10] (It is likely that the striking clarity of the original Franck-Hertz experiment owes much to excitation of a resonance near the threshold of the 6^3P states of mercury.[11]) From an atomic and molecular orbital perspective, resonances can be considered as temporary or transient negative ions and may be classed as belonging to one of two broad types. If the additional electron occupies a previously unfilled orbital of the target in its ground state, the transitory state is referred to as a *single particle resonance*. The term ''*shape resonance*'' applies more specifically, when temporary trapping of the electron is due to the shape of the electron–molecule potential. When electron capture is accompanied by electronic excitation, so that two electrons occupy previously unfilled orbitals, the resonance is called ''*core-excited*.''

The prevalence of resonances in gas-phase electron–molecule collisions and the universal nature of the short-range interactions responsible for their formation have suggested that similar phenomena should exist at higher levels of aggregation in condensed matter. Indeed, experimental studies performed in our laboratory over the past 20 years have consistently shown that electron scattering with condensed molecules is strongly modulated by the formation of transient negative ions. However, and contrary to the gas-phase, where the captured electron must remain attached to a single atom or molecule throughout its lifetime, in solids the transient anion can hop between adjacent sites via interatomic or intermolecular electron transfer.[12] For motion to occur in the case of core-excited resonances, three electrons must be involved in the process,[12] e.g., a two-electron transition accompanied by an electron transfer. Such electron and energy transfer leads to the formation of a transient anion having a specific wave vector in the lattice or at the surface and may be referred to as an ''electron–exciton complex.'' [13]

When an electron resonance occurs, the temporary capture of an electron at an atomic or molecular site increases the interaction time of the electron at that site in proportion to the resonance lifetime ($\tau_a \sim 10^{-16}$–10^{-13} s) and the inverse of the electron transfer rate. This local interaction causes a distortion of the atom (or molecule) that accepts the additional electron—multipole forces. One product of this fundamental interaction, of great relevance to the experimental systems discussed in this article, is dissociative electron attachment (DEA), which arises essentially from the molecular distortion.

Dissociative electron attachment occurs when the molecular transient anion state is dissociative in the Franck–Condon (FC) region, the localization time is of the order of, or larger than, the time required for dissociation along one nuclear coordinate and one of the resulting fragments has positive electron affinity. In this case, a stable atomic or molecular anion is formed along with one or more neutral species. This process is analogous to the well-known Menzel–Gomer–Redhead model of desorption via a FC electronic transition to a repulsive state.[14] DEA usually occurs via the formation of core-excited resonances, since these possess sufficiently long lifetimes to allow for dissociation of the anion before autoionization. Hence, when surface molecules are bombarded with a low-energy (0–20 eV) electron beam, a portion of the neutral and anionic species formed by DEA can desorb.

Within a local complex potential curve crossing model, the cross section for the simple DEA reaction $e + AB \rightarrow AB^- \rightarrow A^- + B$, where AB is a diatomic molecule, may be expressed as[15]

$$\sigma_{DEA}(E) = \sigma_{\mathrm{cap}}(E) P_s , \tag{1}$$

where P_s represents the survival probability of the anion against autodetachment of the electron and E the incident electron energy. The capture cross section σ_{cap} is given by

$$\sigma_{\mathrm{cap}}(E) = \lambda g |\chi_v|^2 \left[\frac{\Gamma_a}{\Gamma_d}\right], \tag{2}$$

where λ is the de Broglie wavelength of the incident electron, g is a statistical factor, and χ_v is the normalized vibrational nuclear wave function. Γ_a is the *local* energy width of the AB^- state in the FC region, and Γ_d is the *extent* of the AB^- potential in the FC region. The width of the transient anion state in the autodetaching region defines the lifetime τ_a in respect to autodetachment, $\tau_a(R) = \hbar/\Gamma_a(R)$, such that the survival probability of the temporary anion, after electron capture, is given by

$$P_s = \exp\left[- \int_{R_E}^{R_c} \frac{dt}{\tau_a(R)} \right], \tag{3}$$

where R_E is the bond length of the anion at energy E and R_c is that internuclear separation beyond which autodetachment is no longer possible. If we define an average lifetime $\overline{\tau_a}$ and let $K \equiv \lambda g |\chi_v|^2$, then Eq. (1) becomes

$$\sigma_{DEA}(E) = K \left[\frac{\Gamma_a}{\Gamma_d}\right] \exp\left[- \frac{\overline{\tau_c}}{\overline{\tau_a}} \right]. \tag{4}$$

Here $\overline{\tau_c}(E) \equiv |R_c - R_E|/v$ where v is the average velocity of separation of the fragments A^- and B upon dissociation. Hence, the DEA cross section depends exponentially on the ratio of the lifetime of the transient anion and the velocities of the fragments. Equation (4) defines most of the *intrinsic* characteristics of the DEA process. It may be seen from this equation that the magnitude of the DEA signal depends on parameters which are influenced by the nature of the solid target; i.e., the attaching electron wavelength λ, the resonance lifetime $\overline{\tau_a}$, and the curve-crossing at R_c between the anion state and a neutral state beyond which autodetachment is no longer possible. This aspect of DEA, its sensitivity to environmental factors, will be dealt with in some detail in the following Sections. It is also important to recognize DEA as a mechanism for producing reactive (ionic and neutral) spe-

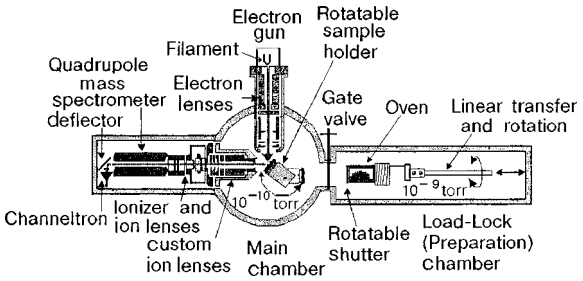

FIG. 1. Schematic overview of an apparatus suitable for measurements of the electron-stimulated desorption of anions from vacuum-deposited films.[18]

cies with nonthermal energies and as such represents an initial step in the more complex reactive pathways induced by low-energy electrons. Examples of such DEA-mediated reactions will also be given.

3. EXPERIMENTAL TECHNIQUES

The experiments described in this article were performed under ultrahigh vacuum, that is within vacuum chambers evacuated by cryogenic, ion, and turbo-molecular pumps to base pressures of between 10^{-11} and 10^{-10} torr. Molecular solid targets are formed by vapor-deposition onto a clean substrate, held at temperatures varying from 15 to 100 K by cryostat. The substrate is usually a polycrystalline metal foil, a Pt monocrystal, or a semiconductor crystal which can be cleaned by resistive heating and/or ion bombardment. The condensed films can be grown by either a gas-volume expansion dosing procedure[16] (and calibrated by monitoring the quantum size effect features observed in ultrathin films[17]) or, for higher molecular mass adsorbates, by timed deposition from an oven source.

Once formed, the sample films can be probed with a variety of electron beam techniques. Dissociative processes (and certain other reactions) are most effectively detected when a fragment ion or neutral species is desorbed into vacuum. Generally, ion desorption is easier to observe than that for neutral species, since desorbed charged particles can be immediately mass analyzed. Figure 1 illustrates schematically an experimental system for ion desorption studies of large organic/biomolecular targets. Note the load-lock section for the introduction of sample slides and/or the degasing of organic molecules within an oven prior to their introduction into the analysis chamber. In this instrument[18] an electron gun produces an electron beam of variable energy having a current of between 5 and 300 nA with an energy resolution of ~250 meV full width at half maximum (FWHM). The electron beam is incident on the cryogenically cooled solid target. The electron energy scale is calibrated to within ± 300 meV with respect to the vacuum level E_{vac} by measuring the onset of the current transmitted through the film. Ions desorbed during electron impact enter an ion lens (containing a set of retardation grids) which precedes a quadrupole mass spectrometer. So-called *ion yield functions* are obtained by recording a particular ion signal as a function of incident energy E. In another ESD instrument, the electron gun is replaced by an electrostatic monochromator which produces an electron beam of 2 nA at a resolution of 80 meV.[19] In this latter instrument double μ-metal shields surround the vacuum chamber to eliminate stray magnetic fields.

In principle, the neutral desorbed products of dissociation can be detected and mass analyzed if they are ionized prior to their introduction into the mass spectrometer. However, such experiments are difficult due to low *effective* ionization efficiencies for desorbed neutrals. Nevertheless, a number of cryogenic systems have been studied by the groups of Feulner,[20] Orlando,[21] and Arumainaygam,[22] for example. In our laboratory, studies of neutral particle desorption have concentrated on self-assembled monolayer targets at room temperature,[23] which fall outside the scope of this review. Under certain circumstances, neutrals desorbed in electronically excited metastable states of sufficient energy can be detected by their de-excitation at the surface of a large-area microchannel plate/detector assembly.[24] Separation of the ESD signal of metastables from UV luminescence can be effected by time of flight analysis.[24]

While desorption measurements provide clear evidence of molecular dissociation, quantitative measurements are difficult to perform, partly because of experimental uncertainties (such as the efficiency of ion transmission through the mass spectrometer) but also because only a small, poorly known fraction of the ions (or neutrals) desorb. However, quantitative measurements are often possible using a modification of low-energy electron transmission (LEET) spectroscopy. In LEET experiments[16] a trochoidal monochromator[25] providing an electron current of between 1 and 10 nA with an intrinsic resolution of between 40 to 60 meV FWHM is incident normally on the film surface. A LEET spectrum is obtained by measuring the current I_t arriving at the substrate as a function of E. Cross sections for electron trapping or stabilization by molecules condensed onto a dielectric film can also be obtained.[26,27] Electronic charge trapped at the surface, following exposure of the film to electrons of a known energy, produces a retarding potential ΔV, which is manifested as a displacement of any subsequent LEET spectrum to higher incident energies. The observed rate of charging A_s (the charging coefficient) can be converted into a charging cross section σ_{CT} as follows:

$$A_s \equiv d\Delta V(t)/dt|_{t=0} = (LI\mu_0/\varepsilon\pi r^2)\sigma_{CT}, \tag{6}$$

where L and ε are the spacer layer thickness and dielectric constant, respectively, and μ_0 is the surface density of molecular targets; I and r are the total current and radius of the incident electron beam, respectively. Analysis of errors, including those associated with the preparation of the target film, suggest a total error of $\pm 50\%$ on the absolute values of the measured cross sections. Combined with the mass spectrometric measurements of anion ESD, σ_{CT} cross sections can on occasion allow absolute cross sections for DEA to be obtained.

Electron-induced changes in film chemistry can also be observed using surface-sensitive techniques such as high-resolution electron energy loss (HREEL) spectroscopy.[28] An HREELS spectrometer allows the energy losses of electrons scattered near the surface of thin films and their dependence on incident electron energy to be measured. In addition to the cryogenically cooled substrate,[29] such an instrument includes

an electron monochromator and an energy analyzer, both of which employ hemispherical electrostatic deflectors to achieve optimal resolution (~5 to 30 meV FWHM). Typically, the monochromator produces a focused electron beam that strikes the film surface at an angle θ_0 from the film normal. Electrons scattered in a narrow pencil about an angle θ_r relative to the surface normal are energy analyzed with the second hemispherical deflector. Energy loss processes include vibrational and electronic excitations of target atoms and molecules. Energy loss spectra are recorded by sweeping the potential of the monochromator or analyzer relative to the grounded target. The energy dependence of the magnitude of a given loss process (i.e., the excitation function) is obtained by sweeping the energy of both deflectors, with the potential difference between them corresponding to the probed energy.

X-ray photoelectron spectroscopy[30] allows quantitative elemental analysis of thin films and provides information on the chemical states of atoms in molecules. It uses the fact that the kinetic energy *KE* of a photoelectron emitted from a film under x-ray bombardment (at $h\nu = 1254$ eV) is related to its binding energy in the atom from which it came, E_B, by the relation $E_B = h\nu - KE$. The kinetic energy, measured with an electrostatic hemispherical analyzer, thus identifies the source atom (and electronic transition) of the photoelectron. Since the binding energies of inner shell electrons are perturbed by chemical bonding, accurate measurements of *KE* allow the chemical state of an atom to be determined (e.g., E_B of a C $(1s)$ electron in CO_2 differs from that of a C $(1s)$ electron in CN). The relative intensities of elemental XPS signals relate directly to the elemental concentrations in the sample.

Both HREELS and XPS can thus be used to determine cross sections for the production of particular atomic and molecular species within a film, following electron bombardment. Effective cross sections may then be obtained by measuring how the amplitude of a signal associated with a particular product varies with the integrated electron current at specific electron energies.

4. ELECTRON-INDUCED DISSOCIATION

Below 20 eV, the electron stimulated desorption (ESD) of anions from condensed systems is attributed to DEA, which produces oscillatory structures in the anion yield functions, and to dipolar dissociation (DD), which produces both anionic and cationic fragments. Typically, DD produces as a featureless signal which increases linearly with electron energy from a threshold lying between 10 and 20 eV. Anion desorption data is often dominated by the DEA process. The first observations of DEA in a solid were made from the ESD of O^- from multilayer O_2 films.[31] Subsequently, the O_2 molecule has served as a model target for studying factors affecting the physics of DEA in condensed phase systems.[6]

The yield of O^- from electron impact on gas-phase and multilayer condensed O_2 is shown in Fig. 2a and 2b, respectively. In the gas phase, the O^- signal is dominated by DEA via the $^2\Pi_u$ state of O_2^- at ~6.7 eV (Ref. 32). In contrast, the anion yield function from multilayer O_2 shows, in addition to DD above ~15 eV, a much broader resonance feature between 5 and 10 eV, and a further structure at 13 eV. Both the

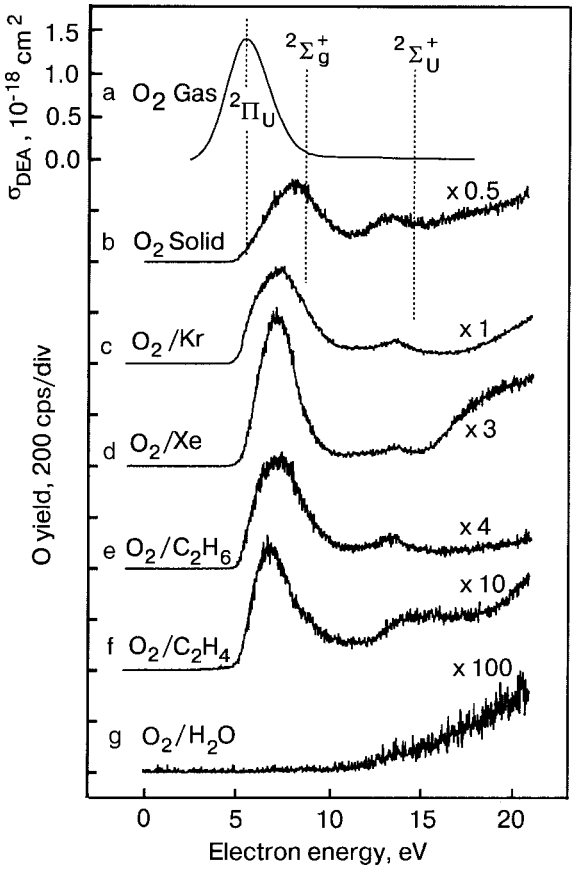

FIG. 2. O^- yield functions for electron impact on gaseous O_2 (a), 4 monolayers (ML) of O_2 (b), and 0.15 ML of O_2 condensed on 4 ML of the indicated substrate (c–g). The dashed lines and bars indicate the known positions of the O_2^- resonances. The gain factor over each curve is relative to curve (c), and the shifted baselines correspond to the zero anion intensity levels. Figure based on the data of Ref. 19.

"broadening" of the lower energy structure and the appearance of the 13 eV structure are attributed to a relaxation of the $\Sigma^- \not\rightarrow \Sigma^+$ selection rule that occurs when the cylindrical symmetry of the molecular wave function is broken by adjacent molecules. The new structures thus correspond to DEA via Σ^+ states between 8 and 10 eV and at 13.5 eV.[33]

Also shown in Fig. 2c–g are the anion yield functions for sub-monolayer quantities of O_2 deposited onto various multilayer atomic and molecular solids. The data represent part of a study[19] on the environmental factors involved in the DEA process. As can be seen, the yield of desorbed ions can vary greatly with substrate composition. These variations were largely attributed to so-called *extrinsic factors* that modify the ESD process at times before attachment and after dissociation, for example electron energy loss processes in the substrate and post-dissociation interactions (PDI) of ions with the surrounding medium. Such processes can be contrasted with *intrinsic factors*, which modify the properties of the resonance (e.g., lifetime, energy, decay channels). In general, the O^- yields per O_2 molecule are higher for O_2 deposited on the rare-gas solids Kr and Xe (Fig. 2c and 2d,—see Ref. 34 for a detailed comparison of O^- desorption from rare-gas solids) than on molecular solids, where extrinsic effects such as electron energy loss processes and PDI are more likely. The weakest O^- signal was observed from O_2 on H_2O (Fig. 2g), which, like the other substrate films, was

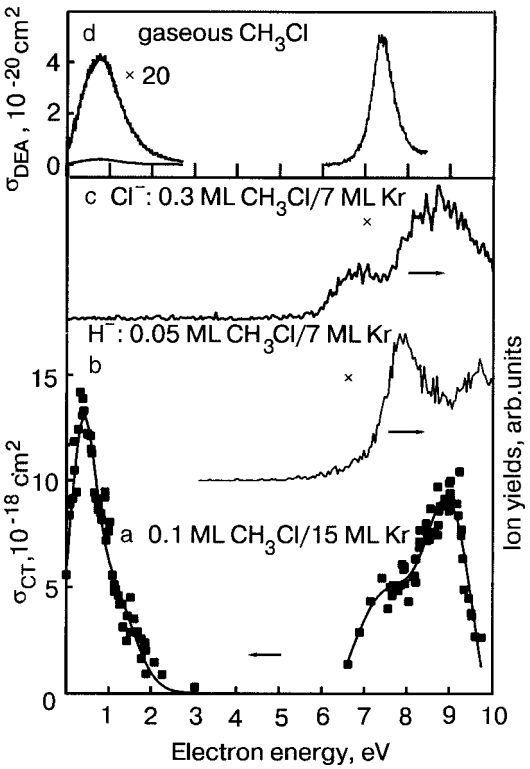

FIG. 3. Charging cross section and anion yields induced by 0–10 eV electron impact on CH_3Cl. (a) Absolute surface charging cross section for 0.1 ML methyl chloride condensed on a 15 ML Kr film. (b) H^- and Cl^- desorption yields from Ref. 41. (c) Total anion yield from gaseous methyl chloride from Ref. 42. Figure taken from Ref. 40.

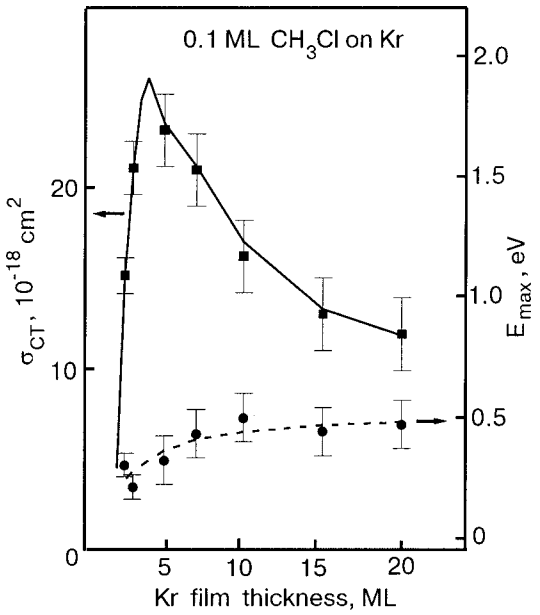

FIG. 4. Variation of maximum of σ_{CT} with Kr film thickness for low-energy electrons incident on 0.1 ML of CH_3Cl deposited on the surface of Kr films. The solid line drawn from the data represents the results of an R-matrix calculation to describe electron–CH_3Cl/Kr scattering. Variation in energy E_{max} of the maximum in σ_{CT} with Kr film thickness. The dashed line is a parametric fit to E_{max} using the image-charge model of Ref. 43 Experimental data taken from Ref. 39.

condensed at a temperature of 20 K. The figure shows that while the DD signal is reduced by approximately a factor of 100 relative to O_2 on Kr, the O^- ESD signal over the energy range associated with DEA is almost entirely absent. Initially this dramatic effect (termed *quenching*) was attributed to some interaction of the transient O_2^- states with the dipole moment of the adjacent water molecules. However, later work[35,36] has shown that amorphous water films formed at 20 K can be highly porous. When O_2 is deposited onto porous ice at 20 K (close to the sublimation temperature of oxygen), it diffuses rapidly over the film's extended surface, so that the effective density of O_2 at the film–vacuum interface is lowered considerably from that obtained when the same quantity is deposited onto a nonporous film. Oxygen ions formed inside the film have a much lower probability of desorption than those generated at the film–vacuum interface since they are more likely to scatter and lose kinetic energy.[37] Thus the signal of desorbed ions derives primarily from DEA to O_2 adsorbed at the film–vacuum interface, and since the number of these latter has been reduced, the desorption signal drops accordingly. Nevertheless, comparisons of O^- ions from O_2 on porous water and benzene films[38] demonstrate that diffusion effects alone are insufficient to explain the startling diminution of signal evidence in Fig. 2g which must therefore derive from a combination of other factors.

The incident-electron energy dependence of the surface charging cross section σ_{CT} for 0.1 ML of CH_3Cl condensed onto a 15-ML Kr film[39,40] is shown in Fig. 3a. The two curves (b) and (c) show the H^- and Cl^- ESD yield functions for a similar quantity of CH_3Cl deposited onto a 7-ML Kr film.[41] No ESD signal was detected below 5 eV. Curve (d) in Fig. 3 is the total anion yield from the gas phase as measured by Pearl and Burrow,[42] and was obtained by subtracting a background signal at 0 eV arising from CCl_4. The 0.8 eV peak in this curve represents a cross section of $(2.0\pm0.4)\times10^{-21}$ cm^2 for anion production, much smaller than the value $(13\pm2)\times10^{-18}$ cm^2 for the 0.5 eV peak in Fig. 3a. Moreover, the origin of this gas-phase structure has been questioned, as the variation of its magnitude with increasing temperature is consistent with the DEA of HCl.[42]

The variation with Kr film thickness of the amplitude (full squares) and energy at maximum (open squares) of the lowest energy charge-trapping cross section feature is shown in Fig. 4. It is apparent that both these quantities are strongly dependent on Kr film thickness. The thickness dependence of the feature's energy is reminiscent of that observed by Michaud and Sanche[43] in the energy of the $^2\Pi_g$ resonance of N_2 on Ar, which was successfully described in terms of the polarizability of the Ar film and the image charge induced in the metal substrate. The lower dashed curve fit to the data uses the same type of function used by Michaud and Sanche to describe the thickness-dependent changes in polarization energy V_p (Ref. 43).

The structure near 0.5 eV in Fig. 3a has been interpreted[39,40] as being due to the formation of Cl^- anions via DEA to the $^2A_1$ state of CH_3Cl^- and the subsequent dissociation of Cl^- and CH_3 along the strongly antibonding C—Cl^- σ^* orbital. Since no ESD signal is observed in Fig. 3b and 3c below 5 eV, the charge-trapping cross section represents an absolute DEA cross section at these low energies. The value reported for CH_3Cl on a 5-ML thick Kr film (Fig. 4) thus represents an enhancement over the gas-phase experimental[42] and theoretical values[44] of between 4 and 6

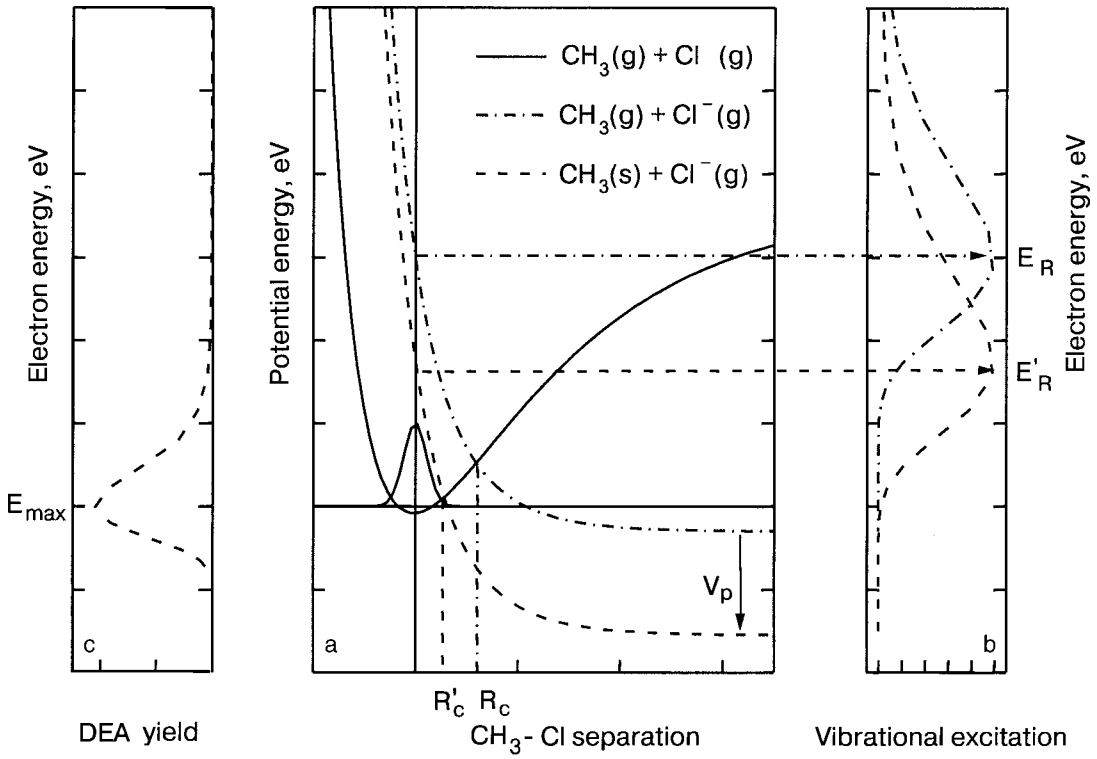

FIG. 5. (a) Effect of polarization energy V_p on the potential energy curves of transient CH_3Cl state, (b) vibration excitation function and (c) DEA yield function. See text for details.

orders of magnitude, respectively. This remarkable enhancement has been attributed to image-charge-induced polarization energy which lowers the potential energy curve of the intermediate transient anion.[39] Similarly, when charging measurements were performed for CH_3Cl molecules sandwiched between Kr layers of variable thickness, where V_p is larger, a further increase of approximately a factor 10 in the DEA cross section was reported.[45]

The process can be qualitatively understood by reference to Fig. 5, which shows idealized potential energy *PE* curves for ground-state CH_3Cl and the $^2A_1$ state of CH_3Cl^- along the C—Cl coordinate. In the gas phase, the $^2A_1$ anion state (the dash-dotted curve in Fig. 5a) lies at a resonance energy $E_R = 3.45$ eV above the neutral ground state in the Franck-Condon region, represented in the figure by the extent of Gaussian-like nuclear wave function. The lifetime is considered too short to allow dissociation of the molecule (the extra electron autodetaches at separations $< R_c$, the crossing point of the anion and neutral curves) but is sufficient to initiate vibrational excitation (panel b) centered at E_R. Upon condensation, the isolated anion's curve is lowered by V_p, to give the *PE* curve for the molecule on the Kr surface (the dashed curve in panel a). The energy of vibrational excitation also shifts by V_p, to a new resonance energy E'_R. Now the new crossing point R'_c of the anion and neutral curves is much closer to the Franck–Condon region, thus reducing the time (and distance) required to dissociate. Some anions thus survive autodetachment to achieve dissociation, but since the process will still favor anions formed at internuclear separations close to R'_c, the maximum in the DEA yield and charge trapping cross section appear at $E_{max} < E'_R$ (panel c). The DEA yield is further enhanced by an increase in anion lifetime that accompanies any decrease in resonance energy as evidenced by changes in the DEA yield of Cl^- ions from gas-phase chloroalkane molecules.[46]

A more quantitative understanding of the effect of V_p on electron attachment to CH_3Cl adsorbed on Kr (Refs. 39 and 40) and within its bulk[45] has been attempted using a modified version of the R-matrix scattering model[44] used with success to describe low-energy electron–CH_3Cl scattering in the gas phase.[47] Essentially the model was modified to include the effects of V_p at short electron–molecule distances. The solid line in Fig. 4 represents the results of the R-matrix calculation. However, to obtain this result it was also necessary to model in semi-empirical fashion the electron's interaction with the metal substrate. The discontinuity represented by the film's surface complicates considerably this type of calculation, which is more straightforward for CH_3Cl embedded within bulk Kr. In this case,[45] good agreement between theory and experiment is possible by adjusting V_p alone. However, it must be noted that the values of V_p required to fit the data for CH_3Cl condensed on and within Kr are approximately 50% larger than those measured elsewhere for Kr films.[43] If these latter values are used, the calculated cross sections are about one order of magnitude too small. This disparity is not the case when comparing similar charging data for CF_3Cl (Ref. 48) with an R-matrix calculation.[49] Comparison of the CH_3Cl and CF_3Cl data and calculations[49] suggest that the CH_3Cl^- *PE* curve may be modified in the Kr environment due to a change of symmetry and/or screening of the CH_3 and Cl^- interaction by the Kr medium at intermediate internuclear separations. Alternatively, Aflatooni and Burrow[43] have suggested that the effective polarization energy seen by CH_3Cl on Kr could indeed be larger than that

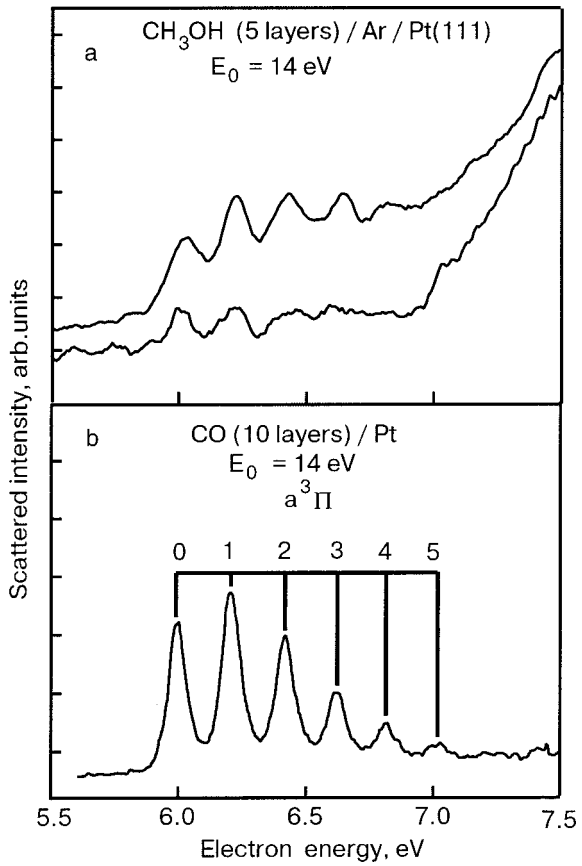

FIG. 6. Electron-energy-loss spectra with 14-eV electrons incident on: (a) a 5-layer film of methanol condensed on an Ar spacer after exposure to small (lower curve) and large (higher curve) electron doses, and (b) a 10-layer film of CO condensed on a platinum substrate. The $a^3\Pi$ excited state of CO is characterized by a vibrational progression having a spacing of about 0.21 eV (Ref. 50).

measured for N_2^- on Kr due to the larger static dipole moment of this molecule.

High-resolution electron energy loss measurements

In two recent papers Lepage, Michaud, and Sanche[50,51] have demonstrated the use of HREELS to measure *in situ* the neutral dissociation products arising from the impact of low-energy electrons on thin physisorbed multilayer films. The technique is similar to that developed earlier by Martel *et al.*,[52] since a single electron beam is used for both the production and detection of the neutral fragments. However, in the experiments of Lepage *et al.*, the neutrals are detected via their electronic excitations, rather than by the spectroscopy of their vibrational levels. This is particularly advantageous in the study of hydrocarbon targets, which often have many strong vibrational losses that can obscure those of the products. Figure 6a shows HREEL spectra of multilayer methanol (CH_3OH) for energy losses in the range 5.5 to 7.5 eV. The incident electron energy was 14 eV. The lower curve in Fig. 6a was taken after 5 mins of electron bombardment of the CH_3OH film. Weak structure is visible in the spectrum at energies below 6.7 eV. The upper curve was recorded after 20 min of exposure to the 14 eV electron beam and shows the evolution of the weak structures into a series of sharp peaks. These peaks correspond almost exactly to the vibrational progression in the lowest electronic state $a^3\Pi$ of condensed CO, shown as recorded for a 10 ML film of pure condensed CO in Fig. 6b.

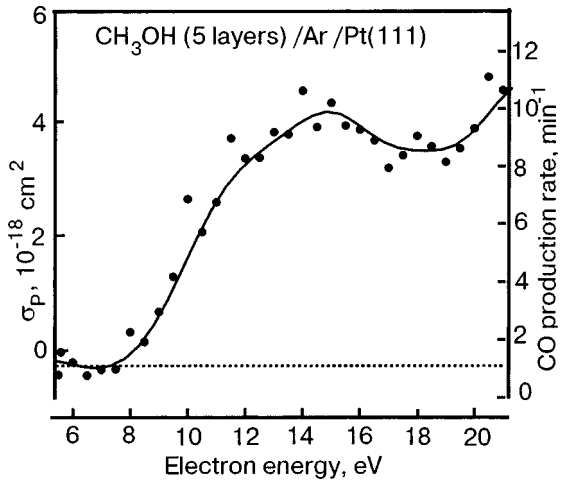

FIG. 7. Electron total scattering cross section σ_p and rate for the production of CO within a 5-layer film of methanol condensed on an Ar spacer as a function of the incident electron energy. The dashed line is the intrinsic minimum rate of CO production due to the measurement at an incident electron energy of 14 eV (Ref. 50).

In their first paper,[50] Lepage, Michaud, and Sanche demonstrated that the appearance of the CO electronic state derives exclusively from the electron-induced fragmentation of condensed methanol molecules. Assuming a uniform electron current density within the electron beam, it can also be shown that for induced CO concentrations below 2% the effective cross section for CO production, σ_p, can be calculated via the formula

$$\sigma_p \cong \frac{n_{\mathrm{CO}} S_0}{n_0 I_0 t}, \tag{7}$$

where I_0 is the incident electron beam current and S_0 is its area; n_0 and n_{CO} are, respectively, the initial number density of target molecules and the number density of CO molecules at time t.

Figure 7 exhipits the incident electron energy dependence of the σ_p and CO production rate as a function of the incident electron energy. The horizontal dashed line represents the intrinsic minimum rate of CO production due to the measurement of the energy loss spectra at 14 eV.

The CO production rate was found to increase linearly with the quantity of deposited methanol, indicating that the CO is generated by the interaction of an electron at a single molecular site, rather than through reactions of fragment species with surrounding (intact) molecules. Processes that could produce CO thus include the following (calculated thermodynamic thresholds for each process are given in parentheses):

$$\mathrm{CH_3OH + e^- \rightarrow CH_3OH^+ + 2e^-}$$
$$\rightarrow \mathrm{H^+ + CO + H_2 + H + 2e^-}, \quad (18.87\ \mathrm{eV}) \tag{8a}$$
$$\rightarrow \mathrm{H_2^+ + CO + H_2 + 2e^-}, \quad (16.22\ \mathrm{eV}) \tag{8b}$$
$$\mathrm{CH_3OH + e^- \rightarrow CH_3OH^- \rightarrow CH_3OH^* + e^-}, \tag{8c}$$
$$\mathrm{CH_3OH^* \rightarrow CO + 4H}, \quad (9.77\ \mathrm{eV}) \tag{8d}$$

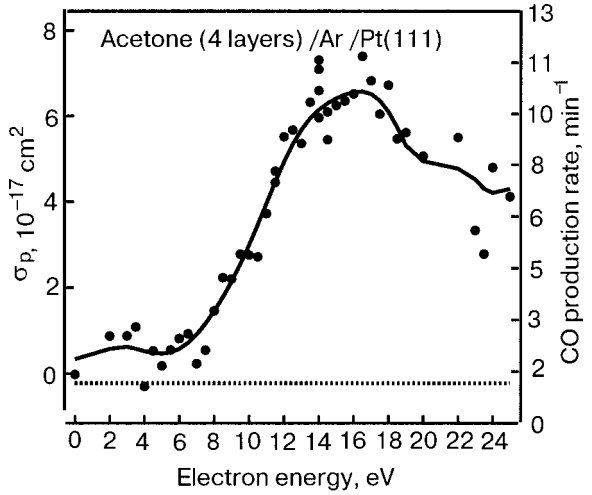

FIG. 8. Electron scattering cross section σ_p and rate for the production of CO within a four-layer film of acetone condensed on an Ar spacer as a function of the incident electron energy. The dashed line is the intrinsic minimum rate of CO production due to the measurement at an incident electron energy of 14 eV. The solid line is a guide to the eye.[51]

$$\rightarrow CO + H_2 + 2H, \quad (5.30\ \text{eV}) \tag{8e}$$

$$\rightarrow CO + 2H_2, \quad (0.80\ \text{eV}) \tag{8f}$$

$$CH_3OH + e^- \rightarrow CH_3OH^- \rightarrow H^- + CO + 3H, \quad (8.97\ \text{eV}) \tag{8g}$$

$$\rightarrow H^- + CO + H_2 + H. \quad (4.50\ \text{eV}) \tag{8h}$$

Ionization processes (8a) and (8b) are not expected to contribute to the CO yield at incident electron energies below ~19 eV, while excitation of neutral repulsive states should produce a CO yield that increases linearly from threshold with E. Consequently, the shape of the CO yield function, visible in Fig. 7, was attributed to the formation of multiple transient anions at these low incident energies. In addition to DEA via long-lived resonances, (8g) and (8h), molecular dissociation is possible via shorter-lived states that decay to neutral repulsive states of CH_3OH. By comparison with the H^- ESD yield functions[53] and vibrational excitation functions[54] for condensed CH_3OH, Lepage and coauthors ascribed the shoulder at 11.5 eV and broad maximum centered at 14.5 eV in Fig. 7 to the $\ldots(6a')^1(3sa')^2$, ^2A, $\ldots(1a'')^1(3sa')^2$, $^2A''$, and $\ldots(5a')^1(3sa')^2$, $^2A'$ core-excited electron resonances, which decay into their parent repulsive states. The rising signal above 19 eV was attributed to direct ionization of CH_3OH.

The same experimental techniques were applied to measure effective cross sections for the electron-induced production of CO from condensed acetone;[51] the results are shown in Fig. 8. The energy dependence of the cross section has a threshold at 8 eV and a strong rise to 14 eV, a broad maximum of $\sigma_p \sim 6.8\times10^{-17}$ cm^2 at 16 eV, followed by a gradual and monotonic decrease to $\sim 4\times10^{-17}$ cm^2 at an energy of 25 eV. Again these measurements indicate that CO is generated by the fragmentation of single molecules by transient anion formation and decay via DEA and/or parent neutral repulsive states of acetone. Definitive statements on the anionic neutral states involved in this process await further experimental measurements.

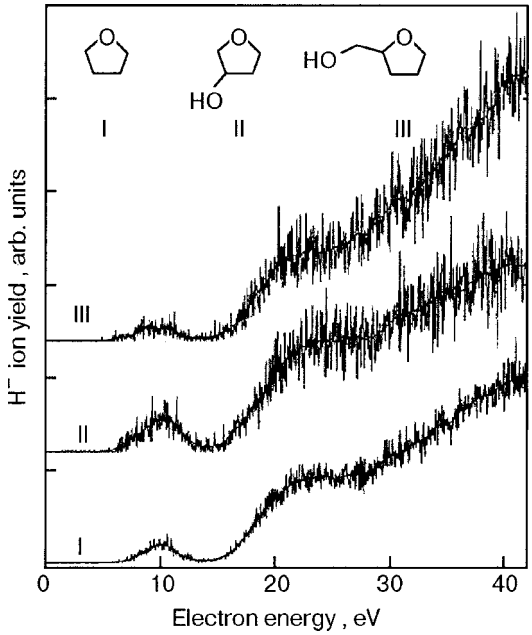

FIG. 9. Comparisons of H- ESD yields produced by impact of 0 to 40-eV electrons on 6-ML-thick films of the DNA backbone sugarlike analog tetrahydrofuran (I), 3-hydroxytetrahydrofuran (II), and α-tetrahydrofurfuryl alcohol (III). The smooth solid lines serve as guides to the eye.[58]

Dissociation of biomolecular targets

Considerable effort has been directed to understanding the genotoxic effects of low-energy electrons in DNA. For example, recent experiments[55] have shown that electrons with energies <5 eV are capable of inducing both single and double strand breaks in super-coiled plasmid DNA. Accurately identifying the mechanisms responsible for this damage requires complementary measurements on simpler molecular targets. The DNA molecule can be considered a molecular assembly consisting of two helical sugar-phosphate backbones, linked together by hydrogen-bonded base pairs (adenine A and thymine T, cytosine Cy and guanine G) and covered by water molecules. Consequently, understanding can be gained by electron-impact experiments with these individual subunits. Of these, condensed water has received the widest attention and our work in this area can be found in Ref. 56 together with references to earlier work. Here we briefly describe recent studies of electron impact on condensed dioxyribose analog[57,58] and DNA bases.[59]

Figure 9 shows the H^- ESD yield functions from multilayer tetrahydrofuran (I), 3-hydroxytetrahydrofuran (II) and α-tetrahydrofurfuryl alcohol (III), together with the chemical identities of these three compounds. These latter were selected for study because of structural similarities with the sugarlike elements of the DNA backbone. For each compound, only H^- was found to desorb under electron impact.[57,58] Similarly, the H^- yield functions for each molecule show a broad peak at 10 eV, which arises from selective dissociation of the C—H bonds and is typical of DEA to hydrocarbon molecules. A second lower-energy resonance near 7.3 eV in II (just visible in the figure) correlated well with a Feshbach resonance observed in solid methanol[60,61] and so was attributed to the DEA to the OH substituent.

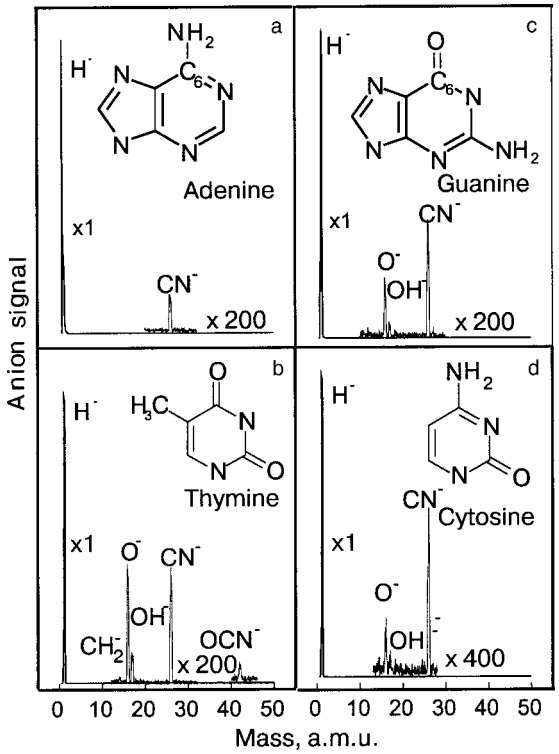

FIG. 10. Masses of stable anions desorbing from 8-monolayer (ML) thick films of adenine (a), thymine (b), guanine (c), and cytosine (d) bombarded by a 500 nA beam current of 20 eV electrons. The chemical structure of each molecule is also given.[59]

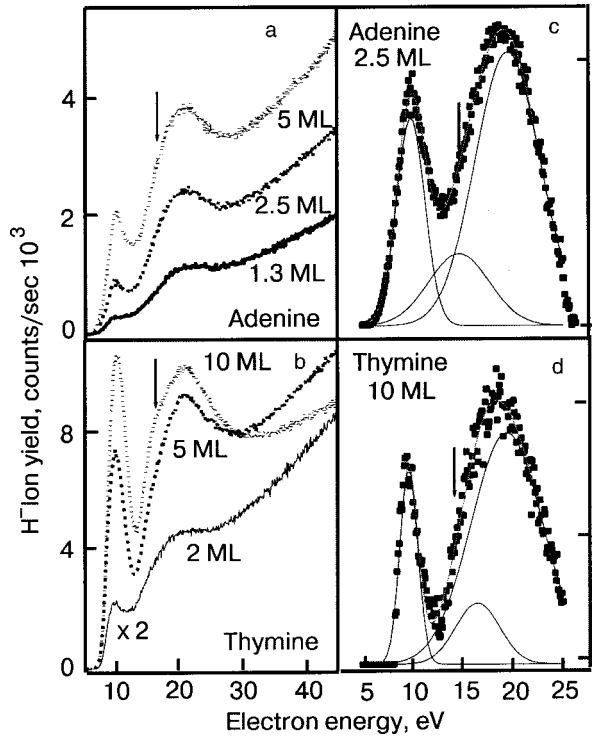

FIG. 11. Electron energy dependence of the H^- ion yield desorbed from adenine (a) and thymine (b), for different film thicknesses or exposure. The arrow indicates the shoulder observed at 14–15 eV incident electron energy. The yield functions of adenine (c) and thymine (d) are obtained by subtracting a linear background from (a) and (b), respectively.[59]

However, no similar Feshbach resonance was observed in the H^- ESD yield from III.

Also apparent in the yield functions of Fig. 9 are broad structures near 23 eV. Measurements of the H^- signal at this energy as a function of coverage of I, II, and III on Ar spacer films[58] show that the 23 eV structure can not be attributed to multiple scattering by incident electrons, but rather to the formation of a resonance lying above the DD threshold. This latter thus decays into an electronic state (or states) that dissociates into H^- and the corresponding positive ion radical.

Electron impact experiments have also been performed on condensed DNA bases[59] and Fig. 10 presents the ESD signal of stable anions desorbed from ~8 ML thick films of adenine, thymine, guanine, and cytosine by a 500 nA beam of 20 eV electrons. Also shown are the chemical identities of these four molecules. The figure demonstrates that in addition to H^- (which is by far the strongest anion signal), electron bombardment produces CN^-, O^-, and OH^- (except for adenine, which does not contain O), and CH_2^-, and OCN^- (only in the case of thymine). Figure 11 presents H^- yield functions for varying quantities of condensed adenine (a) and thymine (b) obtained using a 6 nA electron beam. Curves (c) and (d) were obtained by subtracting a background that increases linearly with energy above a threshold at 10 eV. Readily apparent in both yield functions are two structures at 10 and 20 eV. These are more clearly seen once the background has been subtracted, as is a weak shoulder at 15 eV. The anion yield functions can be effectively fit using three Gaussian functions of widths 3–5 eV at energies close to 10, 15, and 20 eV.

According to *ab initio* calculations,[62] transient anion formation at 8–9 eV and at 14–15 eV in thymine and adenine can be attributed to electron capture by the positive electron affinity of excited states involving excitation of the lone pair $n\rightarrow\pi^*$, $\pi\rightarrow\pi^*$ and/or $\sigma\rightarrow\sigma^*$. Formation of H^- at these energies is likely to occur via dissociation of a core-excited resonance. Furthermore, comparison with gas-phase experiments[63] indicates that H^- production near 10 eV arises from C—H bond cleavage. As with tetrahydrofuran and its derivatives,[57,58] the features at 20 eV are ascribed to the formation of a transient anion and its decay into a dissociative neutral state.

As is seen in Fig. 10, an incident electron currents of 500 nA, weak desorbed signals of heavier anion fragments are observable. Anion yield functions for each fragment were measured, and, as an example of such data, the various CN^- yield functions obtained for the four DNA bases are shown in Fig. 12. Once more the curves display large irregular variations which at energies below ~15 eV can be attributed to molecular fragmentation via DEA.

Sharp resonance features in the CN^- yield functions at 9–10 eV (depending on the molecule) are degenerate with similar structures in the appropriate CH_2^-, OCN^-, O^-, and OH^- yield functions, suggesting that they arise from the formation of the same excited isocyanic anion intermediate $(OCNH)^{*-}$, via close-lying but distinct resonances; i.e., $(G^-, Cy^-, \text{or } T^-)\rightarrow R+(OCNH)^{*-}$, where $(OCNH)^{*-}$ further undergoes fragmentation into different possible dissociative channels: $CN^-+(O+H)$, OH^-+CN or $O^-+(CNH)$. Alternatively, the coincidence of the peak at 9.0 and 10 eV in the yield function of CN^-, OH^-, and O^- ions from Cy or G and T, respectively, may indicate that they are

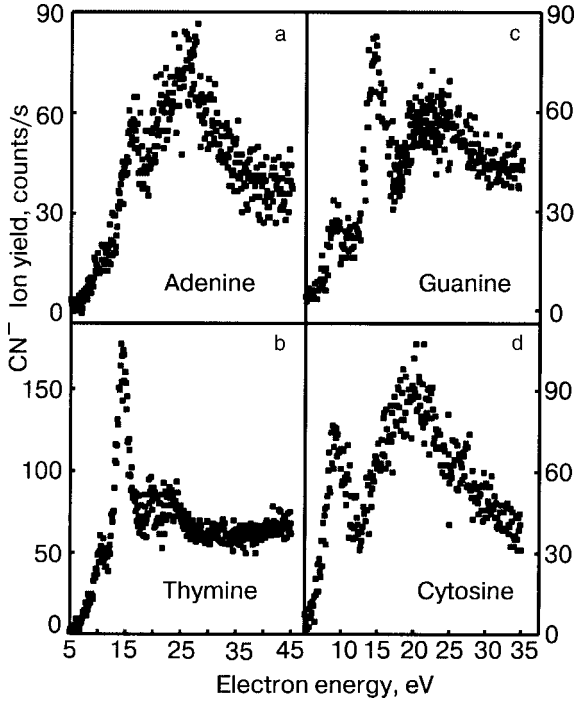

FIG. 12. Incident electron energy dependence of CN^- ion yields desorbed under 500 nA electron bombardment of 8-ML-thick films of adenine (a), thymine (b), guanine (c), and cytosine (d).[59]

induced via a single predissociative resonance, as suggested in the case of gas-phase bromouracil.[64] Such a mechanism would then involve a crossing or saddle point in the multidimensional potential energy surface of the electronically excited state of cytosine, guanine, or thymine anions, along the OCN^--(radical), O^--(radical), and CN^--(radical) coordinates. However, irrespective of the detailed dissociation mechanisms, the desorption of these heavier anions demonstrates that, apart from exocyclic rupture of C—H bonds, low-energy electrons can initiate complex multibond ring dissociation.

5. REACTIONS INITIATED FOLLOWING DISSOCIATION

Reactive scattering

Reactive scattering by DEA fragment ions in condensed media was first noted in the form of OH^- electron-stimulated desorption yields from O_2 embedded in multilayer alkane films[65] and subsequently for aniline physisorbed on top of O_2 solids.[66] The O^- anion produced following DEA to N_2O has also been observed to react with other N_2O molecules within an Ar/N_2O matrix, to generate a desorbed yield of NO^- and NO_2^-, among other products.[67] Part of the H_2 ESD yield observed from multilayer films of H_2O at incident electron energies below 10 eV has also been attributed to proton abstraction by DEA H^- fragments, viz., $H^- + H_2O \rightarrow \{H_3O\}^{*-} \rightarrow H_2 + OH^-$ (Ref. 68), and has thus been associated with part of the unscavengeable H_2 yield formed in water radiolysis.[69] Another (post-DEA) ion–molecule reaction directly observed in the condensed phase for ion kinetic energies well below 5 eV is isotope exchange measured in $^{18}O_2/C^{16}O$ mixed solids,[70] i.e., $^{18}O^- + C^{16}O \rightarrow \{C^{18}O^{16}O\}^{*-} \rightarrow {}^{16}O^- + C^{18}O$. Formation of D_2O in synchrotron-irradiated films of N_2O has also been attributed to associative electron attachment reactions of DEA O^- fragments with matrix D_2 molecules, i.e., $O^- + D_2 \rightarrow D_2O^{*-} \rightarrow D_2O + e^-$ (Ref. 71). Measurements of electron stimulated O_3 production in condensed O_2 films were attributed to post-dissociation reactions of neutral $O(^3P$, or $^1D)$ with adjacent molecules.[72] The threshold energy for this process, being near 3.5 eV, allowed DEA to be identified as the source of $O(^3P)$ at low incident electron energies. Similarly, Azria and co-workers[73] in their measurements of F^- and Cl^- desorption from condensed CF_2Cl_2 have observed the appearance of new features in the Cl^- yield function at long bombardment times. These changes were attributed to the synthesis of Cl_2 in the condensed phase by an as yet unidentified reaction pathway having DEA to CF_2Cl_2 as its initial step. More recently, Tegeder and Illenburger[74] have shown by comparison of anion ESD data and infrared absorption–reflection spectroscopy that DEA is the initial step in the production of N_2F_4 molecules within NF_3 films under bombardment with 0 to 5 eV electrons.

In our initial studies of anion desorption from solid O_2/hydrocarbon mixtures,[65] several observations were made concerning the desorbed signal of OH^-. (1) The OH^- yield functions resembled more closely the yield functions of O^- with $E_k \geqslant 1.5$ eV from pure O_2 films than the H^- signal associated with DEA to the hydrocarbon molecule. (2) The OH^- signal from an O_2 film increases linearly with alkane surface coverage below 1 ML, and (3) the threshold in energy for OH^- desorption coincided with that for O^- desorption, which is at least 2 eV below the onset of H^- desorption. For these reasons, and the fact that O_2^- is the only charged product observed in the gas-phase collisions of H^- with O_2 (Ref. 75), the OH^- desorption signal was attributed to hydrogen abstraction reactions of the type

$$O^- + C_nH_m \rightarrow C_nH_mO^{*-} \rightarrow OH^- + C_nH_{m-1}.$$

The existence of such a $C_nH_mO^{*-}$ intermediate anion collision complex had previously been suggested by Comer and Schulz,[76] who measured the energies of electrons emitted during gas-phase collisions of O^- with C_2H_4. Further evidence for complex anion formation and reactive scattering in the gas phase can be seen in the studies of Parkes[77] and Lindinger.[78]

More-recent measurements[79] reproduced in Fig. 13 show an enhanced H^- signal at *low E* from the O_2/C_4H_{10} mixed films, which varies greatly with film composition. Two trends can be observed in Fig. 13a with increasing O_2 concentration. First, there is a decrease in the yield of H^- at 10 eV, the peak energy of H^- production via direct DEA to the alkane molecule. Second, there is the appearance and development of a second H^- ESD structure at lower energies, such that at an O_2 concentration of 20% a substantial fraction of the H^- yield occurs *at incident electron energies significantly below those required for DEA to* C_4H_{10}. In Fig. 13b the H^- yield function from a *n*-butane film containing 10% O_2 by volume (curve *1*) is resolved into two separate components. One, located at 10 eV, is assumed identical in form to that of H^- desorption from pure C_4H_{10}. The other (bold curve *2*) is obtained from curve *1* when the H^- signal from a pure film normalized to curve *1* at 10 eV (dotted line) is removed. This procedure yields a second quasi-Gaussian-

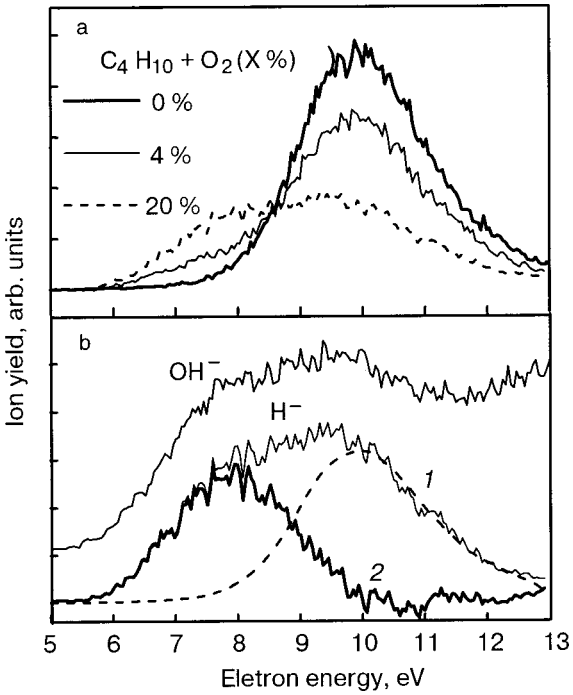

FIG. 13. (a) The H^- yield function from 4-ML-thick films of a O_2/C_4H_{10} mixture of increasing percentage volume concentration of O_2. (b) The H^- signal from a 4-ML-thick mixture of 10% O_2 in C_4H_{10} can be resolved into two components: one centered at 10 eV, associated with H^- production via DEA to the alkane (dotted line) and another at 7.8 eV, associated with reactive scattering of O^- ions (bold line). Also shown is the yield of OH^- ions from the same film.[79]

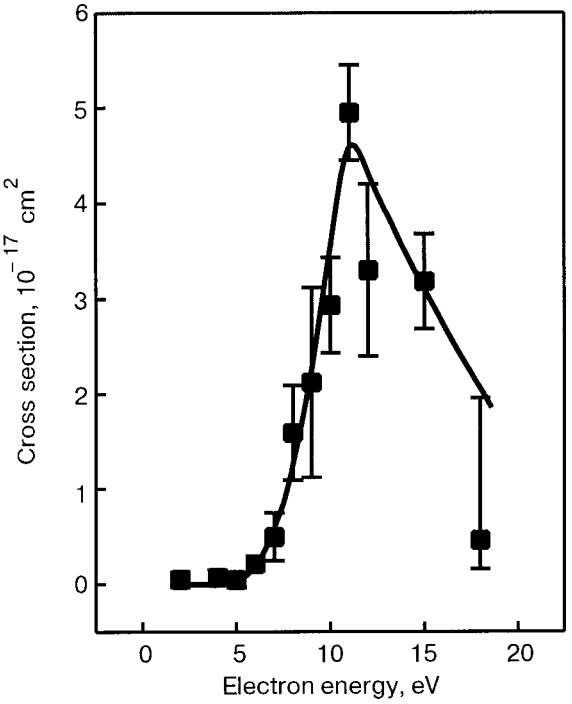

FIG. 14. Experimental cross sections for the electron induced oxidation of the a-H:Si(111) surface as a function of incident electron energy as obtained in Refs. 80 and 81. The solid line is drawn to guide the eye.

shaped structure centered at 7.8 eV, close to the energy of maximum production of O^- via DEA and with a threshold at 5.5 eV, identical to that observed for OH^- production. From these observations, the increase in H^- production at incident electron energies below the threshold for DEA to C_4H_{10} was attributed to reactive scattering of O^- ion and atom-exchange reactions of the type

$$O^- + C_4H_{10} \rightarrow C_4H_{10}O^{*-} \rightarrow H^- + C_4H_9O,$$

involving the same or similar transient anions as those responsible for OH^- production. Evidence for additional channels in the decay of such $C_nH_mO^{*-}$ anions was apparent in the anion yield functions of CH^- and CH_2^- from thin films of C_2H_4/O_2 mixtures[79] as a sub-direct DEA threshold component to the anion signals.

Electron-induced reactions of adsorbates and substrates

X-ray photoelectron spectroscopy has been used to analyze modifications induced by 2 to 20 eV electrons incident on a hydrogen-passivated and sputtered Si(111) surface, onto which thin films of H_2O (Refs. 80 and 81) and (Ref. 82) CF_4 had been *physisorbed*. In both cases, following the electron-induced dissociation of the molecular adsorbate a new XPS signal associated with the *chemisorption* of either O or F onto the Si surface was observed. Cross sections for this process can be obtained from the relation,

$$I(\Phi) = I(\infty)[1 - \exp(-\sigma_{CH}\Phi/A)]. \quad (9)$$

Here, $I(\Phi)$ represents the energy-integrated intensity of the XPS chemisorption feature following a dose of Φ electrons over an area A of the sample, $I(\infty)$ is the (saturated) signal at high doses, and σ_{CH} is the cross section for the chemisorption reaction.

The effective cross section for electron-induced chemisorption of oxygen from a H_2O bilayer onto a hydrogen-passivated Si(111) surface is shown in Fig. 14 as a function of incident electron energy.[80,81] The data were obtained by monitoring the evolution of chemisorbed O 1*s* in the XPS spectra and a subsequent fitting to Eq. (9). The low value of the energy threshold for the chemisorption process (i.e., 5.2 eV) has been interpreted as being due to the formation of OH via the DEA process

$$H_2O[X] - e^- \leftrightarrow H_2O^-[^2B_1, A_1] \rightarrow H^-[^2S_0] + OH[^2\Pi]$$

and its subsequent reaction with the surface, viz.,

$$Si_3 - Si - H + OH \rightarrow Si_3 - Si - OH + H.$$

The chemisorption process has its maximum cross section at ~11 eV, in contrast with the cross sections for the radiolysis of bulk ice. This difference was understood as being dependent on the selective quenching of dissociative electronic states of water due to the resonant charge exchange between the substrate and adsorbate and the absence of multiple inelastic scattering in the H_2O bilayer on Si(111).[80,81]

A similar XPS study has been performed for ~1 ML of CF_4 deposited onto the same hydrogen-passivated Si substrate,[82] the results of which are shown in Fig. 15. Comparisons with gas-phase results[83] and with measurements of ESD[84] and the charge-trapping cross section[85] (this latter is included in Fig. 15) clearly demonstrate that for this molecule the chemisorption of F^--containing species is dependent on the DEA reactions

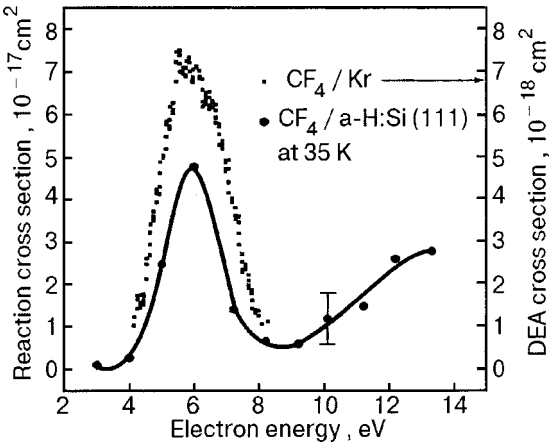

FIG. 15. Experimental cross section for the electron-induced reaction of the H:Si(111) surface with physisorbed CF_4 as a function of electron energy.[82] The solid line is drawn as a guide to the eye. Also shown is the total DEA cross section for CF_4 on Kr, as measured by Bass *et al.*[85]

$$CF_4 + e^- \rightarrow CF_4 \rightarrow F^- + CF_3,$$

$$CF_4 + e^- \rightarrow CF_4 \rightarrow F + CF_3^-$$

as a initial step to further reactions of fragments with the Si substrate.

6. CONCLUSIONS

The data presented in this article illustrate how cryogenics and electron impact techniques may be used to study electron-driven reactions in a number of molecular solid and adsorbate/substrate systems. The simplicity of the experimental approach has allowed certain general observations to be made.

At incident electron energies below ~20 eV the formation of transient negative ions plays an important role in molecular dissociation, via DEA and/or populating neutral dissociative states.

The DEA and ESD processes are affected by environmental factors such as film morphology and composition, which can modulate electron scattering prior to electron attachment and/or affect molecular fragments after dissociation.

Electron-induced dissociation is a general process observed even for multilayer films of molecules of biological significance such as tetrahydrofuran and the DNA bases.

Dissociation may involve significant molecular rearrangement, sufficient to break apart cyclic molecules.

Molecular fragment species may react with surrounding molecules or with a supporting substrate.

From the wide range of molecular solids investigated, it has been shown that the combination of cryogenic techniques and electron impact methods can provide meaningful information for understanding radiation and particle-beam-induced damage in the molecular components of DNA as well as other simpler systems. Such a comprehension has applications (or implications) for diverse fields, ranging from the electron-beam modification of organic SAMS[3] to ozone depletion.[86,87] Unsurprisingly, there is also much current interest in using this experimental approach to mimic conditions in space and so to investigate radiation-induced chemistry occurring at the surfaces of various heavenly bodies.[88]

In the future, electron-impact measurements will be extended to solid targets of progressively greater molecular complexity (i.e., large polymeric materials such as proteins) or compositional complexity (i.e., solids containing more than one or two chemical components). Greater emphasis will also likely be placed on following the reactive steps succeeding electron-induced dissociation, using techniques such as HREELS, and thus tracing the relationship between the initial products of electron impact (or irradiation, etc.,) and those observed at long times.

We gratefully acknowledge the cooperation and contributions of many colleagues in Sherbrooke and elsewhere, without whom this work was not have been possible. This research was supported by the Canadian Institutes of Health Research and by the National Cancer Institute of Canada.

*E-mail: Andrew.Bass@Usherbrooke.ca
**Canada Chair in the Radiation Sciences

[1] L. Sanche, IEEE Trans. Electr. Insul. **28**, 789 (1993).
[2] Jong-Liang Lin, C. Singh Bhatia, and John T. Yates, Jr., J. Vac. Sci. Technol. A **13**, 163 (1995); Jong-Liang Lin and John T. Yates, Jr., *ibid.* **13**, 1867 (1995).
[3] S. Frey, K. Heister, M. Zharnikov, and M. Grunze, Chem. Phys. **2**, 1979 (2000); J. E. Hernandez, H. Ahn, and J. E. Whitten, J. Phys. Chem. B **105**, 8339 (2001).
[4] D. Syomin, J. Kim, B. E. Koel, and G. B. Ellison, J. Phys. Chem. B **105**, 8387 (2001).
[5] V. Cobut, Y. Frongillo, J. P. Patau, T. Goulet, M.-J. Fraser, and J.-P. Jay-Gerin, Radiat. Phys. Chem. **51**, 229 (1998).
[6] L. Sanche, Scanning Microsc. **9**, 619 (1995).
[7] A. D. Bass and L. Sanche, Radiat. Environ. Biophys. **37**, 243 (1998).
[8] L. Sanche, Surf. Sci. **451**, 81 (2000).
[9] J. Franck and G. Hertz, Verh. Dtsch. Phys. Ges. **16**, 512 (1914).
[10] G. J. Schulz, Rev. Mod. Phys. **45**, 378 (1973).
[11] G. F. Hanne, Am. J. Phys. **56**, 696 (1988).
[12] P. Rowntree, H. Sambe, L. Parenteau, and L. Sanche, Phys. Rev. B **47**, 4537 (1993).
[13] L. Sanche, J. Phys. C **13**, L677 (1980).
[14] Ph. Avouris and R. E. Walkup, Annu. Rev. Phys. Chem. **40**, 173 (1989).
[15] T. F. O'Malley, Phys. Rev. **150**, 14 (1966).
[16] L. Sanche, J. Chem. Phys. **71**, 4860 (1979).
[17] G. Perluzzo, G. Bader, L. G. Caron, and L. Sanche, Phys. Rev. Lett. **55**, 545 (1985).
[18] M.-A. Hervé du Penhoat, M. A. Huels, P. Cloutier, J.-P. Jay-Gerin, and L. Sanche, J. Chem. Phys. **114**, 5755 (2001).
[19] M. A. Huels, L. Parenteau, and L. Sanche, J. Chem. Phys. **100**, 3940 (1994).
[20] S. Wurm, P. Feulner, and D. Menzel, Surf. Sci. **400**, 155 (1998); M. Scheuer, D. Menzel, and P. Feulner, *ibid.* **390**, 23 (1997).
[21] G. A. Kimmel, T. M. Orlando, C. Vezina, and L. Sanche, J. Chem. Phys. **101**, 3282 (1994); G. A. Kimmel and T. M. Orlando, Phys. Rev. Lett. **75**, 2606 (1995).
[22] T. D. Harries, D. H. Lee, M. Q. Blumberg, and C. R. Arumainaygam, J. Phys. C **99**, 9530 (1995).
[23] For example: P. Rowntree, C. Dugal, D. Hunting, and L. Sanche, J. Phys. C **100**, 4546 (1996); H. Abdoul-Carime, P.-C. Dugal, and L. Sanche, Radiat. Res. **153**, 23 (2000) (and references therein).
[24] G. Leclerc, A. D. Bass, A. Mann, and L. Sanche, Phys. Rev. B **46**, 4865 (1992).
[25] A. Stomatovic and G. J. Schulz, Rev. Sci. Instrum. **41**, 423 (1970).
[26] R. M. Marsolais, M. Deschenes, and L. Sanche, Rev. Sci. Instrum. **60**, 2724 (1989).
[27] K. Nagesha, J. Gamache, A. D. Bass, and L. Sanche, Rev. Sci. Instrum. **68**, 3883 (1997).
[28] M. Michaud and L. Sanche, Phys. Rev. B **30**, 6067 (1984).
[29] M. Michaud, P. Cloutier, and L. Sanche, Rev. Sci. Instrum. **66**, 2661 (1995).

[30] D. Briggs and M. P. Seah, *Pratical Surface Analysis, Auger and X-ray Photoelectron Spectroscopy* 2nd, D. Briggs and M. P. Seah (Eds.) John Wiley, Chichister, U.K., Vol. 1 (1990).
[31] L. Sanche, Phys. Rev. Lett. **53**, 1638 (1984).
[32] R. J. Van Brunt and L. J. Kieffer, Phys. Rev. A **2**, 1899 (1970).
[33] R. Azria, L. Parenteau, and L. Sanche, Phys. Rev. Lett. **59**, 638 (1987).
[34] M. N. Hedhili, L. Parenteau, M. A. Huels, R. Azria, M. Tronc, and L. Sanche, J. Chem. Phys. **107**, 7577 (1997).
[35] K. P. Stevenson, G. A. Gimmel, Z. Dohnalek, R. S. Smith, and B. D. Kay, Science **283**, 1501 (1999); P. Ayotte, R. Scott Smith, K. P. Stevenson, Z. Dohnálek, G. A. Kimmel, and B. D. Kay, J. Geophys. Res. **106**, 33387 (2001) (and references therein).
[36] E. Vichnevetski, A. D. Bass, and L. Sanche, J. Chem. Phys. **113**, 3874 (2000).
[37] R. Azria, Y. LeCoat, M. Lachgar, M. Tronc, L. Parenteau, and L. Sanche, Surf. Sci. **436**, L671 (1999); *ibid.* **451**, 91 (2000).
[38] A. D. Bass, L. Parenteau, F. Weik, and L. Sanche, J. Chem. Phys. **115**, 4811 (2001).
[39] L. Sanche, A. D. Bass, P. Ayotte, and I. I. Fabrikant, Phys. Rev. Lett. **75**, 3568 (1995).
[40] P. Ayotte, J. Gamache, A. D. Bass, I. I. Fabrikant, and L. Sanche, J. Chem. Phys. **106**, 749 (1997).
[41] P. Rowntree, L. Sanche, L. Parenteau, M. Meinke, F. Weik, and E. Illenberger, J. Chem. Phys. **101**, 4248 (1994).
[42] D. M. Pearl and P. D. Burrow, Chem. Phys. Lett. **206**, 483 (1993).
[43] M. Michaud and L. Sanche, J. Electron Spectrosc. Relat. Phenom. **51**, 237 (1990).
[44] I. I. Fabrikant, J. Phys. B **24**, 2213 (1991); J. Phys. B **27**, 4325 (1994).
[45] I. I. Fabrikant, K. Nagesha, R. Wilde, and L. Sanche, Phys. Rev. B **56**, R5725 (1997).
[46] D. M. Pearl and P. D. Burrow, J. Chem. Phys. **101**, 2940 (1994); K. Aflatooni and P. D. Burrow, *ibid.* **113**, 1455 (2000).
[47] D. M. Pearl, P. D. Burrow, I. I. Fabrikant, and G. A. Gallup, J. Chem. Phys. **102**, 2737 (1995).
[48] K. Nagesha and L. Sanche, Phys. Rev. Lett. **78**, 4725 (1997).
[49] K. Nagesha, I. I. Fabrikant, and L. Sanche, J. Chem. Phys. **114**, 4934 (2001).
[50] M. Lepage, M. Michaud, and L. Sanche, J. Chem. Phys. **107**, 3478 (1997).
[51] M. Lepage, M. Michaud, and L. Sanche, J. Chem. Phys. **113**, 3602 (2000).
[52] R. Martel, A. Rochefort, and P. H. McBreen, J. Am. Chem. Soc. **116**, 5965 (1994).
[53] L. Parenteau, J.-P. Jay-Gerin, and L. Sanche, J. Phys. Chem. **98**, 10277 (1994).
[54] A. T. Wen, M. Michaud, and L. Sanche, Phys. Rev. A **54**, 4162 (1996); A. T. Wen, M. Michaud, and L. Sanche, J. Electron Spectrosc. Relat. Phenom. **94**, 23 (1998).
[55] B. Boudaiffa, P. Cloutier, D. Hunting, M. A. Huels, and L. Sanche, Science **287**, 1658 (2000).
[56] W. C. Simpson, M. T. Sieger, G. A. Kimmell, K. Nagesha, L. Parenteau, T. M. Orlando, and L. Sanche, J. Chem. Phys. **108**, 5027 (1998); W. C. Simpson, M. T. Sieger, G. A. Kimmel, L. Parenteau, L. Sanche, and T. M. Orlando, *ibid.* **107**, 8668 (1997).
[57] D. Antic, L. Parenteau, M. Lepage, and L. Sanche, J. Phys. Chem. B **103**, 6611 (1999).
[58] D. Antic, L. Parenteau, and L. Sanche, J. Phys. Chem. B **104**, 4711 (2000).
[59] H. Abdoul-Carime, P. Cloutier, and L. Sanche, Radiat. Res. **155**, 625 (2001).
[60] M. Michaud, M.-J. Fraser, and L. Sanche, J. Chem. Phys. **91**, 1223 (1994).
[61] L. Parenteau, J.-P. Jay-Gerin, and L. Sanche, J. Phys. Chem. **98**, 10277 (1994).
[62] S. Peng, A. Padva, and P. R. LeBreton, Proc. Natl., Acad. Sci. USA **73**, 2966 (1976); C. Yu, S. Peng, I. Akiyama, J. Lin, and P. R. LeBreton, J. Am. Chem. Soc. **100**, 2303 (1978); J. Lin, C. Yu, S. Peng, I. Akiyama, K. Li, Li Kao Lee, and P. R. LeBreton, J. Phys. Chem. **84**, 1006 (1980).
[63] M. A. Huels, I. Hahndorf, E. Illenburger, and L. Sanche, J. Chem. Phys. **108**, 1309 (1998).
[64] H. Abdoul-Carime, M. A. Huels, F. Bruning, E. Illenberger, and L. Sanche, J. Chem. Phys. **113**, 2517 (2000).
[65] L. Sanche and L. Parenteau, Phys. Rev. Lett. **59**, 136 (1987); J. Chem. Phys. **93**, 7476 (1990).
[66] M. A. Huels, L. Parenteau, and L. Sanche, Chem. Phys. Lett. **279**, 223 (1998).
[67] L. Sanche and L. Parenteau, J. Chem. Phys. **90**, 3402 (1989).
[68] G. A. Kimmel, T. M. Orlando, C. Vezina, and L. Sanche, J. Chem. Phys. **101**, 3282 (1994).
[69] V. Cobut, J.-P. Jay-Gerin, Y. Frongillo, and J. P. Patau, Radiat. Phys. Chem. **47**, 247 (1996).
[70] R. Azria, L. Parenteau, and L. Sanche, Chem. Phys. Lett. **171**, 229 (1990).
[71] D. M. Hanson, *Abstracts of the 46th Annual Meeting of the Radiat. Res. Soc.* Louisville, KY (1998), p. 86.
[72] S. Lacombe, F. Cemic, K. Jacobi, M. N. Hedhili, Y. Le Coat, R. Azria, and M. Tronc, Phys. Rev. Lett. **79**, 1146 (1997).
[73] M. N. Hedhili, M. Lachgar, Y. Le Coat, R. Azria, M. Tronc, Q. B. Lu, and T. E. Madey, J. Chem. Phys. **114**, 1844 (2001).
[74] P. Tegeder and E. Illenberger, Chem. Phys. Lett. **341**, 401 (2001).
[75] M. S. Huq, L. D. Doverspike, and R. L. Champion, Phys. Rev. A **27**, 785 (1983).
[76] J. Comer and G. L. Schulz, Phys. Rev. A **10**, 2100 (1974).
[77] D. A. Parkes, J. Chem. Soc., Faraday Trans. **168**, 613 (1972).
[78] W. Lindinger, D. L. Albritton, F. C. Fehsenfeld, and E. E. Fergusson, J. Chem. Phys. **63**, 3238 (1975).
[79] A. D. Bass, L. Parenteau, M. A. Huels, and L. Sanche, J. Chem. Phys. **109**, 8635 (1998).
[80] D. Klyachko, P. Rowntree, and L. Sanche, Surf. Sci. **346**, L49 (1996).
[81] D. Klyachko, P. Rowntree, and L. Sanche, Surf. Sci. **389**, 29 (1997).
[82] W. Di, P. Rowntree, and L. Sanche, Phys. Rev. B **52**, 16618 (1995).
[83] T. Oster, A. Kuhn, and E. Illenberger, Int. J. Mass Spectrom. Ion Processes **89**, 1 (1989).
[84] M. Meinke, L. Parenteau, P. Rowntree, L. Sanche, and E. Illenberger, Chem. Phys. Lett. **205**, 213 (1993).
[85] A. D. Bass, J. Gamache, L. Parenteau, and L. Sanche, J. Phys. Chem. **99**, 6123 (1995).
[86] Q.-B. Lu and L. Sanche, Phys. Rev. Lett. **87**, 078501 (2001).
[87] Q. B. Lu and L. Sanche, Phys. Rev. B **63**, 153403 (2001).
[88] T. E. Madey, R. E. Johnson, and T. M. Orlando, Surf. Sci. **500**, 838 (2002).

This article was published in English in the original Russian journal. Reproduced here with stylistic changes by AIP.

Effects of electron irradiation on structure and bonding of SF_6 on Ru(0001)

N. S. Faradzhev, D. O. Kusmierek, B. V. Yakshinskiy, and T. E. Madey*

Department of Physics and Astronomy and Laboratory for Surface Modification, Rutgers University, 136 Frelinghuysen Rd., Piscataway, NJ 08854-8019, USA
(Submitted July 22, 2002; revised August 14, 2002)
Fiz. Nizk. Temp. **29**, 286–295 (March 2003)

Electron-stimulated desorption ion angular distribution (ESDIAD) and temperature-programmed desorption (TPD) techniques have been employed to study radiation-induced decomposition of fractional monolayer SF_6 films physisorbed on Ru(0001) at 25 K. Our focus is on the origin of F^+ and F^- ions, which dominate ESD from fractional monolayers. F^- ions escape only in off-normal directions and originate from undissociated molecules. The origins of F^+ ions are more complicated. The F^+ ions from electron-stimulated desorption of molecularly adsorbed SF_6 desorb in off-normal directions, in symmetric ESDIAD patterns. Electron beam exposure leads to formation of SF_x $(x=0-5)$ fragments, which become the source of positive ions in normal and off-normal directions. Electron exposure $>10^{16}$ cm^{-2} results in decomposition of the entire adsorbed SF_6 layer. © *2003 American Institute of Physics.*
[DOI: 10.1063/1.1542442]

1. INTRODUCTION

As part of a program to study radiation-induced processes in adsorbed fluorine and chlorine-containing molecules,[1–4] we are examining electron stimulated desorption (ESD) of SF_6 adsorbed on a single crystal metal surface. This program of study has several components, including: 1) the study[5] of the structure and reactivity of SF_6 on a clean Ru(0001) surface; 2) the influence of coadsorbed atoms and molecules in ESD of SF_6 (including a search for enhancement of the F^- ESD signal[1–3]); 3) electron beam damage processes in the adsorbed layer. The present paper focuses on the last: the effects of electron bombardment on the structure and bonding of SF_6, as revealed by changes in F^+ and F^- ESD yields and angular distributions.

Sulfur hexafluoride SF_6 is a highly symmetric, inorganic, chemically inert, man-made molecule. The sulfur atom resides at the center of a regular octahedron, whose corners are occupied by the six fluorine atoms. SF_6 has a positive electron affinity, whose presently accepted value is $\sim 1.06 \pm 0.06$ eV.[6] Based upon studies of low-energy electron interactions with gaseous SF_6, it is known that gaseous SF_6 attaches thermal and near-thermal electrons, with a very large cross section, to become SF_6^-. This ability to capture thermal electrons makes SF_6 popular for technical applications as an electron scavenger in high-voltage electrical devices.[7] SF_6 is also used as a dry-etching gas in plasma processing[8] and is known to be a greenhouse gas.

Previous experiments with SF_6 adsorbed on Ru(0001) (Ref. 9) and Ni(111) (Ref. 10) indicate that SF_6 is physisorbed on the metal surface. Based upon the structure of SF_6 and of Ru(0001), it was argued that the molecule should be oriented so that one set of three F atoms is in contact with the substrate and the other set of three F atoms lies in a plane parallel to the surface facing the vacuum. Since the threefold symmetry of SF_6 coincides to such a large degree with the symmetry of the (0001) plane of hcp Ru, preferred adsorption sites and some degree of ordering of the molecule are highly probable.

ESD of adsorbed molecules implies desorption of neutral fragments (atoms and molecules) as well as both positive and negative ions. Electron-stimulated desorption ion angular distribution (ESDIAD) is a very useful technique for determining the bonding structure of molecules adsorbed on single-crystal surfaces,[11] since the trajectory of the desorbing particle is determined mainly by the orientation of the bond that is broken. ESDIAD also has a great utility for providing insights into the structure and dynamics of decomposition of adsorbed molecules under electron bombardment:[12] distinct electron-induced changes in the ESDIAD patterns and intensities of specific ions can be monitored and analyzed. In this paper we concentrate on both F^+ and F^- ions produced by ESD of a fractional SF_6 layer (0.25 ML) adsorbed on a Ru(0001) substrate (because of the high electron affinity of the F atom, we expect a strong F^- signal in ESD).

In the gas phase, the low-energy dissociative electron attachment (DEA) resonance that leads to F^- formation is due to the reaction

$$e^-(2.7\ \text{eV}) + SF_6 \rightarrow F^- + SF_5 .$$

The thermodynamic threshold is 0.65 eV.[7] In the condensed phase, the F^- signal is dominated by two resonant features, with maxima at 5.8 eV and $\sim$11 eV. A very weak signal is also detected between 1 and 3 eV (Ref. 7).

In the gas phase, electron-induced dissociation of SF_6 leading to the formation of positive ions becomes significant above $\sim$16 eV, producing SF_x^+ $(x=1,3,4,5)$ and F^+ (Ref. 6). Measurements of electron impact dissociative ionization of gaseous SF_6 give the threshold energy for F^+ formation somewhere in the range of 30–50 eV,[13,14] very different from F^-. The comparison of ESDIAD images for F^+ and F^- should provide insights into the mechanisms of ion formation.

In order to understand better the behavior of adsorbed SF_6 on Ru(0001) under electron irradiation, we utilize several surface-sensitive techniques, mainly temperature-programmed desorption (TPD) and ESDIAD. The major findings of this work include establishing the dissociation dynamics of fractional monolayers of SF_6 adsorbed on Ru(0001), insights into the origins of F^+ and F^- ions, and the difference in sensitivity to electron exposure of fractional monolayer and multilayer coverages of SF_6. We find that the F^- ions originate primarily from undissociated SF_6 molecular adsorbates, while the F^+ ions have a high yield from both molecular SF_6 and adsorbed dissociation fragments.

Section 2 outlines the experimental procedures, Sec. 3 focuses on the results obtained, and Sec. 4 provides a discussion of the results presented and offers possible explanations.

2. EXPERIMENTAL PROCEDURES

Experiments have been carried out in an ultrahigh vacuum (UHV) chamber equipped with apparatus for Auger electron spectroscopy (AES), low-energy electron diffraction (LEED) and temperature-programmed desorption (TPD). The chamber houses two detectors for ESD experiments: a quadrupole mass spectrometer (QMS) and an electron-stimulated desorption ion angular distribution detector. The chamber is ion pumped, reaching a base pressure of $\sim 5 \times 10^{-11}$ torr after system bakeout.

The substrate is a Ru(0001) single crystal mounted on a copper sample holder connected to a manipulator and attached to a closed-cycle helium refrigerator, which cools the sample to ~25 K. The sample can be heated to 1600 K by electron bombardment of its back side. Substrate temperature is measured by a Chromel–Alumel thermocouple attached directly to the sample. The crystal surface is cleaned by sputtering using 1 keV Ar^+ ions, heating in oxygen, followed by annealing in vacuum. The procedure ensures effective cleaning of the surface, which demonstrates a distinct 1×1 LEED pattern. The absence of contaminants is monitored by AES and work function measurements.

High-purity (99.95%) sulfur hexafluoride (SF_6: Matheson) is deposited onto the clean surface at 25 K via a directional capillary array gas doser. Gas purity is checked by QMS (residual-gas analysis mode) as it is introduced into the chamber. Coverages are determined by temperature-programmed desorption measurements. For TPD studies, the Ru sample is heated by radiation from a hot W filament approximately ~1 mm from its back side. A negative bias is applied to the sample to prevent electron bombardment from either the heating filament or QMS filament, as the temperature is increased.

A Kimball Physics series electron gun, providing a focused beam of electrons in the energy range of 20–1000 eV, is the source of electron irradiation in the electron-stimulated desorption experiments. The incidence angle of primary electrons is 55° with respect to the sample normal.

ESD mass spectra of positive ions are obtained using the QMS to detect ions produced upon electron bombardment of adsorbed SF_6. In this mode of operation, the ESD mode, the ion-source filament of the QMS is turned off, and the electron gun is used to bombard the sample with a focused electron beam, ~1 mm^2 in area. Typically, the energy of the incident electrons is 200 eV and the sample is held at +20 V.

The ESDIAD detector allows us to perform angle-resolved ESD studies of both negative and positive ions. Time-of-flight (TOF) mass separation of desorbing species is accomplished by pulsing the primary electron beam and gating a retarding grid with a repetition rate of 10 kHz and duration of 200 ns. Unless otherwise specified, angular distributions of desorbing F^+ have been measured for incident electron kinetic energies of 350 eV (250 eV electron gun energy and sample bias of +100 eV). Measurements for F^- ions were made for incident electron energies of 250 eV (350 eV electron gun energy and sample bias of −100 eV). The sample bias is applied in order to accelerate escaping ions and achieve a wider collection angle. The total electron beam exposure used to obtain the ESDIAD images is $\sim 10^{12}-10^{13}$ cm^{-2}. The details of the experimental technique have been reported elsewhere.[15–17]

All ESDIAD measurements reported in this paper are made with the sample cooled to ~25 K. Thermally induced changes in ESDIAD patterns were ''frozen'' after annealing by cooling to ~25 K before measurements were made.

For experiments involving TPD associated with electron beam damage of the adsorbed layer, the sample is held at +20 V potential and 90-eV electrons from the QMS filament ($I\sim 1.5\ \mu$A, $E\sim 70$ eV) bombard the sample. The QMS filament provides a defocused electron beam that allows for irradiation of the whole sample, in contrast to the electron gun with a focused electron beam that irradiates ~1 mm^2 of the target sample.

TPD measurements[5] indicate that the SF_6 molecules are primarily physisorbed on the Ru substrate. We estimate a constant sticking probability (~1) for SF_6 at 25 K.[5] Based on the packing density of the basal plane of ruthenium (1.58×10^{15} atoms/cm^2) and the molecular size of SF_6, we identify the saturation coverage of SF_6 in the first adsorbed layer as ~0.33 ML (5.3×10^{14} molecules/cm^2).

3. RESULTS

3.1. ESD mass spectra

Figure 1 shows typical ESD mass spectra measured for positive ions at fractional monolayer (Fig. 1a) and multilayer (Fig. 1b) coverages of SF_6 on Ru(0001). Data are obtained using the QMS (ESD mode) with incident electron energies of 200 eV and a sample bias of +20 V. Figure 1c shows the gas phase spectrum for comparison.

In the fractional monolayer regime, the condensed-phase spectrum (Fig. 1a) exhibits a strong F^+ ion signal. The yield of other fragments is suppressed. Increasing the coverage leads to changes in desorption yields of positive ions. As the coverage grows (Fig. 1b, 2.5 ML SF_6), we detect a considerable increase in desorption of singly charged fragments: S^+ and SF_x^+ ions ($x=1,\ldots,5$). SF_6^+ species are not observed. Note the extremely low yield of SF_4^+ fragments, which are barely detected in the spectrum.

The gas-phase spectrum for positive ions shown in Fig. 1c agrees with the NIST Chemistry WebBook,[18] except that we detect higher relative yields of F^+ and S^+ ions, which may be due, in part, to the contribution of ESD from species

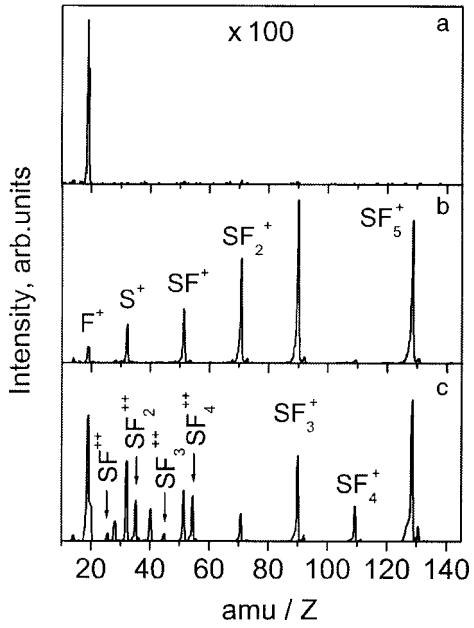

FIG. 1. Mass-spectra for ESD of positive ions from SF_6 on Ru(0001) for coverages: 0.25 ML (a) and 2.5 ML (b). Sample bias is +20 V. Incident electron energy is 220 eV. Gas-phase spectrum for positive ions (equilibrium pressure of SF_6 in chamber is 1×10^{-7} Torr) (c).

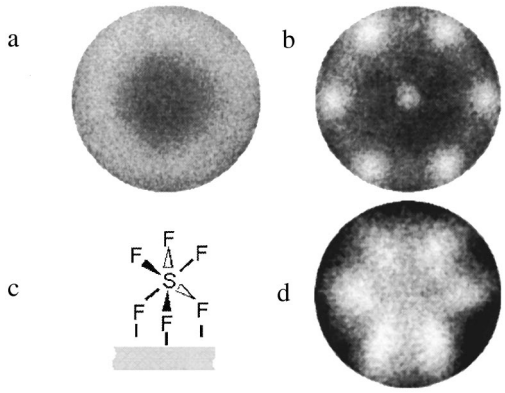

FIG. 2. ESDIAD patterns for F^+ and F^- ions from 0.25 ML of SF_6 on Ru(0001). F^+ ion halo-like pattern after deposition at 25 K (a). Heating the sample to −90 K results in hexagonal patterns for both F^+ (b) and F^- (d) ions. The dynamics observed are consistent with adsorption of the molecule on Ru by 3 fluorine atoms (c). Incident electron energy E_e is 350 eV for F^+ ion patterns and 250 eV for F^- ion pattern.

adsorbed on parts of the QMS. In contrast to thick SF_6 layers (Fig. 1b), the gas-phase SF_4^+ signal (although smaller than the SF_3^+ and SF_5^+ signals) is comparable to yields detected for the other ions. As in the case of the multilayer SF_6 film on Ru (Fig. 1b), no SF_6^+ is detected in the gas phase. It is believed that this ion is unstable both in its ground state and its excited electronic states.[6]

The spectrum in Fig. 1c also reveals the presence of doubly charged fragments: SF_x^{++} $(x=1,...,4)$. The intensities of these fragments are related to the intensities of the corresponding singly charged ions, and are dependent on x. For even values of x (2, 4), the observed intensities of singly- and doubly charged ions are approximately equal, whereas for odd values of x (1, 3) the doubly ionized fragment signals are smaller by about one order of magnitude. This observation is consistent with the partial electron-impact ionization cross sections reported elsewhere.[6]

In spite of the fact that the cracking pattern of ESD for negative ions contains only a few fragments, we observe the same tendency[5] as for positive ions. For fractional monolayer coverages, the F^- ion is the main fragment escaping from the surface. A small fraction of F_2^- ions is also observed, in accordance with previous ESD studies reported[4,19] for other halogenated molecules on Ru(0001). Increasing deposition of SF_6 leads to changes in the spectrum, mainly the emergence of the SF_5^- ion. The yield of this ion gradually increases and eventually even surpasses the F_2^- signal.

A more comprehensive treatment of the ESD mass spectra will be presented elsewhere.[20]

In general, one can conclude that for SF_6 molecules in the first adsorbed molecular layer, which are in contact with the ruthenium surface, desorption of the relatively massive SF_x ions under electron bombardment is suppressed; the ESD signals are dominated by F^+ and F^-. This may be attributed, in part, to higher reneutralization rates for more massive, slow-moving ions, whereas the less massive, fast-moving fluorine ions can easily escape from the substrate.[21]

3.2. Structure and bonding of SF_6; thermal effects

Experiments performed using ESDIAD reveal that after deposition of fractional monolayer coverage (0.25 ML) of SF_6, strong off-normal emission of both F^+ and F^- ions are observed. Typical ''halo'' patterns for F^+ and F^- ions are shown in Fig. 2a and Fig. 3a, respectively.

Heating the adsorbed SF_6 layer results in a transformation of the ESDIAD patterns for both F^+ and F^- ions. As the temperature approaches ~90 K, the initial ''halos'' are replaced by distinct sixfold symmetry patterns for both ions

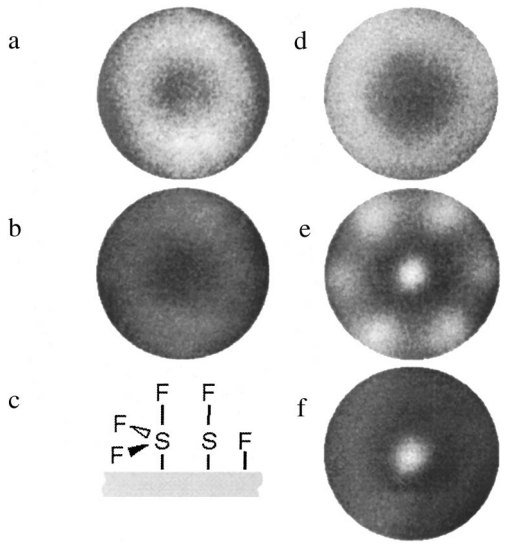

FIG. 3. ESDIAD patterns for F^+ and F^- ions illustrating effects of electron irradiation on adsorbed SF_6: F^- ions after deposition of 0.25 ML of SF_6 on Ru at 25 K (a); F^- ions after electron exposure of 10^{15} cm^{-2} (b); possible sources of F^+ ion emission along surface normal (c), F^+ ions after deposition of 0.25 ML of SF_6 (d); F^+ ions after electron exposure of 10^{15} cm^{-2} (e); F^+ ions after electron exposure of 10^{16} cm^{-2} (f). The patterns (d−f) are measured for 350 eV primary electrons; images (a, b) are detected for 250 eV electrons.

(F^+: Fig. 2b and F^-: Fig. 2d). This temperature corresponds to the maximum rate of desorption of molecules from the first adsorbed layer.[5]

Deposition of SF_6 coverages higher than 0.33 ML (saturation coverage) leads to changes in the angular distributions for both ions. The patterns become quite broad and featureless, with intensity centered on the surface normal, representing a random spatial orientation of molecules in the successive adsorbed molecular layers.

The ''halo'' patterns in Fig. 2a and Fig. 3a indicate a random azimuthal orientation of SF_6 molecules adsorbed on Ru(0001) by 3 fluorine atoms with the other 3 pointing away (Fig. 2c);[5,9] no S–F bonds are oriented along the surface normal. Heating the sample induces a rearrangement and ordering of the molecules, which results in the hexagonal patterns seen in Figs. 2b and 2d. The existence of six beams in Figs. 2b and 2d is attributed to the adsorption of SF_6 in two azimuthally oriented domains on Ru(0001), rotated by 60° with respect to each other.[5]

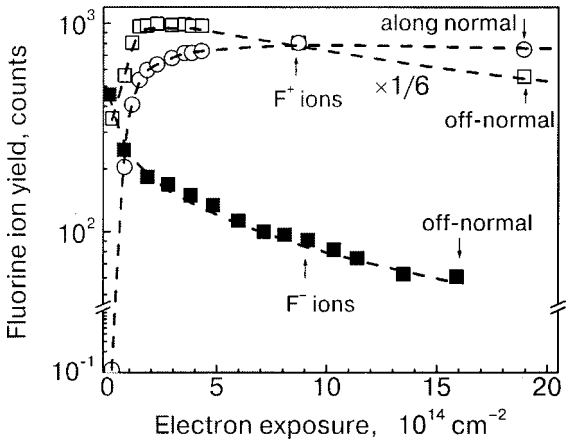

FIG. 4. Emission of fluorine ions from 0.25 ML of SF_6 in two directions: along the surface normal, and off the surface normal (hexagonal beams), as a function of electron exposure. The data are derived from ESDIAD patterns (cf. Fig. 3). The incident electron energy is 350 eV for F^+ ions and 250 eV for F^- ions.

3.3. Electron beam-induced changes in adsorbed SF_6

3.3.1. ESDIAD patterns

Typical transformations of the F^- ESDIAD patterns observed under electron bombardment of 0.25 ML of SF_6 are illustrated in Figs. 3a and 3b. Dynamics of the angular distribution of the F^- ions are as follows: during electron bombardment the initial ''halo'' pattern (Fig. 3a) loses its contrast very quickly (Fig. 3b) and then virtually disappears for electron exposures $>10^{15}$ cm^{-2}. Thus, increasing electron exposure leads to a decrease of the total yield of F^- ions but does not induce a change in the angular distribution (''halo'' pattern) of this fragment; only heating of the surface causes the F^- ESDIAD pattern to change from a ''halo'' to a hexagon.

In contrast to F^- ions, the angular distributions for F^+ ions change under electron bombardment. Figure 3e shows that exposure of 0.25 ML of adsorbed SF_6 molecules to $\sim 10^{15}$ cm^{-2} results in the transformation of the initial ''halo'' (Fig. 3d) into six off-normal beams and a prominent central peak. The angular positions of these beams are similar to those observed after heating (Fig. 2b). The most noticeable difference between the hexagonal F^+ patterns in Fig. 2b and Fig. 3e is in the width of the beams. Further electron bombardment ($\sim 10^{16}$ cm^{-2}) results in the disappearance of the off-normal beams and the gradual growth and saturation of the central peak (Fig. 3f).

The observed changes in the ESDIAD patterns lead us to believe that F^- ions originate primarily from undissociated molecularly adsorbed SF_6, while the F^+ ions originate from SF_x dissociation fragments.

3.3.2. Correlation between F^+ and F^- ion desorption

The behavior of F^+ and F^- ion desorption along normal and off-normal directions as a function of electron exposure is illustrated in Fig. 4. Each data point represents the integrated signal intensity for the indicated region of the ESDIAD patterns. For clarity, the data corresponding to the off-normal desorption of F^+ ions are divided by a factor of 6.

There is evidence for correlated behavior of the curves in Fig. 4. Each data set demonstrates two distinct regions: the ion signals change rapidly for electron beam exposures $\leqslant 2\times10^{14}$ cm^{-2} and change more slowly for exposures $\geqslant 2\times10^{14}$ cm^{-2}. (An exposure of $\sim 2\times10^{14}$ cm^{-2} corresponds approximately to one incident electron per two surface molecules.) In the initial region (at lower exposures) we observe an increase of the F^+ ion yield in the off-normal direction and the appearance of the F^+ signal along the surface normal direction. Under the same conditions the desorption signal for F^- ions in the off-normal direction decreases very rapidly. The rate of the F^- ion drop decreases at higher exposures, where the F^+ ion yield also changes: in the off-normal direction, the curve goes through a maximum and then exhibits exponential decay. Along the surface normal, the F^+ yield saturates and appears to decrease very slowly.

Thus during electron beam exposures we observe a different ESD yield of F^- and F^+ ions in off-normal directions (a) and of F^+ ions along the surface normal and off-normal directions (b). This implies that F^+ and F^- ions are escaping from different species.

3.3.3. Influence of electron irradiation on TPD spectra

In order to gain further insight into the dissociation process of SF_6 on Ru(0001), we have also studied the influence of electron irradiation on TPD spectra. Electron beam exposure leads to a faster decrease of molecular SF_6 in the first adsorbed layer as compared to that in the succeeding multilayers. As illustrated in Fig. 5, irradiation also results in a change of the shape of the monolayer feature, as well as a shift of the maximum desorption rate to higher temperatures. Exposure of 0.25 ML of SF_6 to $\sim 10^{16}$ cm^{-2} leads to an almost complete disappearance of adsorbed molecular SF_6 on the surface. An even more surprising result is that the transformation of the fractional monolayer just described also occurs in the presence of succeeding adsorbed layers of SF_6, which are not affected as strongly by electron beam irradiation (data not shown). In contrast, electron irradiation appears to affect only the amplitude of the multilayer peak in the TPD spectrum, while preserving the peak shape and position.

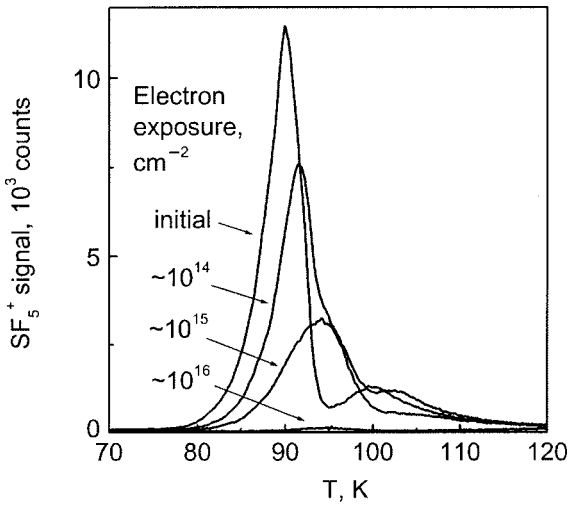

FIG. 5. Evolution of TPD spectra caused by electron irradiation of 0.25 ML of SF_6 on Ru at 25 K. The electron source is the QMS filament, $E_e = 90$ eV.

Thus it appears that molecules in contact with the Ru surface are more sensitive to dissociation than the molecules from upper adsorbed layers, which are isolated from the metal substrate.

4. DISCUSSION

4.1. Structure and bonding of SF_6; thermal effects

The primary issues that we address are the processes that take place in fractional monolayers of SF_6 adsorbed on Ru(0001) upon electron bombardment. As already mentioned in the introduction, a number of studies of the adsorption and ion emission properties of SF_6 adsorbed on various surfaces have been reported.[7–10,21–26] However, a gap in the understanding of the results still exists.

Our data indicate that SF_6 molecules dosed onto Ru(0001) at 25 K are primarily physisorbed, based upon our TPD and ESDIAD results, and previous studies[9] of adsorption of SF_6 on Ru(0001). Physisorption is indicated by the closeness of the temperature at which the maximum rate of desorption of fractional monolayers of SF_6 occurs ($\sim$90 K) and the desorption temperature of condensed SF_6 ($\sim$80 K). Physisorption of molecular SF_6 has also been established on Ni(111)[22] and graphite (HOPG).[8]

The ''halo'' patterns in Figs. 2a and 3a indicate a random azimuthal orientation of SF_6 molecules adsorbed on Ru(0001) by 3 fluorine atoms with the other 3 pointing away.[5,9] The ''halo'' pattern represents all the possible azimuthal orientations of S–F bonds, since ESDIAD provides us with information averaged over a surface area determined by the electron beam size ($\sim$1 mm^2).

Heating to desorption temperatures ($\leqslant$90 K) leads to a redistribution of the F^- ion intensity from an initial ''halo'' to a hexagon.[5] Integration of ESDIAD patterns for F^- ions (Fig. 2) reveals that the total ion intensity is essentially unchanged; upon redistribution of the intensity prior to the onset of desorption (from ''halo'' to hexagon) the integral signal remains nearly constant. As the SF_6 desorbs thermally, the F^- signals decrease.

The behavior of F^+ ions during heating to desorption temperatures ($\leqslant$90 K) is virtually identical to that of F^- ions. The initial ''halo'' pattern transforms into a hexagon and the total F^+ ion intensity remains constant. The F^+ ion hexagon differs slightly from the F^- hexagon, in that a central beam is observed.

Both F^+ and F^- ions are believed to escape from undissociated SF_6 molecules, which have two preferential azimuthal orientations (giving six ion beams, rather than the 3 beams expected for a single molecular orientation). The central beam in Fig. 2b is due to ESD from a thermal decomposition product of SF_6, either chemisorbed F or another fragment with an S–F bond perpendicular to the surface. Dissociation of a small fraction of SF_6 is supported by the persistence of an F^+ signal at temperatures $>$120 K, when desorption of the molecular SF_6 is complete.

We attribute the temperature-induced changes of the ESDIAD patterns to the rearrangement of undissociated SF_6 molecules, as they move to occupy energetically preferential adsorption sites. The rearrangement of the patterns for both F^+ and F^- ions from initial ''halos'' to hexagons indicates ordering of the first adsorbed layer.

The orientation of SF_6 molecules after heating to $\sim$90 K on Ru(0001) is established by comparison of ESDIAD patterns (Figs. 2b and 2d) and LEED images for the clean substrate. We identity the axis defined by the S–F bond in the SF_6 molecule to coincide with the $\langle 10\bar{1}0 \rangle$ direction of ruthenium. A detailed analysis of the adsorption properties and surface geometry of SF_6 on Ru(0001) is presented elsewhere.[5] In this paper we focus primarily on electron beam-induced changes in the adsorbed layer.

4.2. Electron beam-induced changes in adsorbed SF_6

4.2.1. ESDIAD patterns

Electron bombardment causes significant changes in F^+ and F^- ESDIAD patterns. For exposures $\geqslant 10^{14}$ cm^{-2}, the ''halo'' pattern due to F^- ions (Fig. 3a) loses its contrast very quickly and then virtually disappears (Fig. 3b). The initial ''halo'' pattern does not rearrange into a hexagon under electron irradiation. Electron bombardment leads to a decrease in the total ion yield, but the angular distribution of the F^- ions remains the same. This observation leads to the suggestion that F^- ions originate primarily from molecularly adsorbed SF_6.

In contrast to the F^- data, the angular distributions for F^+ ions do undergo significant changes under electron irradiation. As already mentioned, for exposures of $\sim 10^{15}$ cm^{-2}, the initial ''halo'' pattern (Fig. 3d) transforms into six off-normal beams in the shape of a hexagon and a prominent central beam (Fig. 3e), very similar to the transformation that we observe upon heating to $>$90 K (Fig. 2b). More precisely, the azimuthal angles for the thermal- and electron beam-induced hexagon patterns are identical, and the polar angles are very similar. More extensive irradiation (10^{16} cm^{-2}), however, results in the disappearance of the off-normal beams and growth and saturation of the central beam (Fig. 3f). In contrast to the F^- intensity, the F^+ ion intensity increases with increasing electron exposure. These behaviors suggest that F^+ ions originate also from SF_x dissociation fragments.

4.2.2. Ordering of dissociation fragments

The similarity of the transformation of the F^+ ESDIAD patterns from a "halo" to a hexagon upon both heating and electron exposure makes it tempting to suggest that electron beam exposure of disordered SF_6 molecules ("halo" pattern) leads to electron-induced ordering (hexagon pattern), similar to thermally induced ordering. Electron-stimulated mobility of adsorbed species at low temperatures is well known.[27,28] However, the differences between the F^+ and F^- ESDIAD patterns during electron irradiation strongly suggest that electron bombardment causes dissociation of the adsorbed molecular SF_6 rather than ordering of the adsorbed layer, and that F^- ions escape from undissociated SF_6 molecules. This is supported by the observation that the F^- "halo" (Figs. 3a and 3b) simply disappears as the electron exposure increases. This is a consequence of the dissociation of SF_6 under electron bombardment: upon dissociation of SF_6, the F^- signal is reduced, while new features in the F^+ ESDIAD patterns emerge.

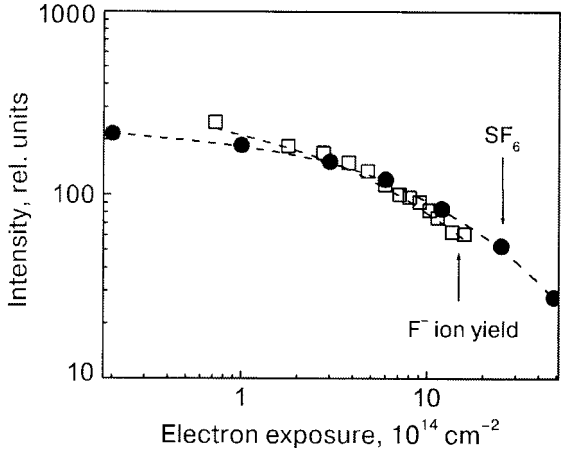

FIG. 6. A comparison of negative fluorine ion yields (derived from ESDIAD patterns, e.g., Fig. 3 and plotted in Fig. 4; $E_e = 250$ eV) and relative concentration of undissociated SF_6 molecules (derived from TPD spectra, Fig. 5; $E_e = 90$ eV) as a function of electron exposure. The data are measured for 0.25 ML of SF_6 on Ru.

4.2.3. Origins of F^-, F^+ ions; nature of molecular fragments

In the following paragraphs we discuss the nature of the molecular species and fragments that contribute to the observed F^+ and F^- ESDIAD patterns. As previously mentioned, the excitations leading to F^- and F^+ ions are very different: F^- is a product of DEA excited by low-energy secondary electrons from the substrate,

$$e^- + SF_6 \rightarrow (SF_6^*)^- \rightarrow SF_5 + F^-$$

with two resonant features at electron energies of 5.8 eV and ~11 eV for the condensed phase; dipolar dissociation also contributes at higher energies.

In contrast, F^+ ions are due to core excitations (probably F $2s$)

$$e^- + SF_6 \rightarrow (SF_6^*)^+ \rightarrow SF_5^+ + F^+ + 2e^-$$

with a threshold energy of ~30 eV.

Our TPD spectra (Fig. 5) support the proposal that F^- ions originate from undissociated SF_6. The area under a TPD curve is known to be proportional to the number of molecules desorbed thermally and, in our case, undissociated SF_6 and/or SF_6 that forms by recombination upon heating the surface. Damage kinetics of SF_6 due to electron bombardment (derived from TPD measurements, Fig. 5) and the dependence of the F^- ion yield on electron exposure (derived from ESDIAD signals) are compared in Fig. 6. The data are normalized for clarity and presented in relative units. The drop in F^- ion yield is correlated with the decay of the concentration of undissociated SF_6 molecules on the surface. The quantitative differences in the two data sets of Fig. 6 are attributed to errors in determining the electron beam exposure in the two experiments (focused beam for ESDIAD versus defocused electron source for TPD) and to the difference in incident electron energy (90 eV for TPD and 250 eV for ESDIAD).

The change in the angular distribution of the F^+ ions indicates that after electron irradiation, the F^+ ions do not escape from undissociated molecular SF_6, but rather from dissociation fragments SF_x. Recently Souda,[25] in a study of secondary-ion emission from SF_6 adsorbed on Pt(111), observed an increase of one order of magnitude in the yield of F^+ ions after electron irradiation. He suggested that the F^+ ions arise from chemisorbed F adatoms or dissociation fragments (SF_x). This observation is in agreement with the increase in the F^+ ion yields with electron exposure seen in Fig. 4. (See Sec. 4.2 for a discussion of Fig. 4). The angular resolution of our ESDIAD images allows us to distinguish between ions that escape normal to the surface, i.e., from SF_x species with an S–F bond perpendicular to the surface or fluorine atoms bound directly to the surface (Fig. 3c), and those that escape from SF_x ($x = 2-5$) with S–F bonds directed in off-normal directions.

The hexagon (Fig. 3e) that is clearly seen after exposures of $\sim 10^{15}$ cm^{-2} is formed by F^+ ions from dissociation fragments (SF_x), which desorb from the surface along an off-normal direction. The F^+ beams observed in the pattern after irradiation (Fig. 3e) look broader and more asymmetric than the beams of the hexagon detected after heating (Fig. 2b), suggesting that several SF_x species with S–F bonds in off-normal directions could be contributing to the six F^+ beams. It is most interesting that these fragments tend to be ordered on the surface (we observe a hexagon instead of a "halo"), in a manner very similar to the results obtained during irradiation-induced decomposition of PF_3 molecules adsorbed on Ru(0001).[27,28] On the basis of the theoretical equilibrium structures of SF_x ($x = 1-6$) (Ref. 29) and simple bonding symmetry considerations similar to those for domains of PF_2 (Ref. 12), it is possible that the hexagon originates, for example, from 3 domains of SF_4 species, or bridge-bonded SF_2 species, azimuthally rotated by 120° as shown in Fig. 7. Other fragments, including inclined SF, could also contribute to the off-normal F^+ ion yields.

The central beam, caused by F^+ ions desorbing normal to the surface, most probably contains contributions from chemisorbed F adatoms. However, fragments such as SF, SF_3, and SF_5 might also contribute to the central beam.[29]

At present the identity of the dissociation fragments is an open issue, as we lack direct knowledge about the stoichiometry and the structure of SF_x fragments adsorbed on the Ru substrate. Additional experiments (e.g., high-resolution

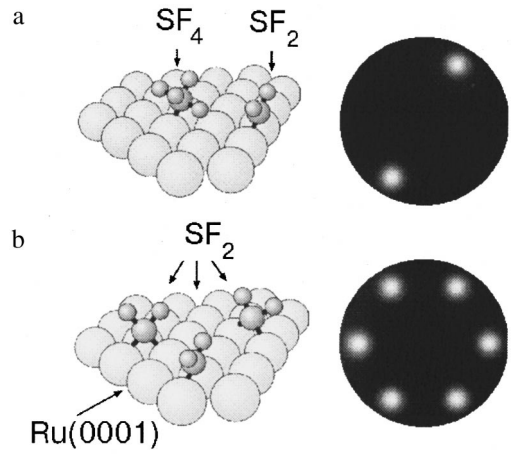

FIG. 7. Schematic representation of bridge-bonded SF_2 and SF_4 species on ruthenium surface (on the left) and corresponding simulated ESDIAD pattern (on the right) (a); illustrates formation of hexagonal ESDIAD pattern (simulated image is on the right) from 3 domains of SF_2 species, azimuthally rotated by 120° (shown on the left) (b).

soft x-ray photoemission spectroscopy)[30] and theoretical guidance are needed to resolve these issues.

Figure 4 is a plot of ESDIAD intensity as a function of electron exposure. Both the ''along normal'' and ''off-normal'' F^+ curves grow rapidly at low electron exposures. The rapid initial rise is probably due to very efficient dissociation in the initial stages of the decomposition of molecular SF_6. In the initial stages (at low electron exposures) there are many adsorption sites available for the dissociation fragments of SF_6 on the Ru(0001) surface. Being in contact with the metal surface enhances the reactivity of fragments and makes them more prone to dissociate. As the dissociation process continues at higher electron exposures, the Ru(0001) surface becomes ''filled'', and the rate of further dissociation is greatly reduced. This suggests that low coverages of SF_6 have a higher dissociation rate than higher coverages.

In concluding this part of the discussion, we note that there is previous evidence from ESD studies of PF_3 and $(CF_3)_2CO$ to support the contention that negative ion desorption arises mainly from molecularly intact adsorbates, while positive ion desorption can be dominated also by dissociative fragments, when they are present.[27] We suggest that the temporary negative ion states formed during DEA of molecules such as SF_6, etc., are more weakly coupled to the surface than similar states associated with more strongly chemisorbed fragments. Thus the lifetime for DEA of intact molecules is expected to be longer than for possible DEA of chemisorbed dissociation fragments, making the probability of F^- desorption from molecules higher than that from fragments.

4.2.4. Estimation of cross sections for desorption and dissociation

In the discussion of the origin of the F^- ion, we made reference to Fig. 6, which clearly shows a correlation between the drop in F^- ion yield with a decrease in the number of undissociated SF_6 molecules left on the surface after irradiation. As described elsewhere,[31] the exposure-dependent surface coverage θ can be roughly expressed by the exponential law:

$$\theta = \theta_0 \exp(-\sigma_{\mathrm{esd}} F_e),$$

where σ_{esd} is the total cross section (cm^2) of molecular SF_6 for electron-stimulated desorption and/or dissociation, and F_e is the electron exposure (cm^{-2}).

Recent measurements[20] indicate that the F^- signal is directly proportional to θ_{SF6}, and we approximate the total cross-section for electron-induced dissociation of a fractional monolayer (0.25 ML) of SF_6 on Ru(0001) from the F^- intensity curve in Fig. 4. We find that for 250 eV incident electron energy, σ_{esd} is $\sim(6\pm2)\times10^{-15}$ cm^2 for electron exposures $<2\times10^{14}$ cm^{-2} and $\sim(8\pm2)\times10^{-16}$ cm^2 for electron exposures $>2\times10^{-14}$ cm^{-2}, an order of magnitude difference. A qualitatively similar result has been derived from damage kinetics of molecular SF_6 shown in Fig. 6 (primary electron energy ~90 eV): $\sim(2\pm1)\times10^{-15}$ cm^2 for exposures $<2\times10^{14}$ cm^{-2} and $\sim(4\pm1)\times10^{-16}$ cm^2 for higher electron exposures. As already indicated in the previous Section, σ_{esd} is expected to be greater at initial electron exposures, since there are many adsorption sites available to the dissociation fragments, allowing them to interact with the Ru substrate and increase their reactivity.

Our rough calculations of σ_{esd} indicate that the total dissociation/desorption cross section for fractional SF_6 adsorbed on Ru for low electron exposures is about 1 order of magnitude greater than for gaseous SF_6. In the case of DEA it has been shown that the cross-section is often greater for molecules condensed on a substrate than for the gas-phase analog. The increase is explained in terms of the induced polarization energy due to the substrate, which stabilizes a negative ion against autodetachment.[32]

In our experiments there are two sources of electrons, primary and secondary, that can cause dissociation: 1) energetic primary electrons can initiate dissociative ionization and/or dipolar dissociation, and 2) low-energy secondary electrons (originating from the Ru substrate) can lead to DEA, and to a lesser extent, dissociative ionization. Secondary electrons have a maximum yield at 0–2 eV with a high energy tail extending to 20–30 eV.

There have been several measurements of electron impact ionization cross sections for gaseous SF_6. Dissociative ionization (which results in the formation of positive ions) of gaseous SF_6 becomes significant for electron energies >16 eV, and exhibits a maximum cross section of $\sim7\times10^{-16}$ cm^2 for electron energies of ~100 eV (Ref. 6).

DEA (which results in the formation of neutral fragments and negative ions) is appreciable only for low-energy electrons, 0–15 eV. The maximum cross section of 2×10^{-16} cm^2 occurs for electron energies of ~0.1–0.5 eV, and is due mainly to the formation of SF_5^- (Ref. 6).

The different behavior of the monolayer and multilayer features in TPD spectra during electron irradiation (see the explanation of Fig. 5 in the previous Section), leads us to believe that the average cross section for electron-induced dissociation of SF_6 fractional monolayer coverages is approximately one order of magnitude greater than for multilayers. The higher rate of dissociation of SF_6 molecules in

contact with the Ru(0001) surface provides indirect evidence of the important contribution of DEA to the total dissociation process of SF_6 on Ru(0001). Low-energy secondary electrons are known to play a major role in DEA,[3] which is an extremely efficient process in collisions of low-energy electrons with gas-and condensed-phase halogenated molecules. In addition, an electronically excited species in contact with the metal tends to react more easily than when it is isolated from the metal.

4.3. ESD mass spectra

The interaction of adsorbed SF_6 molecules with the Ru(0001) substrate is responsible for the substantial differences in the ESD mass spectra (Fig. 1) between fractional monolayer and multilayer coverages. As mentioned in the description of Fig. 1, the ESD mass spectra for fractional monolayer coverages exhibits only a strong F^+ ion signal; the yield of other fragments is suppressed. However, the spectrum for 2.5 ML of SF_6 displays a variety of desorbing species. A very similar effect was observed for the adsorption of C_6H_{12} on Ru(0001): ESD of a C_6H_{12} monolayer was observed to yield only H^+, while multilayer coverages yielded many more ionic fragments.[33] It was suggested that for the monolayer species in direct contact with the substrate, the probability of electron-induced dissociation is high, but that de-excitation processes involving electron tunneling from the substrate also occur with high probability. This leads to suppression of desorption of slow-moving, massive ion fragments (see the discussion of mass effects in ESD by Madey *et al.*[34]) Our ESD mass spectra are consistent with these considerations: for fractional monolayer coverages we observe only a strong F^+ yield, while multilayer coverages yield more ionic fragments.

5. CONCLUSION

We have studied ESD of F^+ and F^- ions from fractional monolayers of SF_6 on Ru(0001) at 25 K as a function of electron irradiation. The origin of these ions appears to be strongly dependent on the electron exposure.

For exposures less than $\sim 10^{13}$ cm^{-2} both F^+ and F^- ions observed in off-normal directions arise from undissociated SF_6 molecules. Higher electron exposures ($\geqslant 10^{14}$ cm^{-2}) lead to stepwise decomposition of the parent SF_6 molecule, with the F^+ and F^- ions escaping from different species: whereas the F^- ion is still emitted by undissociated SF_6 molecules, the F^+ ions escape in off-normal directions from SF_x ($x=2-5$) fragments. That SF_x fragments are ordered on the surface is indicated by the observed hexagonal ESDIAD patterns for F^+ after irradiation. Along directions normal to the surface, the F^+ ions arise most likely from dissociation fragments with an S–F bond normal to the surface, and chemically bonded F adatoms. Adsorbed SF_6 molecules and SF_x fragments decompose almost completely after electron exposures of $\sim 10^{16}$ cm^{-2}. The total cross section for electron-impact dissociation of molecular SF_6 on Ru (incident electron energy ~250 eV) is found to be $\sim(6\pm 2)\times 10^{-15}$ cm^2 for electron exposures $<2\times 10^{14}$ cm^{-2} (which is about 1 order of magnitude greater than for gaseous SF_6), and $\sim(8\pm 2)\times 10^{-16}$ cm^2 for higher electron exposures.

We acknowledge valuable discussions with Professor E. Carter. This work has been supported in part by the US National Science Foundation, Grant No. CHE 0075995.

*E-mail: madey@physics.rutgers.edu

[1] Q.-B. Lu and T. E. Madey, Phys. Rev. Lett. **82**, 4122 (1999).
[2] Q.-B. Lu and T. E. Madey, Surf. Sci. **451**, 238 (2000).
[3] Q.-B. Lu and T. E. Madey, J. Phys. Chem. B **105**, 2779 (2001).
[4] S. S. Solovev, D. Kusmierek, and T. E. Madey (in preparation).
[5] N. S. Faradzhev, D. O. Kusmierek, B. V. Yakshinskiy, S. S. Solovev, and T. E. Madey (submitted to Surf. Sci).
[6] L. G. Christophorou and J. K. Olthoff, J. Phys. Chem. Ref. Data **29**, 267 (2000).
[7] F. Weik, E. Illenberger, J. Chem. Phys. **109**, 6079 (1998).
[8] L. Siller, N. Vanter, and R. E. Palmer, Surf. Sci. **465**, 76 (2000).
[9] G. B. Fisher, N. E. Erickson, T. E. Madey, and J. T. Yates, Surf. Sci. **65**, 210 (1977).
[10] Klekamp, E. Umbach, Chem. Phys. Lett. **171**, 233 (1990).
[11] T. E. Madey, Science **234**, 316 (1986).
[12] T. E. Madey, H. S. Tao, L. Nair, U. Diebold, S. M. Shivaprasad, A. L. Johnson, A. Poradzisz, N. D. Shinn, J. A. Yarmoff, V. Chakarian, and D. Shuh, *Desorption Induced by Electron Transitions DIET V* (1993), p. 182.
[13] T. Stanski and B. Adamczyk, Int. J. Mass Spectrom. Ion Phys. **46**, 31 (1983).
[14] D. Margreiter, G. Walder, H. Deutsch, H. U. Poll, C. Winkler, K. Stephan, and T. D. Märk, Int. J. Mass Spectrom. Ion Processes **100**, 143 (1990).
[15] Q.-B. Lu, Z. Ma, and T. E. Madey, Phys. Rev. B **58**, 16446 (1998).
[16] M. Akbulut, T. E. Madey, L. Patenteau, and L. Sanche, J. Chem. Phys. **105**, 6043 (1996).
[17] Q.-B. Lu and T. E. Madey, J. Chem. Phys. **111**, 2861 (1999).
[18] *IR and Mass Spectra*, in *NIST Chemistry WebBook, NIST Standard Reference Database*, Vol. 69, P. J. Linstrom and W. G. Mallard (Eds.), National Institute of Standards and Technology, Gaithersburg MD (2001); (http://webbook.nist.gov).
[19] N. J. Sack, M. Akbulut, T. E. Madey, P. Klein, H. M. Urbassek, and M. Vicanek, Phys. Rev. B **54**, 5130 (1996).
[20] N. S. Faradzhev, D. O. Kusmierek, B. V. Yakshinskiy, and T. E. Madey (in preparation).
[21] T. E. Madey and J. T. Yates, Surf. Sci. **63**, 203 (1977).
[22] A. Klekamp and E. Umbach, Surf. Sci. **249**, 75 (1991).
[23] A. Klekamp and E. Umbach, Surf. Sci. **271**, 555 (1992).
[24] A. Klekamp and E. Umbach, Surf. Sci. **284**, 291 (1993).
[25] R. Souda, J. Chem. Phys. **114**, 1823 (2001); *ibid.* **114**, 3293 (2001).
[26] A. G. Fedorus, E. V. Klimenko, A. G. Naumovets, E. M. Zasimovich, and I. N. Zasimovich, Nucl. Instrum. Methods Phys. Res. B **101**, 207 (1995).
[27] A. L. Johnson, S. A. Joyce, and T. E. Madey, Phys. Rev. Lett. **61**, 2578 (1988).
[28] S. A. Joyce, A. L. Johnson, and T. E. Madey, J. Vac. Sci. Technol. A **7**, 2221 (1989).
[29] Y.-S. Cheung, Y.-J. Chen, C. Y. Ng, See-Wing Chiu, and Wai-Kee Li, J. Am. Chem. Soc. **117**, 9725 (1995).
[30] H.-S. Tao, U. Diebold, V. Chakarian, D. K. Schu, J. A. Yarmoff, N. D. Shinn, and T. E. Madey, J. Vac. Sci. Technol. A **13**(5), 2553 (1995).
[31] T. E. Madey and J. T. Yates, J. Vac. Sci. Technol. **8**, 525 (1971).
[32] F. Weik, E. Illenberger, K. Nagesha, and L. Sanche, J. Phys. Chem. B **102**, 824 (1998).
[33] T. E. Madey and J. T. Yates, Surf. Sci. **76**, 397 (1978).
[34] T. E. Madey, J. T. Yates, Jr., D. A. King, and C. J. Uhlaner, J. Chem. Phys. **52**, 5215 (1970).

This article was published in English in the original Russian journal. Reproduced here with stylistic changes by AIP.

Soft landing of size-selected clusters in rare gas matrices

J. T. Lau and W. Wurth*

Universität Hamburg, Institut für Experimentalphysik, Luruper Chaussee 149, D-22761 Hamburg, Germany

H.-U. Ehrke and A. Achleitner

Technische Universität München, Physik Department E20, D-85747 Garching, Germany
(Submitted November 10, 2002)
Fiz. Nizk. Temp. **29**, 296–302 (March 2003)

Soft landing of mass-selected clusters in rare gas matrices is a technique used to preserve mass selection in cluster deposition. To prevent fragmentation upon deposition, the substrate is covered with rare gas matrices to dissipate the cluster kinetic energy upon impact. Theoretical and experimental studies demonstrate the power of this technique. Besides STM, optical absorption, excitation, and fluorescence experiments, x-ray absorption at core levels can be used as a tool to study soft landing conditions, as will be shown here. X-ray absorption spectroscopy is also well suited to follow diffusion and agglomeration of clusters on surfaces via energy shifts in core level absorption. © *2003 American Institute of Physics.*
[DOI: 10.1063/1.1542443]

INTRODUCTION

Clusters of atoms or molecules are fascinating objects on which to study the evolution of electronic,[1–3] magnetic, [4–7] or chemical[8–10] properties from isolated atoms to bulk matter. Many types of cluster sources[11–14] have been developed and adapted to investigate a wide range of physical phenomena.[15,16] A cluster experiment typically consists of a cluster production stage with mass selection and of a stage to probe the clusters' physical properties, either in free cluster beams or after cluster deposition.

To study the size dependence of any physical property of clusters, size selection is a prerequisite. In gas-phase experiments on cluster beams, cluster ions can simply be size selected in electric (quadrupole) or magnetic (dipole) fields. To illustrate this, a mass spectrum of positively charged iron clusters mass separated in a magnetic dipole field is shown in Fig. 1. These iron clusters were generated by sputtering[17] of a high purity iron target with a 28 keV Xe^+ beam.[6,7,18] As can be seen in Fig. 1, size-selected cluster current densities typically range from some pA to a few nA per mm^2, depending on cluster size and material.

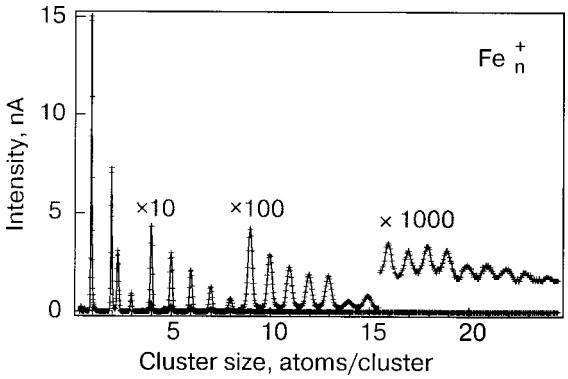

FIG. 1. Mass spectrum of positively charged iron clusters produced with a sputter source and measured on a detector area of 3 mm^2.

In cluster deposition experiments, however, not only size selection of the incoming cluster beam but also the preservation of the preselected cluster size upon and after deposition of the clusters is crucial. The incoming cluster beam of uniform size should not be transformed into a distribution of different cluster sizes on the substrate surface. Therefore, cluster deposition conditions have to be chosen under which no fragmentation, implantation, or agglomeration of the clusters occurs. For this purpose, the soft landing technique has been developed by several groups, both experimentally[19–25] and theoretically.[26–32] As a result, this technique is now well established. The principal idea of soft landing is to put the clusters down onto substrates as gently as possible. This includes deposition at low kinetic energy as well as deposition into soft matrices or buffer layers preadsorbed on the substrate. In most cases, these buffer layers will be rare gas multilayers adsorbed on the substrate material at low temperatures. After cluster deposition, the buffer layer will be desorbed from the sample surface by heating to above the monolayer desorption temperature. This allows one to investigate the clusters directly on the substrate surface. Alternatively, the properties of mass-selected clusters can be studied inside the rare gas matrix.[25] In Fig. 2, the idea of soft landing is illustrated schematically.

THE SOFT LANDING PROCESS

The purpose of soft landing is to gently dissipate the clusters' kinetic energy in the deposition process. In soft landing of size-selected clusters, clusters are size selected in the gas phase, decelerated to a few eV per cluster atom, and deposited into chemically inert buffer layers which have been prepared on the substrate. Bond energies in metal clusters[33,34] are typically on the order of a few eV. By depositing a decelerated cluster beam with kinetic energies typically of some few eV per cluster atom into rare gas multilayers, the surplus kinetic energy will be dissipated by energy transfer into the matrix and ultimately by rare gas

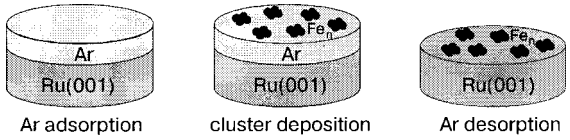

FIG. 2. Schematic representation of the soft landing process: Adsorption of rare gas multilayers as a buffer layer on the substrate (left), cluster deposition at low kinetic energy into the rare gas buffer (center), cluster sample after rare gas desorption (right).

desorption. This process has been studied in detail experimentally[19–25] and theoretically.[26–32] Molecular dynamics (MD) simulations[26,27] of the energy dissipation processes provide insight into the different stages of slowing down the impinging clusters and redistributing their initial kinetic energy.

On collision with the matrix or rare gas buffer the kinetic energy of the clusters is converted to vibrational energy, resulting in a rapid heating of the clusters. Heating rates are on the order of 10^{15} K/s and lead to superheated clusters. In the MD simulations,[26,27] the cluster temperature roughly doubles when argon is used for soft landing instead of neon, and again when xenon is used instead of argon. The clusters cool down via heat transport into the surrounding matrix and via desorption of rare gas atoms. Cooling rates are lower than heating rates and are on the order of $10^{13}-10^{14}$ K/s.

As has been shown in thorough experimental investigations,[19–22,24] the fragmentation rate of small metal clusters can be reduced to about 10% by using proper soft landing conditions. From optical absorption and excitation experiments[20,21,24] on clusters soft landed in rare gas matrices it is known that the efficiency of the soft landing process and the fragmentation rate of the clusters depends on the nature of the rare gas matrix. As discussed above, this is also known from theoretical predictions.[26,27] The lighter the adsorbed rare gas, the softer the buffer layer,[20,21] which in turn leads to a more efficient suppression of cluster fragmentation. Since adsorption temperatures decrease with decreasing mass of the rare gas atoms, cooling the sample down to at least 15 K is desirable for adsorption of argon buffer layers. Low temperatures are also desirable for minimizing cluster diffusion and agglomeration on the substrate surface[35,36] after cluster deposition.

It has also been demonstrated[24] that the fragmentation rate depends on the initial kinetic energy of the clusters and on the binding energy of the cluster atoms. The higher the binding energy, the lower the fragmentation rate for otherwise identical conditions.[24] However, even after cluster deposition into rare gas matrices at a kinetic energy of 50 eV per atom there is a non-negligible fraction of clusters that have not fragmented.[24] MD simulations[32] explain this in terms of recombination: While clusters will gain vibrational energy and may break up upon impact, they are also mobile and can recombine while the clusters and the surrounding matrix are still hot.

STM studies[22] on soft-landed clusters also have shown the power of the soft landing technique. Furthermore, they reveal that most of the soft-landed clusters form highly symmetric equilibrium structures on the substrate surface. Small clusters tend to form two-dimensional structures on a surface.[22,37]

Even though soft landing can be used to preserve size in cluster deposition experiments, the geometry of deposited clusters will differ from the geometry of gas phase clusters due to the interaction with the substrate.[38,39] In the present study, two-dimensional structures can be assumed for the deposited clusters because of their small size.

X-RAY ABSORPTION EXPERIMENTS ON SOFT-LANDED METAL CLUSTERS

Soft landing can not only be studied in STM[19,22] or fluorescence[20,24] experiments, but also in x-ray absorption (XAS) studies. In x-ray absorption, electrons from a core level are promoted into unoccupied states above the Fermi level. XAS is sensitive to the local electronic order and the chemical environment of the excited atom: Different species yield discernible fingerprints. Furthermore, XAS is an element-specific probe, and it is sensitive to submonolayer quantities of adatoms and clusters on surfaces.

The experimental setup[6,37,40] used for cluster deposition consists of a sputter source with mass selection and ultrahigh vacuum (UHV) cluster deposition under soft landing conditions. The UHV chamber is equipped with all the standard tools necessary for substrate surface preparation. A Ru(001) single crystal surface precovered with a (2×1)O superstructure was used as a substrate for cluster deposition to reduce the cluster–substrate interaction. Other than for chromium clusters on (2×1)O/Ru(001), that are highly sensitive to oxidation[37], no indication of oxidation was found for iron clusters. For *in situ* sample preparation the Ru(001) surface was cleaned after sputtering by repeated cycles of heating to 1450 K in UHV and oxygen dosing during cool-down of the sample. The (2×1)O/Ru(001) layer was prepared just before cluster deposition by heating the sample to 1450 K and cooling it down while dosing oxygen onto the Ru(001) surface. Surface quality was checked with XAS, low-energy electron diffraction (LEED), and Xe thermal desorption spectroscopy (TDS). The x-ray absorption experiments were carried out at the synchrotron radiation sources BESSY I (HE-PGM3) and BESSY II (U49/1-PGM). The photon energy scales are calibrated relative to each other with the absorption spectra of stainless steel used as a reference.

Soft landing and fragmentation were studied for small clusters, since for a given kinetic energy the kinetic energy per cluster atom is larger the smaller the cluster. The binding energy per atom, on the other hand, depends on but does not decrease significantly with cluster size.[33,34] Therefore, fragmentation upon deposition is expected most likely to be for small rather than for large clusters, and soft landing conditions are crucial for deposition of small clusters.

Small iron cluster XAS is shown in Fig. 3, where $2p_{3/2}\rightarrow3d$ (L_3) absorption spectra of mass selected iron clusters on (2×1)O/Ru(001) are given for different soft landing conditions.[41] In the lower panel of Fig. 3, Fe_1, Fe_2, and Fe_3 clusters were deposited into approximately 10 layers of argon, which was adsorbed on the (2×1)O/Ru(001) surface at less than 20 K prior to cluster deposition. Acceleration and retardation voltages were set to decelerate the cluster ions to less than 1–2 eV per atom. Since the energy distribution of

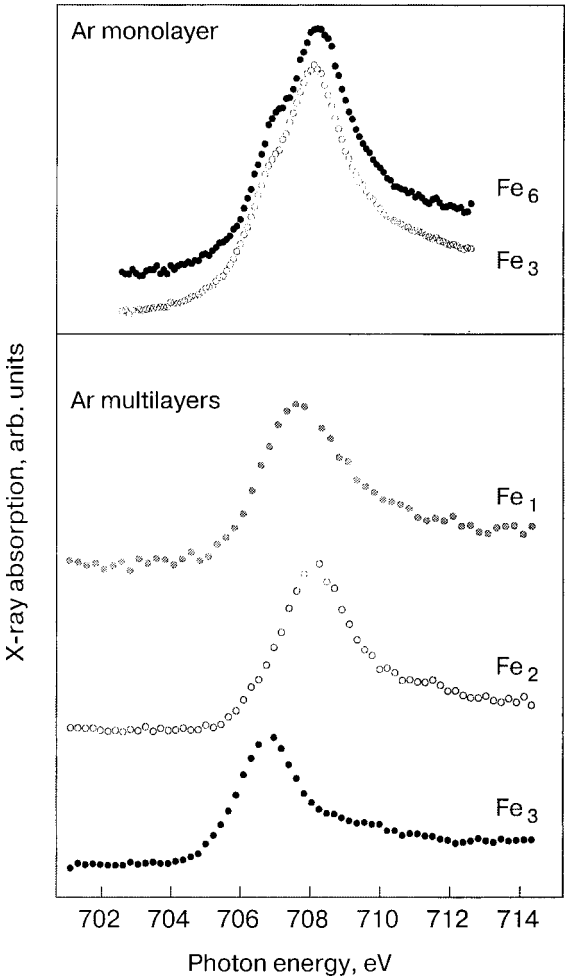

FIG. 3. X-ray absorption at the L_3 edge of mass-selected iron clusters on (2×1)O/Ru(001) for different soft landing conditions.

clusters produced in a sputter source[42,43] is centered about 5–10 eV, with a width of approximately 5–10 eV, the potential applied to the sample was set to 11 V higher than the acceleration voltage. This allows only clusters with an initial kinetic energy of more than 11 eV to reach the sample, and leads to a kinetic energy of less than 1–2 eV per atom even for small clusters. The equivalent coverage of iron atoms on the (2×1)O/Ru(001) surface is approximately 0.05 monolayers in all three cases.

The L_3 absorption edges of iron clusters in the lower panel of Fig. 3 clearly show different absorption energies. There is an energy shift in the L_3 edge absorption of about 0.5 eV to higher energy in going from Fe_1 to Fe_2 and of about 0.8 eV to lower energy in going from Fe_2 to Fe_3. The absorption spectra of these clusters were taken as deposited, at 20 K with the argon layer still present on the sample.

This energy shift in iron L_3 x-ray absorption hints at different electronic structures of the cluster species that can be observed on the surface after the clusters have been deposited into argon multilayers with a kinetic energy of less than 1–2 eV per cluster atom. Different cluster species with different electronic structure yield different L_3 x-ray absorption spectra. From the difference in the absorption spectra it can be deduced that soft landing conditions are fulfilled in this case and no cluster fragmentation occurs. The kinetic energy of the clusters is successfully dissipated by the argon buffer layers.

For comparison, the upper panel of Fig. 3 shows x-ray absorption spectra of Fe_3 and Fe_6 clusters which were deposited onto a (2×1)O/Ru(001) substrate that was covered with only one monolayer of argon atoms. The kinetic energy of the clusters again was 1–2 eV per cluster atom. After cluster deposition, the argon layer was desorbed from the (2×1)O/Ru(001) surface by heating to 100 K. The spectra were taken at 20 K. Two main features distinguish these spectra from the ones shown in the lower panel of Fig. 3. Both spectra in the upper panel look very similar and, in contrast to the clusters deposited into argon multilayers, exhibit one peak with a shoulder at the low-energy tail. From the structure and energy position of the absorption line it can be inferred that not just one but at least two different cluster species exist on the surface. Under these conditions, soft landing clearly fails. Fe_3 and Fe_6 clusters are fragmented or implanted if just one a monolayer of argon is used as a buffer layer for cluster deposition.

CLUSTER DIFFUSION AND AGGLOMERATION

To further test our finding that soft landing in argon multilayers preserves the initial cluster size, iron adatoms, dimers, and trimers deposited under soft landing conditions were annealed stepwise to room temperature. After annealing, the sample was cooled down again to 20 K for the measurements. Again, the size selected clusters were deposited into approximately 10 layers of argon preadsorbed on the (2×1)O/Ru(001) surface. These argon multilayers were desorbed from the sample surface after heating to 100 K. For every cluster deposited, there are also spectra taken prior to argon desorption.

In Fig. 4, x-ray absorption spectra of iron adatoms on (2×1)O/Ru(001) taken at 20 K with argon still present, and after successive annealing steps to 100, 150, 200, and 300 K are shown.

Annealing to 100 K does not significantly change the XAS line shape and position, although the L_3 line is broadened slightly. After annealing to 150 K, however, a double structure evolves in the L_3 line that is even more pronounced after annealing to 200 K. At 300 K, the first peak at approximately 707 eV is already stronger than the second peak at approximately 709 eV. This first peak corresponds nicely to the L_3 line of a bulk iron sample, also given in Fig. 4.

This evolution of the iron L_3 line can be interpreted in terms of diffusion and agglomeration of the iron adatoms. After deposition, the only species on the (2×1)O/Ru(001) surface is iron atoms. Soft landing conditions are sufficient to inhibit implantation, and the coverage is low enough to rule out agglomeration. Obviously, fragmentation cannot occur for single atoms. Upon annealing to 150 K, adatom diffusion leads to agglomeration and formation of iron islands on the (2×1)O/Ru(001) surface, as can be deduced from the evolution of a double peak at the L_3 absorption line. Since the low energy peak around 707 eV corresponds with the L_3 line of bulk iron, it can be ascribed to larger islands of iron atoms that have formed. After annealing to 300 K, most of the iron atoms on the (2×1)O/Ru(001) surface form

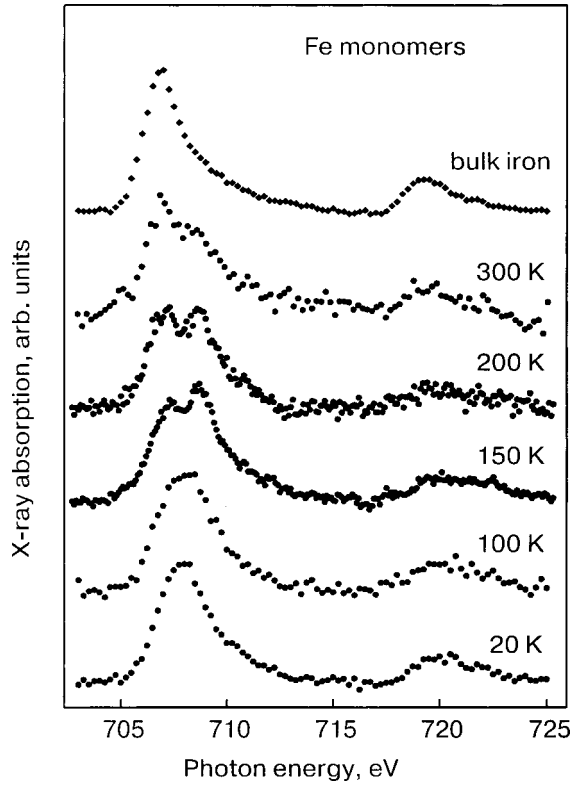

FIG. 4. $L_{2,3}$ x-ray absorption spectra of iron adatoms on (2 $\times$1)O/Ru(001) for different annealing temperatures. A step edge has been subtracted from all the spectra.[41]

these islands. Iron atoms on (2$\times$1)O/Ru(001) seem to be highly mobile even at 150 K.

A similar evolution of the L_3 line is shown in Fig. 5 for iron dimers on (2$\times$1)O/Ru(001). Again, a series of x-ray absorption spectra is shown after stepwise annealing from 20 to 400 K. In this case, iron dimers seem to be less mobile than iron adatoms. As observed in Fig. 4 for iron adatoms, a double structure also evolves in Fig. 5 for dimers at the L_3 line after annealing to 150 K, and is more pronounced after annealing to 200 K. At both annealing temperatures, however, it is less pronounced than in the corresponding iron adatom spectra in Fig. 4. After annealing to 300 and 400 K, the double structure even seems to disappear again. At 600 K (not shown here), only one very weak peak is visible, which has shifted further towards the position of the bulk iron line but has not reached it in energy.

Again, it can be inferred that only iron dimers are present on the (2$\times$1)O/Ru(001) surface after deposition under soft landing conditions. However, iron dimers on (2 $\times$1)O/Ru(001) do not seem to form large islands easily. Even after annealing to 400 and 600 K, the iron dimer L_3 line is at 1 eV higher photon energy than the corresponding bulk iron line.[41]

Iron trimers on (2$\times$1)O/Ru(001) are even more stable against diffusion than iron adatoms and dimers. This can be seen in Fig. 6, where a series of $L_{2,3}$ x-ray absorption spectra of iron trimers on (2$\times$1)O/Ru(001) is shown. Again, soft landing conditions with argon buffer layers and deceleration of the clusters were used for trimer deposition. Upon stepwise annealing to 400 K there is only very little change in the iron x-ray absorption spectra. This clearly shows that

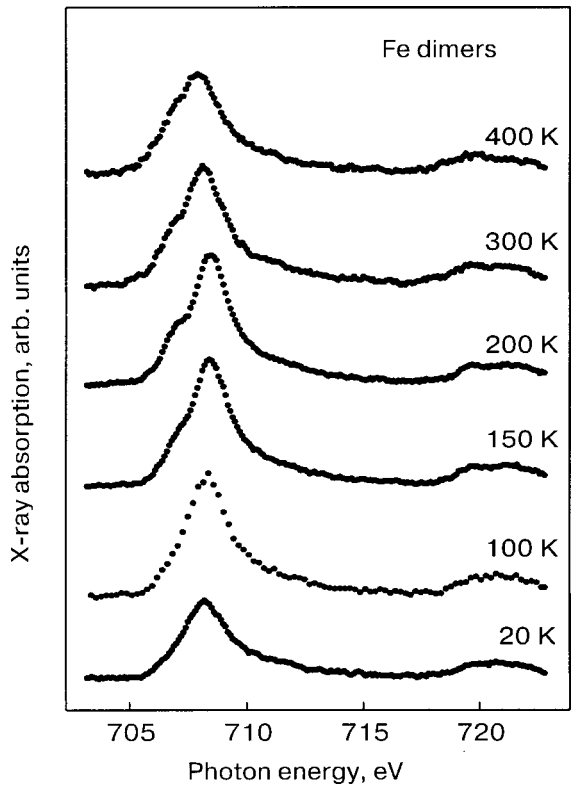

FIG. 5. $L_{2,3}$ x-ray absorption spectra of iron dimers on (2$\times$1)O/Ru(001) for different annealing temperatures. A step edge has been subtracted from all the spectra.[41]

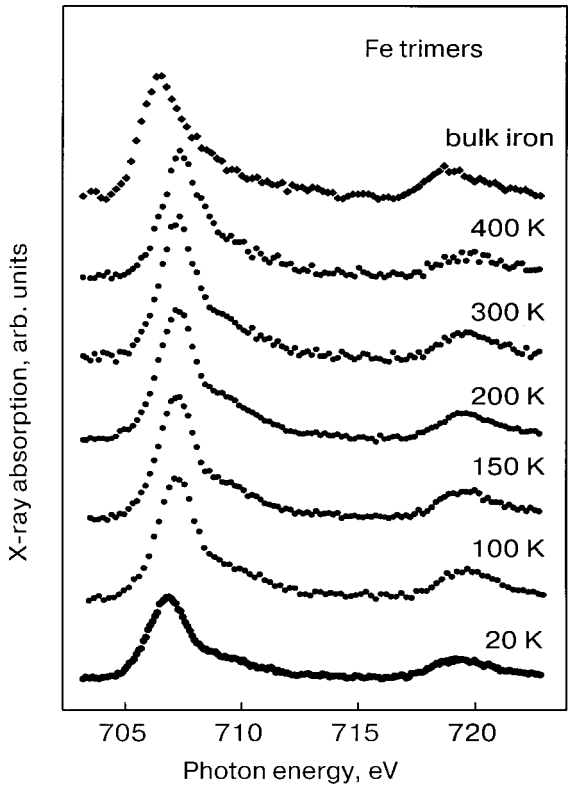

FIG. 6. $L_{2,3}$ x-ray absorption spectra of iron trimers on (2$\times$1)O/Ru(001) for different annealing temperatures. A step edge has been subtracted from all the spectra.[41]

almost no diffusion or agglomeration occurs with iron trimers on (2×1)O/Ru(001).

Iron adatoms, dimers, and trimers on (2×1)O/Ru(001) exhibit characteristic XAS signatures if cluster deposition is carried out with low kinetic energy into argon multilayers. In this case, soft landing is successful, and only one species is present on the sample surface. In contrast, if only one monolayer of argon is used as a buffer layer, soft landing is not successful even at low kinetic energy, and fragmentation occurs, as can clearly be seen in Fig. 2.

After mass selected cluster deposition, iron adatoms, dimers, and trimers show distinctive mobilities. Annealing leads to the formation of larger islands for deposited adatoms, whereas dimers and trimers on (2×1)O/Ru(001) seem to be more stable in respect to diffusion and agglomeration. The discernible fingerprints of different iron clusters on (2×1)O/Ru(001) can be used to characterize soft landing conditions, at least for small clusters. Similar results have been found for small nickel clusters on Ru(001) and (2×1)O/Ru(001).[44]

SUMMARY

Clusters are model systems for studying the evolution of physical properties with size from single atoms to bulk matter, either on free clusters in the gas phase or on deposited clusters. To study this evolution, size selection is a prerequisite. Rare gas matrices at low temperatures can be used as a tool to accomplish nondestructive cluster deposition on surfaces. X-ray absorption spectroscopy and STM and optical absorption and excitation spectroscopy are well suited for studying the soft landing of clusters. With their characteristic XAS signatures, iron adatoms can be distinguished from dimers and trimers on (2×1)O/Ru(001), and diffusion and agglomeration can be followed by monitoring the L_3 x-ray absorption line.

The soft landing experiments on iron clusters reported here were performed at BESSY I and II. Technical assistance from BESSY staff members and from E20 group members at Technische Universität München is gratefully acknowledged. This project was funded by BMBF through grant KS1GUB/5 and by DFG through grant Me 266/22-2.

*E-mail: wilfried.wurth@desy.de

[1] M. Schmidt and H. Haberland, C. R. Physique **3**, 327 (2002).
[2] H. Kietzmann, J. Morenzin, P. S. Bechthold, G. Ganteför, and W. Eberhardt, J. Chem. Phys. **109**, 2275 (1998).
[3] M.-H. Schaffner, F. Patthey, U. Heiz, W.-D. Schneider, O. Kuffer, H.-V. Roy, P. Fayet, J. K. Gimzewski, and R. Berndt, Eur. Phys. J. D **2**, 79 (1998).
[4] I. M. L. Billas, J. A. Becker, A. Châtelain, and W. A. de Heer, Phys. Rev. Lett. **71**, 4067 (1993).
[5] I. M. L. Billas, A. Châtelain, and W. A. de Heer, Science **265**, 1682 (1994).
[6] J. T. Lau, A. Föhlisch, R. Nietubyć, M. Reif, and W. Wurth, Phys. Rev. Lett. **89**, 057201 (2002).
[7] J. T. Lau, A. Föhlisch, M. Martins, R. Nietubyć, M. Reif, and W. Wurth, New J. Phys. **4**, 98.1–98.12 (2002).
[8] G. Schulze Icking-Konert, H. Handschuh, G. Ganteför, and W. Eberhardt, Phys. Rev. Lett. **76**, 1047 (1996).
[9] J. Ho, E. K. Parks, L. Zhu, and S. J. Riley, Chem. Phys. **201**, 245 (1995).
[10] L.-S. Wang, H. Wu, and S. R. Dhesi, Phys. Rev. Lett. **76**, 4853 (1996).
[11] H. R. Siekmann, C. Luder, J. Faehrmann, H. O. Lutz, and K.-H. Meiwes Broer, Z. Phys. D **20**, 410 (1991).
[12] M. Gartz, C. Keutgen, S. Kuenneke, and U. Kreibig, Eur. Phys. J. D **9**, 127 (1999).
[13] M.-H. Schaffner, J.-F. Jeannet, F. Patthey, and W.-D. Schneider, J. Phys. D: Appl. Phys. **31**, 3177 (1998).
[14] R. Klingeler, P. S. Bechthold, M. Neeb, and W. Eberhardt, Rev. Sci. Instrum. **73**, 1803 (2002).
[15] P. Jensen, Rev. Mod. Phys. **71**, 1695 (1999).
[16] J. A. Alonso, Chem. Rev. **100**, 637 (2000).
[17] C. Staudt, R. Heinrich, and A. Wucher, Nucl. Instrum. Methods Phys. Res. B **164–165**, 677 (2000).
[18] J. T. Lau, Ph.D. thesis, Universität Hamburg (2002), DESY-THESIS-2002-016.
[19] K. Bromann, C. Félix, H. Brune, W. Harbich, R. Monot, J. Buttet, and K. Kern, Science **274**, 956 (1996).
[20] W. Harbich, Philos. Mag. **79**, 1307 (1999).
[21] W. Harbich and C. Félix, C. R. Physique **3**, 289 (2002).
[22] R. Schaub, H. Jödicke, F. Brunet, R. Monot, J. Buttet, and W. Harbich, Phys. Rev. Lett. **86**, 3590 (2001).
[23] K. Bromann, H. Brune, C. Félix, W. Harbich, R. Monot, J. Buttet, and K. Kern, Surf. Sci. **377–379**, 1051 (1997).
[24] S. Fedrigo, W. Harbich, and J. Buttet, Phys. Rev. B **58**, 7428 (1998).
[25] C. Félix, C. Sieber, W. Harbich, J. Buttet, I. Rabin, W. Schulze, and G. Ertl, Phys. Rev. Lett. **86**, 2992 (2001).
[26] H.-P. Cheng and U. Landman, Science **260**, 1304 (1993).
[27] H.-P. Cheng and U. Landman, J. Phys. Chem **98**, 352 (1994).
[28] B. Nacer, C. Massobrio, and C. Félix, Phys. Rev. B **56**, 10590 (1997).
[29] G. Vandoni, C. Félix, and C. Massobrio, Phys. Rev. B **54**, 1553 (1996).
[30] S. Takami, K. Suzuki, M. Kubo, and A. Miyamoto, J. Nanoparticle Res. **3**, 213 (2001).
[31] K. Kholmurodov, I. Puzynin, W. Smith, K. Yasuoka, and T. Ebisuzaki, Comput. Phys. Commun. **141**, 1 (2001).
[32] M. Ratner, W. Harbich, and S. Fedrigo, Phys. Rev. B **60**, 11730 (1999).
[33] L. Lian, C.-X. Su, and P. B. Armentrout, J. Chem. Phys. **97**, 4072 (1992).
[34] L. Lian, C.-X. Su, and P. B. Armentrout, J. Chem. Phys. **96**, 7542 (1992).
[35] S. C. Wang, U. Kürpick, and G. Ehrlich, Phys. Rev. Lett. **81**, 4923 (1998).
[36] A. Golzhauser and G. Ehrlich, Phys. Rev. Lett. **77**, 1334 (1996).
[37] J. T. Lau, A. Achleitner, and W. Wurth, Surf. Sci. **467**, 834 (2000).
[38] N. A. Levanov, A. A. Katsnel'son, and A. E. Moroz, Phys. Solid State **41**, 1216 (1999).
[39] F. J. Palacios, M. P. Iñiguez, M. J. López, and J. A. Alonso, Phys. Rev. B **60**, 2908 (1999).
[40] J. T. Lau, A. Achleitner, and W. Wurth, Chem. Phys. Lett. **317**, 269 (2000).
[41] H.-U. Ehrke, Ph.D. thesis, Technische Universität München (2000).
[42] A. Wucher, N. K. Dzhemilev, I. V. Veryovkin, and S. V. Verkhoturov, Nucl. Instrum. Methods Phys. Res. B **149**, 285 (1999).
[43] A. Wucher, A. D. Bekkerman, N. K. Dzhemilev, S. V. Verkhoturov, and I. Veryovkin, Nucl. Instrum. Methods Phys. Res. B **140**, 311 (1998).
[44] A. Achleitner, J. T. Lau, and W. Wurth (in preparation).

This article was published in English in the original Russian journal. Reproduced here with stylistic changes by AIP.

Element-specific and site-specific ion desorption from adsorbed molecules by deep core-level photoexcitation at the *K*-edges

Y. Baba*

Synchrotron Radiation Research Center, Japan Atomic Energy Research Institute Tokai-mura, Naka-gun, Ibaraki-ken 319-1195, Japan

(Submitted November 20, 2002)
Fiz. Nizk. Temp. **29**, 303–320 (March 2003)

This article reviews our recent work on the ion desorption from adsorbed and condensed molecules at low temperature following the core-level photoexcitations using synchrotron soft x-rays. The systems investigated here are adsorbed molecules with relatively heavy molecular weight, containing third-row elements such as Si, P, S, and Cl. Compared with molecules composed of second-row elements, the highly element-specific and site-specific fragment-ion desorptions are observed when we tune the photon energy at the dipole-allowed $1s \rightarrow \sigma^*(3p^*)$ resonance. On the basis of the resonance Auger decay spectra around the $1s$ ionization thresholds, the observed highly specific ion desorption is interpreted in terms of the localization of the excited electrons (here called ''spectator electrons'') in the antibonding σ^* orbital. In order to separate the direct photo-induced process from the indirect processes triggered by the secondary electrons, the photon-stimulated ion desorption was also investigated in well-controlled mono- and multilayer molecules. The results confirmed that the resonant photoexcitation not in the substrate but in the thin films of adsorbates plays a significant role in the realization of the highly specific ion desorption. [DOI: 10.1063/1.1542444]

1. INTRODUCTION

Photo-induced processes at solid surfaces have attracted much attention not only as fundamental science but also as technological applications, because we can possibly synthesize new materials through nonthermal reactions. Among various photo-induced processes, those induced by energy-tunable synchrotron soft x rays have been the focus of considerable attention because the x-ray-induced reaction has the excellent properties known as ''element specificity'' and ''site specificity''. An x-ray-induced chemical reaction is triggered by the excitation and ionization of core-level electrons which are localized at the atomic site even in a multielement material. Thus we can possibly excite a specific element or specific chemical bond by tuning the energy of x rays at the inner-shell ionization threshold of the specific element. Using this characteristic, there exists a possibility that we can control a chemical reaction at a solid surface. For example, we can cut a specific chemical bond around a specific element as if we were using scissors or a knife. Recent progresses in this approach is reviewed in some of the articles cited as Refs. 1–4.

One might want to know, in what case can we cut a specific chemical bond? or, in other words, is there any general theory or general rule for realizing a specific bond scission? As to these questions, I would like to stress the following three general principles for realizing the highly specific chemical bond scission by core-level photoexcitation. First, the photoexcitation at the *K* edge is more efficient than those at the L_1, $L_{2,3}$, and *M* edges. This is simply understood by the absorption-edge jump, which is defined as the ratio of the photoionization cross sections σ_L/σ_H, where *L* and *H* refer, respectively, to the low- and high-energy sides of the absorption edges. The absorption-edge jumps of the *K* edge in all of the elements are higher than those of the *L* and *M* edges in the respective elements.[5] Second, the element specificity clearly shows up with increasing difference in the atomic number of the two elements. This is simply estimated by the calculated values of the photon-energy dependences of the photoionization cross sections.[6,7] A typical example is observed for the deep core-level excitation of a heavy element in a light-element matrix. Similarly, the shallow core-level excitation of a light element in a heavy-element matrix is also effective. The third factor is the resonance effect. If the resonance excitation from the core to valence unoccupied orbitals in a compound is a dipole-allowed transition, and the absorption-edge jump dramatically increases, which may result in highly specific fragmentation.

On the basis of the above speculations, this article deals mainly with the results for ion desorption following the resonant photoexcitations at the *K* edges for the adsorbed molecules. Especially, we concentrate on the ion desorption from relatively heavy molecules containing third-row elements such as Si, P, S, and Cl, because we found that the element specificity and site specificity clearly show up in the $1s \rightarrow 3p^*(\sigma^*)$ resonant photoexcitation in the third-row elements. Next, we shall discuss the mechanism of the observed highly specific ion desorption from condensed molecules on the basis of the photon-energy dependences of the desorption yields and the Auger decay spectra. In the adsorbed systems, the chemical reaction by the core-level excitation is caused by two processes, i.e., direct process triggered by the core-level photoexcitation and indirect processes which are induced by the secondary electrons. Therefore I finally present the results for the stimulated ion desorption from well-

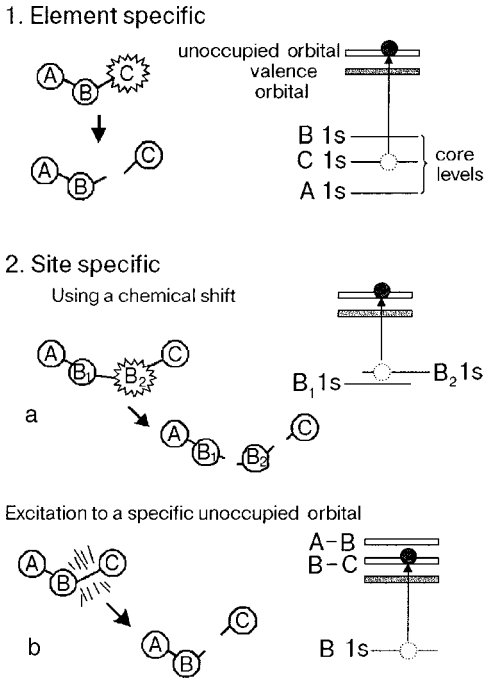

FIG. 1. Schematics of specific chemical reactions induced by inner-shell electron excitation using energy-tunable synchrotron soft x rays. The photon energies are tuned at the resonance excitation from core levels to the valence unoccupied orbitals.

controlled mono- and multilayers in order to elucidate the mechanism more clearly by separating these two processes.

2. GENERAL DESCRIPTIONS FOR ELEMENT-SPECIFIC AND SITE-SPECIFIC BOND SCISSIONS

The specific fragmentation and desorption initiated by core-level photoexcitation is characterized by the different patterns shown in Fig. 1. The first is the ''element-specific'' reaction depicted in Fig. 1(1). This is the most principal characteristic of core-level photo-excitation. In this simplified model, the photon energy is tuned at the core level of the element C. The element C is selectively excited leading to the breaking of only the B–C bond but not the A–B bond. For solid surfaces, the desorption of the element C is expected. The second case is the ''site-specific'' reaction. This is further divided into two cases. In the upper model (a), the core levels of the elements B have two energy levels (B_1 and B_2) depending on the chemical environment. This energy shift is called a chemical shift. If we tune the x-ray energy at the core level of B_2, only the B_2 atom is excited without exciting the B_1 atom. Consequently, the B_2–C or B_2–B_1 bond would be broken without cutting the A–B_1 bond. In the lower model (b), the element B has only a single core-level state, but the valence unoccupied state is divided into two levels localized at the B–C and A–B bond. In this figure, the core electrons in the element B are resonantly excited into the unoccupied state which is localized at the B–C bond. If this state has an antibonding character, the B–C bond would be broken but not the A–B bond.

3. EXPERIMENTAL DETAILS

A schematic diagram of the equipment around the sample is shown in Fig. 2. The samples investigated here are molecules containing third-row elements such as silane derivatives, disulfide, and chloromethane. Most of the samples are liquid at room temperature. The samples were purified and degassed through several freeze–pump–thaw cycles in the gas-dosing vacuum system connected with the analyzer chamber. Then the samples are dosed onto the clean surface of a metal or semiconductor single crystal cooled at 80 K.

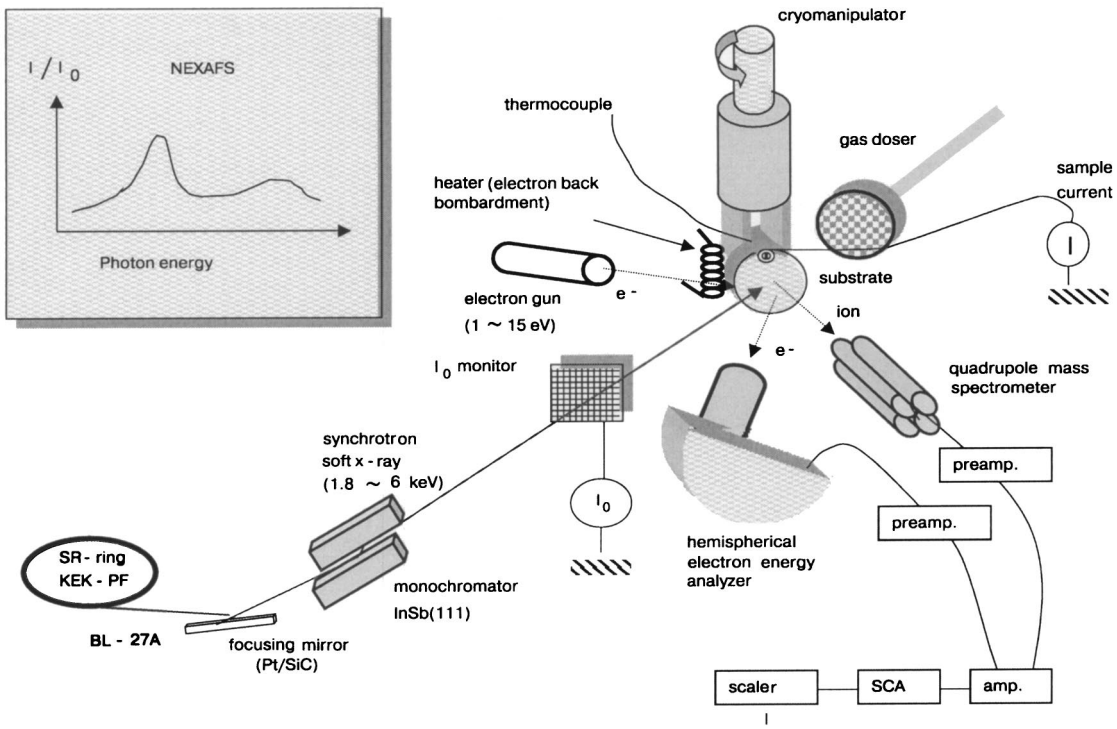

FIG. 2. Schematic diagram of the apparatus used for the experiments in this review.

Most of the experiments were conducted at the beam line (BL, 27A) station of the Photon Factory of the High Energy Accelerator Research Organization (KEK-PF). The detailed performance of this beam line has been described elsewhere.[8] The energy range of this beam line is 1.8–6 keV, which covers the *K* edges of third-row elements such as silicon, phosphorus, sulfur, and chlorine. For comparison, the resonance experiments at the *K* edges for second-row elements such as carbon and oxygen were also carried out at the beam line (BL, 7A) station of the KEK-PF.

The ultrahigh-vacuum system used in this work consisted of a cryomanipulator which can rotate around the vertical axis, an electron back bombardment system for sample heating, a temperature control system, quadrupole mass spectrometer (Q-mass), hemispherical electron energy analyzer, low-energy electron diffraction (LEED), sputter ion gun, low-energy electron gun, and gas doser. The x-ray absorption spectra were taken by plotting the sample drain current as a function of the photon energy. This method is called the ''total electron yield'' mode. The x-ray absorption spectrum around the core-level threshold is termed the ''x-ray absorption near-edge structure'' (XANES) or ''near edge x-ray absorption fine structure'' (NEXAFS). The desorbed ions were detected by the Q-mass operating in a pulse counting mode. The photon flux was always normalized by the drain current of the copper mesh located in front of the sample.

4. ELEMENT-SPECIFIC DESORPTION FROM CONDENSED MOLECULES

4.1. Condensed $SiCl_4$

The most essential question concerning the x-ray-induced processes in solid is: Are there any differences when the core levels in the different elements are excited in a multi-element solid? However, a clear answer to this simple question has not yet been given. For the photon-stimulated desorption from condensed light molecules, the fragment-ion desorption from solid CO and NO following the *K* edge excitations have been investigated by Rosenberg *et al.*[9] For solid CO they have observed enhancement of the C^+/O^+ ratios of about 30% under C *K* edge photoexcitation. It is obvious that the element specificity of the desorption depends primarily on the ratio of the photoionization cross sections, $\sigma_i/\sigma_{\text{total}}$, where σ_i and σ_{total} are the inner-shell photoionization cross sections of the element *i* and the total molecule, respectively. Based on this simple speculation, it can be deduced, that the element specificity more clearly shows up in a heavy element rather than a light element.

A typical example for a heavy molecule containing third-row elements is shown in Fig. 3.[10] This figure compares the mass spectral patterns of the desorbed ions from condensed $SiCl_4$ molecules irradiated by two kinds of photon energies corresponding to the Si *K* edge (upper spectrum) and the Cl *K* edge (lower spectrum). The photon-energy dependences of the ionization cross sections of silicon and chlorine are shown at the top of the figure. The x-ray absorption near-edge structure spectrum is displayed in the small inset in each mass spectrum. The photon energies are tuned at the respective resonance maxima of the $1s\rightarrow\sigma^*(3p^*)$ excitations. For Si *K*-edge excitation, not only molecular ions

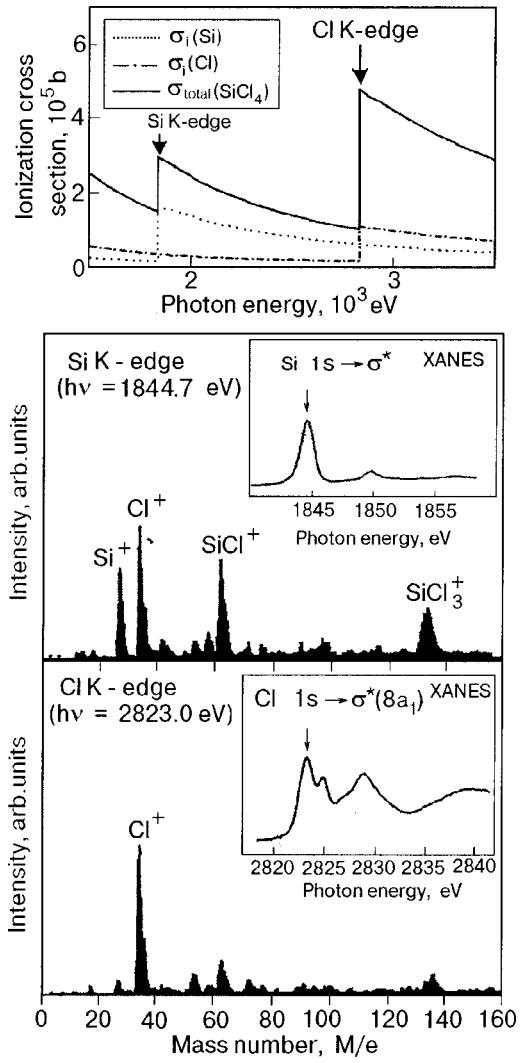

FIG. 3. Comparison of the mass spectral patterns of the desorbed ions from condensed $SiCl_4$ molecules irradiated by two kinds of photon energies, corresponding to the Si and Cl *K* edges. The x-ray absorption near-edge structure taken by the total electron yield is displayed in the small inset in each mass spectrum. The photon energy for the mass spectral measurements was tuned at the respective resonance maximum of $1s\rightarrow\sigma^*$ indicated in the XANES spectra. The photon-energy dependences of the ionization cross sections of silicon and chlorine[6] are shown at the top of the figure.

($SiCl^+$, $SiCl_3^+$) but also atomic ions (Si^+, Cl^+) are desorbed in comparable intensity, while most of the desorbed species following the Cl *K*-edge excitation are atomic Cl^+ ions. This is quite surprising because the core-level excitation is primarily followed by Auger decay, whose time scale is of the order of 10^{-15} s, which is faster by about three orders of magnitude than the time scale of the chemical bond-breaking. If the delocalization of the excitation happens before the chemical bond scission, the Auger electrons and the succeeding secondary electrons are the main trigger of the bond-breaking and ion desorption. This means that the same mass patterns should be observed even if the different core levels are excited. The present results suggest that the time scale of the Si–Cl bond scission and Cl^+ desorption is comparable to or faster than that of the delocalization of the excited states. Such highly element-specific desorption has been also observed for simple condensed molecules com-

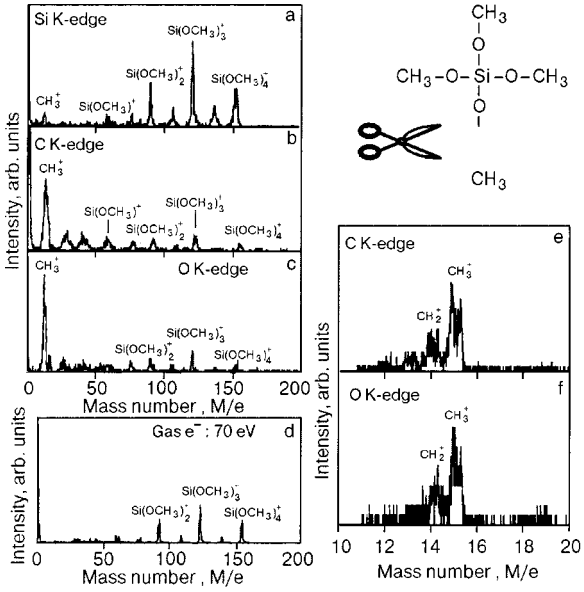

FIG. 4. Mass spectra for desorbed ions from condensed $Si(OCH_3)_4$ following silicon *K*-edge (a), carbon *K*-edge (b), and oxygen *K*-edge photoexcitations (c). The photon energy of each spectrum is tuned just at the $1s \rightarrow \sigma^*$ resonance maximum of the respective absorption edge. The mass spectrum of fragment ions for gas-phase $Si(OCH_3)_4$ excited by 70-eV electrons (so called cracking pattern) is in panel (d). Mass spectra in narrow regions with higher mass-resolution for C *K*-edge (e) and O *K*-edge excitations are shown at right (f).

posed of two kinds of third-row elements, such as PCl_3, S_2Cl_2 (Refs. 11 and 12).

4.2. Condensed silicon alkoxides

The element specificity of the core-level excitation has potential for future applications in photochemical processes at semiconductor surfaces. In silicon technology, for example, one of the key techniques is the deposition and etching of semiconductor surfaces without heating and damaging the substrate. The photochemical process is one of the candidate methods for this purpose. For metal–oxide–semiconductor (MOS) devices, it is required to fabricate an ultrathin and homogeneous oxide overlayer in a controlled small area on the semiconductor substrate. Silicon alkoxides such as tetramethoxysilane (TMOS) and tetraethoxysilane (TEOS) are excellent source materials for SiO_2 deposition on Si surface because of the conformal step coverage of SiO_2 layer and its nontoxic property. Niwano *et al.* have demonstrated the potentiality of synchrotron-radiation-induced CVD for the fabrication of SiO_2 films on Si using silicon alkoxides as source materials.[13–15] In their works, broadband synchrotron radiation in the vacuum ultraviolet (VUV) region emerging from the bending magnet has been used, and therefore the photon-energy dependences of the reaction remain unclear.

Our results using monochromatized synchrotron beam are shown in Fig. 4.[16] The left figures show the mass spectra of desorbed ions from condensed $Si(OCH_3)_4$ following (a) silicon *K*-edge, (b) carbon *K*-edge, and (c) oxygen *K*-edge excitations. The thickness of the adsorbates was 300 layers. The photon energy of each spectrum was tuned just at the $1s \rightarrow \sigma^*$ resonance maximum of the respective absorption edges. For comparison, the mass spectrum of fragment ions for gas-phase $Si(OCH_3)_4$ excited by 70-eV electrons (the so-called cracking pattern) is displayed in Fig. 4d. Since the electron energy for the gas-phase spectrum is lower than the Si $2p$, C $1s$, and O $1s$ thresholds, the gas-phase spectrum exhibits an ionic fragmentation pattern following not inner-shell excitation but valence excitation. The desorption spectrum at the Si *K*-edge excitation resembles the gas-phase one. For the C and O *K*-edge excitations, on the other hand, the most intense peak (except for H^+) is located around $M/e=15$. The long-time measurements with higher mass-resolution shown in Figs. 4e and 4f reveal that the most intense peaks originate from the CH_3^+ ions ($M/e=15$), but no O^+ ions ($M/e=16$) are observed. This indicates that the C–O bonds are selectively cut off following both carbon and oxygen *K*-edge excitations, but the Si–O bonds mostly remain unbroken. These results shed light on the possibility of selective C–O bond scission in condensed $Si(OCH_3)_4$ using monochromatized synchrotron radiation.

5. SITE-SPECIFIC DESORPTION

5.1. General descriptions

Next we consider examples of the site-specific desorption shown in Fig. 1(2). If the molecule has the same elements but inequivalent chemical environments, we can selectively excite each atom shown in Fig. 1(2a). Such an example was first found for a gas-phase molecule by Eberhardt *et al.*[17] They selectively excited two kinds of carbon atoms in acetone, which has inequivalent carbon atoms, and succeeded in observing the different ionic photofragmentation patterns depending on the atomic site being excited. Although some controversy still remains as to their results, this pioneering work stimulated the site-specific fragmentation in molecules following inner-shell photoexcitation. Clear examples of site-specific fragmentation using chemical shifts were recently reported by Nagaoka *et al.* for condensed molecules.[18,19] Even for an equivalent molecule like N_2, Romberg *et al.* recently demonstrated that one of the two nitrogen atoms in an adsorbed N_2 molecule can be selectively excited using a high-resolution synchrotron beam.[20,21] They observed different desorption patterns depending on the atomic site being excited.

In what follows we shall concentrate on the second case in Fig. 1(2b) The site-specific ion desorption from a solid surface represented by Fig. 1(2b) has been reported in many systems, such as organic polymers[22–27] and adsorbed molecules[28–40] following *K*-edge excitation in second-row elements. Here I shall give examples of highly site-specific ion desorption from adsorbed molecules following the $1s \rightarrow 3p^*$ resonance in the third-row elements, because the site specificity clearly shows up in deep-core excitations, as described previously.

5.2. Adsorbed $Si(CH_3)_3F$

Figure 5 shows the mass spectra of trimethyfluorosilane ($Si(CH_3)_3F$, TMFS). The upper figure displays the mass pattern of desorbed ions from TMFS adsorbed on the Cu (111) surface.[39] The thickness of the adsorbed layer was just one monolayer, which was precisely calibrated. Due to the highly

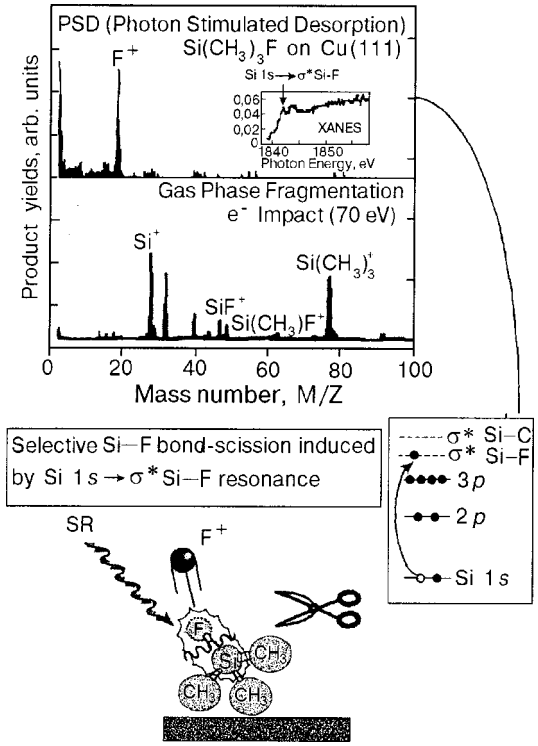

FIG. 5. Mass spectrum for desorbed ions from adsorbed $Si(CH_3)_3F$ following the Si 1*s* resonance photoexcitation (upper figure). The mass spectrum of fragment ions produced by 70 eV electron impact is shown in the lower figure.

electronegative character of the fluorine atom, the unoccupied valence orbitals of TMFS are split into two states. One consists of the σ^* orbitals localized at the Si–C bond (denoted as $\sigma^*_{(Si-C)}$), and the other of those localized at the Si–F bond (denoted as $\sigma^*_{(Si-F)}$). Here the photon energy was tuned at the resonance maximum from the Si 1*s* to unoccupied $\sigma^*_{(Si-F)}$ orbitals. For comparison, the mass spectrum of fragment ions in gas-phase TMFS following 70-eV electron impact is also shown in the lower figure. Electron impact produces many fragment ions containing silicon, which exhibits the mass cracking pattern following valence excitation. On the other hand, the Si $1s\rightarrow\sigma^*_{(Si-F)}$ resonance excitation in adsorbed TMFS results in the desorption of only F^+ ions other than hydrogen ions, which are the most abundant ions. The difference of the two mass patterns clearly indicates that resonant excitation from the Si 1*s* into the antibonding $\sigma^*_{(Si-F)}$ selectively breaks the Si–F bond without cutting the Si–C bond.

5.3. Condensed $(CH_3S)_2$

The data presented second is the fragment-ion desorption from condensed $(CH_3S)_2$ (dimethyl-disulfide, DMDS).[30] The sulfur atoms in this molecule are coordinated to two different kinds of atoms, i.e., sulfur and carbon. DMDS is chosen because this molecule is the simplest prototype of amino acid containing an S–S bond, such as cyctine, and the primary process of the x-ray-induced fragmentation is quite important in the fields of radiation biology.

The XANES spectrum taken by the total electron yield mode for multilayered DMDS is displayed in Fig. 6a as the top most spectrum (solid line). A sharp resonance peak with a double structure (marked *A*) and a broad peak (marked *B*) are observed in this energy region. In comparison with many of the gas-phase XANES spectra for alkylated divalent sulfur compounds,[41–43] the first intense peak *A* can be assigned as the S $1s\rightarrow\sigma^*$(S $3p^*$) excitation, and the second broad peak *B* is ascribed to the shape resonance corresponding to the excitation into higher-energy unoccupied orbitals such as S $3d^*$ and S $5s^*$. It is noticeable that the peak *A* is further split into two components. Figure 6b shows the same spectra but in an expanded energy scale. The energy separation of the two components in the XANES spectrum is 1.2 eV. Such peak splitting in the S $1s\rightarrow\sigma^*$ is never seen in divalent sulfur compounds containing a single S atom, such as dimethyl sulfide.[43] The occupied valence shell of the ground state of DMDS is $(9a)^2(10a)^2(9b)^2(10b)^2(11b)^2(11a)^2(12a)^2(13a)^2(12b)^2$ (Ref. 44). The outermost 12*b* and 13*a* orbitals are almost nonbonding, and their main components are S $3p$ orbitals.[45] The 12*a* orbital consists of σ(S–S) and the 11*a* and 11*b* orbitals have σ(S–C) character.[45] The energy levels of the σ(S–S) and σ(S–C) orbitals for gas-phase DMDS have been measured by ultraviolet photoelectron spectroscopy (UPS).[46] The energy separation between the 11*a* and 12*a* orbitals in the UPS spectrum is close to the present value of the energy splitting of the S $1s\rightarrow\sigma^*$ peak. It has been established that the relative energy levels of molecular orbitals scarcely change from the gas phase to the van der Waals molecular condensate. This is indeed the case for DMDS adsorbed on the Cu (111) surface at various temperatures.[46] Considering a mirror-like structure between occupied and unoccupied levels in the valence region, we assign the lower- and higher-energy components as the excitations from the S 1*s* to the σ^* localized at the S–S bond (hereafter referred to as $\sigma^*_{(S-S)}$) and to the σ^* localized at the S–C bond (hereafter referred to as $\sigma^*_{(S-C)}$), respectively. This is consistent with the simple assignment of the XANES spectrum of gas-phase DMDS by Hitchcock *et al.*[47] Similar energy splittings in the S $1s\rightarrow\sigma^*$ resonance peaks have also been observed in condensed layers of the S–S-containing compounds such as dichlorodisulfide (Cl–S–S–Cl) and dibutyldisulfide $(C_4H_9–S–S–C_4H_9)$.[48]

The desorbed species following the S *K*-edge excitation are mainly S^+ and CH_3^+ ions. The photon-energy dependences of the S^+- and CH_3^+-ion yields are presented in Fig. 6a as dotted curves. They are also shown in Fig. 6b in an expanded energy scale. Two different features are seen between the electron yield and desorption yield curves. First, excitation at the shape resonance (peak *B* in Fig. 6a) yields scarcely any ion desorption. Second, the S^+ ions are desorbed mainly at the S $1s\rightarrow\sigma^*_{(S-S)}$ resonance while the CH_3^+ ions are desorbed predominantly at the S $1s\rightarrow\sigma^*_{(S-C)}$ excitation (Fig. 6b). The latter feature clearly shows that the site-specific desorption apparently happens by photoexcitation from the same core orbital to different unoccupied valence orbitals. If the excited electrons are localized at the respective chemical bonds until the fragmentation happens, the observed tendency that the S $1s\rightarrow\sigma^*_{(S-S)}$ resonance yields S^+ desorption and the S $1s\rightarrow\sigma^*_{(S-C)}$ resonance induces CH_3^+ desorption is quite natural because both of the σ^* orbitals are strongly antibonding. The localized nature of the primary

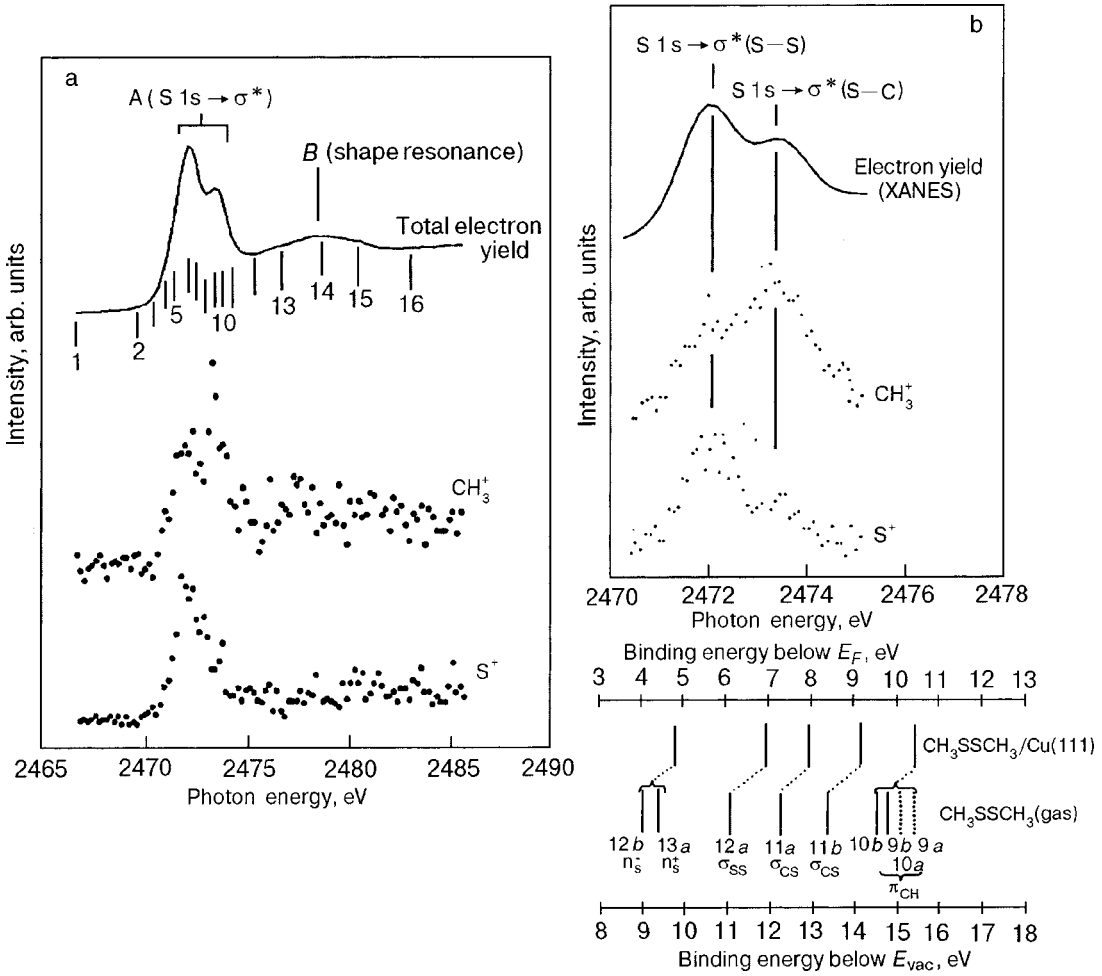

FIG. 6. Photon-energy dependences of the total electron yield (solid line) and ion desorption yield (dotted lines) for multilayered dimethyldisulfide (DMDS) around the sulfur *K*-edge photoexcitation. Total electron yield curve corresponds to the x-ray absorption spectrum (XANES). The number indicated in the total electron-yield curve represents the photon energy used for the measurements (Fig. 9a) of the Auger decay spectra (a). Same as Fig. 6a but in an expanded energy scale around the S $1s \rightarrow \sigma^*$ resonance (b).

photoexcitations will be discussed on the basis of the Auger decay spectra in the next Section.

6. AUGER DECAY AND MECHANISM OF ION DESORPTION

6.1. Patterns of Auger decay

In the previous Sections, I have presented some examples where the core-level excitations induce highly element-specific and site-specific ion desorptions. The data for the element-specific desorption show that localization of the core-electrons is the main cause of the specific ion desorption. Also the results for the site-specific desorption indicate that localization of the excited electrons in the antibonding state plays an important role in the specific ion desorption. Since the core-level excitation in low-*Z* elements is primarily followed by Auger decay,[49] I shall next present the Auger decay spectra in the present systems.

Let us first explain the Auger decay patterns in the present systems. For the third-row elements, the main decay channel following the ionization of the *K*-shell electron is primarily the $KL_{2,3}L_{2,3}$ Auger transition (radiative decay, i.e., fluorescence x-ray emission plays a minor role in the present system and is therefore not considered here).

Figure 7 shows the three types of Auger transitions which happen around the ionization threshold. The excitation into the continuum is followed by the $KL_{2,3}L_{2,3}$ normal Auger decay (a) resulting in two holes in the $L_{2,3}$ levels. This state is further followed by the $L_{2,3}VV$ Auger decay, which results in the final electronic configuration of V^{-4}, where V denotes the valence states and the superscript indicates the number of electrons taken away. The kinetic energy of the normal Auger electron is constant. For the core-to-valence resonant excitations, two other decay channels have to be taken into account. First is the participant Auger decay (b), where the excited electron participates the Auger decay process. The excited electron itself decays into the core hole, and another electron is emitted from the *L* shell. This process is virtually identical to photoemission of the *L*-shell electron. Thus the kinetic energy of the participant Auger electrons are the same as that of photoelectron from the $L_{2,3}$ shell directly excited by photons at the same energy. The second is the spectator Auger decay (c). In this case, the excited electron remains in the unoccupied orbital as a spectator, and another electron decays into the core hole. Then another second electron is emitted. The kinetic energy of the spectator Auger electron is close to that of the normal Auger electron. Re-

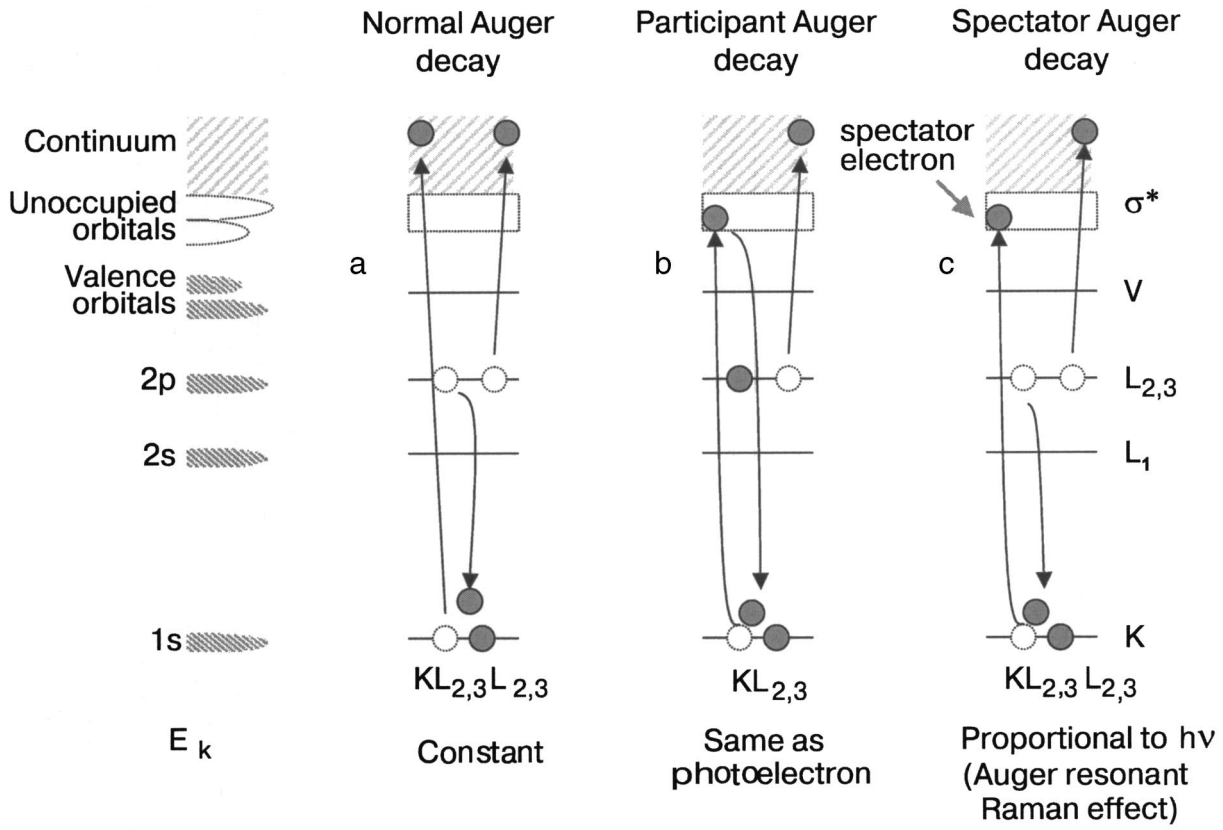

FIG. 7. Three types of the Auger transitions which happen around the inner-shell ionization threshold. The normal Auger decay following ionization is shown in (a); for the core-to-valence resonant excitations, two decay channels exist; (b) is the participant Auger decay, where the excited electron participates the Auger decay; (c) is the spectator Auger decay, where the excited electron remains in the unoccupied orbital as a spectator, and another electron decays into the core hole. Then another second electron is emitted. The remaining electron is called a ''spectator'' electron.

garding the energy of the spectator Auger electrons, we have observed that the kinetic energy of the Si KLL spectator Auger electrons in SiO_2 after Si K-edge excitation shifts linearly with the incident photon energy.[50,51] This phenomenon is observed in deep-core excitations for many adsorbed, condensed and solid systems, and the cause of the energy dispersion is ascribed to the Auger resonant Raman effect.[52–58] Therefore we can easily distinguish the spectator Auger peak from the normal one. The Auger resonant Raman effect more clearly shows up in condensed molecules and insulating solids than in metals and monolayer adsorbates. In the following discussion, it should be noted that the important point in the spectator Auger decay is that the excited electron remains in the unoccupied orbitals until the Auger decay. We will call the remaining electron a ''spectator electron'' (see Fig. 7).

6.2. Condensed $SiCl_4$

Concerning the element-specific desorption, let us go back to the $SiCl_4$ case (Fig. 3). For Cl K-edge excitation, most of the desorbed species are Cl^+ ions. The electron and Cl^+ ion yields around the Cl K-edge are displayed in Fig. 8e.[59] The XANES spectrum is basically in good agreement with those reported[60] for gas-phase $SiCl_4$. Mainly three peaks are observed (numbered 2, 4, and 6), which originate from Cl $1s \rightarrow \sigma^*(8a_1)$, Cl $1s \rightarrow \sigma^*(9t_2)$, and double excitation (shake-up satellite), respectively. However, a clear dissimilarity between electron yield and Cl^+ yield curves is seen. The Cl^+ yield curve has only one maximum, corresponding to the peak 2.

The electron energy spectra taken at various photon energies are displayed in Figs. 8a,b. Figure 8a includes the Cl KL participant and Cl KLV normal and Cl KLV spectator Auger decays. Figure 8b covers the Cl KLL normal and spectator Auger decays. In Fig. 8a a slight enhancement of the Cl $2p$ photoelectron peak around the Cl$\rightarrow\sigma^*$ resonance maximum ($h\nu = 2823.0$ eV) is observed. In column (c) the intensities of the Cl $2s$ and Cl $2p$ photoelectron peaks are plotted as a function of the incident photon energy. The increase in the Cl $2p$ intensity is about 25% at the Cl $1s \rightarrow \sigma^*(8a_1)$ resonance maximum. This enhancement corresponds to the Cl $KL_{2,3}$ participant Auger decay. In Fig. 8b we can clearly see the Cl $KL_{2,3}L_{2,3}$ spectator Auger lines (peak B), which shift linearly to higher energy with increase in the photon energy. The lower kinetic-energy peaks (A), which are observed at high photon energies, are due to the Cl $KL_{2,3}L_{2,3}$ normal Auger electrons. The intensities of the Cl $KL_{2,3}L_{2,3}$ spectator and normal Auger peaks are plotted in column (d) as a function of the photon energy. The plots of the intensity of the three types of the Auger peaks reveal that more than 98% of the Cl $1s \rightarrow \sigma^*(8a_1)$ resonance excitation is followed by spectator Auger decays (including KLL and KLV), while the contribution of the Cl $2p$-derived participant decay is less than 2%. It is also seen that the excitation

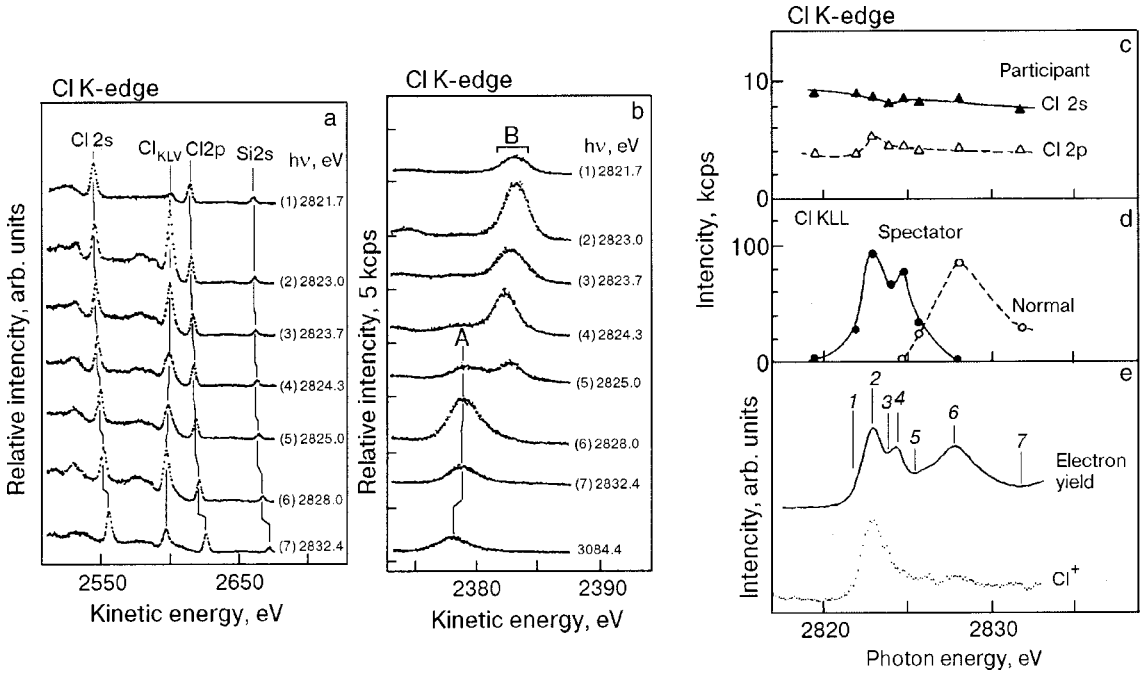

FIG. 8. Auger decay spectra of multilayered $SiCl_4$ in Cl $KL_{2,3}$ participant (a) and Cl $KL_{2,3}L_{2,3}$ spectator (b) regions excited by various photon energies around the Cl K edge. In the figure on the right, the intensities of the resonance peaks and the total electron yield and Cl^+ yield are plotted as a function of the photon energy.

at peak 6 is followed only by normal Auger decay. The most essential difference between normal and spectator Auger decays is whether or not the excited electron remains in the unoccupied orbitals in the course of the Auger electron emission (see Fig. 7). For excitation at peak 6, therefore, the excited electron is immediately delocalized before the movement of the Cl atom. Thus it is concluded that the existence of a ''spectator electron'' in the σ^* orbital is essential for the fragmentation which results in Cl^+ desorption.

When we compare two σ^* resonances with different symmetry, i.e., $8a_1$ (peak 2) and $9t_2$ (peak 4), the Cl^+ ions desorb mainly at peak 2 rather than at peak 4, although both excitations result in spectator Auger decay. Coulman *et al.* have found that the desorption of H^+ ions from a multilayer of H_2O after O $1s$ excitation is extremely enhanced by the O $1s\rightarrow 4a_1$ excitation.[61,62] They have ascribed this phenomenon to the strong antibonding character of the $4a_1$ orbital. The present results for $SiCl_4$ can be interpreted in a similar manner. The Cl $3p^*$ orbital content is higher in the $8a_1$ than in the $9t_2$ (Ref. 63), and consequently the spectator electron in the $8a_1$ is more effective for dissociation of the Si–Cl bond than the spectator electron in the $9t_2$. This speculation supports the above conclusion that the spectator electron in an antibonding orbital is essential for Cl^+ desorption. The high desorption yield by the Cl $1s\rightarrow\sigma^*(8a_1)$ resonance indicates that the nuclear motion of the Si–Cl bond is equivalent to or faster than the core life time. This means that the Franck–Condon transition cannot be applied to the bond dissociation process. As described above, such ultrafast non-Franck–Condon-like dissociation was reported for H^+ desorption by core excitation from condensed molecules such as H_2O (Refs. 61 and 62) and benzene (Ref. 64). The present results reveal that such a non-Franck–Condon-like process exists even for the desorption of heavier atoms like chlorine.

6.3. Condensed $(CH_3S)_2$

Again, we go back to the site-specific desorption in condensed DMDS (Fig. 6). In this case, the most intense Auger lines after the S $1s\rightarrow\sigma^*$ excitation would be the sulfur $KL_{2,3}L_{2,3}$ spectator Auger lines and the sulfur $KL_{2,3}$ participant Auger line. The former appears near the sulfur $KL_{2,3}L_{2,3}$ normal Auger line and the latter is observed as enhancement of the sulfur $L_{2,3}$(S $2p$) photoelectron. The Auger decay spectra around the sulfur $KL_{2,3}L_{2,3}$ region taken at various photon energies around the S $1s\rightarrow\sigma^*$ resonance are shown in Fig. 9a. The number indicated in each spectrum corresponds to the photon energy shown in the electron yield curve in Fig. 6a. The normal Auger peak with fixed kinetic energy apparently begins to appear from spectrum 11. The higher kinetic-energy peaks observed in the spectra 2–11 originate from the spectator Auger decay. A linear kinetic-energy shift with photon energy is also observed for the spectator Auger peaks. In Fig. 9b the kinetic energies of the sulfur $KL_{2,3}L_{2,3}$ Auger peaks are plotted as a function of incident photon energy. A two-step linear kinetic-energy dispersion is clearly observed in the spectator Auger peaks. Such two-step linear dispersion was explained by a fact that two kinds of the resonant excitations induce respective Auger resonant Raman effect. When the photon energy regions of linear dispersions are compared with those of the double structures in XANES spectrum (Fig. 6a), the first linear line marked as spectator (1) corresponds to the sulfur $KL_{2,3}L_{2,3}$ spectator Auger peak following S $1s\rightarrow\sigma^*_{(S-S)}$ excitation, and the second one marked as spectator (2) originates from that following S $1s\rightarrow\sigma^*_{(S-C)}$ excitation. Therefore it is important that both the S $1s\rightarrow\sigma^*_{(S-S)}$ and S $1s\rightarrow\sigma^*_{(S-C)}$ excitations are primarily followed by the respective spectator Auger decays. This finding suggests that the spectator electrons are local-

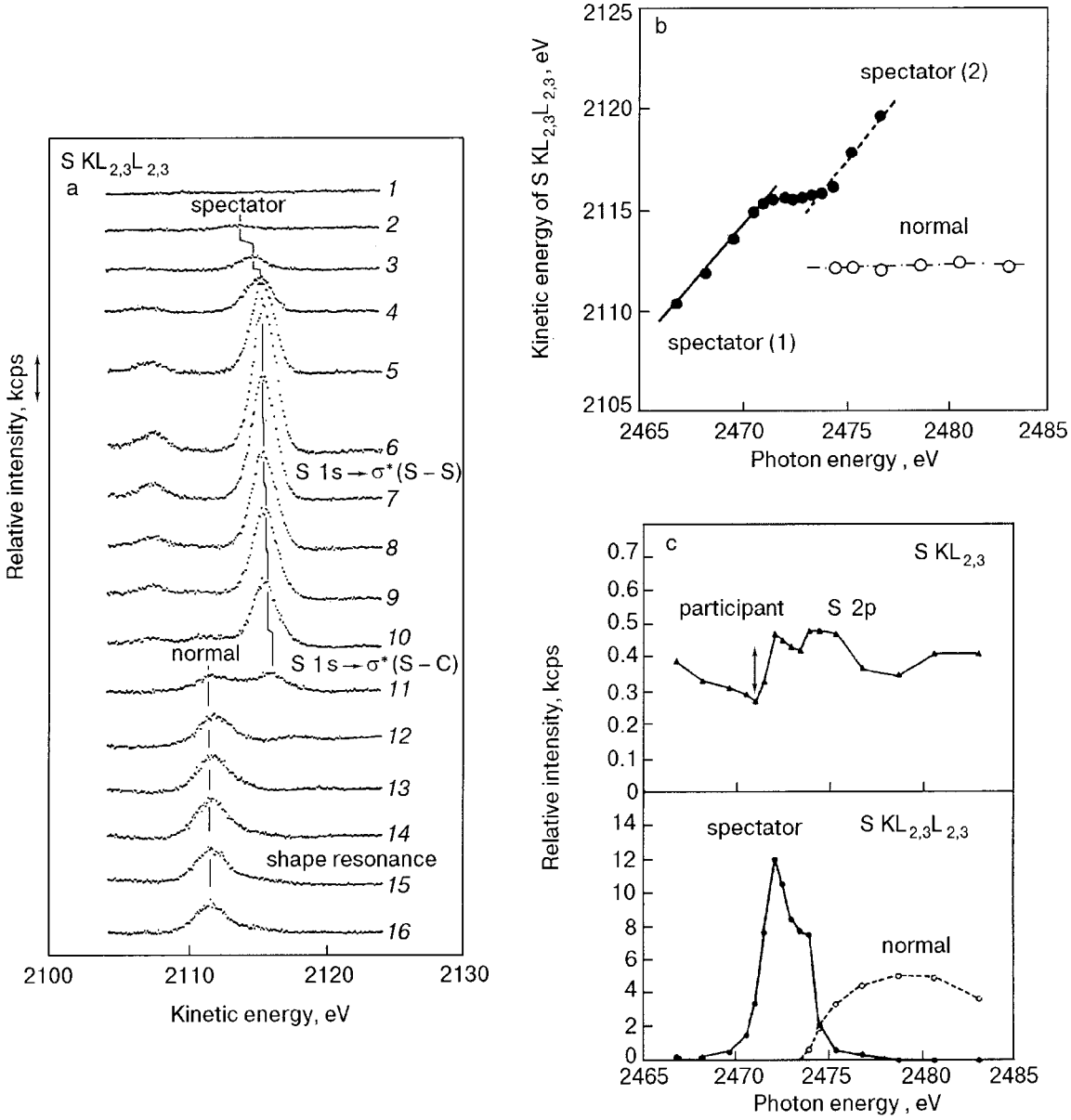

FIG. 9. Auger decay spectra of multilayered DMDS in the sulfur $KL_{2,3}L_{2,3}$ region excited by various photon energies around the sulfur *K* edge. The number indicated in each spectrum corresponds to the photon energy shown in the total electron yield curve in Fig. 6a (a). Relation between incident photon energy and the kinetic energy of the sulfur $KL_{2,3}L_{2,3}$ Auger line for multilayered DMDS around the sulfur *K*-edge excitation (b). Intensities of the Auger peaks as a function of photon energy (c).

ized at the respective chemical bonds in the course of the Auger decay. Figure 9c summarizes the photon-energy dependences of the peak intensities of various Auger lines. We have measured the other possible primary decay channels such as sulfur $KL_1L_{2,3}$, KL_1L_1, $KL_{2,3}V$, and KL_1V spectator decays and sulfur KL_1 participant decays, but it turned out that the contributions of these decay channels are less than 10% of the $KL_{2,3}L_{2,3}$ decay. When we compare Fig. 9c with the XANES spectrum in Fig. 6a, it is revealed that the $S\,1s\rightarrow\sigma^*$ resonant excitation is mostly followed by the sulfur $KL_{2,3}L_{2,3}$ spectator Auger decay but the participant decay channels play a minor role. Also it is seen that the shape resonance is essentially followed by the sulfur $KL_{2,3}L_{2,3}$ normal Auger decay.

The main decay channels and possible sequences of the electronic configurations are summarized in Table I for the four primary excitation modes, i.e., the $S\,1s\rightarrow\sigma^*_{(S-S)}$ resonance, $S\,1s\rightarrow\sigma^*_{(S-C)}$ resonance, shape resonance, and $S\,1s$ ionization. In this table, σ^{*1} represents the spectator electron and v denotes the valence orbital. The positive and negative indices marked in the orbital show the number of electrons and holes, respectively. The primary $KL_{2,3}L_{2,3}$ transitions are followed by the $L_{2,3}VV$ Auger decays, where V represents the valence orbital. It was shown that the $2p^{-2}\sigma^{*1}$ state created by the $KL_{2,3}L_{2,3}$ spectator Auger decay in a similar molecule is followed by the initial $L_{2,3}VV$ Auger decay with one $2p$ hole, which yields two valence holes, and succeeding $L_{2,3}VV$ decay without a $2p$ hole, which yields four valence holes. Although we could not distinguish between spectator and normal Auger decays in the $L_{2,3}VV$ Auger decay spectra due to the broad peak structures, we tentatively conclude that the spectator Auger decay would be predominant by taking the KLL results into consideration. Thus the final electronic

TABLE I. The main Auger decay channels and possible sequences of the electronic configurations; v represents one of the valence orbitals, and the index shown in each orbital denotes the number of electrons; σ^{*1}_{S-S} and σ^{*1}_{S-C} are the spectator electrons localized in the S–S and S–C bonds, respectively.

Excitation mode	Electronic configuration	Desorption
S $1s \rightarrow \sigma^{*}_{S-S}$	$[1s^{-1}\sigma^{*1}_{S-S}] \rightarrow [2p^{-2}\sigma^{*1}_{S-S}] \rightarrow [2p^{-1}v^{-2}\sigma^{*1}_{S-S}] \rightarrow [v^{-4}\sigma^{*1}_{S-S}]$ $KL_{2,3}L_{2,3}$ (spectator) $L_{2,3}VV$ $L_{2,3}VV$	$\rightarrow S^+, CH_3^+$
S $1s \rightarrow \sigma^{*}_{S-C}$	$[1s^{-1}\sigma^{*1}_{S-C}] \rightarrow [2p^{-2}\sigma^{*1}_{S-C}] \rightarrow [2p^{-1}v^{-2}\sigma^{*1}_{S-C}] \rightarrow [v^{-4}\sigma^{*1}_{S-C}]$ $KL_{2,3}L_{2,3}$ (spectator) $L_{2,3}VV$ $L_{2,3}VV$	$\rightarrow$ mostly, CH_3^+
S $1s \rightarrow 3d^{*}(5s^{*})$	$[1s^{-1}3d^{*1} \rightarrow [2p^{-2}] \rightarrow [2p^{-1}v^{-2}] \rightarrow [v^{-4}]$ $KL_{2,3}L_{2,3}$ (normal) $L_{2,3}VV$ $L_{2,3}VV$	$\rightarrow$ few
S $1s \rightarrow$ ionization	$[1s^{-1}] \rightarrow [2p^{-2}] \rightarrow [2p^{-1}v^{-2}] \rightarrow [v^{-4}]$ $KL_{2,3}L_{2,3}$ (normal) $L_{2,3}VV$ $L_{2,3}VV$	$\rightarrow$ few

configuration at the S $1s \rightarrow \sigma^*$ resonance is shown as $v^{-4}\sigma^{*1}$ in Table I.

It has been established that the positive-ion desorption following the inner-shell ionization is in many cases well explained on the basis of the localization of two or more positive holes in valence orbitals which are created by the sequence of Auger decays (KF model).[65] The Coulomb interaction between the two holes in an Auger final state leads to localization of this state if the Coulomb energy is larger than the bandwidth of the corresponding hole state. Then ultimately fragmentation and desorption due to the Coulomb repulsion will happen. This scenario is indeed the case for the adsorbed molecules (condensate) with a relatively narrow bandwidth of the one-hole state, except for monolayer adsorbates on a metal substrate, where the valence holes are well screened by the electrons in the metal substrate (discussed in the following section). Also in the present case, the KF process would be predominant in the photon energy range where the normal Auger decay happens. On the other hand, at the core-to-valence resonant excitation where the spectator Auger decay happens, the effect of the remaining electron in the σ^* orbital on the desorption process must also be taken into account. If the KF model can be applied not only to the core ionization but also to the resonant core excitation, the photon-energy dependence curve of the ion desorption yield would be identical to that of the total electron yield, because the total electrons are mostly composed of inelastically scattered low-energy electrons irrespective of the primary Auger decay processes. However, this is not the case for the present results (Fig. 6). Therefore, the observed dissimilarity between the XANES spectrum and ion yield curve suggests that there exists a process other than the KF process in the S^+ and CH_3^+ desorption.

The first point of dissimilarity is the disappearance of the shape resonance peak in the desorption yield curves (Fig. 6a). This result implies that the desorption of some fragment ion is enhanced by a special core-to-valence photoexcitation mode. Similar results have been reported for condensed H_2O (Refs. 61 and 62) benzene (Ref. 64) at the *K*-edge photoexcitation. Also the present authors have observed[66] the enhancement of the atomic Cl^+ desorption from multilayered CCl_4 and $SiCl_4$ at the Cl *K*-edge excitation, where the Cl $1s \rightarrow \sigma^*$ resonant excitation yields Cl^+ desorption, but higher-energy resonances such as Cl $1s \rightarrow 3d^*$ and $5s^*$ induce scarcely any Cl^+ desorption. In both the sulfur and chlorine cases the primary decay channels at the higher-energy resonances are completely $KL_{2,3}L_{2,3}$ normal Auger decay. This fact implies that the final electronic configuration like V^{-4} does not contribute very much to the fragmentation and ion desorption. It is the spectator electron in the σ^* orbital that is essential for the fragmentation.

The second point of dissimilarity between electron and ion yield curves is the intensity ratio of the S $1s \rightarrow \sigma^*_{(S-S)}$ and S $1s \rightarrow \sigma^*_{(S-C)}$ peaks (Fig. 6b). The Auger decay spectra show that both resonances are predominantly followed by the sulfur $KL_{2,3}L_{2,3}$ spectator Auger decay. As discussed above, the high desorption yield of Cl^+ ions at the Cl $1s \rightarrow \sigma^*$ resonance in adsorbed $SiCl_4$ is due to the excited electron (spectator electron) in the highly antibonding σ^* orbital. Similarly, the high desorption yields of the CH_3^+ and S^+ ions at the S $1s \rightarrow \sigma^*$ resonances in comparison with those at higher-energy excitation is interpreted in terms of the spectator electrons in the highly antibonding σ^* orbital. The special point in the present case is that the spectator electrons in the $\sigma^*_{(S-S)}$ and $\sigma^*_{(S-C)}$ bonds are localized at the respective sites, as is confirmed by the two-step linear kinetic-energy dispersion (Fig. 9b). Therefore the spectator electrons localized at the $\sigma^*_{(S-C)}$ orbital would break the S–C bond, while those localized at the $\sigma^*_{(S-S)}$ orbital would cut the S–S bond. The cleavage of the S–C bond will mainly produce CH_3^+ ions (higher charged ions such as CH_3^{2+} were not separated in the present experiment). On the other hand, breaking the S–S bond may produce CH_3S^+ ions. However, the intensity of the CH_3S^+ ions at the S $1s \rightarrow \sigma^*_{(S-S)}$ resonance is extremely low, and only CH_3^+ and S^+ ions are observed in comparable intensity. Concerning the desorption of molecular ions, we have observed that the desorption of the relatively light atomic Cl^+ ions from solid CCl_4 is induced by the spectator electron in the σ^* orbital, but the desorption of heavier molecular CCl_3^+ ions is not specially caused by the Cl $1s \rightarrow \sigma^*$ resonance due to the slow movement of such heavier molecular species.[66] This explanation holds for the absence of the CH_3S^+ desorption at the S $1s \rightarrow \sigma^*_{(S-S)}$ resonance. We consider that the comparable yields of the CH_3^+ and S^+ ions in mass spectrum are ascribed to the dissociation

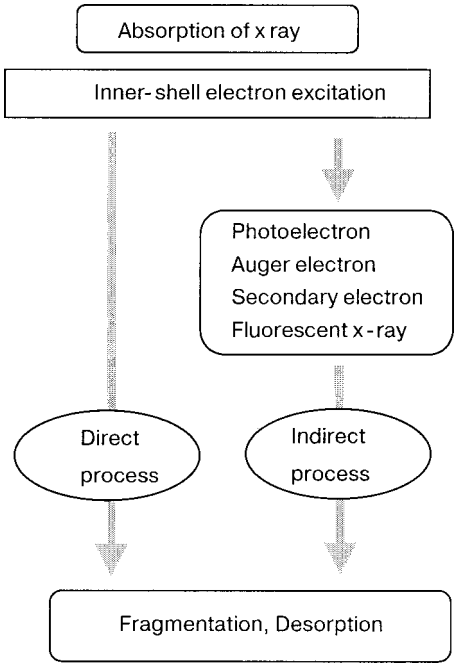

FIG. 10. Schematic of the direct and indirect processes in photofragmentation and desorption induced by inner-shell electron excitation.

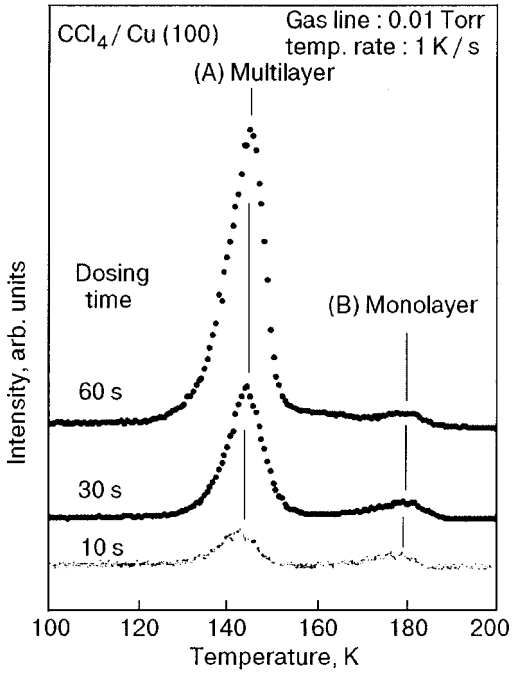

FIG. 11. Temperature-programmed-desorption spectra for CCl_4/Cu(100). The pressure of the gas-dosing vacuum line was kept at 0.01 Torr, and the surface was dosed at the respective time indicated in each spectrum.

of the CH_3S^+ in the course of the desorption process.

7. DIRECT AND INDIRECT PROCESSES IN X-RAY INDUCED ION DESORPTION

Up to here, we have presented some examples where the core-to-valence resonance excitations in condensed and solid molecules induce element-specific and site-specific ion desorption. The remaining question is, in what case does such a specific reaction happen? and, the other way, in what case does a specific reaction not happen? To answer these questions, it is important to separate two processes. The first is a ''direct'' process. This is the reaction directly induced by core excitation. If this process is predominant in the fragmentation and desorption, a specific excitation of core-level electrons would be followed by specific fragmentation and desorption. The second is an ''indirect'' process or ''secondary'' process. This is the reaction induced mainly by the secondary electrons, such as photoelectrons, Auger electrons, and inelastically scattered low-energy electrons. Even if the direct process at the core-to-valence resonance induces a specific reaction, the secondary electrons would also induce a nonspecific reaction. This situation is illustrated schematically in Fig. 10. One of the approaches used to separate the two processes in adsorbed systems is the coincidence technique, in which the desorbed ions are detected in coincidence with the photoelectrons and Auger electrons. This approach was reviewed in detail elsewhere by Mase *et al.*[67–70] Another approach is to prepare well-controlled mono- and multilayer films of molecules on a substrate, and compare the desorption features between adsorbate excitation and substrate excitation. The main idea is as follows. For the multilayer, the core excitation in the molecules takes place inside the layer. So the effect of secondary electrons on the reaction cannot be ignored. On the other hand, if we prepare a precise physisorbed monolayer and excite only adsorbed molecules, most of the secondary electrons are emitted into vacuum, so we can pick up only the direct process. For this purpose it is essential to prepare a pure physisorbed monolayer, because an island structure containing a multilayer region would severely affect the desorption features.

Figure 11 shows the examples of the temperature-programmed-desorption (TPD) spectra for CCl_4/Cu(100) taken at various dosing times.[71] The intensity of the lower-temperature peak (*A*) around 145 K increases proportionally with the dosing time, while that of the higher-temperature peak (*B*) around 180 K is constant. Therefore we assigned the peaks *A* and *B* as the desorption signals from the physisorbed multilayer and monolayer, respectively. The number

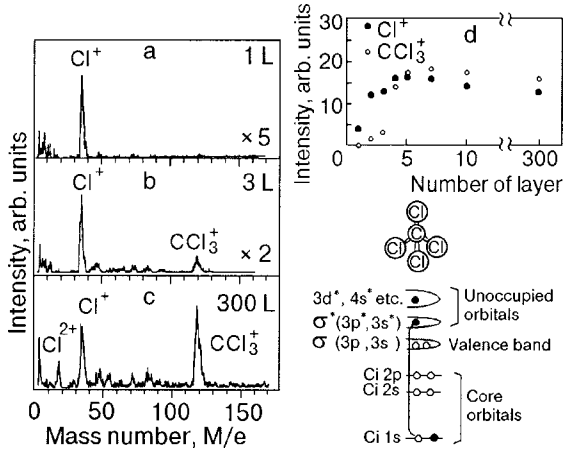

FIG. 12. Mass spectra of desorbed ions from adsorbed CCl_4 at various film thickness following the Cl $1s \rightarrow \sigma^*$ resonant photoexcitation ($h\nu = 2824.8$ eV). The number of layers indicated in each column was precisely determined by TPD measurements (a,b,c). Relative intensities of the Cl^+ and CCl_3^+ ions desorbed by the Cl $1s \rightarrow \sigma^*$ resonance as a function of the number of layers (d).

of the layer was precisely determined by the calibration curve for the intensity ratio of the peak *A* to peak *B* as a function of dosing time. For preparation of the pure monolayer we dose several layers at 80 K and then heat the substrate up to 165 K. This procedure results in the formation of a pure homogeneous monolayer.

Figure 12a, b, c shows the mass spectra of the desorbed ions from $CCl_4/Cu(100)$ at various thicknesses following the Cl $1s \rightarrow \sigma^*$ resonant photo-excitation ($h\nu = 2824.8$ eV).[72] For the multilayer, both atomic Cl^+ and molecular CCl_3^+ ions are desorbed in almost comparable intensity. In contrast, only Cl^+ ions are desorbed from the monolayer. In Fig. 12d the desorption intensities of these two species are plotted as a function of the film thickness. Predominance of the Cl^+ ions over the CCl_3^+ ions is observed in films thinner than 3 layers. The intensities of both ions are almost saturated at 4 layers. We consider that this phenomenon is due to the difference in the mass of the desorbed species. The desorption of the Cl^+ ions is ascribed to the fast bond-breaking process due to the spectator electron in the σ^* orbital, as previously discussed. This means that the movement of the Cl atom in the highly repulsive C–Cl potential curve begins already during the Auger transition, overcoming the screening by the copper substrate. This may induce the CCl_3^+ desorption as a counterpart. But due to the relatively slow movement of the heavier CCl_3^+ ions, the $v^{-4}\sigma^*$ state is quenched by the screening before the desorption of the CCl_3^+ ions happens. This means that for multilayered adsorbates (molecular condensates), the screening effect on the top surface layer is reduced as compared with that for the monolayer, because the adsorbates themselves behave as a spacer layer which hinders the charge transfer screening from the metal substrate. It has been reported that when a rare-gas spacer layer is introduced between the molecular adsorbate and metal substrate, the features of electron-stimulated desorption are not identical to those without a spacer layer, due to the weakening of the charge-transfer screening;[73] this is well consistent with the present results.

As to the photon-energy dependence of the desorption yield, Cl^+ desorption from the monolayer is observed only when the photon energy is tuned at the Cl $1s \rightarrow \sigma^*$ resonance in adsorbates. Note that the excitation of the substrate does not induce any ion desorption. This was clearly confirmed in similar systems where the core-to-valence resonant excitation in adsorbed thin films dominates the ion desorption over the secondary-electron-induced ion desorption following the substrate excitation.[74,75]

More-direct evidence for the screening effect of the substrate on the ion desorption can be obtained when we compare the ion desorption following the core excitation in physisorbed molecules by changing the electronic property of the substrate. The systems investigated are the photon-stimulated ion desorption by Cl *K*-edge excitation for a monolayer of CCl_4 on metallic Cu(100) (strong coupling), semiconducting Si(100) (medium coupling), and insulating SiO_2 with a wide band gap (weak coupling).[71] Figure 13 shows the mass spectra of the desorbed ions following the Cl *K*-edge excitation ($h\nu = 2824.2$ eV) for monolayer CCl_4 on three different substrates. The thickness of the layers was precisely adjusted by the TPD spectrum. It is clearly seen

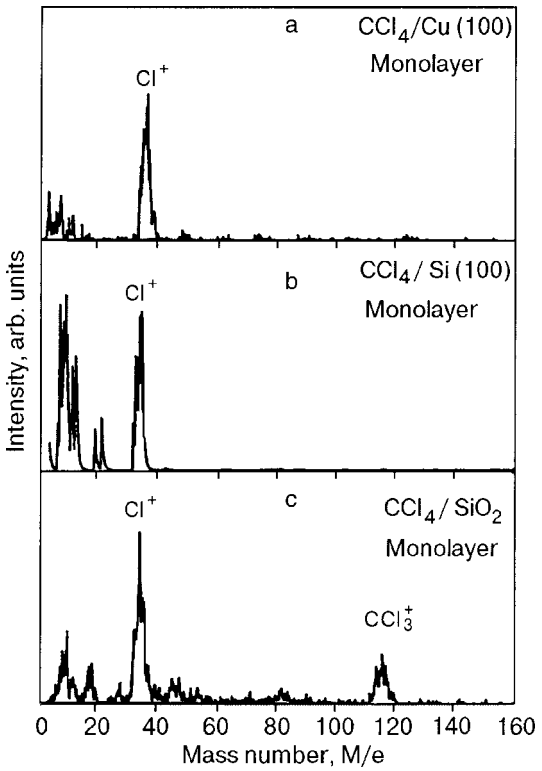

FIG. 13. Mass spectra of desorbed ions from $CCl_4/Cu(100)$ (a), $CCl_4/Si(100)$ (b), and CCl_4/SiO_2 (c) following the Cl *K*-edge excitation. The number of layers in each sample was precisely adjusted to be one monolayer based on the TPD measurements. The energy of the x ray is tuned at 2824.2 eV, which corresponds to the Cl $1s \rightarrow \sigma^*$ resonance excitation.

that only atomic Cl^+ ions are desorbed from monolayer CCl_4 on Cu(100) and Si(100) surfaces, while both atomic Cl^+ and molecular CCl_3^+ ions are desorbed from CCl_4/SiO_2. The difference in the mass spectral pattern suggests that excited states leading to the CCl_3^+ desorption are quenched in the strong- and medium-coupling systems, while they survive in weak-coupling system.

Figure 14 displays the photon-energy dependences of the total electron yields (TEY) and desorption yields around the Cl *K*-edge excitation for (a) $CCl_4/Cu(100)$ and (b) CCl_4/SiO_2. The peak positions and relative intensities of the TEY curve are almost the same as those reported for gas-phase CCl_4 and condensed CCl_4. The most intense peaks around 2824.2 eV originate from the resonant excitation from the Cl $1s$ to unoccupied σ^* orbital, and the higher-energy peaks centered around 2832 eV are attributed to excitations to a mixture of $5s^*$ and $3d^*$ orbitals. For $CCl_4/Cu(100)$, the Cl^+ desorption happens only at the Cl $1s \rightarrow \sigma^*$ resonance. The desorption peak at the Cl $1s \rightarrow 5s^*$, $3d^*$ resonance is missing. On the other hand, for CCl_4/SiO_2 a small maximum of the Cl^+ desorption is seen at the Cl $1s \rightarrow 5s^*$, $3d^*$ resonance.

In the bottom panels in Fig. 14 the kinetic energies of the Cl $KL_{2,3}L_{2,3}$ Auger peaks are plotted as a function of the incident photon energy. The kinetic energy of the spectator Auger peaks shifts linearly with increase in the photon energy. This phenomenon is characteristic to the spectator Auger electron and was interpreted in terms of the Auger resonant Raman effect,[52–58] as previously discussed. Note that

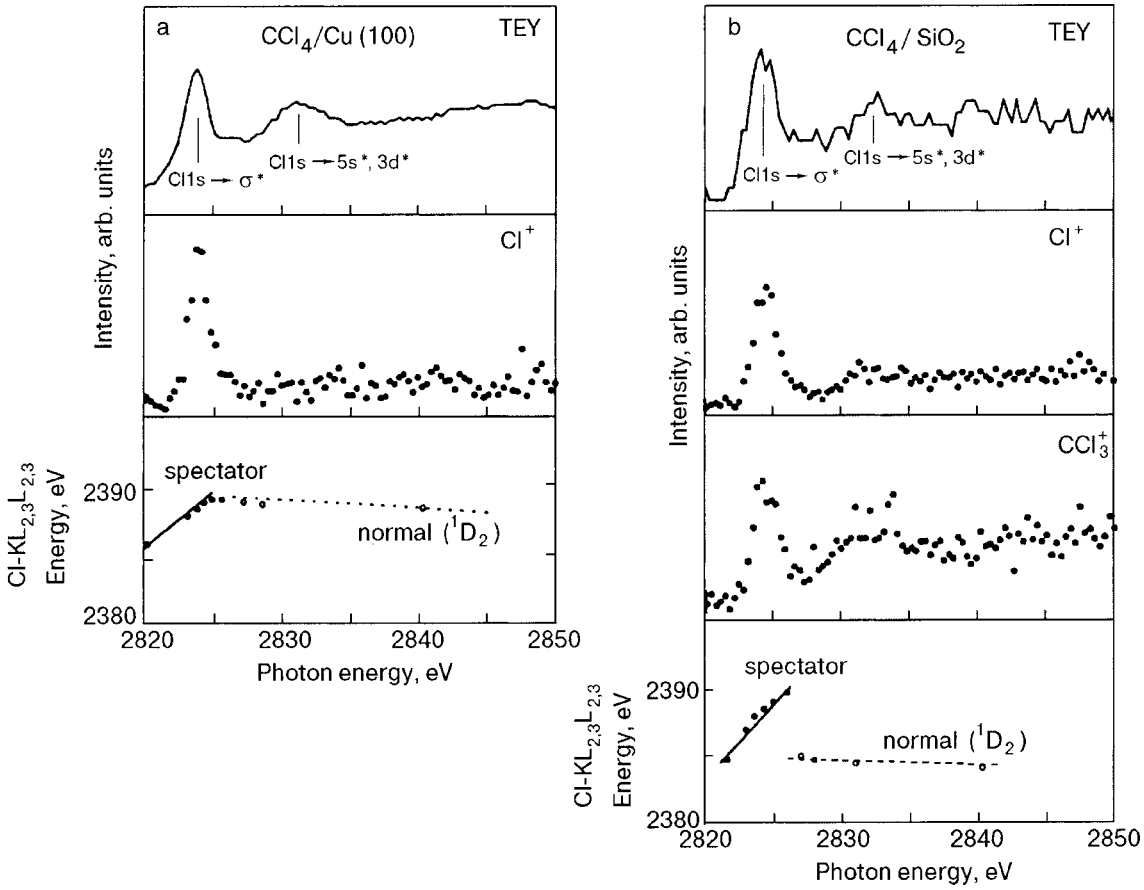

FIG. 14. Photon energy dependences of the total electron yields (XANES) and ion desorption yields for CCl_4/Cu(100) (a) and CCl_4/SiO_2 (b). In the bottom panels, the kinetic energies of the Cl $KL_{2,3}L_{2,3}$ Auger electrons are plotted as a function of the photon energy.

the discontinuity of the Cl $KL_{2,3}L_{2,3}$ energy is observed around the Cl $1s$ threshold, $h\nu = 2826$ eV, for CCl_4/SiO_2, while the spectator Auger peak changes continuously into the normal Auger peak for CCl_4/Cu(100). It was revealed that for strongly bound molecular adsorbates the Auger decay starts from a fully relaxed neutral core excited state, independently of the primary excitation (neutral or ionic). Actually the continuous energy shifts (from spectator to normal) was observed in monolayer adsorbates but not in multilayer adsorbates.[55] The observed discontinuity in CCl_4/SiO_2 suggests that the Auger decay below the Cl $1s$ threshold starts from not relaxed core excited state but fully localized $1s^{-1}\sigma^*$ state, resulting in the different final electronic configuration from that of the normal Auger decay.

On the basis of the results, the possible desorption mechanisms are as follows. For CCl_4/Cu(100) and CCl_4/Si(100), the Cl^+ desorption happens only at the Cl $1s \rightarrow \sigma^*$ resonance by the fast bond-breaking surviving the screening effect due to the remaining electron (the "spectator" electron) in the highly antibonding σ^* orbital. The missing of the CCl_3^+ desorption can be again interpreted by the quenching of the $V^{-4}\sigma^*$ states by the charge-transfer screening due to the relatively slow movement of molecular species. For the CCl_4/SiO_2 system, on the other hand, the existence of the CCl_3^+ ions indicates that even heavy molecular species survive because the screening effect is negligible. The CCl_3^+ yield curve fairly resembles the TEY curve (Fig. 14b). Such similarity between desorption yield curve of ionic fragment and XANES spectrum is a rather ordinary phenomenon in a condensed layer (multilayer), and this is interpreted by the effect of the inelastically scattered low-energy secondary electrons which are emitted following the Auger transition regardless of the Auger decay types. In a weakly screening substrate such as an insulator, such relatively slow processes as the secondary-electron effect survive until the molecular-ion desorption occurs, even in a monolayer molecular adsorbate. It is found that such slow processes play a key role in photochemical reactions on insulator surfaces. For the Cl^+ ion desorption from CCl_4/SiO_2, the contribution of the spectator-electron-induced fast bond-breaking would be included at the Cl $1s \rightarrow \sigma^*$ resonance. However, the weakly observed Cl^+ desorption at the Cl $1s \rightarrow 5s^*$, $3d^*$ resonance (Fig. 14b) cannot be interpreted in terms of the effect of the spectator electron because this excitation is apparently followed by normal Auger decay, whose final electronic configuration is V^{-4}. This slight enhancement would be attributed to the Coulomb repulsive force among the multivalence holes as a final state of the normal Auger decay.

8. CONCLUDING REMARKS

This article summarizes recent work on ion desorption from adsorbed molecules following irradiation by soft x rays. The data presented here are focused on the positive fragment-ion desorption from adsorbed and condensed molecules containing third-row elements following the *K*-edge

excitations. The element-specific and site-specific fragment-ion desorptions are clearly observed in condensed $SiCl_4$ and $Si(OCH_3)_4$. Examples of the site-specific ion desorption are also presented for adsorbed $Si(CH_3)_3F$ and condensed $(SCH_3)_2$. Such site-specific ion desorptions are characterized by resonant photoexcitation from the same core-level into different unoccupied orbitals. In order to clarify the mechanism of the highly specific ion desorption, we have measured the Auger decay spectra excited by the photons around the core-level ionization thresholds and the photon-energy dependences of the electron and ion yields. As a result, it is found the localization of the excited electrons in the antibonding valence orbitals (termed as ''spectator'' electrons) play key roles in the specific ion desorption as well as the localization of the core levels. The excitation of core levels in an adsorbed system is followed by the emission of various secondary electrons which may induce a nonspecific reaction. Therefore we separate the direct and indirect processes by preparing well-controlled mono- and multilayers. It is revealed that the resonant excitation in thin films of adsorbates induce highly specific desorption of light atomic ions. In contrast, the specificity becomes weak in multilayers due to the effect of the secondary electrons.

Understanding of the processes of element-specific and site-specific fragmentation and desorption from solid surfaces will shed light on the future application of x-ray-induced photochemical processes to the modification of materials surfaces.

The work reported here has been done with the excellent collaboration of Drs. T. A. Sasaki, H. Yamamoto, K. Yoshii, Y. Teraoka, T. Sekiguchi, and I. Shimoyama of Japan Atomic Energy Research Institute (JAERI). The most of the experiments presented here were performed at the BL-27A station of the Photon Factory of the High Energy Accelerator Research Organization (KEK-PF). I am deeply grateful to the support of the stuff of the KEK-PF, in particular Professor K. Kobayashi. Also Drs. H. Motohashi, H. Konish, A. Yokoya, and the stuff of JAERI are gratefully acknowledged for technical support in the experiments as well as fruitful discussion.

*E-mail: ybaba@popsvr.tokai.jaeri.go.jp

[1] R. A. Rosenberg and V. Rehn, Synchrotron Radiat. Res. **1**, 267 (1992).
[2] R. A. Rosenberg, S. P. Frigo, and J. K. Simon, Appl. Surf. Sci. **79/80**, 47 (1994).
[3] S. Nagaoka, K. Mase, and I. Koyano, Trends in Chem. Phys. **6**, 1 (1997).
[4] K. Tanaka, T. Sekitani, E. Ikenaga, K. Fujii, K. Mase, and N. Ueno, J. Electron Spectrosc. Relat. Phenom. **101–103**, 135 (1999).
[5] E. P. Bertin, *Principles and Practice of X-Ray Spectrometric Analysis*, Plenum Press, New York-London (1975), p.60.
[6] B. L. Henke, E. M. Gullikson, and J. C. Davis, At. Data Nucl. Data Tables **54**, 181 (1993). The data on the photoionization cross sections are accessible from the home page of the Center for X-Ray Optics (CXRO) at the Lawrence Berkeley National Laboratory (LBNL) (http://www-cxro.lbl.gov/).
[7] S. M. Seltzer, Radiat. Res. **136**, 147 (1993). The data on the mass absorption coefficients are accessible from the home page of the National Institute of Standards and Technology (NIST). (http://physics.nist.gov/PhysRefData/contents.html).
[8] H. Konishi, A. Yokoya, H. Shiwaku, H. Motohashi, T. Makita, Y. Kishihara, S. Hashimoto, T. Harami, T. A. Sasaki, H. Maeta, H. Ohno, H. Maezawa, S. Asaoka, N. Kanaya, K. Ito, N. Usami, and K. Kobayashi, Nucl. Instrum. Methods Phys. Res. A **372**, 322 (1996).
[9] R. A. Rosenberg, P. J. Love, P. R. LaRoe, V. Rehn, and C. C. Parks, Phys. Rev. B **31**, 2634 (1985).
[10] Y. Baba, K. Yoshii, and T. A. Sasaki, Surf. Sci. **341**, 190 (1995).
[11] Y. Baba, K. Yoshii, H. Yamamoto, T. A. Sasaki, and W. Wurth, Proc. Inter. Symp. Mater. Chem. Nucl. Environ, Tsukuba (1996), p. 391.
[12] Y. Baba, K. Yoshii, H. Yamamoto, T. A. Sasaki, and W. Wurth, Surf. Sci. **377–379**, 699 (1997).
[13] M. Niwano, N. Miyamoto, J. K. Simons, S. P. Frigo, and R. A. Rosenberg, Appl. Surf. Sci. **79/80**, 403 (1994).
[14] M. Niwano, J. K. Simons, S. P. Frigo, and R. A. Rosenberg, J. Appl. Phys. **75**, 7304 (1994).
[15] K. Kinashi, M. Niwano, J. Sawahata, F. Shimoshikiryo, and N. Miyamoto, J. Vac. Sci. Technol. A **13**, 1879 (1995).
[16] Y. Baba and T. Sekiguchi, J. Vac. Sci. Technol. A **18**, 334 (2000).
[17] W. Eberhardt, T. K. Sham, R. Carr, S. Krummacher, M. Strongin, S. L. Weng, and D. Wesner, Phys. Rev. Lett. **50**, 1038 (1983).
[18] S. Nagaoka, K. Mase, M. Nagasono, S. Tanaka, T. Urisu, and J. Ohshita, J. Chem. Phys. **107**, 10751 (1997).
[19] S. Nagaoka, K. Mase, M. Nagasono, S. Tanaka, T. Urisu, J. Ohshita, and U. Nagashima, Chem. Phys. **249**, 15 (1999).
[20] R. Romberg, N. Heckmair, S. P. Frigo, A. Ogurtsov, D. Menzel, and P. Feulner, Phys. Rev. Lett. **84**, 374 (2000).
[21] P. Feulner, R. Romberg, S. P. Frigo, R. Weimar, M. Gsell, A. Ogurtsov, and D. Menzel, Surf. Sci. **451**, 41 (2000).
[22] M. C. K. Tinone, K. Tanaka, J. Maruyama, N. Ueno, M. Imamura, and N. Matsubayashi, J. Chem. Phys. **100**, 5988 (1994).
[23] M. C. K. Tinone, T. Sekitani, K. Tanaka, J. Maruyama, and N. Ueno, Appl. Surf. Sci. **79/80**, 89 (1994).
[24] N. Ueno and K. Tanaka, Jpn. J. Appl. Phys. **36**, 7605 (1997).
[25] K. Fujii, T. Sekitani, K. Tanaka, S. Yamamoto, K. Okudaira, Y. Harada, and N. Ueno, J. Electron Spectrosc. Relat. Phenom. **88–91**, 837 (1998).
[26] K. Tanaka, T. Sekitani, E. Ikenaga, K. Fujii, K. Mase, and N. Ueno, J. Electron Spectrosc. Relat. Phenom. **101–103**, 135 (1999).
[27] K. Fujii, H. Tomimoto, K. Isshiki, M. Tooyama, T. Sekitani, and K. Tanaka, Jpn. J. Appl. Phys. **38**, 321 (1999).
[28] D. Menzel, G. Rocker, H. P. Steinrück, D. Coulman, P. A. Heimann, W. Huber, P. Zebisch, and D. R. Lloyd, J. Chem. Phys. **96**, 1724 (1992).
[29] H. I. Sekiguchi, T. Sekiguchi, and K. Tanaka, Phys. Rev. B **53**, 12655 (1996).
[30] Y. Baba, K. Yoshii, and T. A. Sasaki, J. Chem. Phys. **105**, 1996 (1996).
[31] H. Ikeura, T. Sekiguchi, and K. Tanaka, J. Electron Spectrosc. Relat. Phenom. **80**, 121 (1996).
[32] T. Sekiguchi, H. I. Sekiguchi, K. Obi, and K. Tanaka, J. Phys. IV, 7 (C2, *X-Ray Absorption Fine Structure*, Vol. 1), 505 (1997).
[33] J. M. Chen, K. T. Lu, R. G. Liu, J. W. Lay, and Y. C. Liu, J. Chem. Phys. **106**, 9105 (1997).
[34] T. Sekitani, E. Ikenaga, K. Tanaka, K. Mase, M. Nagasono, S. Tanaka, and T. Usiru, Surf. Sci. **390**, 107 (1997).
[35] H. I. Sekiguchi and T. Sekiguchi, Surf. Sci. **390**, 214 (1997).
[36] J. M. Chen, K. T. Lu, R. G. Liu, J. W. Lay, Y. C. Liu, and T. J. Chuang, J. Chem. Phys. **108**, 7849 (1998).
[37] J. M. Chen, R. G. Liu, Y. J. Hsu, S. C. Yang, Y. C. Liu, Y. P. Lee, C. R. Wen, and T. J. Chuang, J. Chem. Phys. **109**, 8027 (1998).
[38] T. Sekitani, E. Ikenaga, H. Matsuo, S. Tanaka, K. Mase, and K. Tanaka, J. Electron Spectrosc. Relat. Phenom. **88–91**, 831 (1998).
[39] T. Sekiguchi and Y. Baba, Surf. Sci. **433–435**, 849 (1999).
[40] H. I. Sekiguchi, T. Sekiguchi, M. Imamura, N. Matsubayashi, H. Shimada, and Y. Baba, Surf. Sci. **454–456**, 407 (2000).
[41] S. Bodeur and J. M. Esteva, Chem. Phys. **100**, 415 (1985).
[42] C. Dezarnaud, M. Tronc, and A. P. Hitchcock, Chem. Phys. **142**, 455 (1990).
[43] C. Dezarnaud, M. Tronc, and A. Modelli, Chem. Phys. **156**, 129 (1991).
[44] K. Kimura, S. Katsumata, Y. Achiba, T. Yamazaki, and S. Iwata, *Handbook of He I Photoelectron Spectra of Fundamental Organic Molecules*, Science Society Press, Tokyo (1981).
[45] J. Tokue, A. Hiraya, and K. Shobatake, Chem. Phys. **130**, 401 (1991).
[46] S. Bao, C. F. McConville, and D. P. Woodruff, Surf. Sci. **187**, 133 (1987).
[47] A. P. Hitchcock, S. Bodeur, and M. Tronc, Physica B **158**, 257 (1989).
[48] Y. Baba, K. Yoshii, and T. A. Sasaki (unpublished).
[49] M. O. Kraus, J. Phys. Chem. Ref. Data **8**, 307 (1979).
[50] Y. Baba, T. A. Sasaki, and H. Yamamoto, Phys. Rev. B **49**, 709 (1994).
[51] Y. Baba, H. Yamamoto, and T. A. Sasaki, Surf. Sci. **307**, 896 (1994).
[52] T. A. Sasaki, Y. Baba, K. Yoshii, H. Yamamoto, and T. Nakatani, Phys. Rev. B **50**, 15519 (1994).

[53] T. A. Sasaki, Y. Baba, K. Yoshii, and H. Yamamoto, J. Phys.: Condens. Matter **7**, 463 (1995).
[54] T. A. Sasaki, Y. Baba, K. Yoshii, and H. Yamamoto, J. Electron Spectrosc. Relat. Phenom. **76**, 411 (1995).
[55] K. Yoshii, Y. Baba, and T. A. Sasaki, J. Electron Spectrosc. Relat. Phenom. **79**, 215 (1996).
[56] K. Yoshii, Y. Baba, and T. A. Sasaki, J. Phys.: Condens. Matter **9**, 2839 (1997).
[57] K. Yoshii, Y. Baba, and T. A. Sasaki, Phys. Solid State **206**, 811 (1998).
[58] K. Yoshii, Y. Baba, and T. A. Sasaki, J. Electron Spectrosc. Relat. Phenom. **93**, 105 (1998).
[59] Y. Baba, K. Yoshii, and T. A. Sasaki, Surf. Sci. **357–358**, 302 (1996).
[60] S. Bodeur, I. Nenner, and P. Millie, Phys. Rev. A **34**, 2986 (1986).
[61] D. Coulman, A. Puschmann, W. Wurth, H. P. Steinrück, and D. Menzel, Chem. Phys. Lett. **148**, 371 (1988).
[62] D. Coulman, A. Puschmann, U. Hofer, H. P. Steinrück, W. Wurth, P. Feulner, and D. Menzel, J. Chem. Phys. **93**, 58 (1990).
[63] H. Ishikawa, K. Fujima, J. Adachi, E. Miyauchi, and T. Fujii, J. Chem. Phys. **94**, 6740 (1991).
[64] D. Menzel, G. Rocker, H. P. Steinrück, D. Coulman, P. A. Heimann, W. Huber, P. Zebisch, and D. R. Loyd, J. Chem. Phys. **96**, 1724 (1992).
[65] M. L. Knotek and P. J. Feibelman, Phys. Rev. Lett. **40**, 964 (1978).
[66] Y. Baba, K. Yoshii, and T. A. Sasaki, Surf. Sci. **376**, 330 (1997).
[67] K. Mase, M. Nagasono, S. Tanaka, M. Kamada, T. Urisu, and Y. Murata, Rev. Sci. Instrum. **68**, 1703 (1997).
[68] K. Mase, M. Nagasono, S. Tanaka, T. Urisu, E. Ikenaga, T. Sekitani, and K. Tanaka, J. Chem. Phys. **108**, 6550 (1998).
[69] K. Mase and S. Tanaka, Jpn. J. Appl. Phys. **38**, 233 (1999).
[70] K. Mase, S. Tanaka, M. Nagasono, and T. Urisu, Surf. Sci. **451**, 143 (2000).
[71] Y. Baba and T. Sekiguchi, Surf. Sci. **433–435**, 843 (1999).
[72] Y. Baba, K. Yoshii, and T. A. Sasaki, Surf. Sci. **402–404**, 115 (1998).
[73] M. Scheuer and D. Menzel, Surf. Sci. **390**, 23 (1997).
[74] J. M. Chen, S. C. Yang, and Y. C. Liu, Surf. Sci. **391**, 278 (1997).
[75] T. Sekiguchi, Y. Baba, Y. Li, and M. Ali (unpublished).

This article was published in English in the original Russian journal. Reproduced here with stylistic changes by AIP.

Ion desorption from molecules condensed at low temperature: A study with electron-ion coincidence spectroscopy combined with synchrotron radiation (Review)

Kazuhiko Mase

Photon Factory, Institute of Materials Structure Science, High Energy Accelerator Research Organization, 1-1 Oho, Tsukuba 305-0801, Japan

Mitsuru Nagasono[a)]

Institute for Molecular Science, Okazaki 444-8585, Japan

Shin-ichiro Tanaka[b)]

Department of Physics, Graduate School of Science, Nagoya University Furo-cho, Chikusa-ku, Nagoya 464-8602, Japan

Tetsuji Sekitani

Department of Physical Science, Graduate School of Science Hiroshima University, Higashi-Hiroshima 739-8526, Japan

Shin-ichi Nagaoka[c)]

Chemistry Group, Department of Fundamental Material Science, Faculty of Science, Ehime University, Matsuyama 790-8577, Japan

(Submitted May 24, 2002)
Fiz. Nizk. Temp. **29**, 321–341 (March 2003)

This article reviews our recent work on photostimulated ion desorption (PSID) from molecules condensed at low temperature. We have used electron–ion coincidence (EICO) spectroscopy combined with synchrotron radiation. The history and present status of the EICO apparatus is described, as well as our recent investigations of condensed H_2O, NH_3, CH_3CN, and CF_3CH_3. Auger electron photon coincidence (AEPICO) spectra of condensed H_2O at the O:1s ionization showed that H^+ desorption was stimulated by O:KVV Auger processes leading to two-hole states (normal-Auger stimulated ion desorption (ASID) mechanism). The driving forces for H^+ desorption were attributed to the electron missing in the O–H bonding orbitals and the effective hole–hole Coulomb repulsion. The normal ASID mechanism was also demonstrated for condensed NH_3. The H^+ desorption at the $4a_1 \leftarrow$ O(N):1s resonance of both condensed H_2O and condensed NH_3 was found to be greatly enhanced. Based on the AEPICO spectra the following four-step mechanism was proposed: (1) the $4a_1 \leftarrow 1s$ transition, (2) extension of the HO–H (H_2N–H) distance within the lifetime of the $(1s)^{-1}(4a_1)^1$ state, (3) spectator Auger transitions leading to $(\text{valence})^{-2}(4a_1)^1$ states, and (4) H^+ desorption. The enhancement of the H^+ desorption yield was attributed to the repulsive potential surface of the $(1s)^{-1}(4a_1)^1$ state. At the $3p \leftarrow$ O:1s resonance of condensed H_2O, on the other hand, the H^+ yield was found to be decreased. The AEPICO spectra showed that the H^+ desorption was stimulated by spectator Auger transitions leading to $(\text{valence})^{-2}(3p)^1$ states. The decrease in the H^+ yield was attributed to a reduction in the effective hole–hole Coulomb repulsion due to shielding by the $3p$ electron. Photoelectron photon coincidence (PEPICO) spectra of condensed H_2O showed that the core level of the surface H_2O responsible for the H^+ desorption was shifted by 0.7 eV from that of the bulk H_2O. The H^+ desorption from condensed CH_3CN was also investigated. In a study of condensed CF_3CH_3 using PEPICO spectroscopy, site-specific ion desorption was directly verified; that is, H^+ and CH_3^+ desorption was predominant for the C:1s photoionization at the -CH_3 site, while $C_2H_n^+$, $CFCH_m^+$, and CF_3^+ desorption was predominantly induced by the C:1s photoionization at the -CF_3 site. These investigations demonstrate that EICO spectroscopy combined with synchrotron radiation is a powerful tool for studying PSID of molecules condensed at low temperature. © *2003 American Institute of Physics.* [DOI: 10.1063/1.1542445]

1. INTRODUCTION

Photo-stimulated ion desorption (PSID) induced by core-electron excitations of atoms and molecules on surfaces is an active research field in surface science.[1–6] Detailed investigations of this topic have been very valuable for the following areas: (1) vacuum technology to suppress ion desorption induced by electron impact, (2) chemical reactions induced by high-energy particles on the inner walls of accelerators and fusion reactors, and (3) radiation damage of biomol-

ecules and x-ray optics. In addition, PSID at low temperature seems to play important roles in the solar system,[7] for example, in production of O_2 on icy satellites,[8] as a substantial source of sodium in the lunar atmosphere,[9] and in the formation of interstellar molecular hydrogen on the surfaces of cosmic dust grains.[10,11]

In studies of PSID, the electron–ion coincidence (EICO) method is a very powerful tool because it can be used to measure ion desorption yields for core excitation and subsequent Auger transitions. Although excitations of surfaces by x-ray-induced electrons (photoelectrons, Auger electrons, and secondary electrons) lead to ion desorption (x-ray-induced electron-stimulated desorption),[12] the EICO spectrum exhibits a peak only for the ion desorption initiated by the emission of a selected primary electron. Ionic fragments formed by x-ray-induced electron-stimulated desorption, as well as false counts due to the coincidence of a primary electron emitted from one molecule and an ion dissociated from another molecule, contribute only to a flat background noise. Although reneutralization by electron transfer from the substrate is efficient, and far fewer ions than neutrals are desorbed from the surface,[13–15] by using the EICO method to detect the surviving ionic fragments we can possibly obtain information about the process initiating the desorption.

Electron–ion coincidence spectroscopy combined with synchrotron radiation has traditionally been developed into a very powerful tool for investigating the fragmentation dynamics of molecules in the vapor phase.[16] Measurements of energy-selected EICO in the vapor phase, however, are not easy. The coincidence count rate is low even under experimental conditions in which strong irradiation is produced by an undulator beamline, and long data collection times are thus necessary.[17] In contrast, the coincidence count rate is high on a surface because the sample density there is much higher than that in a vapor. Furthermore, in the vapor phase an electric-field gradient applied across a wide ionization region (typically 1 mm) greatly smears the energy distribution of photoelectrons and Auger electrons.[18] An electric-field gradient of 10 V/mm, for example, lowers the energy resolution of the photoelectrons and Auger electrons to more than 10 eV. In contrast, the electric-field gradient applied across the ionization region on a surface is low, and an electric field applied for the purpose of detecting ions does not smear the energy distribution of the photoelectrons and Auger electrons. This makes it easy to use EICO spectroscopy to detect a fragment ion and an energy-selected photoelectron or Auger electron from a surface.

Thus, in 1985 Knotek and Rabalais developed an EICO apparatus combined with an electron beam for surface studies.[19] They applied it to investigate F^+ desorption from a fluorinated, oxidized Ti(100) surface. The coincidence spectra, however, were not clear enough to determine the ion desorption mechanism. After that pioneering work, however, EICO spectroscopy was not applied for surface studies at all until 1996, because of several problems characteristic to surfaces, such as the abundance of secondary electrons and the high probability of recapture or neutralization of ions.

In 1996, two of the authors (K.M. and M.N.) and their collaborators developed an improved EICO apparatus.[20] It was implemented with an electron beam[20] and synchrotron radiation.[21] Synchrotron radiation is more advantageous than an electron beam because the resonant excitations are accessible and the secondary electrons are drastically reduced. Since then, K.M. and his collaborators have constructed a total of four EICO analyzers[20–26] and are now testing the performance of their latest model.[25,26] EICO spectroscopy has now been widely applied for studies of ion desorption from condensed molecules such as H_2O (Refs. 23,27–32), NH_3 (Refs. 33–35), CH_3CN (Refs. 36–38), $Si(CH_3)_4$ (Ref. 39), and C_6H_6 (Ref. 40), and for molecules showing site-specific fragmentation (Refs. 23,41–45). This method has also been applied for polymethyl methacrylate thin film,[38,46–48] a Si(100) surface terminated by fluorine,[22] H_2O dissociatively chemisorbed on a Si(100) surface [H_2O/Si(100)],[31,49,50] a CaF_2(111) film epitaxially grown on Si(111),[22,51] and a TiO_2(110) surface.[52] The ion desorption mechanisms that have been elucidated by EICO spectroscopy so far have been described in detail in previous overviews.[53–55]

In this article we describe the present status of the EICO apparatus (Sec. 2) and discuss six recent investigations for H_2O (Secs. 3.1.1 and 3.1.2), NH_3 (Secs. 3.2.1 and 3.2.2), CH_3CN (Sec. 3.3), and CF_3CH_3 (site-specific fragmentation, Sec. 3.4) condensed at low temperature. In Sec. 4, we summarize our conclusions and discuss the future direction of EICO spectroscopy in surface science.

2. ELECTRON–ION COINCIDENCE APPARATUS

Figure 1 shows pictures of the first and second EICO analyzers, together with a schematic diagram of the first EICO apparatus implemented with synchrotron radiation. The first analyzer[21] consisted of an electron gun, a coaxial cylindrical mirror analyzer (CMA), a time-of-flight ion mass spectrometer (TOF-MS), a power supply, and an electronic system for measurements. The CMA consisted of a magnetic shield, semi-cylinders 58 and 120 mm in diameter (solid angle$=0.24$ sr), three sets of compensation electrodes to maintain a radial electric field, retarding grids, a cylindrical slit, and tandem microchannel plates (MCPs). The CMA had a resolving power of $E/\Delta E=80$ without a retarding field. The TOF-MS consisted of an electric field shield, a drift tube with an ion-extraction grid ($T1$), a 96-mm drift tube ($T2$ and $T3$), a deflector, a focusing system, and MCPs. The deflector was added to prevent scattered synchrotron radiation and emitted soft x rays from impinging on the MCPs. The distances between the sample and $T1$, and between $T1$ and $T2$, were 13 and 1 mm, respectively. A pair of conical electrodes was spotwelded to the shield and $T1$ as a lens system to collect ions desorbed into all solid angles. The transmittance of the three meshes inserted perpendicular to the axis of the TOF tube was 0.47, and the ion detection efficiency of the MCPs was 0.60. The angle between the axes of the CMA and the electron gun was 5 deg, and that between the CMA and the TOF-MS was 30 deg. Most of the metallic parts of the CMA were made of SS 316L, whose residual magnetism was diminished by annealing. The CMA,

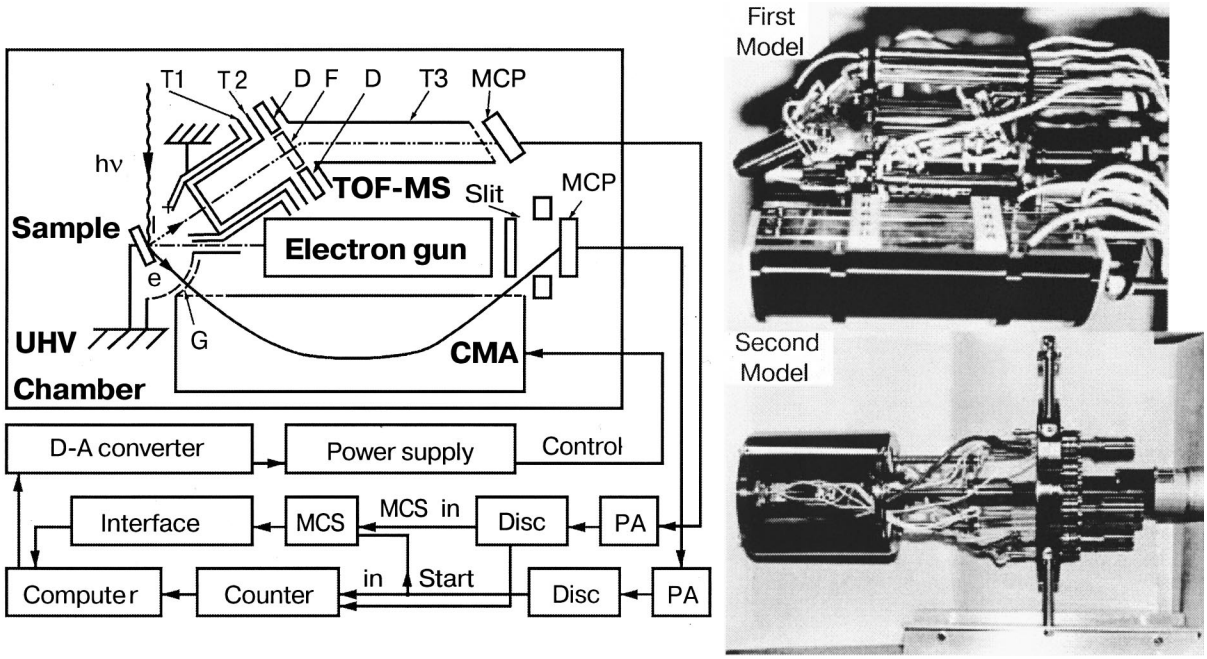

FIG. 1. Pictures of the first and second EICO analyzers and a schematic diagram of the first model implemented with synchrotron radiation. The abbreviations used are defined as follows: PA, preamplifier; Disc, discriminator; T1, drift tube with an extraction grid; T2 and T3, 95-mm drift tube; F, focusing system; D, deflector; G, retarding grids; UHV, ultrahigh vacuum; MCP, microchannel plate; TOF-MS, time-of-flight ion mass spectrometer; CMA, cylindrical mirror analyzer; MCS, multichannel scaler.

the TOF-MS, and a 75-mm retraction mechanism were mounted on a 203-mm-diameter conflat flange.

The sample surface was excited by synchrotron radiation, and the energy of the emitted electrons was analyzed with the CMA, while the desorbed ions were accelerated towards the TOF-MS. The surface normal was set coaxial to the TOF-MS. The angle between the surface normal and the synchrotron radiation was 60 deg. The voltage supplies for the CMA were controlled with a personal computer via a D–A converter board. The electron and ion signals were transformed to negative NIM pulses by using preamplifiers and discriminators. The ion counts were recorded, as a function of the TOF difference between the energy-selected electrons and the ions, with a multichannel scaler (MCS) by taking the electron signal as the starting trigger. The MCS was also controlled from the computer via an interface board. Ions desorbed in coincidence with the detected electrons give a coincidence signal at a specific TOF, while ions irrelevant to the electrons increase the background level. As the data accumulation time t_a increases, the ratio of the coincidence signal to the background level improves in proportion to $t_a^{1/2}$, because the background is derived from statistical fluctuations. Since the selected electron kinetic energy corresponds to a particular photoelectron or Auger-electron emission, the coincidence signal intensity represents the yield of the ion desorption induced by the photoelectron emission or Auger process.

The second model[22] did not contain an electron gun and consisted of a CMA, a TOF-MS, and a 50-mm retraction mechanism. The CMA had a solid angle of 1.0 sr (semicylinders 56.0 and 132.0 mm in diameter and six sets of compensation electrodes) and a resolving power of $E/\Delta E = 80$. The metallic parts of the analyzer were made of nonmagnetic SS 310.

Figure 2 shows a schematic diagram and picture of the third EICO analyzer.[23,24] To achieve a decent signal-to-background ratio within a reasonable data collection time, the solid angle of the CMA was designed to be 1.1 sr (cylinders 54.0 and 133.0 mm in diameter and six sets of compensation electrodes). The TOF-MS without a deflector was positioned coaxially with the CMA, and the desorbed ions flew straight ahead to the MCPs. With these improvements the signal-to-background ratio was improved by a factor of 5 compared to the second model. The designed resolving power of the CMA was limited to $E/\Delta E = 100$ because of the large solid angle. The actual resolving power, however, was degraded to $E/\Delta E = 80$ due to the ion extraction field (17 V/mm) and the relatively large spot size of the monochromatized synchrotron radiation used (1×1 mm). The resolving power was not impressive but was still effective for various ion desorption studies.

Figure 3 shows a typical EICO spectrum for condensed H_2O (see Sec. 3.1.1) measured with the third EICO analyzer. The influence of the scattered synchrotron radiation and emitted soft x rays was found to be negligible. The third EICO apparatus is currently active at the BL2B1 beamline installed with a 2-m grasshopper monochromator at the UV-SOR synchrotron-radiation facility in Okazaki, Japan. The typical photon intensity is 10^8–10^9 photons/s at an energy resolving power of $E/\Delta E = 500$. The third EICO apparatus is also used at the BL13 beamline at the HiSOR synchrotron-radiation facility in Higashi-Hiroshima, Japan.

K. M. and his collaborators are now testing the performance of the latest (fourth) model at the PF synchrotron-radiation facility in Tsukuba, Japan (Fig. 4).[25,26] The advantage of this model is that instead of a conventional CMA, a new coaxially symmetric mirror analyzer developed by Siegbahn *et al.*[56] is employed as the electron energy analyzer.

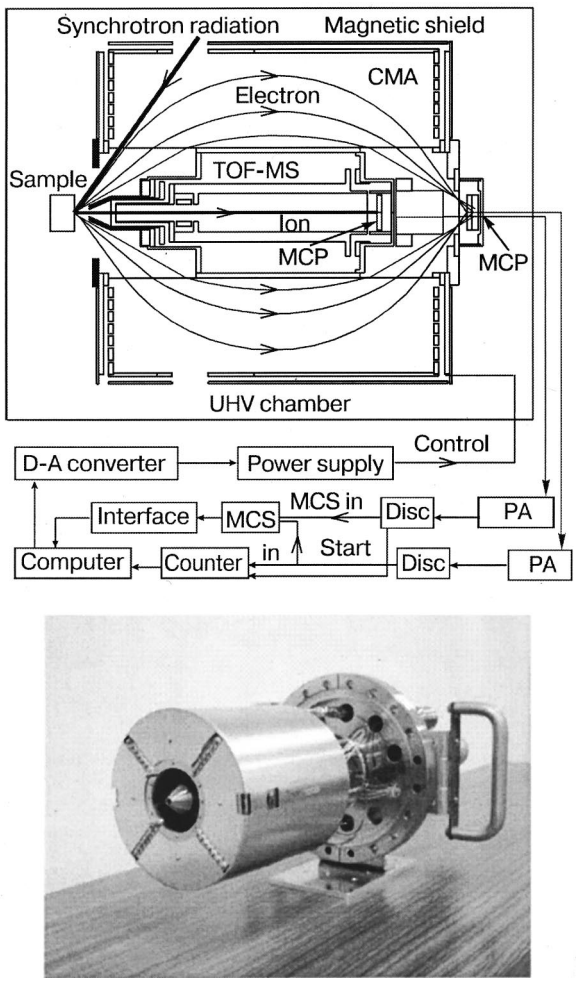

FIG. 2. Schematic diagram and picture of the third EICO analyzer implemented with synchrotron radiation.

The analyzer consists of an inner electrode, an outer electrode, three sets of compensation electrodes, and a magnetic shield. The solid angle of this analyzer is designed to be 1.2 sr, while the designed and actual resolving powers are $E/\Delta E = 300$ and 120, respectively. A short TOF-MS is installed coaxially inside the electron energy analyzer.

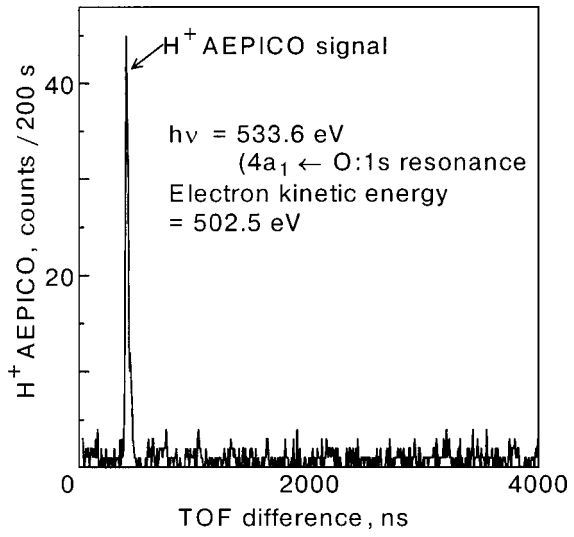

FIG. 3. Typical EICO spectrum of condensed H_2O.

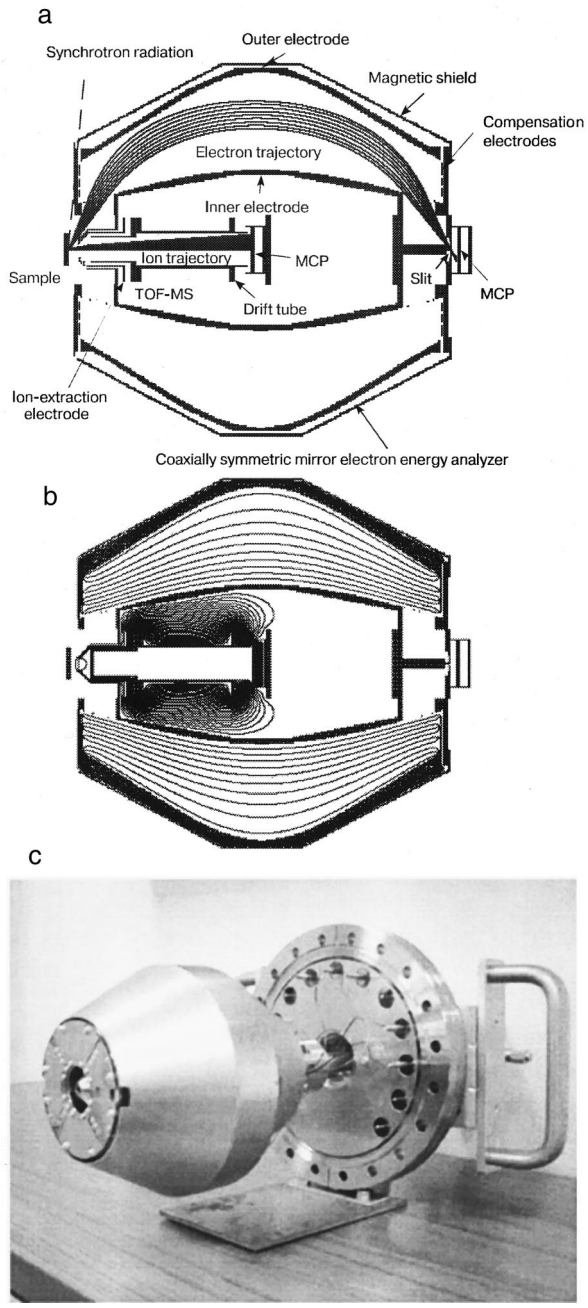

FIG. 4. (a) Schematic diagram of the latest EICO analyzer implemented with synchrotron radiation. (b) Isoelectric lines simulated with SIMION 3D version 7.0 (Idaho National Engineering and Environmental Laboratory) under the conditions that the voltages of the inner electrode and the magnetic shield are 0 V, that of the outer electrode is −100 V, and that of the ion-extraction grid of the TOF-MS is −30 V. Electron and ion trajectory lines simulated with SIMION 3D are also shown in Fig. 4a, under the conditions that the electron kinetic energy is 182.75 eV and the electron emission angles are 52–67 deg. (c) Picture of the latest EICO analyzer.

The first, second, and third EICO apparatus were used for the investigations described in Sec. 3.2, Secs. 3.3 and 3.4, and Sec. 3.1, respectively. Unless otherwise noted, in the investigations described in Secs. 3.1, 3.2.1, and 3.3, the substrate was cooled by liquid nitrogen to about 100 K. In the investigation described in Secs. 3.2.2 and 3.4, the substrate was cooled by flowing cold helium gas to about 50 K. Then, the sample surface was prepared by exposing the substrate to a sample gas or by spraying a sample gas onto the substrate with a pulsed valve.

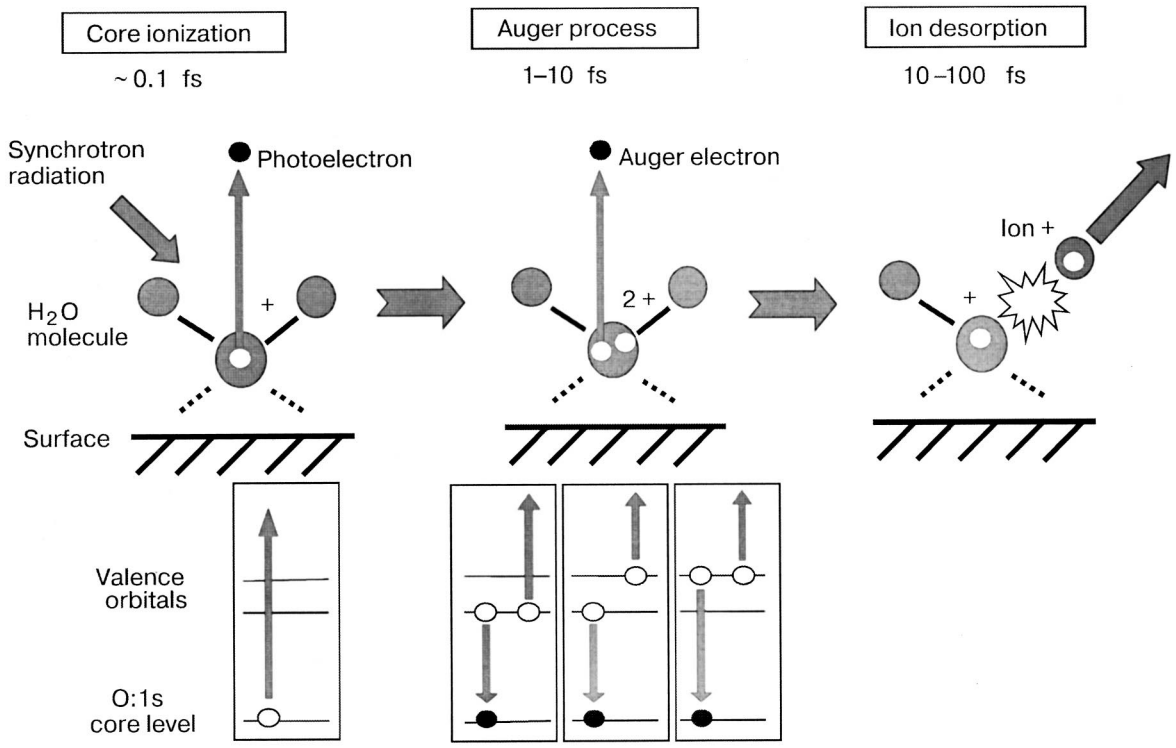

FIG. 5. Three-step H^+ desorption mechanism for the O:1*s* ionization of condensed H_2O (normal ASID): (1) formation of a core-hole by an O:1*s* photoelectron emission (~0.1 fs), (2) formation of a two-hole state by an O:KVV transition (1–10 fs), and (3) H^+ desorption induced by Coulomb repulsion between two holes and by electrons missing from O–H bonding orbitals (10–100 fs).

3. PHOTOSTIMULATED ION DESORPTION FROM CONDENSED MOLECULES STUDIED WITH EICO SPECTROSCOPY

3.1. H_2O

3.1.1. PSID mechanism studied with AEPICO. The most probable model of ion desorption is the Auger-stimulated ion desorption (ASID) mechanism (Fig. 5), which is simply described as a sequence of three steps: (1) a core-electron transition leaving a core hole (~0.1 fs), (2) an Auger transition leaving multiple valence holes (1–10 fs), and (3) decay of the multi-hole state, causing ion desorption (10–100 fs). The ASID mechanism was initially proposed by Knotek and Feibelman for O^+ desorption induced by Ti:3*p* ionization at a TiO_2 surface, where the driving force was attributed to the Coulomb repulsion between Ti^{2+} and O^+ created by an interatomic Auger process.[57] Later, the ASID model was extended for covalently bonded systems.[58] Several theoretical groups reported that two holes are localized on one molecule in Auger final states,[59] which are sufficiently long lived to stimulate ion desorption.[60–62] However, the details of the ASID mechanism, the factors that influence desorption probability, and the decay processes competing with desorption have hardly been explored, because there have been no tools for investigating the intermediate Auger transitions responsible for ion desorption. In addition, ion desorption by x-ray-induced electron impact often dominates the primary processes.[12] Recently, however, we have found that Auger electron photon coincidence (AEPICO) spectroscopy is an ideal tool for investigating the ASID mechanism, because it provides the yield for the ion desorption channel caused by selected Auger transitions.

In this Section we describe a study of the H^+ desorption mechanism for the O:1*s* ionization[23,27,29,31,53–55] and resonant excitations[23,28,30,31,54,55] of condensed H_2O by using AEPICO spectroscopy. Since the nature of the surface of condensed H_2O is critically important for many fields, extensive studies have been carried out.[63–65] Ion desorption stimulated by electronic transitions from the O:1*s* core level in condensed H_2O has been investigated theoretically,[66] by using an electron beam,[67] and by using synchrotron radiation.[68,69]

Figure 6 shows the total ion yield (TIY, solid line), Auger electron yield (AEY, dashed line), and TIY/AEY spectra (solid circles) in the range of the O:1*s* excitation of condensed H_2O. The TIY spectrum shows the H^+ desorption yield, as will be described later. The AEY spectrum represents the photoabsorption spectrum in the range of the O:1*s* excitation, and the TIY/AEY intensity is proportional to the number of H^+ ions desorbed per photon absorbed. The TIY/AEY spectrum shows a characteristic threshold peak at the $4a_1 \leftarrow$O:1*s* resonance ($h\nu = 533.6$ eV) and a suppression at the $3p \leftarrow$O:1*s* resonance ($h\nu = 535.4$ eV). The spectrum is nearly constant above the O:1*s* ionization threshold ($h\nu > 547.6$ eV).

Figure 7a shows the O:1*s* normal Auger-electron spectrum (AES) of condensed H_2O taken at a photon energy of 547.6 eV. The electronic configuration of H_2O is given by $(1a_1)^2(2a_1)^2(1b_2)^2(3a_1)^2(1b_1)^2$, where $1a_1$ is approximately characterized as O:1*s*, $2a_1$ and $1b_2$ as O–H bonding valence orbitals V_B, and $3a_1$ and $1b_1$ as nonbonding lone pair orbitals of oxygen V_{NB} (Ref. 66). Accordingly, the Auger final states with two holes are as follows:

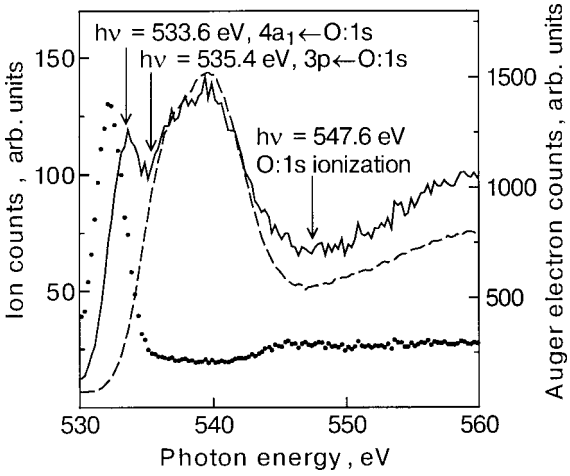

FIG. 6. TIY (solid line), AEY (electron kinetic energy=490 eV, dashed line), and TIY/AEY spectra (solid circles) of condensed H_2O. The TIY spectrum shows a $4a_1 \leftarrow$O:1s peak at 533.6 eV, but the peak energy of the TIY/AEY spectrum (532.6 eV) is lower by 1 eV. The reason for this would be that the $4a_1 \leftarrow$O:1s peak energy of surface H_2O, from which ion desorption takes place, is lower than that of bulk H_2O (Ref. 75) and that excitations by x-ray-induced electrons coming from bulk H_2O induce ion desorption from surface H_2O at 533.6 eV.

$(2a_1)^{-2}$, $(2a_1)^{-1}(1b_2)^{-1}$, $(1b_2)^{-2}$, $(2a_1)^{-1}(3a_1)^{-1}$, $(2a_1)^{-1}(1b_1)^{-1}$, $(1b_2)^{-1}(3a_1)^{-1}$, $(1b_2)^{-1}(1b_1)^{-1}$, $(3a_1)^{-2}$, $(3a_1)^{-1}(1b_1)^{-1}$, and $(1b_1)^{-2}$. The peak assignments according to previous reports[70,71] are also shown in Fig. 7a. The O:1s Auger intensity is proportional to the Auger transition probability leading to the individual Auger final states with two holes.

Figure 3 shows an example of an AEPICO spectrum of condensed H_2O. One can see that a great portion of the H^+ ions are desorbed coincidentally. Other species such as O^+ and OH^+ are negligible due to the lower desorption efficiencies.[69]

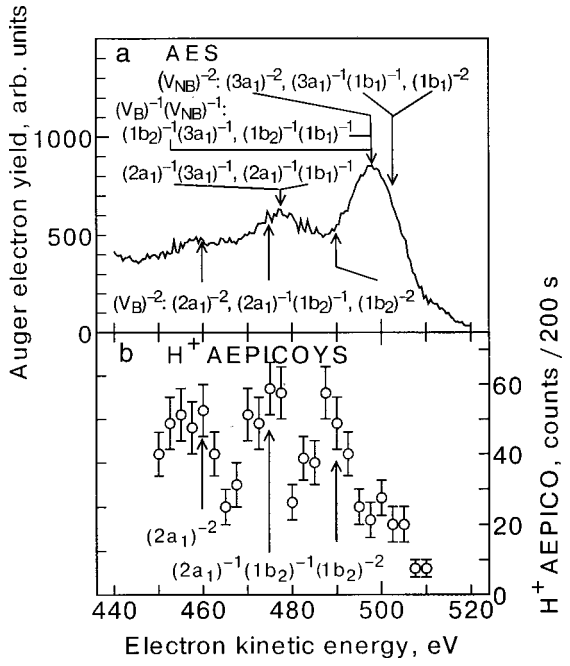

FIG. 7. (a) O:1s normal AES of condensed H_2O. (b) H^+ AEPICOYS for the O:1s normal Auger transitions of condensed H_2O. The spectra in panels a and b were taken at a photon energy of 547.6 eV.

Figure 7b shows the H^+ AEPICO yield spectrum (AEPICOYS), in which the integrated AEPICO count for H^+ is plotted as a function of the Auger-electron kinetic energy. The AEPICO yield is proportional to the product of the Auger transition probability (the formation probability of the Auger final state with two holes) and the ion desorption probability from the Auger final state. By comparing Fig. 7a with Fig. 7b, we can obtain information about the ion desorption probability from the individual Auger final states.

The two-hole states of condensed H_2O are classified into three categories: $(V_B)^{-2}$, $(V_{NB})^{-2}$, and $(V_B)^{-1}(V_{NB})^{-1}$. The order of decreasing Auger electron yield is $(V_{NB})^{-2} > (V_B)^{-1}(V_{NB})^{-1} > (V_B)^{-2}$ (Fig. 7a), while the order of decreasing H^+ AEPICO yield is $(V_B)^{-2} > (V_B)^{-1}(V_{NB})^{-1} > (V_{NB})^{-2}$ (Fig. 7b). Since the number of H^+ ions desorbed per photon absorbed is proportional to the quantity (H^+ AEPICO yield/Auger electron yield), these results show that the order of decreasing number of H^+ ions desorbed per photon absorbed is $(V_B)^{-2} > (V_B)^{-1}(V_{NB})^{-1} > (V_{NB})^{-2}$. As the number of holes in V_B increases, the number of H^+ ions desorbed per photon absorbed increases. Thus, the normal ASID mechanism is reasonable, and the cause of the H^+ desorption is the Coulomb repulsion between the two holes formed in V_B (Fig. 5). As H^+ ions are released into the vacuum due to the Coulomb repulsion between H^+ and OH^+, the OH^+ ions are pushed toward the substrate and neutralized or recaptured.

Next we describe a study of the H^+ desorption mechanism for the $4a_1 \leftarrow$O:1s resonant excitation of condensed H_2O.[23,28,30,31,54,55] As shown in Fig. 6, the H^+ desorption yield has a characteristic threshold peak at the $4a_1 \leftarrow$O:1s resonance. The H^+ desorption mechanism for the $4a_1 \leftarrow$O:1s resonance thus seems very different from that in the O:1s ionization. The subject of the H^+ desorption mechanism for the $4a_1 \leftarrow$O:1s resonant excitation is interesting from the viewpoint of ultrafast photodissociation, i.e., bond-breaking during the lifetime of the core-excited state. Ultrafast photodissociation was, for the first time, found in the $4p\sigma^* \leftarrow$Br:3d resonance of HBr.[72] Evidence for the ultrafast photodissociation of neutral H has also been shown for the $4a_1 \leftarrow$O:1s resonance of isolated H_2O.[73,74] The neutral H yields from condensed H_2O and condensed NH_3, however, show no enhancement by ultrafast dissociation in the $4a_1 \leftarrow 1s$ resonance.[75]

Figure 8a shows the $4a_1 \leftarrow$O:1s resonant AES of condensed H_2O taken at a photon energy of 533.6 eV (solid line), together with the normal AES taken at a photon energy of 547.6 eV (dashed line). The spectator Auger transition, in which the excited electron does not participate, occurs primarily in the resonant Auger transition.[74] When the resonant tunneling of the excited electron to a neighboring molecule accelerates the delocalization of the electron, the normal Auger transition is seen, in addition to the spectator Auger transition, in the AES.[76–78] Thus, for the solid line in Fig. 8a, the normal AES is likely to be superimposed on the spectator AES. In the AES the peak of the spectator Auger transition is located a few electron-volts above that of the corresponding normal Auger transition, because the excited electron shields

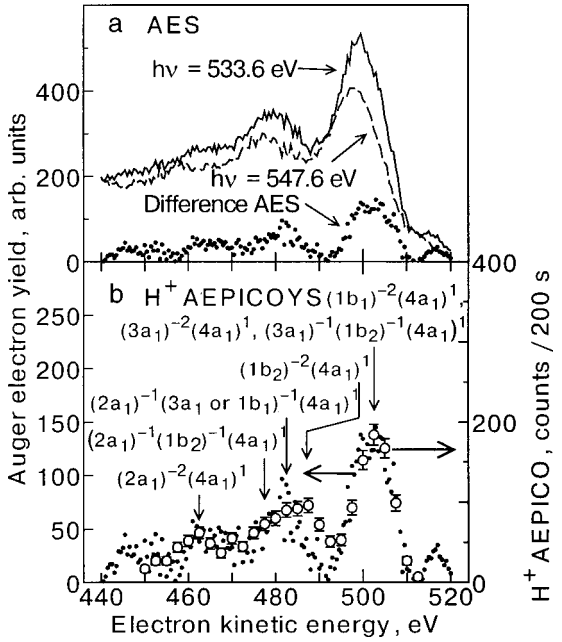

FIG. 8. (a) $4a_1 \leftarrow$O:1s spectator AES (solid line), O:1s normal AES (dashed line), and difference AES (solid circles) of condensed H_2O; (b) H^+ AEPICOYS for the $4a_1 \leftarrow$O:1s spectator Auger transitions (open circles) and difference AES (solid circles) of condensed H_2O.

the hole–hole Coulomb repulsion and stabilizes the spectator Auger final state. To obtain the pure spectator AES, we subtracted the dashed line from the solid line in Fig. 8a (difference AES). The pure spectator AES thus obtained (solid circles in Figs. 8a and 8b) shows three peaks at 502.5, 482.5, and 462.5 eV. Since the peak of the spectator Auger transition is, as described above, located a few electron-volts above that of the normal Auger transition (Fig. 7a), these three peaks at 502.5, 482.5, and 462.5 eV are assigned to the spectator Auger final states with characters of $(\mathrm{O}:2p)^{-2}(4a_1)^1$, $(2a_1)^{-1}(\mathrm{O}:2p)^{-1}(4a_1)^1$, and $(2a_1)^{-2}(4a_1)^1$, respectively.[70,71] Here, O:2p denotes a $1b_2$, $3a_1$, or $1b_1$ orbital.

Figure 8b shows the H^+ AEPICOYS for the $4a_1 \leftarrow$O:1s spectator Auger transitions (open circles), together with the difference AES (solid circles, the same data as in Fig. 8a). Since the three peaks of the H^+ AEPICOYS are at the same positions as the peaks of the difference AES and the two spectra are similar to each other, the H^+ desorption is considered to be caused by the spectator Auger transition. The spectator Auger intensity is proportional to the Auger transition probability leading to the individual Auger final states with two holes in some valence orbitals and an excited electron in the $4a_1$ orbital. The H^+ AEPICOYS intensity is proportional to the product of the spectator Auger transition probability and the H^+ desorption probability from the Auger final state. Therefore, the H^+ desorption probability seems to be independent of the valence orbitals occupied by holes in the spectator Auger final state.

In addition to these results, we must take two facts into account to understand the H^+ desorption mechanism for the $4a_1 \leftarrow$O:1s resonance. One is that the potential surface of the $(\mathrm{O}:1s)^{-1}(4a_1)^1$ state is repulsive with respect to the O–H direction, because the $4a_1$ orbital is an antibonding orbital of the O–H bond. The other is that the period of the O–H stretching vibration is comparable to the lifetime of the O:1s hole. On the basis of the experimental results and these two facts, we propose a four-step H^+ desorption mechanism for the $4a_1 \leftarrow$O:1s resonance (Fig. 9): (1) the $4a_1 \leftarrow$O:1s transition, (2) extension of the HO–H distance in the $(\mathrm{O}:1s)^{-1}(4a_1)^1$ state (ultrafast OH extension), (3) a spectator Auger transition leading to a two-hole state with an excited electron in the $4a_1$ orbital, and (4) H^+ desorption tak-

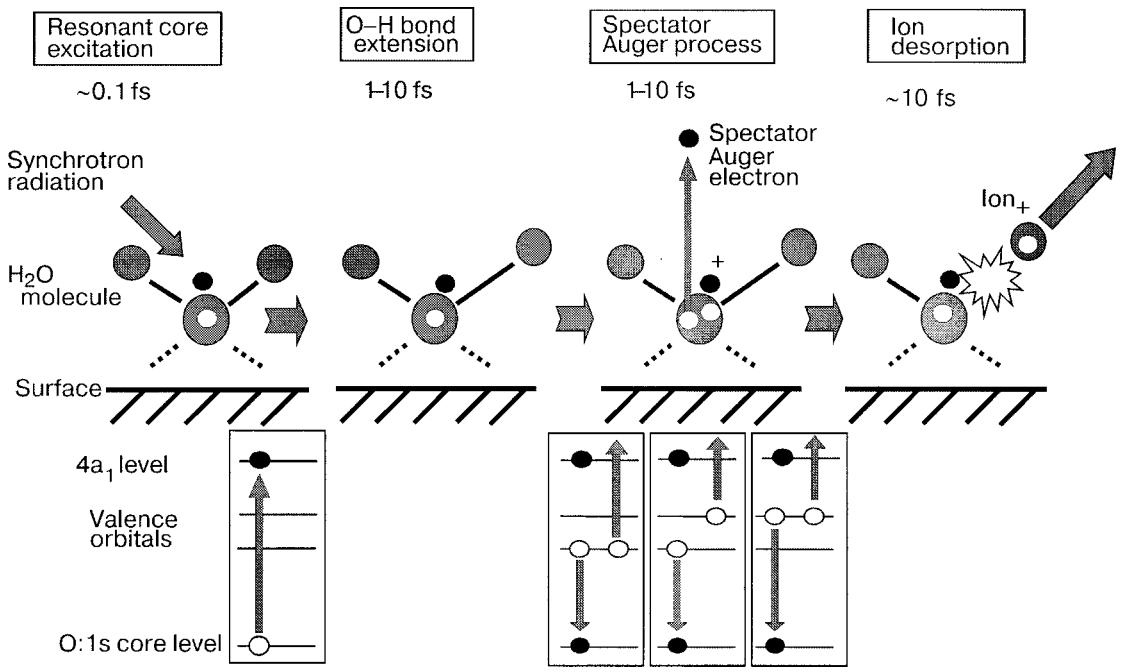

FIG. 9. Four-step H^+ desorption mechanism for the $4a_1 \leftarrow$O:1s resonance of condensed H_2O: (1) the $4a_1 \leftarrow$O:1s transition, (2) extension of the HO–H distance in the $(\mathrm{O}:1s)^{-1}(4a_1)^1$ state, (3) a spectator Auger transition leading to a two-hole state with an excited electron in the $4a_1$ orbital, and (4) H^+ desorption. The H^+ desorption is driven mainly by the O–H repulsive potential surface of the $(\mathrm{O}:1s)^{-1}(4a_1)^1$ state.

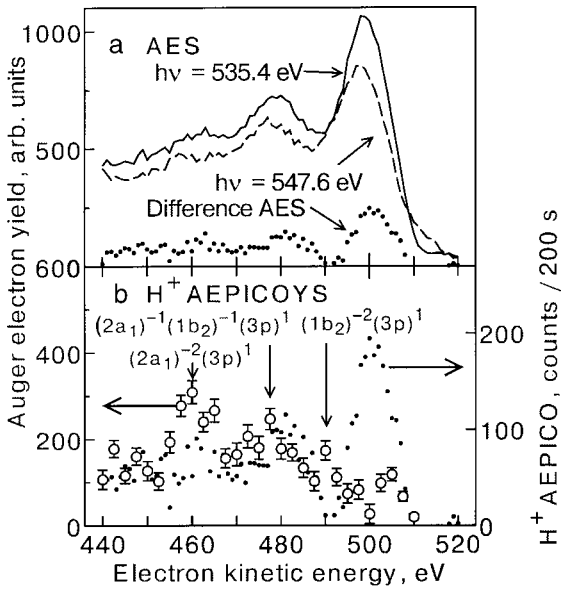

FIG. 10. (a) $3p \leftarrow O{:}1s$ spectator AES (solid line), $O{:}1s$ normal AES (dashed line), and difference AES (solid circles) of condensed H_2O. (b) H^+ AEPICOYS for the $3p \leftarrow O{:}1s$ spectator Auger transitions (open circles) and difference AES (solid circles) of condensed H_2O.

ing place in turn. The increase in the TIY/AES spectrum at the $4a_1 \leftarrow O{:}1s$ resonance (Fig. 6) is driven mainly by the O–H repulsive potential surface of the $(O{:}1s)^{-1}(4a_1)^1$ state.

Next we describe a study of the H^+ desorption mechanism for the $3p \leftarrow O{:}1s$ resonant excitation of condensed H_2O.[23,30,31,54] Figure 10a shows the $3p \leftarrow O{:}1s$ spectator AES of condensed H_2O taken at a photon energy of 535.4 eV (solid line), together with the normal AES taken at a photon energy of 547.6 eV (dashed line). Figure 10b shows the H^+ AEPICOYS in the $3p \leftarrow O{:}1s$ spectator Auger transitions (open circles). At the $3p$ resonance ($h\nu = 535.4$ eV), the AEPICOYS displays major, medium, and minor peaks at electron kinetic energies of 460, 475, and 490 eV, respectively. According to previous reports,[70,71] these peaks are assigned to the $(2a_1)^{-2}(3p)^1$, $(2a_1)^{-1}(1b_2)^{-1}(3p)^1$, and $(1b_2)^{-2}(3p)^1$ spectator Auger final states. The difference AES obtained by subtracting the AES at the $O{:}1s$ ionization ($h\nu = 547.6$ eV) from that at the $3p \leftarrow O{:}1s$ resonance ($h\nu = 535.4$ eV) is also shown in Fig. 10 (solid circles). The difference AES is expected to correspond to the pure spectator Auger component, as described above. The remarkable difference in spectral shape between the difference AES and the AEPICOYS shows that the H^+ desorption probability varies with the spectator Auger final state. In contrast to the $4a_1 \leftarrow O{:}1s$ spectator Auger transition, the H^+ desorption probability depends on the valence orbitals occupied by holes in the $3p \leftarrow O{:}1s$ spectator Auger final state. This result indicates that the pure spectator ASID mechanism is responsible for the $3p \leftarrow O{:}1s$ resonance; that is, the repulsive potential surface of the $(\text{valence orbitals})^{-2}(3p)^1$ state is responsible for the H^+ desorption.

On the basis of these results, we propose a three-step H^+ desorption mechanism for the $3p \leftarrow O{:}1s$ resonance (Fig. 11): (1) the $3p \leftarrow O{:}1s$ transition, (2) a spectator Auger transition, and (3) H^+ desorption taking place in turn. In contrast to the $4a_1 \leftarrow O{:}1s$ resonance, the HO–H distance is not extended before the Auger process. This is because the potential surface of the $(O{:}1s)^{-1}(3p)^1$ state is expected to be similar to that of the ground state, because the $O{:}1s$ and $3p$ orbitals are irrelevant to the O–H bonding. The decrease in the TIY/AES spectrum at the $3p \leftarrow O{:}1s$ resonance (Fig. 6) is attributed to the reduction in the hole–hole Coulomb repulsion due to shielding by the $3p$ electron.

3.1.2. Determination of $O{:}1s$ *level of* H_2O *from which* H^+ *is desorbed in PSID of condensed* H_2O. Core-level pho-

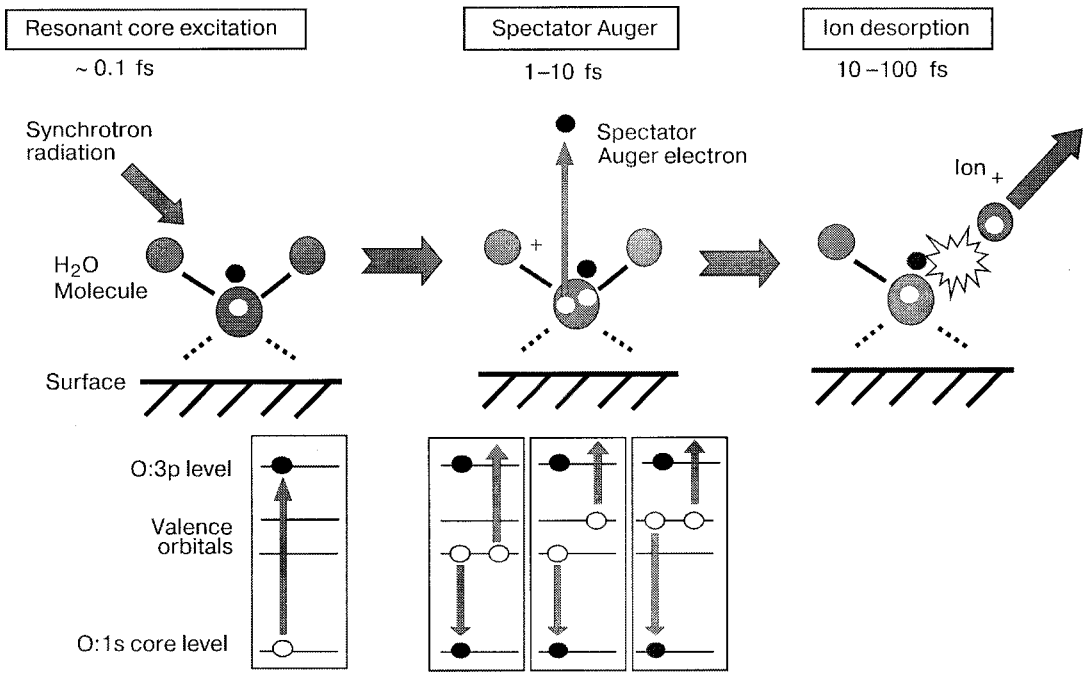

FIG. 11. Three-step H^+ desorption mechanism for the $3p \leftarrow O{:}1s$ resonance of condensed H_2O: (1) the $3p \leftarrow O{:}1s$ transition, (2) a spectator Auger transition, and (3) H^+ desorption. The H^+ desorption is suppressed by the reduction in the hole–hole Coulomb repulsion due to shielding by the $3p$ electron.

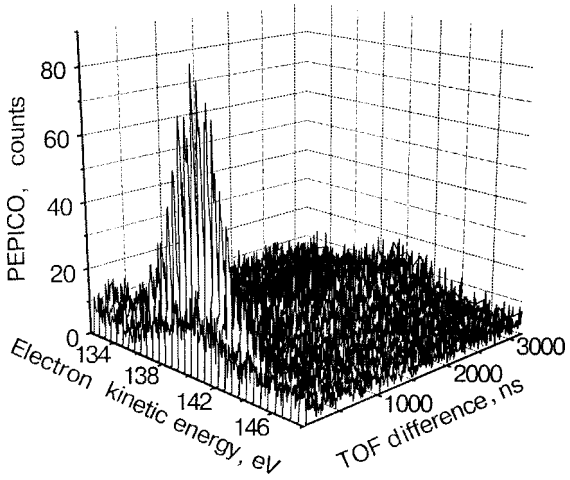

FIG. 12. A series of PEPICO spectra for H_2O condensed on a $TiO_2(110)$ surface. These spectra were taken, at intervals of 0.5 eV in electron kinetic energy, at a photon energy of 680 eV.

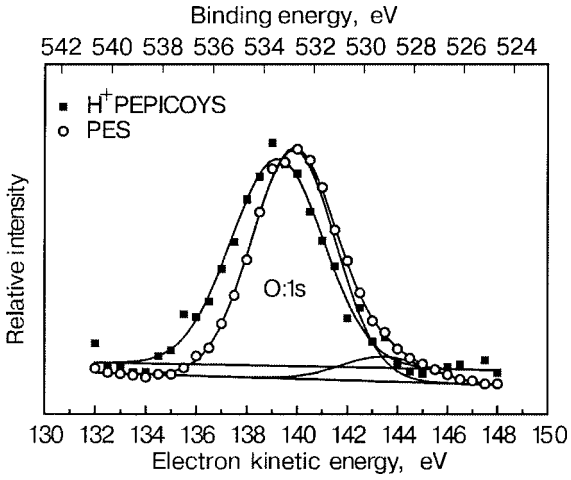

FIG. 13. H^+ PEPICOYS (solid squares) and PES (open circles) for H_2O condensed on a $TiO_2(110)$ surface ($h\nu = 680$ eV). The Gaussian curves drawn with linear backgrounds (solid lines) were calculated by the least-squares fitting method.

toelectron spectroscopy, also called x-ray photoelectron spectroscopy (XPS), has been used to investigate solids and their surfaces.[79] This technique is surface sensitive due to the small escape depth of photoelectrons. As described in Sec. 3.1.1, by using EICO spectroscopy it is possible to obtain the kinetic energy spectrum of the electron that coincides with a specific ion desorption (for example, see Figs. 7b, 8b, and 10b). Therefore, because ions have an even shorter escape depth than electrons, EICO spectroscopy can be used as an extremely surface-sensitive form of XPS.[80] That is, although conventional XPS detects core-level photoelectron emission from the bulk of a solid (within the escape depth of the photoelectron), EICO spectroscopy selectively detects photoelectron emissions from the upper molecular layers (especially the uppermost molecular layer) of a surface. As a result, the so-called surface core-level shift can easily be observed. In this section, we apply the EICO technique to a surface of condensed H_2O to detect the surface core-level shift of the O:1*s* level,[23,32] thus demonstrating the advantages and possibilities of EICO spectroscopy for surface analysis.

Since the nature of the surface of condensed H_2O is of critical importance in many fields (as mentioned in Sec. 3.1.1), this topic has been studied extensively.[63–65] According to one previous study,[63] the surface of condensed H_2O contains several types of H_2O molecules, including two- or three-coordinated molecules with a dangling hydrogen, two- or three-coordinated molecules with a dangling oxygen coordination, and four-coordinated molecules with a distorted tetrahedron. Although condensed H_2O has been studied by XPS,[81,82] to the best of our knowledge no study has examined the surface core-level shift of the O:1*s* level at the surface of condensed H_2O.

Figure 12 shows a series of O:1*s* photoelectron–photon coincidence (PEPICO) spectra for H_2O condensed on a $TiO_2(110)$ surface. These spectra were taken, at intervals of 0.5 eV in electron kinetic energy, at a photon energy of 680 eV. The H^+ desorption intensity reaches its maximum around an electron kinetic energy of 139 eV.

Figure 13 shows the H^+ PEPICO-yield spectrum (PEPICOYS, solid squares), in which the integrated PEPICO count for H^+ in Fig. 12 is plotted as a function of the electron kinetic energy. The figure also shows the photoelectron spectrum (PES) obtained under the same conditions (open circles). The Gaussian curves drawn with linear backgrounds (solid lines) were calculated by the least-squares fitting method. The small peak at 144 eV in the PES is due to O:1*s* photoelectron emission from the substrate. The peak of the H^+ PEPICOYS is not located at the same energy as the peak of the PES, but rather is shifted to a lower kinetic energy by about 0.7 eV.

The reason for the peak shift between the H^+ PEPICOYS and the PES is that the O:1*s* binding energy of H_2O from which H^+ is desorbed in PSID is different from the O:1*s* binding energies of the other types of H_2O molecules. In the upper molecular layers at the surface of condensed H_2O, some of the hydrogen bonds between molecules are broken, forming dangling hydrogens. It seems reasonable to assume that the H^+ ions are desorbed from the molecules with the dangling hydrogens (probably two-coordinated molecules), because these hydrogens are easily desorbed. Thus, the PEPICOYS only reflects the binding energy of an oxygen atom bonded to a dangling hydrogen atom in (or located very close to) the uppermost molecular layer. Meanwhile, since the O:1*s* photoelectron is emitted from all the oxygen atoms within the escape depth of the photoelectron, the observed peak in the PES is a convolution of many peaks for the photoelectrons emitted from all the bulk species located within the escape depth.

Previously, it was reported that the O:1*s* binding energy observed in the XPS spectrum of bulk H_2O was shifted by -7.1 eV (Ref. 81), (without a correction in the work function) or -2.3 eV (Ref. 82), (with a correction in the work function) from that of H_2O vapor. The O:1*s* binding energy of the less coordinated molecules, which contain dangling hydrogens in (or very close to) the uppermost molecular layer, is expected to fall within the range between that of the bulk and that of the vapor phase, because the properties of the less-coordinated molecules are expected to be somewhere between those of fully coordinated molecules in bulk H_2O and those of H_2O molecules in the vapor phase. In fact,

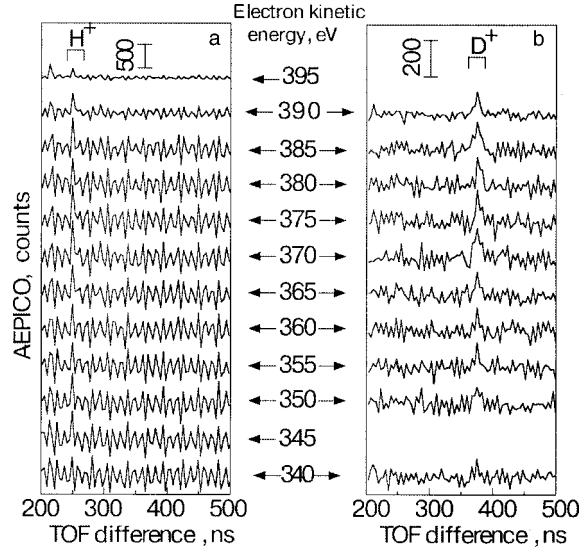

FIG. 14. AEPICO spectra for the N:KVV normal Auger transitions of condensed NH_3 (a) and condensed ND_3 (b). The spectra were taken at a photon energy of 429 eV.

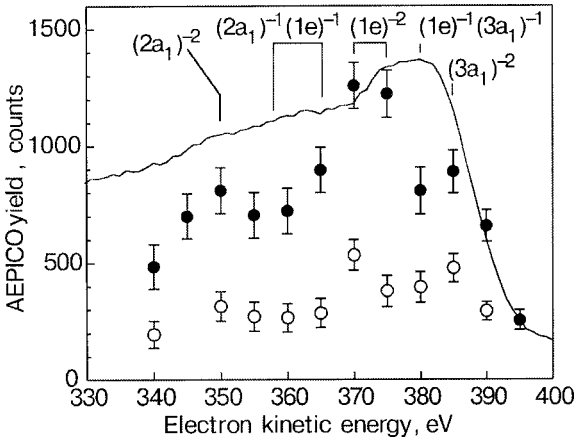

FIG. 15. AEPICOYS for H^+ (solid circles) and D^+ (open circles), and AES (solid line) for the N:KVV normal Auger transitions of condensed $NH_3(ND_3)$. The spectra were taken at a photon energy of 429 eV.

this assumption is consistent with the result that the binding energy of the less-coordinated H_2O molecules is shifted by $+0.7$ eV from that of bulk H_2O (Fig. 13). The peaks caused by the less coordinated H_2O molecules are negligible in the PES (Fig. 13) because those H_2O molecules are a very small fraction of the bulk H_2O.[63]

Our view is supported by comparing the results for $H_2O/Si(100)$ and H_2O condensed on Si(100) at 100 K under the same experimental conditions. It is known that H_2O is dissociatively chemisorbed to form Si–OH and Si–H species on the Si(100) surface at room temperature.[64] The H^+ PEPICOYS and PES exhibit peaks at similar electron kinetic energies in $H_2O/Si(100)$ because all the oxygen atoms at the Si(100) surface are present as an OH species. There is no reason to expect a peak shift between the H^+ PEPICOYS and the O:1*s* PES for $H_2O/Si(100)$ because each method depends on the same OH species, in contrast to the case of condensed H_2O. However, for H_2O condensed on Si(100), the 0.7-eV shift shown in Fig. 13 was also observed, in contrast to the case of $H_2O/Si(100)$.

To the best of our knowledge, this is the first observation of the surface core-level shift of condensed H_2O. This demonstrates the advantages and possibilities of EICO spectroscopy for surface analysis. EICO spectroscopy can thus be used as a form of extremely surface-sensitive and site-specific XPS. Moreover, EICO spectroscopy can be used to investigate the chemical conditions of surfaces, because ion desorption is strongly affected by the surface chemical bonds and the relaxation process of the excited state.

3.2. NH_3

3.2.1. PSID mechanism studied with AEPICO. In this Section we describe a study using EICO spectroscopy to examine the H^+ desorption mechanism for the N:1*s* ionization[33,53] and the resonant excitation[34] of condensed NH_3. Figure 14 shows a series of AEPICO spectra for the N:KVV normal Auger transitions of condensed NH_3 (a) and ND_3 (b). A peak located in a TOF difference range of 246–258 ns for NH_3 (Fig. 14a) is assigned to the true coincidence signal of H^+, while a peak between 366–382 ns for ND_3 (Fig. 14b) is assigned to D^+. The normal AEPICO spectra of condensed NH_3 and ND_3 exhibit only H^+ and D^+, respectively.

Figure 15 shows the normal AEPICOYS for H^+ and D^+ in condensed NH_3 (solid circles) and ND_3 (open circles), together with the AES (solid line). The AEPICO yields of both H^+ and D^+ are enhanced at the electron kinetic energy of the N:KVV Auger transition. These results show that the photoions are produced through normal ASID, in which the N:KVV Auger decay stimulates cleavage of an N–H or N–D bond (Fig. 5). The fine structures of these AEPICOYS, however, are different from those of the AES. Accordingly, we conclude that the probability of normal ASID depends on the Auger final state, as in condensed H_2O (Fig. 7).

The electronic configuration of NH_3 is $(1a_1)^2(2a_1)^2(1e)^4(3a_1)^2$. The $1a_1$ is characterized as the core level (N:1*s*), the $2a_1$ and $1e$ orbitals are classified as bonding orbitals V_B, and the $3a_1$ orbital with the character of a nitrogen lone pair is classified as a weak bonding orbital V_{WB} because it is spread out somewhat toward the N–H bond. Based on a previous report by Larkins and Lubenfeld,[83] the energy positions of the Auger final states are given in Fig. 15. The Auger final states with characters of $(2a_1)^{-2}$, $(2a_1)^{-1}(1e)^{-1}$, and $(1e)^{-2}$ correspond to the normal Auger process of KV_BV_B, while those for $(2a_1)^{-1}(3a_1)^{-1}$ and $(1e)^{-1}(3a_1)^{-1}$ correspond to KV_BV_{WB}, and that of $(3a_1)^{-2}$, to $KV_{WB}V_{WB}$.

The AEPICO yields of H^+ and D^+ are enhanced at the electron kinetic energy associated with $(1e)^{-2}$, while the Auger electron yield is significantly enhanced in the $(1e)^{-1}(3a_1)^{-1}$ and $(3a_1)^{-2}$ Auger final states. As in the case of condensed H_2O, these results indicate that KV_BV_B leads to normal ASID more efficiently than $KV_{WB}V_B$ or $KV_{WB}V_{WB}$.

The AEPICO yield of D^+ is one-third to one-half that of H^+ over the whole electron kinetic energy range studied (Fig. 15). This result indicates that H^+ has a high yield (because of its low mass and fast exit velocity), reducing the effectiveness of reneutralization relative to D^+ (Refs. 84–86).

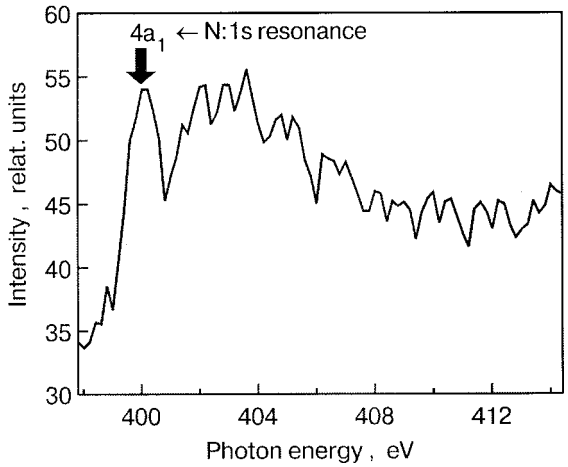

FIG. 16. TIY of NH_3/Xe, which shows the H^+ desorption yield.

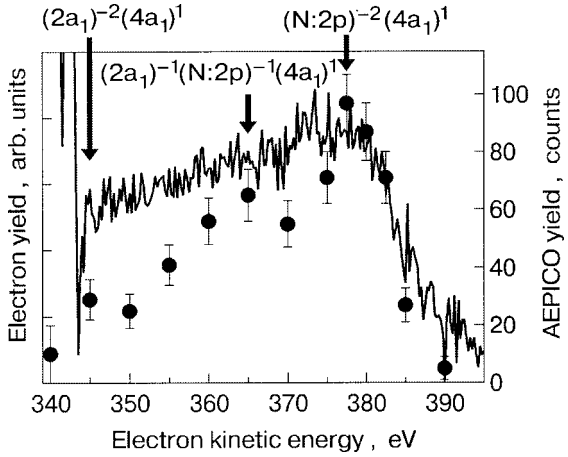

FIG. 17. H^+ AEPICOYS for the $4a_1 \leftarrow$N:1s spectator Auger transitions ($h\nu = 400$ eV, solid circles) and difference AES (solid line, pure spectator AES) of NH_3/Xe.

We also studied the H^+ desorption at the $4a_1 \leftarrow$N:1s resonant excitation of condensed NH_3 (Ref. 34). The TIY/AEY spectrum showed a characteristic threshold peak at the $4a_1 \leftarrow$N:1s resonance. The peak position of the H^+ AEPICOYS was found to be the same as that of the resonant AES. These results suggest that H^+ is desorbed by a four-step mechanism similar to that of condensed H_2O at the $4a_1 \leftarrow$O:1s resonance; that is, the mechanism consists of (1) the $4a_1 \leftarrow$N:1s transition, (2) extension of the H_2N–H distance in the $(N{:}1s)^{-1}(4a_1)^1$ state, (3) a spectator Auger transition leaving the $(\text{valence})^{-2}(4a_1)^1$ state, and (4) H^+ desorption. This was difficult to conclude, however, because the electrons emitted from bulk NH_3 dominated those emitted from the upper molecular layers from which H^+ could be desorbed.

3.2.2. Submonolayer adsorbed on Xe film. As suggested in Sec. 3.2.1, to clarify the H^+ desorption mechanism for the $4a_1 \leftarrow$N:1s resonant excitation of NH_3 it is necessary to investigate an NH_3 submonolayer adsorbed on a chemically inactive substance. Accordingly, we studied the H^+ desorption of an isolated NH_3 submonolayer adsorbed on a Xe film (NH_3/Xe).[35] The NH_3/Xe sample was prepared by exposing a gold foil to 300 L (1 L$=1\times10^{-6}$ Torr·s) of Xe followed by exposure to 1 L of NH_3, and the coverage of NH_3 is less than 1 ML (unity sticking factor, monolayers). Figure 16 shows the TIY spectrum in the range of the N:1s excitation of NH_3/Xe. This spectrum is similar to that reported for condensed NH_3 by Menzel *et al.*[87] and displays a characteristic threshold peak at a photon energy of 400 eV. The peak is assigned to the resonant excitation from N:1s to the $4a_1$ orbital with an N–H antibonding character.[88]

Figure 17 shows the H^+ AEPICOYS for the $4a_1 \leftarrow$N:1s spectator Auger transitions (solid circles), together with the difference AES (solid line, pure spectator AES). Three peaks in the AEPICOYS are assigned to the spectator Auger final states with characters of $(2a_1)^{-2}(4a_1)^1$, $(2a_1)^{-1}(N{:}2p)^{-1}(4a_1)^1$, and $(N{:}2p)^{-2}(4a_1)^1$. Here, N:2p denotes the $1e$ or $3a_1$ orbital. Since the shape of the AEPICOYS roughly looks like that of the spectator AES, the four-step H^+ desorption mechanism (Fig. 9) is the most plausible mechanism for the $4a_1 \leftarrow$N:1s resonance of NH_3, as in the $4a_1 \leftarrow$O:1s resonance of condensed H_2O.

3.3. CH_3CN

In this Section we describe a study using EICO spectroscopy to investigate the H^+ desorption mechanism for the C:1s resonant excitation[36–38] of condensed CH_3CN (acetonitrile). The valence electronic configuration of CH_3CN is $(6a_1)^2(1e)^4(7a_1)^2(2e)^4$ (Ref. 89). The characters of the $6a_1$, $1e$, $7a_1$, and $2e$ orbitals are the σ_{C-C} (including the C:2s character), π_{CH3} (pseudo π), σ_{CN}, and π_{CN} bonding orbitals, respectively.

Figure 18 shows the AEY (a, solid line), TIY (b, solid line), and TIY/AEY (b, dashed line) spectra in the range of the C:1s excitation of condensed CH_3CN. The AEY spectrum is close to the carbon-K near-edge spectrum of condensed CH_3CN reported by Stevens *et al.*[90] The most intense peak corresponds to the $\pi^*_{CN} \leftarrow$C:1s resonance. The assignments of the structures in the AEY spectrum are shown in Fig. 18a. The TIY spectrum in Fig. 18b shows the H^+ de-

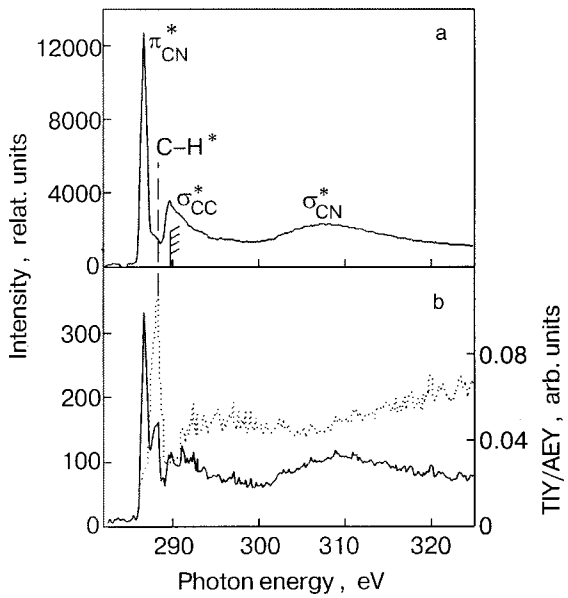

FIG. 18. AEY (a, solid line, electron kinetic energy=255 eV), TIY (b, solid line), and TIY/AEY (b, dashed line) in the range of the C:1s excitation of condensed CH_3CN. The hatching in (a) shows the ionization limit taken from Ref. 90.

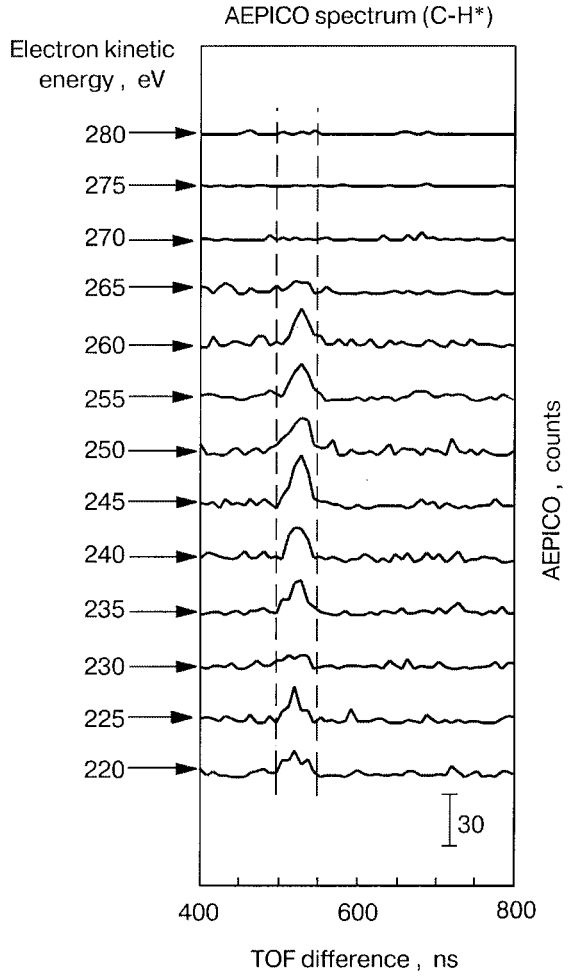

FIG. 19. A series of spectator AEPICO spectra taken at the C–H*←C:1s resonance ($h\nu$=288.1 eV) of condensed CH_3CN.

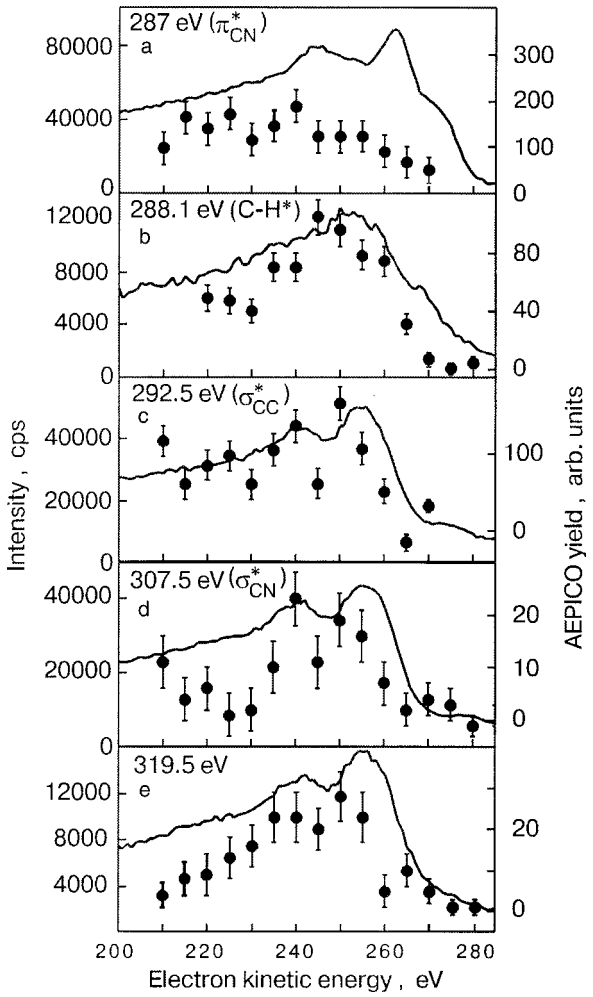

FIG. 20. H^+ AEPICOYS (solid circles) and AES (solid lines) for the C:KVV spectator and normal Auger transitions of condensed CH_3CN.

sorption yield, as will be described later. The TIY/AEY spectrum shows a large peak at the C–H*←C:1s resonance (288.1 eV, Fig. 18b). This fact indicates that the desorption efficiency increases substantially at the C–H*←C:1s resonance.

We made AEPICO measurements at the π^*_{CN}←C:1s, C–H*←C:1s, σ^*_{CC}←C:1s, and σ^*_{CN}←C:1s resonances of condensed CH_3CN. Figure 19 shows a series of spectator AEPICO spectra taken at the C–H*←C:1s resonance ($h\nu$ =288.1 eV). The dominant peak at 528 ns was assigned to the H^+ signal. Ionic species other than H^+ were negligible in the AEPICO spectra. We also made AEPICO measurements at other photon energies in the C:KVV Auger-electron transition, but ions other than H^+ were also negligible in this case. We consider the reneutralization of heavier ionic species to be more effective than for H^+, because of these species' large mass and slow exit velocity.[84–86]

Figure 20 shows a series of H^+ AEPICOYS (solid circles) together with the AES (solid lines). At the π^*_{CN} ←C:1s resonance (Fig. 20a), in comparison with the spectator AES, the H^+ desorption is suppressed at the peak located at 262 eV. This peak corresponds to the spectator Auger final state in which two holes are formed in the $2e$, $7a_1$, or $1e$ orbitals.[38] The $2e$ and $7a_1$ electrons do not contribute to the C–H bonding. The initially excited electron occupies the π^*_{CN} orbital, which is mainly distributed over the CN bonding and unrelated to the CH_3 group. The π^*_{CN} electron reduces the hole–hole repulsion on account of the shielding effect, so that H^+ desorption is suppressed. At the σ^*_{CC} ←C:1s resonance (Fig. 20c), in comparison with the spectator AES, the AEPICOYS is enhanced near 250 eV, which corresponds to the energy of the $(1e)^{-2}(\sigma^*_{CC})^1$ and $(1e)^{-1}(6a_1)^{-1}(\sigma^*_{CC})^1$ spectator Auger final states.[38] The H^+ desorption from the Auger final states with one or two holes in the $1e$ orbital is enhanced. This effect is attributed to the removal of electrons from the C–H bond. At the C–H* ←C:1s resonance (Fig. 20b), the AEPICOYS is also enhanced at the $(1e)^{-2}$(C–H*)^1 and $(1e)^{-1}(6a_1)^{-1}$(C–H*)^1 states. This is because in these states the excited electron is in the antibonding C–H* orbital and one or two holes are occupied by the pseudo-π_{CH3} $1e$ orbital.

In summary, the electron excitation to the C–H* antibonding orbital and the removal of the electron from the pseudo-π_{CH3} orbital ($1e$) both enhance H^+ ion desorption. On the other hand, electron excitation to an orbital irrelevant to the C–H bonding suppresses H^+ desorption. Further investigation is needed to determine the predominant H^+ desorption mechanism.

3.4. Site-specific fragmentation of CF_3CH_3

The core electrons of atoms in molecules are localized at their atoms of origin, and the chemical shift shown by an

atom depends on the chemical environment of that atom. Like atoms in different chemical environments thus show different chemical shifts. For almost 20 years these properties have been used to study site-specific fragmentation,[13,42,91–95] which is potentially useful for controlling chemical reactions through selective bond dissociation. Site-specific fragmentation also offers the possibility of analyzing the structures and properties of molecules, molecular assemblies, and nanoscale devices by controlling matter at the level of individual atoms. To develop these exciting prospects, we need to understand what controls behavior at the atomic level.

Since the chemical shifts of like atoms in a molecule differ site-by-site when the atoms are in different chemical environments, the photoelectron spectrum of the core electrons of those atoms is expected to show a number of peaks equal to the number of different kinds of sites in which the atoms are found. The normal Auger transition caused by photoelectron emission produces two valence holes in molecular orbitals that have a large probability density on the core-ionized atomic site (that is, the Auger transition is localized), and these holes weaken the chemical bonds to which the molecular orbitals are related. Since these molecular orbitals with valence holes have a large probability density on the core-ionized atom, the valence holes weaken the bonds to the core-ionized atom. As a result, site-specific fragmentation occurs at the core-ionized atomic site. The molecule thus ''memorizes'' the site of the initial energy deposition.[96] To observe a site-specific fragmentation process, we should selectively detect fragments produced by an energy-selected photoelectron emission that corresponds to one of the peaks in the photoelectron spectrum of the core electrons.

S.N. and his collaborators have studied the site-specific fragmentation caused by core-level photoionization of vaporized molecules[42,97–99] and molecules condensed or adsorbed on surfaces.[23,41–45,53] They found that this fragmentation is often better studied on a surface than in a vapor.[41–44] The advantages of EICO experiments on surfaces were explained in Sec. 1.

In this Section we explain the site-specific fragmentation caused by the C:1*s* photoionization of CF_3CH_3 (1,1,1-trifluoroethane, TFEt) condensed on a Au surface.[44] TFEt is the simplest organic molecule with two carbon sites in different chemical environments; one of the carbon atoms is bonded to three hydrogen atoms (C[H]), while the other is bonded to three fluorine atoms (C[F]). Accordingly, TFEt is suitable for such a study because it is a prototypical example of a molecule exhibiting site-specific fragmentation.

Figure 21 shows the PES of TFEt condensed on a Au surface. The peak assignments in the figure were inferred by comparison with the PES and AES of C and Au.[100,101] The PES has two peaks in the range of the C:1*s* electron emission. The low-energy and high-energy peaks were, respectively, assigned to the C[H]:1*s* and C[F]:1*s* electron emissions based on comparison with the zero-kinetic-energy photoelectron-yield spectrum[96] and the PES[102] of TFEt vapor. The PES of condensed TFEt thus clearly shows that the chemical shifts (binding energies) at the two carbons are different.

The site-specific fragmentation caused by the C:1*s* core-level photoionization of TFEt can be observed by using the PEPICO technique. Figure 22 shows PEPICO spectra obtained with emission of the C[H]:1*s* and C[F]:1*s* electrons. The intensity of the PEPICO signal is proportional to the ion desorption yield measured for a selected electron emission. H^+, CH_3^+, and CF_3^+ ions are desorbed coincidentally with the C[H]:1*s* electrons (Fig. 22a), and $C_2H_n^+$ and $CFCH_m^+$ ions are additionally desorbed with the C[F]:1*s* electrons (Fig. 22b). These PEPICO spectra are very different from the mass spectrum obtained by electron impact in the vapor phase.[103] It should be noted that the C[F]:1*s* ionization induces the desorption of $C_2H_n^+$ and $CFCH_m^+$, both of which contain a C–C bond, but that its desorption is negligible in the C[H]:1*s* ionization. In contrast, H^+, CH_3^+, and CF_3^+, which do not contain a C–C bond, are desorbed with not only the C[F]:1*s* electrons but also the C[H]:1*s* electrons. The intensity ratios of the coincidental desorption with the C[H]:1*s* electron to that with the C[F]:1*s* electron are 1.1 for H^+, 1.2 for CH_3^+, and 0.8 for CF_3^+. The predominant production of CH_3^+ caused by the C[H]:1*s* photoionization is also observed in the normal AEPICO spectrum.[44]

Although the site-specificity for H^+, CH_3^+, and CF_3^+ in TFEt is less remarkable than expected from results obtained[41] for condensed $F_3SiCH_2CH_2Si(CH_3)_3$, the pre-

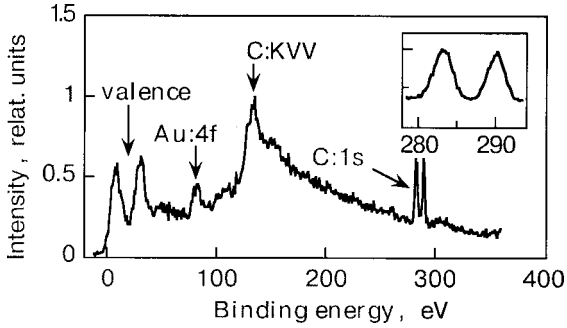

FIG. 21. PES of condensed TFEt, taken at a photon energy of 393.4 eV. The inset shows the range of the C:1*s* electron emission with an enlarged horizontal scale.

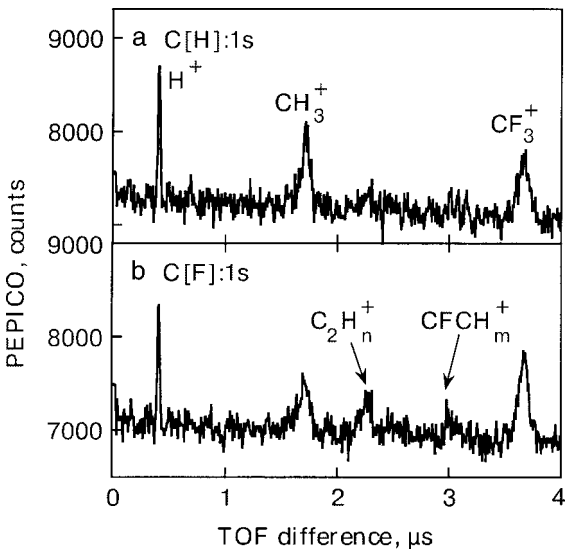

FIG. 22. PEPICO spectra of condensed TFEt, taken at a photon energy of 393.4 eV. (a) C[H]:1*s* electron emission, (b) C[F]:1*s* electron emission.

dominant fragmentation processes caused by the C[H]:1*s* and C[F]:1*s* photoionizations are as follows.

C[H]:1*s* ionization:

$$\mathrm{TFEt}+h\nu\rightarrow \mathrm{TFEt}^{2+}+2e \tag{1a}$$

(photoionization and normal Auger process),

$$\rightarrow \mathrm{H}^{+}+\mathrm{n.p.}, \tag{1b}$$

$$\rightarrow \mathrm{CH}_3^{+}+\mathrm{n.p.} \tag{1c}$$

C[F]:1*s* ionization:

$$\mathrm{TFEt}+h\nu\rightarrow \mathrm{TFEt}^{2+}+2e \tag{2a}$$

(photoionization and normal Auger process),

$$\rightarrow \mathrm{CF}_3^{+}+\mathrm{n.p.}, \tag{2b}$$

$$\rightarrow \mathrm{CFCH}_m^{+}+\mathrm{n.p.}, \tag{2c}$$

$$\rightarrow \mathrm{C}_2\mathrm{H}_n^{+}+\mathrm{n.p.}\ \ (n\leqslant m\leqslant 3), \tag{2d}$$

where n.p. stands for ''neutral product''. It is assumed that the normal ASID mechanism also plays an important role for TFEt.

The C[H]:1*s* ionization induces the breaking of the C–H bonds [reaction (1b)] and the C–C bond [reaction (1c)], while the C[F]:1*s* ionization induces the breaking of the C–C bond [reaction (2b)] and the C–F bonds [reactions (2c) and (2d)]. Thus, site-specific fragmentation occurs around the carbon atom where the photoionization has taken place. The KVV normal Auger transition is localized, and energy randomization destroying the memory of the ionization process does not take place extensively before fragmentation. TFEt moderately memorizes the site of the initial energy deposition, exhibiting the chemical memory effect.[96]

Although a strong effect from the site of the initial energy deposition is observed for the fragments $\mathrm{C}_2\mathrm{H}_n^{+}$ and CFCH_m^{+} released from TFEt, the site-specificity for H^{+}, CH_3^{+}, and CF_3^{+} is, as mentioned above, less remarkable than that previously shown[41] for condensed $\mathrm{F_3SiCH_2CH_2Si(CH_3)_3}$. We cannot yet explain the fragmentation processes for CF_3^{+} in the C[H]:1*s* ionization and for H^{+} and CH_3^{+} in the C[F]:1*s* ionization, but the lesser degree of site-specificity for H^{+}, CH_3^{+}, and CF_3^{+} in TFEt is thought to be caused by the proximity of the two carbon sites to each other. In fact, we previously showed that site-specificity in $\mathrm{X_3Si(CH_2)}_n\mathrm{Si(CH_3)_3}$ (X=F or Cl, $n=0-2$) decreases with decreasing distance between the two silicon sites.[43] We previously mentioned that site-specific fragmentation is potentially useful for controlling chemical reactions through selective bond dissociation. The present results, however, as well as those for $\mathrm{X_3Si(CH_2)}_n\mathrm{Si(CH_3)_3}$ (X=F or Cl; $n=0-2$),[43] show that for this process to work well, the atomic site of interest must be far from any atomic site at which bond dissociation is undesirable.

Müller-Dethlefs and his collaborators investigated site-specific fragmentation by studying the ionic fragmentation processes caused by the C:1*s* photoionization of TFEt in the vapor phase.[92,96] The experimental results on the site-specific fragmentation of TFEt were compared with theoretical predictions.[104] The presence of different chemical shifts (different binding energies) that were obtained for TFEt on the surface in the present work is consistent with that obtained for the vapor phase.[92,96] However, the site-specific fragmentation products of TFEt on the surface and in the vapor phase are very different from each other (Table I). In the vapor phase, the ionic fragments CFH_2^{+}, $\mathrm{CF_2CH}_2^{+}$, CF_3^{+}, C^{+}, and CF^{+} were the most sensitive to the site of the initial energy deposition:[96] the C[H]:1*s* ionization led to much higher counts of CFH_2^{+} and $\mathrm{CF_2CH}_2^{+}$ than did the C[F]:1*s* ionization. The C[H]:1*s* ionization or excitation enhanced the production of CF_3^{+}, whereas the C[F]:1*s* ionization or excitation enhanced the production of C^{+} and CF^{+}. The C–C bond of the TFEt vapor was more easily broken by C[F]:1*s* ionization or excitation than by C[H]:1*s* ionization or excitation. The fragmentation products of condensed TFEt, in contrast, show that $\mathrm{C}_2\mathrm{H}_n^{+}$ and CFCH_m^{+} are the most sensitive to the site of the initial energy deposition (Fig. 22). Of the fragments whose signals are evident in the spectra of Fig. 22, only $\mathrm{C}_2\mathrm{H}_n^{+}$ and CFCH_m^{+} have a C–C bond, and those ions are desorbed site-specifically after the C[F]:1*s* ionization. The C–C bond in TFEt on the surface is thus more easily broken by C[H]:1*s* ionization than by C[F]:1*s* ionization. In contrast to what was observed for the vapor phase, CF_3^{+} is the predominant product of desorption induced by C[F]:1*s* ionization on the surface [reaction (2b)].

TABLE I. Site-specific fragmentation products of TFEt.

	Condensed TFEt (this work)	TFEt vapor (Ref. 96)
C[H]:1*s*	H^{+}, CH_3^{+}	CFH_2^{+}, $\mathrm{CF_2CH}_2^{+}$,[a] CF_3^{+}
C[F]:1*s*	$\mathrm{C}_2\mathrm{H}_n^{+}$,[a] CFCH_m^{+},[a] CF_3^{+}	C^{+}, CF^{+}

Note: [a]Fragment with a C–C bond.

We do not know exactly why the site-specific fragmentation of TFEt on the surface differs from that of TFEt in the vapor phase, but we can suggest a possible explanation. Tinone *et al.*[105] previously noted that the reneutralization path is less probable in the vapor phase, all the ions produced are collected by the ion detection apparatus, and the resulting spectrum is an average of all fragmentation paths. For excitation on a solid surface, however, the ions produced through the fast and energetic path are detected selectively. The above-mentioned difference in fragmentation process between TFEt vapor and condensed TFEt may also originate from the difference suggested by Tinone *et al.*

4. CONCLUSIONS AND FUTURE PERSPECTIVE

In this article we have described the present status of the EICO apparatus and six recent investigations of condensed $\mathrm{H_2O}$, $\mathrm{NH_3}$, $\mathrm{CH_3CN}$, and $\mathrm{CF_3CH_3}$ (site-specific fragmentation) at low temperature. The EICO method is thus a very powerful tool for studies of PSID.

Although condensed molecules are important targets in low-temperature physics, a monolayer of a molecule adsorbed on a well-defined surface is more advantageous as a target of EICO studies.[22,31,45,49–51] From this standpoint, a half monolayer of $\mathrm{H_2O}$ or $\mathrm{NH_3}$ adsorbed on $\mathrm{H_2O/Si(100)}$ would be interesting. Since $\mathrm{H_2O}$ is dissociatively chemisorbed to form Si–OH and Si–H species on Si(100),[64] $\mathrm{H_2O}$ and $\mathrm{NH_3}$ are expected to be adsorbed on the Si–OH sites through an intermolecular hydrogen bond, forming a good

model for the uppermost molecular layer of the condensed molecules with intermolecular hydrogen bonds. For condensed molecules without intermolecular hydrogen bonds, hydrogen-terminated Si(111) may be an adequate substrate.

An interesting subject for future work would be development of advanced coincidence apparatus. EICO spectroscopy using a reflection TOF-MS[106] would be useful for the study of polymer surfaces. Coincidence between an electron and an energy-selected ion will offer information on the potential energy surface responsible for PSID. Coincidence between an electron and an angle-resolved ion will clarify the configuration of the surface species responsible for PSID. By using photoelectron–Auger-electron–photoion triple coincidence spectroscopy, one would be able to directly connect the photoionization initial state, the Auger final state, and the resultant ion desorption. Coincidence between a photoelectron (or an Auger electron) and a photon emitted from a neutral fragment would also be interesting. Although neutral species are not easily detected by ordinary methods, detection of their photon emission would not be very difficult. EICO spectroscopy combined with vacuum ultraviolet light, hard x rays, an electron beam, ion beam, multiply charged ion beam, energetic neutral beam, metastable atom beam, positron beam, and so on is a promising field. EICO spectroscopy also holds hope as a surface analysis technique, because EICO spectra can be used as highly sensitive PES and AES (Sec. 3.1.2) and because EICO spectroscopy can detect a surface hydrogen atom and can specify the atom to which a desorbed ion is bonded. The coincidence method is a promising method for further studies of surface science.

The ''we'' in this paper is not necessarily synonymous with only K.M., M.N., S.T., T.S., and S.N., but also represents contributions from various combinations of the authors' collaborators. Their contributions are greatly acknowledged. We also express our sincere thanks to the members of the UVSOR and PF synchrotron radiation facilities for their valuable help during the course of the experiments.

[a]Present address: Department of Materials Science and Engineering, Graduate School of Engineering, Kyoto University, Sakyo-ku, Kyoto 606-8501, Japan
[b]Present address: The Institute of Scientific and Industrial Research Osaka University, 8-1 Mihogaoka, Ibaraki 567-0047, Japan
[c]E-mail: nagaoka@ehimegw.dpc.ehime-u.ac.jp

[1]T. E. Madey, Surf. Sci. **299/300**, 824 (1994).
[2]D. E. Ramaker, in *Desorption Induced by Electronic Transitions*, DIET-II, Vol. 4 of Springer Series in Surface Sciences, W. Brenig and D. Menzel (eds.) Springer, Berlin (1985), p. 10.
[3]V. Rehn and R. A. Rosenberg, in *Synchrotron Radiation Research: Advances in Surface and Interface Science*, Vol. 1, R. Z. Bachrach (Ed.) Plenum, New York (1992), p. 327.
[4]R. A. Rosenberg and V. Rehn, in *Synchrotron Radiation Research: Advances in Surface and Interface Science*, Vol. 2, R. Z. Bachrach (Ed.) Plenum Press, New York (1992), p. 267.
[5]R. Treichler, W. Wurth, W. Riedl, P. Feulner, and D. Menzel, Chem. Phys. **153**, 259 (1991).
[6]R. A. Rosenberg and S. P. Frigo, in *Chemical Applications of Synchrotron Radiation Part I: Dynamics and VUV Spectroscopy*, T. -K. Sham (Ed.) World Scientific, Singapore (2002), p. 462.
[7]T. E. Madey, R. E. Johnson, and T. M. Orlando, Surf. Sci. **500**, 838 (2002).
[8]M. T. Sieger, W. C. Simpson, and T. M. Orlando, Nature (London) **394**, 554 (1998).
[9]B. V. Yakshinskiy and T. E. Madey, Nature (London) **400**, 642 (1999).
[10]D. A. Williams, in *Dust and Chemistry in Astronomy*, D. A. Williams and T. J. Millar (eds.), IOP Publishing, Philadelphia (1993), p. 143.
[11]E. Herbst, Annu. Rev. Phys. Chem. **46**, 27 (1995).
[12]D. E. Ramaker, T. E. Madey, R. L. Kurtz, and H. Sambe, Phys. Rev. B **38**, 2099 (1988).
[13]R. Romberg, N. Heckmair, S. P. Frigo, A. Ogurtsov, D. Menzel, and P. Feulner, Phys. Rev. Lett. **84**, 374 (2000).
[14]P. Feulner, R. Romberg, S. P. Frigo, R. Weimar, M. Gsell, A. Ogurtsov, and D. Menzel, Surf. Sci. **451**, 41 (2000).
[15]R. Weimar, R. Romberg, S. P. Frigo, B. Kassühlke, and P. Feulner, Surf. Sci. **451**, 124 (2000).
[16]*VUV and Soft X-Ray Photoionization*, U. Becker and D. A. Shirley (Eds.) Plenum Press, New York (1996) and references cited therein.
[17]R. Murphy and W. Eberhardt, J. Chem. Phys. **89**, 4054 (1988).
[18]W. Eberhardt, E. W. Plummer, I.-W. Lyo, R. Carr, and W. K. Ford, Phys. Rev. Lett. **58**, 207 (1987).
[19]M. L. Knotek and J. W. Rabalais, in *Desorption Induced by Electronic Transitions*, DIET-II, Vol. 4 of Springer Series in Surface Sciences, W. Brenig and D. Menzel (eds.) Springer, Berlin (1985), p. 77.
[20]K. Mase, M. Nagasono, T. Urisu, and Y. Murata, Bull. Chem. Soc. Jpn. **69**, 1829 (1996).
[21]K. Mase, M. Nagasono, S. Tanaka, M. Kamada, T. Urisu, and Y. Murata, Rev. Sci. Instrum. **68**, 1703 (1997).
[22]K. Mase and S. Tanaka, Jpn. J. Appl. Phys. **38–1**, 233 (1999).
[23]K. Mase, S. Tanaka, S. Nagaoka, and T. Urisu, Surf. Sci. **451**, 143 (2000).
[24]K. Mase, Kanae, **13**, 18 (2000) (in Japanese).
[25]K. Isari, K. Tanaka, S. Nagaoka, T. Gejo, H. Yoshida, and K. Mase, J. Vac. Soc. Jpn. (in Japanese), in press.
[26]K. Isari, E. Kobayashi, K. Mase, and K. Tanaka, Surf. Sci., in preparation.
[27]M. Nagasono, K. Mase, and T. Urisu, Surf. Sci. **363**, 342 (1996).
[28]K. Mase, M. Nagasono, S. Tanaka, T. Urisu, E. Ikenaga, T. Sekitani, and K. Tanaka, Surf. Sci. **390**, 97 (1997).
[29]M. Nagasono, K. Mase, S. Tanaka, and T. Urisu, Chem. Phys. Lett. **298**, 141 (1998).
[30]K. Mase, M. Nagasono, S. Tanaka, T. Urisu, E. Ikenaga, T. Sekitani, and K. Tanaka, J. Chem. Phys. **108**, 6550 (1998).
[31]K. Mase, M. Nagasono, and S. Tanaka, J. Vac. Soc. Jpn. **42**, 84 (1999) (in Japanese).
[32]S. Tanaka, K. Mase, M. Nagasono, S. Nagaoka, M. Kamada, E. Ikenaga, T. Sekitani, and K. Tanaka, Jpn. J. Appl. Phys. **39**, 4489 (2000).
[33]M. Nagasono, K. Mase, S. Tanaka, and T. Urisu, Surf. Sci. **377–379**, 380 (1997).
[34]M. Nagasono, K. Mase, S. Tanaka, and T. Urisu, Surf. Sci. **390**, 102 (1997).
[35]M. Nagasono, K. Mase, S. Tanaka, and T. Urisu, Jpn. J. Appl. Phys. Suppl. **38–1**, 325 (1999).
[36]T. Sekitani, E. Ikenaga, K. Tanaka, K. Mase, M. Nagasono, S. Tanaka, and T. Urisu, Surf. Sci. **390**, 107 (1997).
[37]T. Sekitani, E. Ikenaga, H. Matsuo, S. Tanaka, K. Mase, and K. Tanaka, J. Electron Spectrosc. Relat. Phenom. **88–91**, 831 (1998).
[38]T. Sekitani, E. Ikenaga, K. Fujii, K. Mase, N. Ueno, and K. Tanaka, J. Electron Spectrosc. Relat. Phenom. **101–103**, 135 (1999).
[39]K. Mase, M. Nagasono, S. Tanaka, T. Urisu, and S. Nagaoka, Surf. Sci. **377–379**, 376 (1997).
[40]I. Shimoyama, T. Mochida, Y. Otsuki, H. Horiuchi, S. Saijyo, K. Nakagawa, M. Nagasono, S. Tanaka, and K. Mase, J. Electron Spectrosc. Relat. Phenom. **88–91**, 793 (1998).
[41]S. Nagaoka, K. Mase, M. Nagasono, S. Tanaka, T. Urisu, and J. Ohshita, J. Chem. Phys. **107**, 10751 (1997).
[42]S. Nagaoka, K. Mase, and I. Koyano, Trends Chem. Phys. **6**, 1 (1997).
[43]S. Nagaoka, K. Mase, M. Nagasono, S. Tanaka, T. Urisu, J. Ohshita, and U. Nagashima, Chem. Phys. **249**, 15 (1999).
[44]S. Nagaoka, S. Tanaka, and K. Mase, J. Phys. Chem. B **105**, 1554 (2001).
[45]S. Nagaoka, K. Mase, A. Nakamura, M. Nagao, J. Yoshinobu, and S. Tanaka, J. Chem. Phys. **117**, 3961 (2002).
[46]E. Ikenaga, K. Isari, K. Kudara, Y. Yasui, S. A. Sardar, S. Wada, T. Sekitani, K. Tanaka, K. Mase, and S. Tanaka, J. Chem. Phys. **114**, 2751 (2001).
[47]E. Ikenaga, K. Kudara, K. Kusaba, K. Isari, S. A. Sardar, S. Wada, K. Mase, T. Sekitani, and K. Tanaka, J. Electron Spectrosc. Relat. Phenom. **114–116**, 585 (2001).
[48]K. Tanaka, E. O. Sako, E. Ikenaga, K. Isari, S. A. Sardar, S. Wada, T. Sekitani, K. Mase, and N. Ueno, J. Electron Spectrosc. Relat. Phenom. **119**, 255 (2001).

[49]S. Tanaka, K. Mase, M. Nagasono, and M. Kamada, Surf. Sci. **390**, 204 (1997).
[50]S. Tanaka, K. Mase, S. Nagaoka, M. Nagasono, and M. Kamada, J. Chem. Phys. **117**, 4479 (2002).
[51]S. Tanaka, K. Mase, M. Nagasono, and M. Kamada, J. Electron Spectrosc. Relat. Phenom. **92**, 119 (1998).
[52]S. Tanaka, K. Mase, M. Nagasono, S. Nagaoka, and M. Kamada, Surf. Sci. **451**, 182 (2000).
[53]K. Mase, M. Nagasono, S. Tanaka, and S. Nagaoka, J. Jpn. Soc. Synchrotron Radiation Res. **10**, 375 (1997) (in Japanese).
[54]K. Mase, M. Nagasono, and S. Tanaka, J. Electron Spectrosc. Relat. Phenom. **101–103**, 13 (1999).
[55]K. Mase, Chem. Chem. Ind. **53**, 111 (2000) (in Japanese).
[56]K. Siegbahn, N. Kholine, and G. Golikov, Nucl. Instrum. Methods Phys. Res. A **384**, 563 (1997).
[57]M. L. Knotek and P. J. Feibelman, Phys. Rev. Lett. **40**, 964 (1978).
[58]R. Franchy and D. Menzel, Phys. Rev. Lett. **43**, 865 (1979).
[59]D. R. Jennison, J. A. Kelber, and R. R. Rye, Phys. Rev. B **25**, 1384 (1982).
[60]P. J. Feibelman, Surf. Sci. **102**, L51 (1981).
[61]M. Cini, Phys. Rev. B **32**, 1945 (1985).
[62]D. E. Ramaker, C. T. White, and J. S. Murday, Phys. Lett. A **89**, 211 (1982).
[63]J. P. Devlin and V. Buch, J. Phys. Chem. **99**, 16534 (1995).
[64]P. A. Thiel and T. E. Madey, Surf. Sci. Rep. **7**, 211 (1987).
[65]M. A. Henderson, Surf. Sci. Rep. **46**, 1 (2002).
[66]D. E. Ramaker, Chem. Phys. **80**, 183 (1983).
[67]M. T. Sieger, W. C. Simpson, and T. M. Orlando, Phys. Rev. B **56**, 4925 (1997).
[68]R. A. Rosenberg, P. R. LaRoe, V. Rehn, J. Stöhr, R. Jaeger, and C. C. Parks, Phys. Rev. B **28**, 3026 (1983).
[69]D. Coulman, A. Puschmann, U. Höfer, H.-P. Steinrück, W. Wurth, P. Feulner, and D. Menzel, J. Chem. Phys. **93**, 58 (1990).
[70]H. Siegbahn, L. Asplund, and P. Kelfve, Chem. Phys. Lett. **35**, 330 (1975).
[71]H. Ågren, S. Svensson, and U. I. Wahlgren, Chem. Phys. Lett. **35**, 336 (1975).
[72]P. Morin and I. Nenner, Phys. Rev. Lett. **56**, 1913 (1986).
[73]M. N. Piancastelli, A. Hempelmann, F. Heiser, O. Gessner, A. Rüdel, and U. Becker, Phys. Rev. A **59**, 300 (1999).
[74]I. Hjelte, M. N. Piancastelli, R. F. Fink, O. Björneholm, M. Bässler, R. Feifel, A. Giertz, H. Wang, K. Wiesner, A. Ausmees, C. Miron, S. L. Sorensen, and S. Svensson, Chem. Phys. Lett. **334**, 151 (2001).
[75]R. Romberg, S. P. Frigo, A. Ogurtsov, P. Feulner, and D. Menzel, Surf. Sci. **451**, 116 (2000).
[76]C. Keller, M. Stichler, G. Comelli, F. Esch, S. Lizzit, W. Wurth, and D. Menzel, Phys. Rev. Lett. **80**, 1774 (1998).
[77]C. Keller, M. Stichler, G. Comelli, F. Esch, S. Lizzit, D. Menzel, and W. Wurth, Phys. Rev. B **57**, 11951 (1998).
[78]W. Wurth and D. Menzel, Chem. Phys. **251**, 141 (2000).
[79]W. F. Egelhoff, Jr., Surf. Sci. Rep. **6**, 253 (1987).
[80]M. Akbulut, N. J. Sack, and T. E. Madey, Surf. Sci. Rep. **28**, 177 (1997).
[81]N. Martensson, P.-Å. Malmquist, S. Svensson, E. Basilier, J. J. Pireaux, U. Gelius, and K. Siegbahn, Nouv. J. Chim. **1**, 191 (1976).
[82]B. Baron and F. Williams, J. Chem. Phys. **64**, 3896 (1976).
[83]F. P. Larkins and A. Lubenfeld, J. Electron Spectrosc. Relat. Phenom. **15**, 137 (1979).
[84]R. D. Ramsier and J. T. Yates, Jr., Surf. Sci. Rep. **12**, 243 (1991).
[85]J.-G. Lee, J. Ahner, and J. T. Yates, Jr., J. Chem. Phys. **114**, 1414 (2001).
[86]J.-G. Lee, J. Ahner, P. Maksymovych, and J. T. Yates, Jr., Chem. Phys. Lett. **340**, 21 (2001).
[87]D. Menzel, G. Rocker, D. Coulman, P. Feulner, and W. Wurth, Phys. Scr. **41**, 588 (1990).
[88]J. Schirmer, A. B. Trofimov, K. J. Randall, J. Feldhaus, A. M. Bradshaw, Y. Ma, C. T. Chen, and F. Sette, Phys. Rev. A **47**, 1136 (1993).
[89]K. Kimura, S. Katsumata, Y. Achiba, T. Yamazaki, and S. Iwata, *Handbook of He I Photoelectron Spectra of Fundamental Organic Molecules*, Japan Scientific Societies Press/Halsted Press, Tokyo/New York (1981).
[90]P. A. Stevens, R. J. Madix, and J. Stöhr, J. Chem. Phys. **91**, 4338 (1989).
[91]W. Eberhardt, T. K. Sham, R. Carr, S. Krummacher, M. Strongin, S. L. Weng, and D. Wesner, Phys. Rev. Lett. **50**, 1038 (1983).
[92]K. Müller-Dethlefs, M. Sander, L. A. Chewter, and E. W. Schlag, J. Phys. Chem. **88**, 6098 (1984).
[93]D. M. Hanson, Adv. Chem. Phys. **77**, 1 (1990).
[94]N. Ueno and K. Tanaka, J. Jpn. Soc. Synchrotron Radiation Res. **9**, 29 (1996) (in Japanese).
[95]I. Nenner, C. Reynaud, H. C. Schmelz, L. Ferrand-Tanaka, M. Simon, and P. Morin, Z. Phys. Chem. (Leipzig) **195**, 43 (1996).
[96]W. Habenicht, H. Baiter, K. Müller-Dethlefs, and E. W. Schlag, J. Phys. Chem. **95**, 6774 (1991).
[97]S. Nagaoka, J. Ohshita, M. Ishikawa, K. Takano, U. Nagashima, T. Takeuchi, and I. Koyano, J. Chem. Phys. **102**, 6078 (1995).
[98]S. Nagaoka, T. Fujibuchi, J. Ohshita, M. Ishikawa, and I. Koyano, Int. J. Mass Spectrom. Ion Phys. **171**, 95 (1997).
[99]S. Nagaoka, T. Fujibuchi, J. Ohshita, U. Nagashima, and I. Koyano, Chem. Phys. **276**, 243 (2002).
[100]C. D. Wagner, W. M. Riggs, L. E. Davis, J. F. Moulder, and G. E. Muilenberg, *Handbook of X-ray Photoelectron Spectroscopy*. Perkin-Elmer, Eden Prairie, Minnesota (1979).
[101]K. D. Childs, B. A. Carlson, L. A. LaVanier, J. F. Moulder, D. F. Paul, W. F. Stickle, D. G. Watson, and C. L. Hedberg, *Handbook of Auger Electron Spectroscopy 3rd Edition*, Physical Electronics, Eden Prairie, Minnesota (1995).
[102]A. P. Hitchcock, Phys. Scr. **T31**, 159 (1990).
[103]J. M. Simmie and E. Tschuikow-Roux, Int. J. Mass Spectrom. Ion Phys. **7**, 41 (1971).
[104]I. Salman, J. Silberstein, and R. D. Levine, J. Phys. Chem. **95**, 6781 (1991).
[105]M. C. K. Tinone, K. Tanaka, J. Maruyama, N. Ueno, M. Imamura, and N. Matsubayashi, J. Chem. Phys. **100**, 5988 (1994).
[106]U. Boesl, R. Weinkauf, and E. W. Schlag, Int. J. Mass Spectrom. Ion Processes **112**, 121 (1992).

This article was published in English in the original Russian journal. Reproduced here with stylistic changes by AIP.

Absolute yields of the exciton-induced desorption at the surface of solid rare gases

I. Arakawa* and T. Adachi

Department of Physics, Gakushuin University, Mejiro, Tokyo 171-8588, Japan

T. Hirayama

Department of Physics, Rikkyo University, Ikebukuro, Tokyo 171-8501, Japan

M. Sakurai

Department of Physics, Kobe University, Nada, Kobe 657-8501, Japan

(Submitted December 10, 2002)
Fiz. Nizk. Temp. **29**, 342–350 (March 2003)

Absolute yields of the photo-induced desorption at the surface of solid rare gases are studied in the excitonic excitation region. Both metastable and total desorption yields depend strongly on excitation energy and film thickness of rare gas solids. The absolute desorption yields and their dependence on film thickness are quantitatively reproduced by a simulation based on the diffusion of excitons in the bulk and the kinetic energy release by a cavity ejection mechanism and an excimer dissociation mechanism followed by internal sputtering. © *2003 American Institute of Physics.* [DOI: 10.1063/1.1542446]

1. Introduction

When the surface of a solid rare gas is irradiated with vacuum ultraviolet light, it can eject atoms and clusters in ground, electronically and vibrationally excited, or ionized states. A variety of desorption mechanisms have been proposed for each desorbed species and for the excitation energy region. Two types of mechanisms are known to play an essential role in the desorption induced by the excitonic excitation: a cavity ejection (CE) mechanism due to the repulsive interaction between an excited atom with an inflated electron cloud and a matrix with negative electron affinity, and an excimer dissociation (ED) mechanism, the dissociation of an excimer in the vicinity of the surface. The investigation of the desorption phenomena initiated by the excitonic excitation is one of the most powerful tools for revealing the dynamical character of the exciton in rare gas solids.[1] The desorption of excited neutral particles of Ne and Ar has been investigated extensively for two decades;[2] the close relationship between exciton formation[3] and the details of the desorption mechanisms[4] has been almost fully elucidated. On the other hand, the desorption mechanism of the ground state neutral and its desorption yield have not been clarified yet, though it can safely be said that such atoms are the main component in the desorbed species.

We report the measured results on absolute yields of the metastable and total desorption induced by excitonic excitation from the surfaces of solid Ne, Ar, and Kr. We also show that the experimental results for Ne and Kr are satisfactorily reproduced by a simple model simulation of the desorption process.

2. Desorption mechanism

Negative electron affinity of the matrix is known to be essential for the CE process to have a repulsive interaction between the excited atom and the surrounding ground state atoms. The metastables desorbed through the CE process were observed for solids whose electron affinities E_A are negative, namely, solid Ne ($E_A=-1.4$ eV) and Ar (-0.4 eV), but not for solid Kr (0.3 eV) and Xe (0.5 eV).[5] The kinetic energy E_k of the metastable desorbed through the CE process originates from the lattice distortion energy around the exciton, which can be estimated roughly from the difference between the excitation energy E_x of the exciton and the excitation energy E_g of the corresponding state of an isolated atom in the gas phase.[1] The energy difference, E_x-E_g, is divided among three terms: E_k, the kinetic energy of a desorbing particle; E_{coh}, the cohesive energy of an atom on the surface; and E_{latt}, the energy absorbed in the lattice.[6] It has been revealed that 30–70% of the lattice distortion energy is transferred into the kinetic energy of the desorbing metastable from the surface exciton S1 of Ne and Ar.[4] It has been also studied experimentally by a molecular dynamics calculation.[7] In the case of Ne, for example, E_k of the metastable which is desorbed by the first-order surface exciton is 0.18 eV at the peak of the distribution, while the excitation energy E_x is (17.17 ± 0.03) eV and the E_g of the corresponding $2p^5 3s$ states are 16.619–16.848 eV.[8] The excitation energy E_x of the bulk exciton B1 of Ne is (17.57 ± 0.03) eV. Considering the low cohesion energy, 0.019 eV, of Ne, the lattice distortion energy, E_x-E_g, of 0.9–0.7 eV is large enough to squeeze the excited atom out of a second or third underlying layer to the vacuum. The squeezed excited atom may push overlying atoms forward. This internal sputtering process can result in a large total desorption yield of Ne. In solid Ar, though the lattice distortion energy is estimated at about 0.7–0.4 eV, the internal sputtering process must be less efficient because of its larger cohesion energy of 0.068 eV.

Dissociative relaxation of a rare gas excimer in the gas phase yields a kinetic energy of about 1 eV.[9] It is known that the ED process in a solid produces crystal defects.[10] If ED occurs in the vicinity of the surface of a rare gas solid, a

large number of atoms in the surface layer will be released into vacuum by the internal sputtering process.

3. Experimental

The experimental apparatus for the photostimulated desorption (PSD) study was installed at the BL5B beamline in the UVSOR facilities of the Institute for Molecular Science, Okazaki, Japan.[11–13] A solid rare gas film was prepared on a platinum substrate at a temperature of about 6 K, which was attached to a liquid helium cryostat in an ultrahigh-vacuum chamber with a base pressure below 10^{-8} Pa. The amount of the gas condensed on the substrate, the film thickness, was calculated from the exposure, which was the product of the pressure and the duration of deposition, assuming the condensation coefficient to be unity.

The wavelength resolution, $\lambda/\Delta\lambda$, of the vacuum ultraviolet light source was about 500 ± 200 in the range of λ between 20 and 100 nm. The light intensity was monitored by the photoelectron current from a goldplated mesh, through which the light beam was introduced onto the sample surface. We adopted the value of 0.07 electrons/photon as the photoelectron yield at a gold surface, which is the average value of the published data by Samson[14] between 52 and 100 nm of wavelength. The intensity of the photon flux ranged between 10^{11} and 10^{12} photons/s in the continuous mode and between 10^5 and 10^6 photons/pulse in pulsed mode within a diameter of 3 mm at the sample.

3.1. Metastable desorption measurement

The monochromatized photon beam is pulsed by a mechanical chopper in order to measure the time-of-flight (TOF) spectra of the desorbed metastable atoms. The width and the interval of the pulsed beam are 15 μs and 2.5 ms, respectively. The photon beam is incident at 20 deg to the normal direction of the sample surface.

The desorbed metastable atoms are detected by an open electron multiplier tube (EMT, Hamamatsu, R595) with a CuBe dynode as a first electrode. The EMT is fixed at a distance of 360 mm from the sample in the normal direction of the sample. The diameter of the entrance of EMT is 8 mm, which corresponds to a detection solid angle of $3.1\cdot10^{-5}$ sr. The lifetimes of the metastable ($^3P_{0,2}$) rare gas atoms are known to be much longer than the flight time of the detected atoms, which is less than 1 ms in our experimental system. The charged particles are rejected by applying suitable voltages to the grid mesh in front of the detector and the 1st dynode of EMT. In order to calculate the overall metastable yields, which were integrated for all direction in half space, we utilized the angular distributions of the desorbed metastables, which have been reported previously by our group.[15–17]

3.2. Total desorption measurement

The total desorption rate was calculated from the pumping speed and the rise of the partial pressure in the vacuum chamber during irradiation of the sample. The pumping speed of the turbomolecular pump and cold surfaces for desorbed rare gas was determined from the pressure measured by an extractor gauge installed in the chamber and from the flow rate calibrated volumetrically using a reference volume and a Baratron pressure gauge as a reference. A small rise of the partial pressure during irradiation was detected by a quadrupole mass spectrometer, which was calibrated against the extractor gauge. It should be noted that the uncertainty of the relative sensitivity of the extractor gauge was cancelled in the present method of determining the desorption rate.

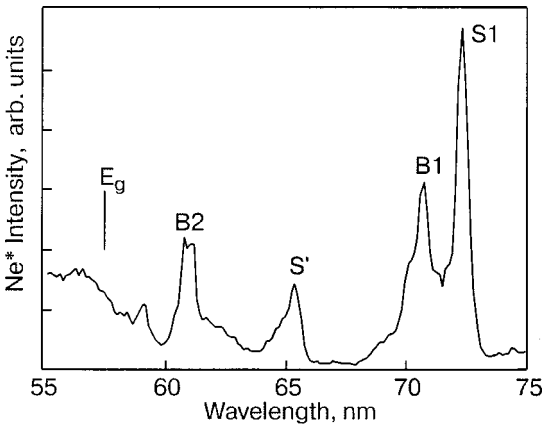

FIG. 1. The desorption yields of the Ne metastable in the excitonic excitation region as a function of incident wavelength.

3.3. Accuracy of measurements

In the metastable yield determination, the uncertainty of the results was estimated to be $\pm30\%$ by a quadrature sum of all sources of error; light intensity measurement, detection efficiency of the photomultiplier, geometrical configuration, etc. The main part of the error came from the estimation of the amount of higher-order light from the monochromator.[12,18]

The uncertainty in determining the absolute yield of the total desorption was estimated to be as large as $\pm1/3$ of an order of magnitude; an error bar ranging from -50% to $+100\%$ of the obtained value should be added to the values obtained. In addition to the uncertainty in the intensity measurement of the incident photon, it was caused by difficulties in determining the sensitivity of the mass spectrometer and the pumping speed for the desorbed species.

Noticeable changes in the desorption yields were observed after a few hours exposure of the sample in the chamber at a pressure in the lower 10^{-8} Pa range, where the main component was the rare gas itself. It was probably due to the adsorption of the common residual gases, H_2, H_2O, CO, in the UHV system.[19,20] The uncertainty caused by this impurity effect is within the above-mentioned error bar in the present experiment.

4. Desorption of Ne

4.1. Experimental results

The desorption yields of metastable Ne in the excitonic excitation region is shown in Fig. 1 as a function of incident wavelength. Most of the observed peaks in the figure can be assigned to a series of bulk (B) and surface (S) excitons reported by Saile and Koch,[21] where the peak S′ is caused by the exciton in the $2p^5 3p$ state, which is allowed at the sur-

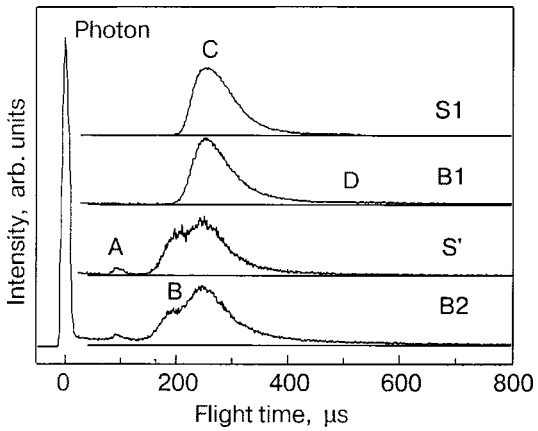

FIG. 2. The time-of-flight spectra of the metastable Ne desorbed by the excitation of the four types of excitons.

face because of the reduced symmetry.[22] The four TOF spectra of the metastable Ne in Fig. 2 were obtained by the excitations at the S1, B1, S′, and B2 excitons.

The wavelength dependence of the absolute yield of the total photodesorption in the range between 52 and 77 nm is shown in Fig. 3 for a film thickness of 73 atomic layers, where the peaks caused by the exciton excitation are also clearly seen. The absolute value of the desorption yield in the figure represents the average number of the Ne atoms desorbed by one incident photon. The large and continuous background was due to the desorption induced by ionization by the second- or higher-order light from the monochromator. The peaks caused by the bulk excitons, B1 and B2, develop at a film thickness of a few tens of atomic layers, and the absolute yields seem to saturate at around 1.6 and 1 atoms/photon, respectively, for films thicker than 100 atomic layers. The peak heights due to the surface excitons seem to remain constant at values of about 0.3 and 0.1 atoms/photon for S1 and S′, respectively, over the entire thickness range, as expected for surface excitations. The absolute yields of the metastable and total desorption by the four different excitonic excitations are summarized in Table I.

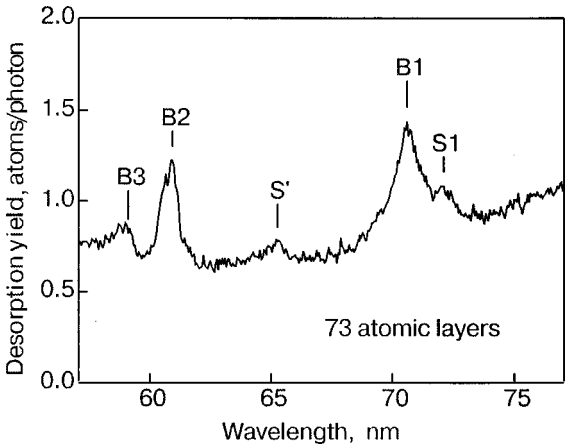

FIG. 3. The absolute yields of the total desorption of the Ne in the excitonic excitation region as a function of incident wavelength.

4.2. Schematic model of the desorption process

The operative mechanism in each desorption process and the branching ratio of the relaxation cascade which leads to the desorption can be deduced from a careful examination of the TOF spectra of the metastables and the absolute yields of the metastable and total desorption. The operative mechanisms in the desorption process are also listed in Table I.

The higher kinetic energy peak A ($E_k=(1.4\pm0.1)$ eV)[23] in Fig. 2, which is only observed by the excitation of the higher-order excitons (S′ and B2), is caused by the excimer dissociation of the highly excited dimer: $Ne_2^{**}\rightarrow Ne+Ne^*+E_k$. This is also the case for Ar.[24] The lower kinetic energy peak, that is, the CE peak, is obviously composed of two components B ($E_k=(0.21\pm0.02)$ eV) and C ($E_k=(0.18\pm0.02)$ eV).[12] The metastables which compose the peaks B and C are ejected directly from the surface excitons S′ and S1, respectively.[15] The difference in the kinetic energy is caused by the difference in the magnitude of the repulsive interaction. The low-energy tail D is only observed by the bulk excitations (B1 and B2)[15] and is likely caused by a bulk exciton trapped in the underlying layer just below the surface. They are ejected into the vacuum, losing their kinetic energy by collision with atoms in the overlayer. These TOF spectra can be used as a fingerprint to identify each exciton. These spectra also show clearly the relaxation channel of the excitons from the higher-energy state to the lower one; from B1 to S1, from S′ to S1 and excimer, and from B2 to S′, S1, and excimer.

The quantum efficiency of the exciton creation can be estimated from the photo-absorption coefficient of solid Ne at the wavelength corresponding to the bulk exciton (B1) excitation. We assume here that the excitation probability of S1 is the same as that of B1 in each layer at their own excitation energy. An estimation based on the data by Pudewill *et al.*[25] leads to the value of 0.1 excitons/photon in each layer.

The relaxation cascade of the first order surface exciton S1 of solid Ne is shown schematically in Fig. 4. Incident light of wavelength 72.2 nm will excite surface excitons with a probability of 0.1 excitons/photon in the first layer. 90% of the incident photons pass through the solid Ne film and will be scattered or absorbed at the substrate. The surface exciton may decay radiatively or may be desorbed by the CE mechanism as a metastable in the $^3P_{2,0}$ state or as an excited atom in the $^3P_1$ or $^1P_1$ state, which decay into the ground state with a short lifetime of 1–10 ns. In our study, we have determined the absolute yields of the metastable desorption, 0.0023 Ne*/photon, and of the total desorption, 0.3 Ne/photon. Considering the absolute total desorption yield of 0.3 atoms/photon at S1 excitation, the value 0.1 excitons/photon for the initial excitation probability must be underestimated, since it is likely that a surface exciton can lead to desorption of only a single excited atom in the CE process. The larger desorption yield may be explained by other desorption processes: the desorption of a dimer by the CE process and an ED process which yields two or more desorbed atoms. However, the branching ratio to these two processes must be far smaller than that to the single atom desorption by the CE process. Another possibility is excitation by light reflected at the substrate surface. If this is the case, the initial excitation

TABLE I. The absolute yields of the metastable and the total desorption from solid Ne, Ar, and Kr.

Rare gases	Initial excitation	Desorbed species	Yield, atoms/photon	Desorption mechanisms
Ne	S1	metastable	$(2.3 \pm 0.7)\cdot 10^{-3}$	CE
		total	0.3	CE + S/CE(?%) + S/ED(?%)
	S′	metastable	$(7.8 \pm 2.3)\cdot 10^{-4}$	CE + ED(≤ 1%)
		total	0.1	CE + S/CE(?%) + S/ED(?%)
	B1	metastable	$(1.4 \pm 0.4)\cdot 10^{-3}$	CE + S/CE(a few %)
		total	1.6 ± 0.3	S/CE + CE(≈ 10%) + S/ED(a few %)
	B2	metastable	$\approx 1\cdot 10^{-3}$	CE + S/CE(a few %) + ED(≤ 1%)
		total	1 ± 0.2	S/CE + CE(≈ 10%) + S/ED(a few %)
Ar	S1	metastable	$\approx 1\cdot 10^{-5}$	CE
		total	0.1	CE
	S2	metastable	not determined	CE + ED
		total	0.1	CE
	B1	metastable	not determined	CE
		total	0.23	CE + S/ED
	B2	metastable	not determined	CE + ED
		total	0.16	CE + S/ED
Kr	S1(3/2)	total	0.015	S/ED
	S1(1/2)	total	0.01	S/ED
	S2(3/2)	metastable	not determined	ED
		total	$\leq 10^{-3}$	S/ED
	B1(3/2)	total	0.03	S/ED
	B1(1/2)	total	0.02	S/ED
	B2(3/2)	metastable	not determined	ED
		total	$\leq 10^{-3}$	S/ED

probability doubles at most. In any case, it can be concluded that almost all the surface excitons yield the desorption of one Ne atom or, in other words, that the desorption probability of the surface excitons S1 is almost unity. A comparison between the metastable and the total desorption yields shows that about 1% of the desorbed Ne atoms are in the metastable state.

The above-mentioned scheme cannot be applied to the analysis of the desorption yield caused by S′ excitation because the quantum efficiency for S′ creation cannot be estimated in the same manner; the excitation of the $2p^5 3p$ state is allowed only at the surface of the solid. It can be said from a comparison between the total desorption yields by S′ and by S1, if we assume that the desorption probability of S′

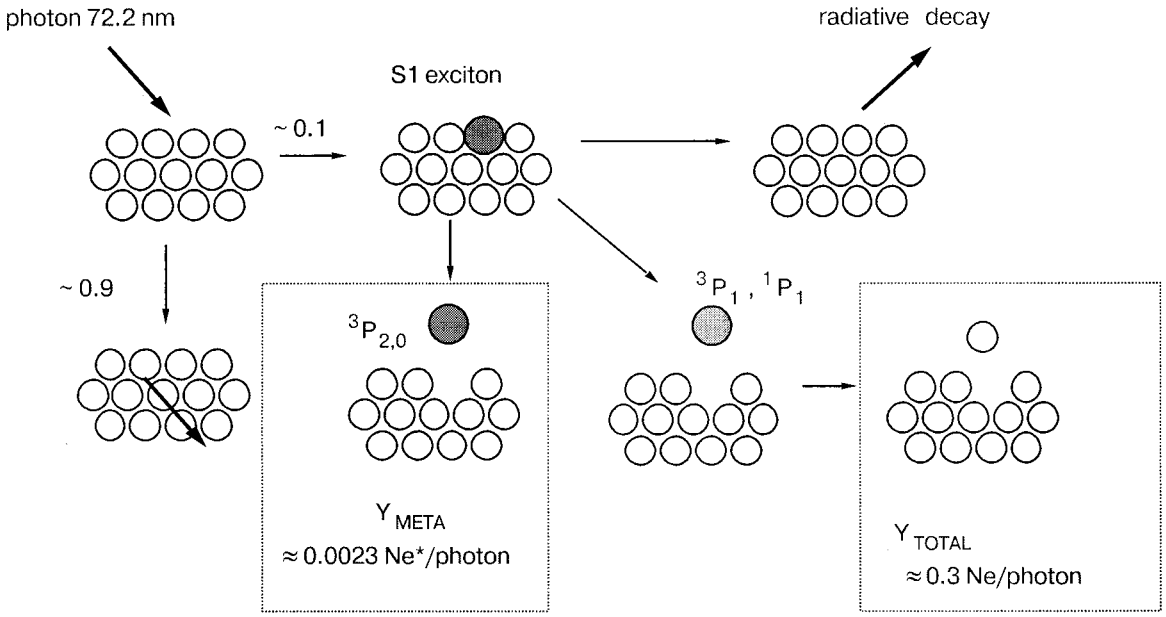

FIG. 4. Schematic chart of the relaxation cascade of the first-order surface exciton S1 in solid Ne.

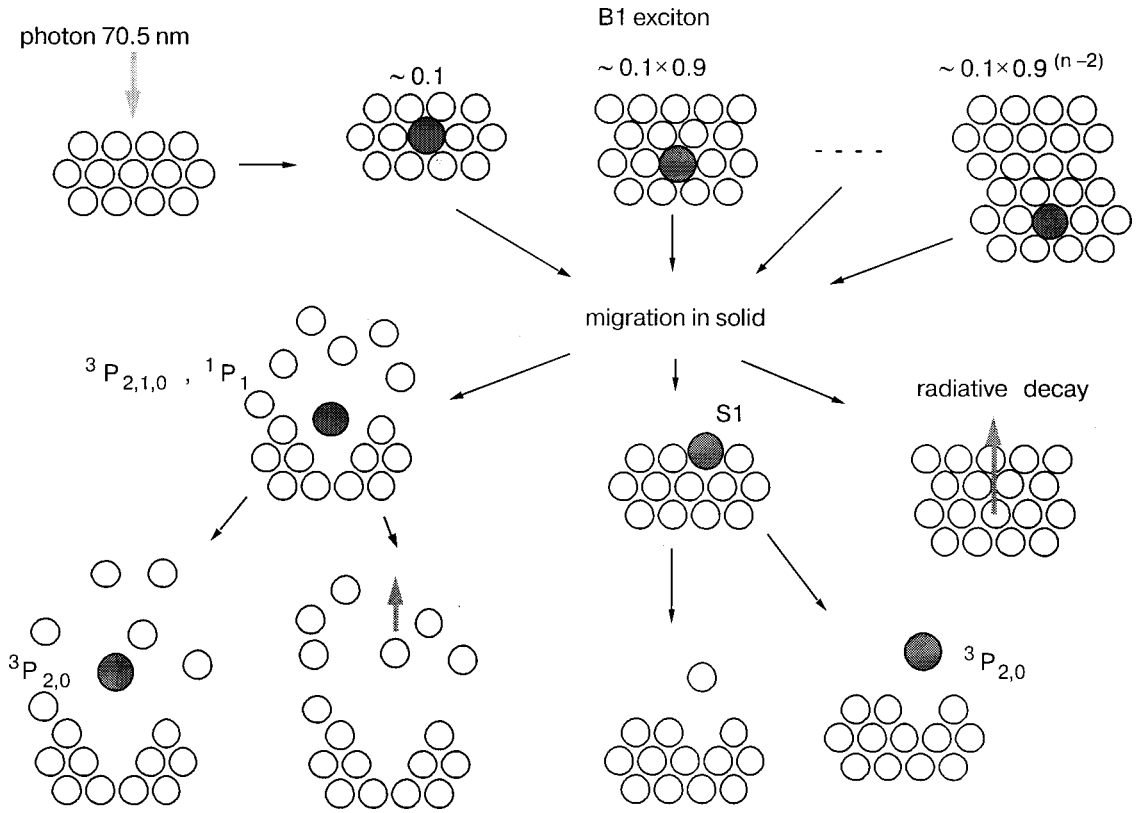

FIG. 5. Schematic chart of the relaxation cascade of the first-order bulk exciton B1 in solid Ne.

exciton is also unity, that the excitation cross section of S′ is one-third of that of S1. The metastable TOF spectrum by S′ excitation shows that almost two thirds of the S′ exciton decays into the S1 state at the surface before the desorption and that a few % of S′ forms excimers in a higher excited state. It is also worth noting that the ratio of the number of the metastable species to the total number of desorption events is about 1% in the case of S′ excitation also.

The relaxation cascade of the first-order bulk exciton B1 of solid Ne are shown schematically in Fig. 5. When solid Ne is irradiated by 70.5-nm photons, the probability for bulk exciton creation in the second underlying layer is estimated as 0.1 excitons/photon, as 0.09 in the third layer, and as $0.1(1-0.1)^{(n-2)}$ in the *n*th layer. Radiative decay may occur immediately or in the course of migration in the bulk. Some of these excitons may reach the surface and convert into the surface exciton S1, which will follow the scenario in Fig. 4. The experimentally determined value of the metastable yield, 0.0014 Ne*/photon, via the S1 state suggests that the total desorption yields via S1 excitons are about 0.2 atoms/photon considering the ratio of the total yield to the metastable one in the case of S1 excitation. This means that the conversion rate from B1 exciton to S1 exciton is 0.2. The excited atom in the second or third layers can be squeezed out because of the large lattice distortion and can blow a number of atoms in the surface layer away. The desorption of metastable Ne from the underlying layers, which loses kinetic energy by collisions with neutral atoms in the overlayers, was experimentally identified in the TOF spectra of Fig. 2 as a tail *D*. The large desorption yields of the order of unity brought about by the bulk exciton can be attributed to this internal sputtering mechanism by excited atoms in the second and deeper layers beneath the surface.[7]

The TOF spectrum of metastables desorbed by the excitation of the B2 exciton is quite similar to that for S′ except for the signal caused by a long-lifetime (several hundred μs) luminescence. The relaxation of B2 into S1, S′, and the excimer is clearly distinguished from the spectrum. Though the total number of excitons excited by B2 excitation is essentially the same as that by B1 excitation, there is an obvious difference between the total desorption yields by B1 and B2 excitations. This is probably because of the difference in the distribution of the initial excitation in the Ne film and because of the relaxation channel of B2, which yields the luminescence stated above.

5. Desorption of Kr

5.1. Metastable desorption

The desorption of metastable species from solid Kr, which has been observed by electron and high-energy ion bombardment, is attributed to the ED mechanism. However, it has been reported that adsorption of a small amount of hydrogen makes it possible to desorb metastables by the CE mechanism by changing the electron affinity to negative.[26] Because of this phenomenon, it is difficult to determine the absolute desorption yields of a metastable via a process intrinsic to pure solid Kr. This is also the case for solid Xe.

5.2. Total desorption

The wavelength dependence of the photo-desorption intensities from solid Kr for three different film thicknesses is

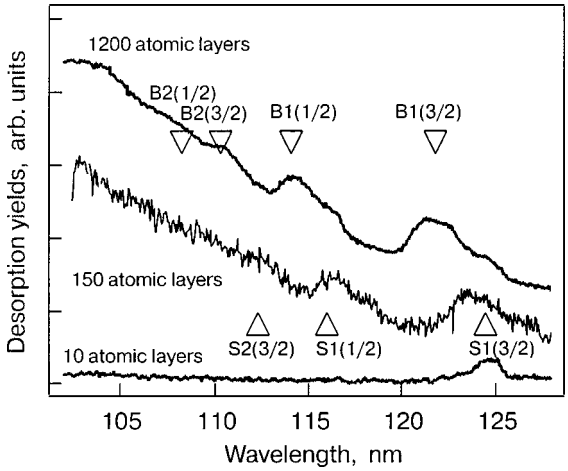

FIG. 6. The total desorption yields as a function of incident wavelength for three different thicknesses of Kr films.

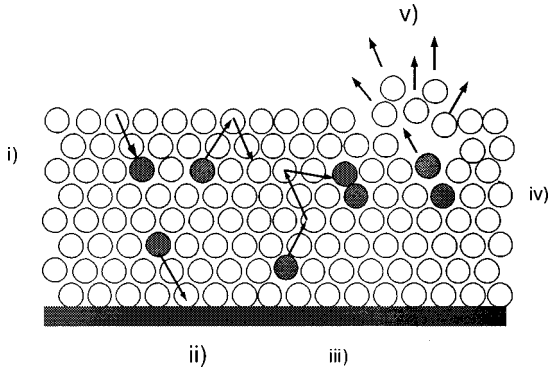

FIG. 7. The model of sequential steps of the excimer dissociation process in solid Kr.

shown in Fig. 6, where the curves are the direct output from the mass spectrometer with no compensation applied for higher-order light. The arrows show the wavelength corresponding to the excitation of the series of excitons in solid Kr. The coincidence between the exciton excitation energies and the peaks or the shoulders in the figure clearly shows that the excitons induce the desorption. The desorption yields were estimated by the peak height above the continuous background which was due to the bulk ionization caused by the higher-order light from the monochromator. The desorption yield at S1(3/2) excitation has apparently no thickness dependence and is about 0.015 atoms/photon. The desorption by bulk exciton creation becomes detectable at a few tens of atomic layers under our experimental conditions. The desorption yields at B1(3/2) and B1(1/2) excitation increase with the film thickness and reach saturated values of 0.03 and 0.02 atoms/photon, respectively, at a thickness of about 100 atomic layers. The absolute yields of the total desorption by the five different excitonic excitations are summarized in Table I.

5.3. Desorption model and simulation of total desorption yields

The desorption process caused by excimer dissociation and internal sputtering after bulk exciton excitation is considered as sequential processes, as shown schematically in Fig. 7: i) creation of a free exciton, ii) migration of the exciton, iii) formation of an excimer, iv) dissociation of the excimer, and v) collision cascade followed by internal sputtering. In order to calculate the desorption yields, each step must be evaluated quantitatively. The details of the calculation will be published elsewhere.[27] Though the behavior of the exciton at a vacuum interface and metal substrate is not well understood, the photoemission data of Kr were well described by assuming that the metal surface is a perfect sink and that the vacuum interface is a perfect reflector for the exciton.[28] The final process v), which is one of the most important factors in giving the theoretical desorption yields, has been studied extensively by a classical molecular dynamic simulation.[7] The distribution of the initial excitation in the process i) and the diffusion length in the migration ii) affect the depth profile of the distribution of the trapped excimer and, therefore, determine the film thickness dependence of the total desorption yield. The initial distribution of the excited bulk excitons is estimated from the photoabsorption coefficient.[29] The only unknown parameter is the diffusion length L of the free exciton, which is expected to be highly affected by the condition of the crystal and by temperature. As is shown in Fig. 8, both the absolute value and the thickness dependence were satisfactorily reproduced by choosing the parameter L between 5 and 10 nm. This value shows good agreement with the estimate of between 1 and 10 nm by Schwentner *et al.* from the photoemission study.[28] We have also applied this method of simulation to the ESD case of solid Kr and obtained satisfactory results.[27]

Though we assume that the CE mechanism does not work at the surface of solid Kr, surface exciton excitation resulted in significant total desorption. This may be caused by excimer dissociation on the surface. However, we cannot exclude the effect of hydrogen adsorption, which makes the CE process efficient.

6. Desorption of Ar

The desorption of metastables from solid Ar by both the CE and ED mechanisms has been reported by many researchers.[24,30,31] However, there are some experimental difficulties in determining the absolute yields of metastable Ar; the unknown angular distribution of desorbed Ar, the low

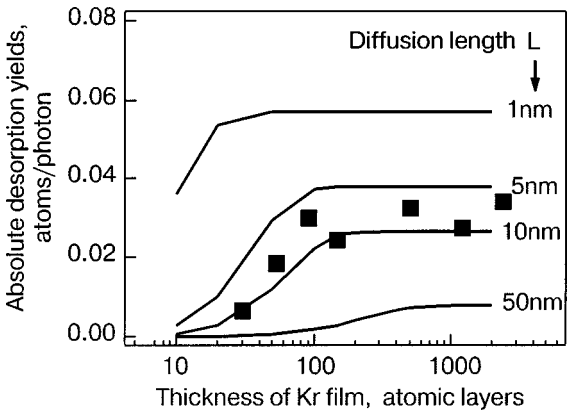

FIG. 8. Thickness dependence of the total desorption yield of solid Kr; the experimental results (solid squares) and the simulated results (lines), with the diffusion length as a parameter.

signal intensity, and the unstable detection efficiency of secondary electron multipliers. Nevertheless we have obtained a rough estimate of the absolute metastable yield of 1×10^{-5} atoms/photon by S1 excitation.[12] Though the determination of the absolute yields of total desorption has already been made in the same way as for Kr (see Table I) the comparison between the experimental results and the simulation is not so straightforward as in the Kr case. It is expected for solid Ar that both the CE and ED mechanisms contribute to the total desorption in comparable measure. The model calculation of the total yield at B1 excitation, in which only the ED mechanism is assumed under conditions similar to the Kr case, gives a theoretical desorption yield of almost one-tenth of the experimental value. This large discrepancy is probably because the bulk excitons are efficiently converted to surface ones at the vacuum interface and lead to desorption by the CE mechanism. A model simulation which takes both CE and ED mechanisms into account is in progress.

7. Summary

We have measured the absolute yields of metastable and total desorption at the surface of solid Ne, Ar, and Kr by the photostimulated desorption technique. The experimental results are well explained by the model in which the excitons play a crucial role. However, the mechanism that leads to the desorption for each rare gas is different. For solid Ne, the predominant mechanism which works for both the metastable and total desorptions is the CE mechanism. The large lattice distortion energy makes the internal sputtering process possible and results in a large total desorption yield of the order of 1 atoms/photon by bulk exciton excitation. For solid Kr, the desorption process can be well described solely with the ED mechanism, in which the migration of a free exciton before trapping into the excimer state determines the absolute yield and its film thickness dependence. In solid Ar, both the CE and ED mechanisms work for the desorption, which make the model calculation of the desorption yield difficult. The mechanism which works in the desorption process from solid Xe must be solely the ED one, as is the case for solid Kr. Unfortunately, we have not obtained data on the absolute total desorption yields which can be compared with the simulation result. This is because of the experimental difficulty due to the low desorption signal intensity and the limitation of our experimental apparatus.

It was demonstrated that the desorption study could reveal the dynamics of excitons in rare gas solids. A promising step in future study may be a systematic investigation of the temperature dependence of the desorption phenomena on a well-defined sample crystal. A study of desorption at the surface of a rare gas alloy[32] will also yield interesting information on the dynamics of the exciton in a heterogeneous system.

This work was supported by the Joint Studies Program of the Institute for Molecular Science and partly by a Grant-in-Aid for Scientific Research from the Ministry of Education, Science, Sports, and Culture, Japan.

*E-mail: ich.arakawa@gakushuin.ac.jp

[1] I. Arakawa, Mol. Cryst. Liq. Cryst. **314**, 47 (1998).
[2] F. Colletti, J. M. Debever, and G. Zimmerer, J. Phys. Lett. **45**, 467 (1984).
[3] P. Feulner, T. Muller, A. Puschmann, and D. Menzel, Phys. Rev. Lett. **59**, 791 (1987).
[4] T. Kloiber and G. Zimmerer, Radiat. Eff. Defects Solids **109**, 219 (1989).
[5] N. Scwentner, F.-J. Himpsel, V. Saile, M. Skibowski, W. Steinmann, and E. E. Koch, Phys. Rev. Lett. **34**, 528 (1975).
[6] D. E. Weibel, A. Hoshino, T. Hirayama, M. Sakurai, and I. Arakawa, in *Desorption Induced by Electronic Transitions DIET V*, E. B. Stechel, A. Burns, and D. R. Jennison (Eds.), Springer, Berlin (1993), p. 333.
[7] S. Cui, R. E. Johnson, and P. T. Cummings, Phys. Rev. B **39**, 9580 (1989).
[8] N. E. Small-Warren and L.-Y. Chow Chiu, Phys. Rev. A **11**, 1777 (1975).
[9] T. R. Connor and M. A. Biondi, Phys. Rev. A **140**, 778 (1965).
[10] I. Ya. Fugol', O. N. Grigorashchenko, A. N. Ogurtsov, and E. V. Savchenko, J. Lumin. **53**, 517 (1992).
[11] M. Sakurai, T. Hirayama, and I. Arakawa, Vacuum **41**, 217 (1990).
[12] T. Hirayama, A. Hayama, T. Koike, T. Kuninobu, I. Arakawa, K. Mitsuke, M. Sakurai, and E. V. Savchenko, Surf. Sci. **390**, 266 (1997).
[13] I. Arakawa, T. Adachi, T. Hirayama, and M. Sakurai, Surf. Sci. **451**, 136 (2000).
[14] J. A. R. Samson, J. Opt. Soc. Am. **54**, 6 (1964).
[15] I. Arakawa, D. E. Weibel, T. Nagai, M. Abo, T. Hirayama, M. Kanno, K. Mitsuke, and M. Sakurai, Nucl. Instrum. Methods Phys. Res. B **101**, 195 (1995).
[16] M. Sakurai, T. Nagai, M. Abo, T. Hirayama, and I. Arakawa, J. Vac. Soc. Jpn. **38**, 298 (1995).
[17] D. E. Weibel, T. Hirayama, and I. Arakawa, Surf. Sci. **283**, 204 (1993).
[18] M. Sakurai, T. Adachi, T. Hirayama, and I. Arakawa, UVSOR Activity Report 2001 **UVSOR-29**, 58 (2002).
[19] T. Kuninobu, A. Hayama, T. Hirayama, and I. Arakawa, Surf. Sci. **390**, 272 (1997).
[20] A. Hayama, T. Kuninobu, T. Hirayama, and I. Arakawa, J. Vac. Sci. Technol. A **16**, 979 (1998).
[21] V. Saile and E. E. Koch, Phys. Rev. B **20**, 784 (1979).
[22] K. Inoue, H. Sakamoto, and H. Kanzaki, Solid State Commun. **49**, 191 (1984).
[23] T. Hirayama, T. Nagai, M. Abo, I. Arakawa, K. Mitsuke, and M. Sakurai, J. Electron Spectrosc. Relat. Phenom. **80**, 101 (1996).
[24] I. Arakawa and M. Sakurai, in *Desorption Induced by Electronic Transitions DIET IV*, G. Betz and P. Varga (Eds.), Springer, Berlin (1990), p. 246.
[25] D. Pudewill, F. Himpsel, V. Saile, N. Schwentner, M. Skibowski, and E. E. Koch, Phys. Status Solidi B **74**, 485 (1976).
[26] Hayama, T. Kuninobu, T. Hirayama, and I. Arakawa, J. Vac. Sci. Technol. A **16**, 979 (1998).
[27] T. Adachi, T. Hirayama, T. Miura, I. Arakawa, and M. Sakurai, Surf. Sci. (to be published).
[28] N. Schwentner, G. Martens, and H. W. Rudolf, Phys. Status Solidi B **106**, 183 (1981).
[29] B. Sonntag, in *Rare Gas Solids*, Vol. II, M. L. Klein and J. A. Venables (Eds.), Academic, New York (1977).
[30] D. J. O'Shaughnessy, J. W. Boring, S. Cui, and R. E. Johnson, Phys. Rev. Lett. **61**, 1635 (1988).
[31] I. Arakawa, M. Takahashi, and K. Takeuchi, J. Vac. Sci. Technol. A **7**, 2090 (1989).
[32] D. E. Weibel, T. Nagai, T. Hirayama, I. Arakawa, and M. Sakurai, Langmuir **12**, 193 (1996).

This article was published in English in the original Russian journal. Reproduced here with stylistic changes by AIP.

Biexcitons in solid neon

P. Wiethoff, B. Kassühlke, D. Menzel, and P. Feulner*

Physikdepartment E20, Technische Universität München, D-85747 Garching, Germany
(Submitted January 15, 2003)
Fiz. Nizk. Temp. **29**, 351–355 (March 2003)

We study the creation of biexcitons in neon films on a metal substrate by one-photon processes. We demonstrate that photon-stimulated desorption of ions is a perfect tool for the investigation of these excitation processes, which possess very low cross sections. We show that the principle of the equivalent-core approximation which is well known from inner shell experiments can also be applied to the neon biexciton case. Comparing the equivalent-core molecules Ne_2^{**} and Na_2, we find that neon biexcitons can be described well in a Frenkel picture. © *2003 American Institute of Physics*. [DOI: 10.1063/1.1542447]

INTRODUCTION

Biexcitons or excitonic molecules have been known since 1958.[1,2] They arise from nonzero interaction energies of two excitons. They have been studied extensively in experiment as well as in theory (see, e.g., Ref. 3). Recently they have attracted interest as objects for Bose—Einstein condensation, for nonlinear optical processes,[4,5] and for quantum computing.[5]

Most previous investigations focus on narrow gap insulators and on semiconductors,[3,4] with a rapidly increasing interest in nanocrystals, microcavities, and quantum structures,[6,7] and also in organic materials.[8] Biexciton binding energies in quantum structures can be very large.[7] The main signatures of biexcitons or excitonic molecules in these experiments are three different optical processes, namely the luminescence occurring when a biexciton decays into a single exciton, the inverse process wherein a biexciton is formed from a single exciton by photoabsorption, and the biexciton creation in a two-photon process with increased cross section, the so-called giant two-photon absorption.[3]

More than a decade ago our group showed that biexcitons exist in solid argon as well, and that these biexcitons can be excited in a one-step process either with electrons[9] or with photons.[10] In particular, the creation of two excitations on different centers in a solid by one photon is an interesting process. As has been shown by Dexter in the theoretical interpretation of experiments by Varsanyi and Dieke, the two excitations need to be coupled in order to enable a nonzero transition probability (see Ref. 11 and references therein). This is the case for excitons forming excitonic molecules, and in particular for the argon case, where the interaction energy is in the range of 10 to 20% of the one-exciton binding energy.[10] Although the transition matrix element for one-photon biexciton excitation is nonzero on account of this interaction, it is much smaller than matrix elements for one-electron excitations, or even for two-electron transitions where both electrons belong to the same atom.[10,12] In normal photoabsorption experiments these biexcitonic one-photon absorption processes remain invisible against the large background of competitive transitions. In order to investigate them, we need a physical process which selectively projects them out.

Photon-stimulated ion desorption (PSID) is such a projection tool. The solids of the light rare gases Ar and Ne show negative electron affinity.[13] The edges of their conduction bands lie above the vacuum level, i.e., the interaction between an additional electron and the closed shell of the Ar or Ne atoms forming the matrix is repulsive. This repulsive interaction is not only encountered by free electrons, but also by the extended wave functions of excitons. As a result, excitons are trapped in atomic centers by the creation of cavities around them. If this self-trapping occurs at the surface, the repulsive forces are unbalanced and the excited particles are ejected into the vacuum.[13,14] This process stimulates desorption of electronically excited atoms,[13–15] dimers,[16] and doubly excited dimers which correspond to the trapped form of biexcitons.[9,10] Singly excited atoms or dimers de-excited by photon emission yield neutral products. For doubly excited dimers enough energy is available for autoionization. Depending on whether the autoionization process leads to bound or dissociative states of the final ionomer state, atomic or dimer ions are detected.[9,10] By evaluation of the dependence of the signal amplitude on the layer thickness, surface and bulk processes can be discriminated.[9,10] Because the competitive photoabsorption processes in the same energy range do not create ions, the biexcitonic processes can be separated in the experiment. We note that PSID is also helpful for the discrimination of multi-electron excitations with low cross sections in the inner-shell excitation region.[17]

In this paper we extend our previous study of argon to solid neon, the other rare gas solid with negative electron affinity. Our goal is threefold: First, we want to demonstrate the potential of PSID for the discrimination of exotic excitations with low cross sections using another system as a typical example. Second, we show that biexcitons exist in solid neon as in solid argon (they probably also exist in the heavier rare gas solids, in which access via PSID by cavity ejection is not possible due to their positive electron affinities). Third, we compare our biexciton results with theoretical data on Na_2 molecules and show that their electronic properties are very similar. From this we conclude that biexcitons in solid neon can be well described in a Frenkel, i.e., in a localized, molecular picture.

EXPERIMENT

All of the experiments were performed in a UHV chamber with base pressure better than $5 \cdot 10^{-9}$ Pa. For enhanced surface sensitivity, grazing incidence of the synchrotron light at 7 degrees with respect to the surface was used. We condensed the neon layers onto the (001) surface of a 7 K cold ruthenium single crystal. Before dosing, we cleaned the substrate by sputtering with Ar^+ ions, repeated heating to 1450 K in 10^{-4} Pa of oxygen, and final flashing to 1570 K. We checked the cleanliness of the substrate by x-ray photoelectron spectroscopy and by thermal desorption spectroscopy of physisorbed xenon. The saturated Xe monolayer shows a desorption maximum associated with a 2D phase transition that is strongly suppressed by even very small amounts of impurities.[18] We note that a clean substrate is important for the perfect growth of Ne layers with minimum contamination. Reproducible amounts of neon (cleanliness better than 10^{-2} %) were dosed through a microcapillary doser onto the substrate. We calibrated the thickness of our films by comparing the relative areas of their thermal desorption peaks to those of well-defined monolayers.[19]

For TEY (total electron yield) excitation spectra, we used a simple PEY (partial electron yield) detector assembled from two grids and a large-area electron multiplier. The grid assembly, which in the PEY mode served as a high pass for the emitted electrons, was grounded for the TEY. Desorbing ions were mass selected and recorded with a quadrupole mass spectrometer.

All measurement were done at TGM dipole beamlines of BESSY, Berlin. The photon energy scale was recorded by taking gas phase photoabsorption spectra at elevated pressure (typically 10^{-5} Pa) *in situ*, and by comparison with energy values from the literature.

RESULTS AND INTERPRETATION

Figure 1 shows Ne^+ and Ne_2^+ PSID spectra from a neon film more than 100 layers thick. Both signals show maxima at 33.5, 34.19, 35.6, 36.1, 36.85, and 37.8 eV. The maxima at 33.5 and 35.6 eV persist for films which are only 3 layers thick, for which the other structures vanish. We therefore assign them to surface excitations. The other features grow in with increasing thickness and saturate at about 100 layers. All of these features can be assigned neither to resonant one-electron nor to multi-electron states of a *single* neon atom. For condensed neon, no resonant one-electron states exist between the $[2p]$ ionization edge at 21.55 eV (Ref. 20) and the lowest $[2s]np$ exciton around 47 eV (Refs. 23 and 24). The lowest two-electron excitation of a single neon atom occurs at 45.5 eV $\{\mathrm{Ne}2p^4(^3P)3s(^2P)3p(^1P)\}$ at the surface,[24] which is also well above the energy range of Fig. 1. The PSID peaks are, however, very close to the sums of two one-exciton excitation energies, as is indicated in Fig. 1, although not exactly at those positions. In particular, the maximum at 33.5 eV is below the value which is obtained by doubling the energy of the lowest resonant excitation, i.e., the $[2p_z]3s$ surface state (we use the Frenkel notation here which we believe to be justified for the excitons with a low principal quantum number of neon,[25] and we have averaged the energy positions of individual multiplet lines; we note

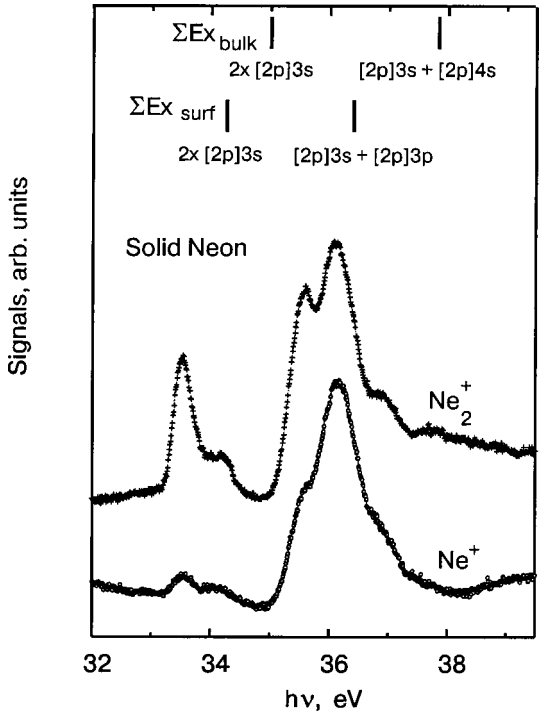

FIG. 1. TEY and photon stimulated desorption of Ne_2^+ and Ne^+ ions from a Ne film more than 100 layers thick. The sums of the bulk ($[2p]3s$, $[2p]4s$; Ref. 20) and surface ($[2p]3s$, $[2p]3p$; Refs. 20–22) exciton excitation energies are indicated for comparison (the multiplet structures have been averaged).

that the normally dipole-forbidden $[2p]3p$ excitation is exclusively seen at the surface, with its reduced symmetry[21,22]). We therefore conclude that the maxima seen in PSID in this energy range must be due to excitations of excitonic molecules in a one-photon process because no other channels for a resonant process exist. The deviation of the peak positions from the sums of one-exciton excitation energies reflect the redshift due to the binding of the excitonic molecules. These results to a large extent resemble those obtained for argon. As there, PSID is brought about by cavity ejection of localized biexcitons and by subsequent autoionization and eventual (in the Ne^+ case) dissociation. Comparing the shapes of the Ne^+ and Ne_2^+ signals, we find that nondissociative autoionization is enhanced for the surface contributions. We believe that these excitations exist for the heavier rare gases as well, although PSID by cavity ejection is not possible, making their detection much more difficult.

In the TEY we found small features in this energy range which were not well reproducible. For thin layers and for reduced photon exposure, i.e., under conditions where charging and beam damage was minimized, they were below the detection limit. We therefore believe that these TEY structures were most likely due to secondary effects, i.e., accumulated lattice defects created by cavity formation and stimulated desorption. Lattice defects will affect the electron transport and charging, and this can cause modulations of the TEY as observed.

We have shown that biexcitons exist in solid neon and that PSID is a very powerful method for their detection. In the next step we try to analyze the main features of these excitations, namely their binding energy. We assume that we

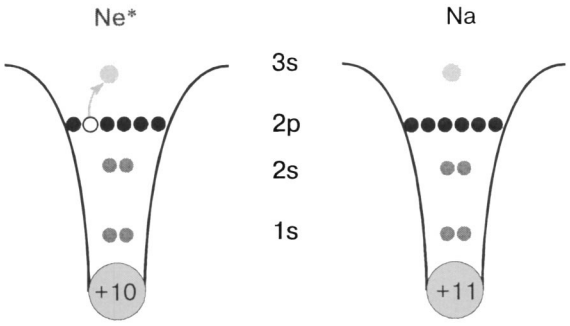

FIG. 2. Equivalent-core picture: Assuming a small spatial extension of the $[2p]$ ionized Ne^+ ion core, a $[2p]3s$ excited neon atom corresponds to a sodium atom, and a $([\mathrm{Ne}2p]3s)_2$ excitonic molecule to a Na_2 molecule.

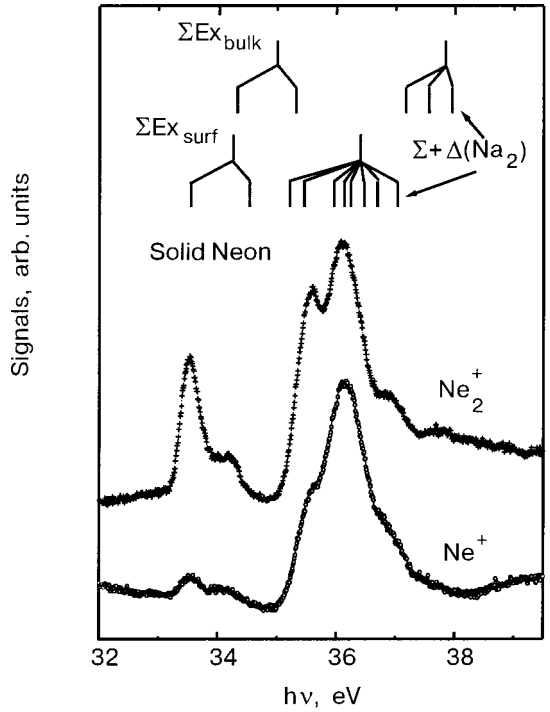

FIG. 3. Vertical bars: An estimate of biexciton energies obtained from the equivalent core picture (Fig. 2). The vertical bars denote energy positions obtained by adding Na–Na interaction energies from calculated Na_2 potential curves[27] to the sums of exciton energies. All values are for the next nearest-neighbor distance of solid neon. The positions in particular of the surface peaks of the experimental data are well reproduced.

can describe them as localized excitons, i.e., in a Frenkel picture. The Frenkel, i.e., atomic picture, has been shown to be an appropriate description for the $n=1(=[2p]3s)$ bulk exciton of solid neon.[25] We note, however, that for the excitons with higher quantum number and for the heavier rare gases the Mott–Wannier description is more appropriate. We further assume that we can apply the equivalent-core approximation, which is a very powerful principle for the interpretation of inner-shell excitation phenomena: A hole in an inner shell is small; its positive charge has nearly the same effect on the outer orbitals which govern the chemistry as the addition of a positive charge in the nucleus, i.e., the core-excited atom behaves chemically like a $Z+1$ ground-state atom. Holes in valence orbitals commonly are not small and are usually not restricted to a single atom; so the equivalent-core approximation can normally not been applied to them. However, valence-excited rare gases are a special case because of their small ion radii. The interaction between two rare gas ions deviates from the Coulomb law only for small distances. This can be seen, e.g., from calculated potential curves for Ar_2^{++} (Ref. 26; unfortunately, similar data for Ne_2^{++} do not seem to exist). The potential curves of the singlet states dissociating into two Ar^+ (^2P) atoms are very close to $1/r$ for $r>5$ bohr, which is much less than the nearest-neighbor distance of solid Ar which is 7.1 bohr (see Fig. 1 of Ref. 26). For Ne, we expect similar relations. We therefore try to obtain the binding energies of the Ne biexcitons from its $Z+1$ analog which is a Na_2 molecule; see Fig. 2. We take Na–Na interaction energies from calculated Na_2 potential curves[27] for the nearest-neighbor distance of the Ne solid (5.97 bohr)[28] and add them to those sums of exciton energies which show the correct asymptotic behavior. Figure 3 shows the result. In particular, the two surface peaks at 33.5 and 35.6 eV are well reproduced by bonding Na_2 states aligned to sums of surface exciton energies. The peak at 34.16 eV, which vanishes for thin layers is most probably the lowest bulk biexciton. The maximum at 36.1 eV can also be described by surface contributions, although combinations of bulk and surface states fit as well (not shown). The maximum at 37.8 eV could be due to bonding states dissociating into $3s$ and $4s$ bulk excitons; we admit, however, that the Frenkel picture may be not adequate for them because of their larger radii. Without straining the analogy too much, we find that the Na_2 analogy reproduces the lowest biexciton states of Ne surprisingly well.

In summary, we have shown that biexcitons also exist for solid Ne, as had been found before for solid Ar. Their one-photon excitation cross sections are low, requiring sensitive experimental tools for their investigation. PSID is an ideal probe. Application of the $Z+1$ approximation reproduces the binding energies of the lowest bulk and surface biexcitons very well.

We thank the staff of BESSY and R. Scheuerer and H. U. Ehrke for help during the experiments. Support by the Deutsche Forschungsgemeinschaft (projects SFB 338 and Me 266/21-2) and by the German Israeli Foundation (GIF; project 1-557-217.05/97) is gratefully acknowledged.

*E-mail: Feulner@e20.physik.tu-muenchen.de

[1] S. A. Moskalenko, Zh. Opt. Spektroks. **5**, 147 (1958).
[2] M. A. Lampert, Phys. Rev. Lett. **1**, 450 (1958).
[3] M. Ueta, H. Kanzaki, K. Kobayashi, Y. Toyozawa, and E. Hanamura, *Excitonic Processes in Solids*, Springer, Berlin (1986).
[4] S. A. Moskalenko and D. W. Snoke, *Bose Einstein Condensation of Excitons and Biexcitons*, Cambridge University Press, Cambridge (2000).
[5] T. H. Stiefvater, Xiaoqin Li, D. G. Steel, D. Gammon, D. S. Katzer, and D. Park, Phys. Rev. B **65**, 205319 (2002).
[6] A. L. Ivanov, H. Haug, and L. V. Keldysh, Phys. Rep. **296**, 237 (1998); Young-Nam Hwang, Koo-Chul Je, Dongho Kim, and Seung-Han Park, Phys. Rev. B **64**, 041305(R) (2001); P. Borri, W. Langbein, U. Woggon, J. R. Jensen, and J. M. Hvam, Phys. Rev. B **62**, R7763 (2000).
[7] U. Woggon, K. Hild, F. Gindele, W. Langbein, M. Hetterich, M. Grün, and C. Klingshirn, Phys. Rev. B **61**, 12632 (2000).
[8] S. Pleutin, Phys. Rev. B **61**, 4554 (2000), and references therein.
[9] Y. Baba, G. Dujardin, P. Feulner, and D. Menzel, Phys. Rev. Lett. **66**, 3269 (1991).

[10] T. Schwabenthan, R. Scheuerer, E. Hudel, and P. Feulner, Solid State Commun. **80**, 773 (1991).
[11] D. L. Dexter, Phys. Rev. **126**, 1962 (1962).
[12] K. Codling, R. P. Madden, and D. L. Ederer, Phys. Rev. **155**, 26 (1967).
[13] M. Runne and G. Zimmerer, Nucl. Instrum. Methods Phys. Res. B **101**, 156 (1995); I. Ya. Fugol, Adv. Phys. **27**, 1 (1978); *ibid.* **37**, 1 (1988).
[14] L. Coletti, J. M. Debever, and G. Zimmerer, J. Phys. Lett. **45**, L467 (1984); E. I. Rashba and E. Ya. Sherman, Sov. J. Low Temp. Phys. **12**, 618 (1986); M. Runne and G. Zimmerer, Nucl. Instrum. Methods Phys. Res. B **101**, 156 (1995), and references therein.
[15] S. Cui, R. E. Johnson, and P. T. Cummings, Phys. Rev. B **39**, 9580 (1989); I. Ya. Fugol, A. G. Belov, V. N. Samovarov, V. N. Svishchev, and V. M. Zhuravlev, JETP Lett. **46**, 308 (1987).
[16] S. T. Cui, R. E. Johnson, C. T. Reimann, and J. W. Boring, Phys. Rev. B **39**, 12345 (1989); W. T. Buller and R. E. Johnson, Phys. Rev. B **43**, 6118 (1991).
[17] P. Feulner, M. Ecker, R. Romberg, R. Weimar, and A. Föhlisch, Surf. Rev. and Lett. **9**, 759 (2002).
[18] H. Schlichting and D. Menzel, Surf. Sci. **272**, 27 (1992).
[19] H. Schlichting and D. Menzel, Surf. Sci. **285**, 209 (1993).
[20] V. Saile and E. E. Koch, Phys. Rev. B **20**, 784 (1979).
[21] T. Kloiber and G. Zimmerer, Radiation Effects and Defects in Solids **109**, 219 (1989).
[22] B. Kassühlke, R. Romberg, P. Averkamp, and P. Feulner, J. Low Temp. Phys. **111**, 723 (1998).
[23] R. Haensel, G. Keitel, N. Kosuch, U. Nielsen, and P. Schreiber, J. Phys. (Paris), Colloq. **32**, C4-236 (1971), and references therein.
[24] B. Kassühlke, Ph.D. thesis, Technische Universität München, 1998, Utz-Verlag, München (1998).
[25] E. Boursey, M.-C. Castex, and V. Chandrasekharan, Phys. Rev. B **16**, 2858 (1977); V. Chandrasekharan and E. Boursey, Phys. Rev. B **19**, 3299 (1979).
[26] G. Cachoncinlle, J. M. Pouvesle, G. Durand, and F. Spiegelmann, J. Chem. Phys. **96**, 6085 (1992).
[27] G. Jeung, J. Phys. B **16**, 4289 (1983).
[28] G. Zimmerer, in *Excited-State Spectroscopy in Solids*, North Holland, Amsterdam (1987), p. 37.

This article was published in English in the original Russian journal. Reproduced here with stylistic changes by AIP.

Exciton-induced lattice defect formation

E. V. Savchenko* and A. N. Ogurtsov

B. Verkin Institute for Low Temperature Physics and Engineering of the National Academy of Science of Ukraine, 47 Lenin Ave., Kharkov 61103, Ukraine

G. Zimmerer

Institut für Experimentalphysik der Universität Hamburg, Hamburg 22761, Germany
(Submitted December 25, 2002)
Fiz. Nizk. Temp. **29**, 356–360 (March 2003)

The lattice defect formation induced by electronic excitation in solid Ne is studied using the selective vacuum ultraviolet spectroscopy method. The samples are excited with synchrotron radiation in the range of excitonic absorption $n=2\Gamma(3/2)$. The dose dependence of the intensity distribution in the band of atomic-type self-trapped exciton luminescence is analyzed. Direct evidence of the formation and accumulation of point lattice defects in solid Ne via the excitonic mechanism is obtained for the first time. A model of permanent lattice defect formation is discussed. [DOI: 10.1063/1.1542448]

INTRODUCTION

The mechanisms of material modification via the electronic subsystem are of considerable interest from the point of view of the fundamental solid-state physics, and their understanding is an important prerequisite for many novel technological applications in material and surface sciences, micro- and nanoelectronics, and photochemistry. The basis for the physics of electronically induced lattice rearrangement is a concentration of the excitation energy in the relaxation process within a volume about that of a unit cell, followed by energy transfer to the crystal surroundings. A variety of inelastic processes induced by excitation of the electronic subsystem have been studied in wide-gap insulators[1–6] and more recently have even been found in narrow-gap materials.[7] The main phenomena under investigation are atomic processes such as lattice defect formation or annealing of existing defects, mass diffusion, and the desorption of atoms, ions, and molecules from surfaces.

Considerable progress has been made towards an insight into their mechanisms. However, many details of the electronically induced processes underlying these phenomena are still not deeply understood. Rare gas solids (RGS) with their simple lattice and well-defined electronic structure are excellent objects for investigation of the electronically induced phenomena. Small binding energies in conjunction with a strong exciton–phonon interaction result in a high quantum yield of electronically induced defect formation and desorption that makes RGS especially suitable for experimental study. Moreover, study of electronically induced atomic processes in the above solids offers a unique possibility for elucidating the role of acoustic phonons in these processes. The pronounced effects of exciton self-trapping observed in RGS are essential for efficient energy localization and transfer to induce a lattice modification. It is well known[1–3,8–10] that in solid Ne the excitons are self-trapped predominantly into atomic-type states (A-STE). A rich structure of the atomic transitions has already been found in the early high-resolution studies of luminescence from solid Ne.[11–13] It has been shown[11] that the emissions observed arise from the transitions $^1P_1 \rightarrow {}^1S_0$, $^3P_1 \rightarrow {}^1S_0$, and $^3P_2 \rightarrow {}^1S_0$. The spectral features related to the surface and to the bulk were distinguished by their dependence on sample thickness and exciting electron energy.[13] The narrow emission lines were assumed[14] to stem from the desorbing atoms in the states $^1P_1$ and $^3P_1$. The wider bulk emissions matched to the transitions $^3P_1 \rightarrow {}^1S_0$ and $^1P_1 \rightarrow {}^1S_0$ were found to be of a doublet structure.[13] The similar features observed in Ref. 14 were interpreted in the framework of the coexistence of exciton self-trapping in a regular lattice and trapping in the vicinity of initial nonequilibrium defects of structure, e.g., trapping near a vacancy. Note that the transformation of defects involving A-STE and mobile thermal vacancies at a ''high'' temperature of 19 K, close to the melting point, was considered in Ref. 15.

In order to elucidate the internal structure of A-STE emission bands, special experiments on low-temperature irradiation by high- and low-energy electron beams were performed.[16,17] In the first case the electrons of superthreshold energy $E_e > E_{\text{thr}}$ ($E_{\text{thr}} = 1$ keV) produced point defects (Frenkel pairs) during excitation via the knock-on mechanism. Based on the dose dependence, the defect-related spectral features were clearly identified. For comparison purposes the same luminescence spectra and their dose behavior were studied under irradiation by an electron beam of subthreshold energy $E_e < E_{\text{thr}}$, i.e., by electrons of energy deficient for moving a lattice atom from the substitutional site to an interstitial one via the knock-on mechanism. A striking resemblance found in the dose behavior—the increase in the intensity of the defect-related components, has given conclusive evidence of the formation of electronically induced point defects and their accumulation in the lattice of Ne.[16,17] It has been suggested that the self-trapping of excitons into A-STE states is a stimulating factor. However, direct proof of the excitonic mechanism requires state-selective experiments. Synchrotron radiation providing intense vacuum ultraviolet

(VUV) light tunable through the exciton absorption range is best suited to this kind of experiments.

The paper reports the results of a synchrotron radiation study of permanent lattice defect formation in solid Ne via the excitonic mechanism. The experimental findings are compared with the results of recent molecular dynamics studies of the evolution of the self-trapped excitons into permanent lattice defects.[18,19]

EXPERIMENTAL

The selective excitation experiments were carried out at the SUPERLUMI station at the Hamburger Synchrotronstrahlungslabor HASYLAB. Since we are interested in control of the lattice permanent defect creation induced by excitation of the electronic subsystem the quality of the samples under study (the concentration of initial defects and impurities) is of critical importance. The samples were grown in a special closed cell mounted on a He-flow cryostat holder in an ultrahigh vacuum (UHV) environment (10^{-10} mbar). High-purity Ne gas (99,998%) was used, and the gas handling system was operated under UHV conditions. The samples were condensed from the vapor phase at elevated temperatures under isobaric conditions ($P=10$ Pa). The initial temperature of 18 K was fixed, whereupon the sample was cooled down to 5 K at a constant rate of 0.1 K/s. After the sample preparation the cell was removed and the free-standing crystal was studied. The high-quality optically transparent polycrystalline sample of 1 mm thickness was then subjected to a long-duration exposure to the VUV light. Selective photon excitation was performed with a band pass of $\Delta\lambda=0.25$ nm. The excitation energy of 20 eV was chosen in the range of the $n=2$ term of the excitonic series. The luminescence analysis was carried out using a 1 m near-normal incidence monochromator equipped with a position-sensitive detector. The spectra were recorded with spectral resolution ($\lambda/\Delta\lambda$) of 750 and 1500. The resonance lines of gaseous Ne were used for the energy calibration. The dose dependence of the luminescence intensity spectral distribution was measured, and the influence of the annealing at 11.5 K on the spectral features was examined.

RESULTS AND DISCUSSION

The typical photoemission spectra of self-trapped excitons in solid Ne taken with different resolution are presented in Fig. 1. Spectrum 2, recorded with the spectral resolution of 1500, shows a number of overlapping spectral peaks. The weak, wide band *W* on the low-energy side is known to be vibrationally hot luminescence of M-STE in solid Ne (see, e.g., Refs. 11 and 14). The contributions to the *W* band from M-STE in the bulk and at the surface were discriminated in Ref. 20. It is very likely that the desorption of Ne_2^* observed in Refs. 21 and 22 also contributes the *W* band. However, this presumption needs a special check. The most intense structured composite of bands is the A-STE emission in the range 16.6–17 eV. Experiments with highly effective excitation of solid Ne by an electron beam[11,13,14,16,17] made it possible to observe the luminescence from the three atomic states $^1P_1$, $^3P_1$, and $^3P_2$—the *a*, *b*, and *c* bands in the notation given in Ref. 16. All of the bands have an internal

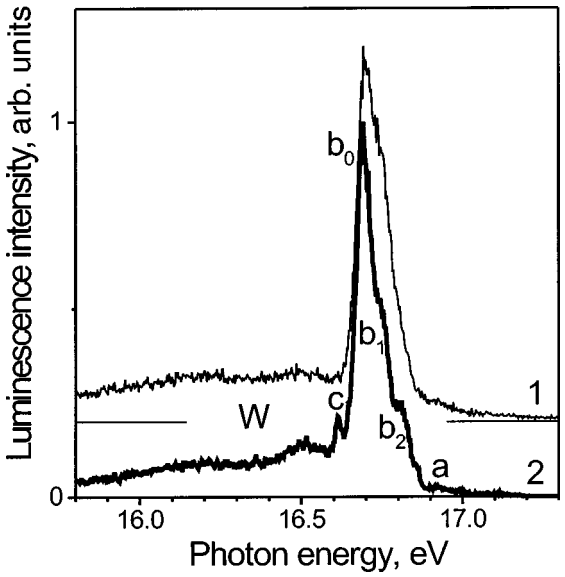

FIG. 1. STE luminescence of solid Ne excited by 20 eV (curve 1) and with 22 eV (curve 2) photons. Curve 2 was recorded with a higher resolution ($\lambda/\Delta\lambda=1500$). The spectra were measured at $T=5$ K.

structure with components of different origin. The narrow "0" peaks coinciding in energy with the transitions $^1P_1 \rightarrow {}^1S_0$ and $^3P_1 \rightarrow {}^1S_0$ in the gas phase were identified as emissions from the desorbing atoms in the excited states.[14] The components labeled 1 and 2 which fall into pairs with a splitting close to the spin–orbit splitting, stem from the A-STE centers in the bulk. The 1 components were found to be related to the lattice defects, whereas the 2 components were associated with the A-STE in the regular lattice.[14,16,17] Several features were assigned to the A-STE at the surface. In experiments[23] performed with tunable synchrotron radiation the authors were able to isolate some of the peaks by choosing the appropriate excitation energy and time gating. The relevant peak positions and their assignments are listed in Table I.

The intention of the present study was to measure the dose dependence of the intensity distribution in the luminescence spectra of solid Ne under selective excitation in the range of free excitons. We tuned the excitation energy to the band of exciton absorption $n=2\Gamma(3/2)$. Due to the low ab-

TABLE I. Positions at $T=5$ K, FWHM, and assignments of the A-STE luminescence components in the range of resonance transitions.

Band	Position, eV	FWHM, meV	Assignment
b_0	16.671	–	$^3P_1$ (desorbing atom)
b_1 *	16.746 ± 0.002	48 ± 5	$^3P_1$ (defect related A-STE)
b_2 *	16.807 ± 0.002	48 ± 6	$^3P_1$ (A-STE in the bulk)
a_0	16.848	–	$^1P_1$ (desorbing atom)
a_1 **	16.931 ± 0.005	50 ± 5	$^1P_1$ (defect related A-STE)
a_2 **	16.992 ± 0.01	45 ± 5	$^1P_1$ (A-STE in the bulk)

Comment. Position and in full width at half maximum (FWHM) are given by the data in Refs. 23 (*) and 14 (**).

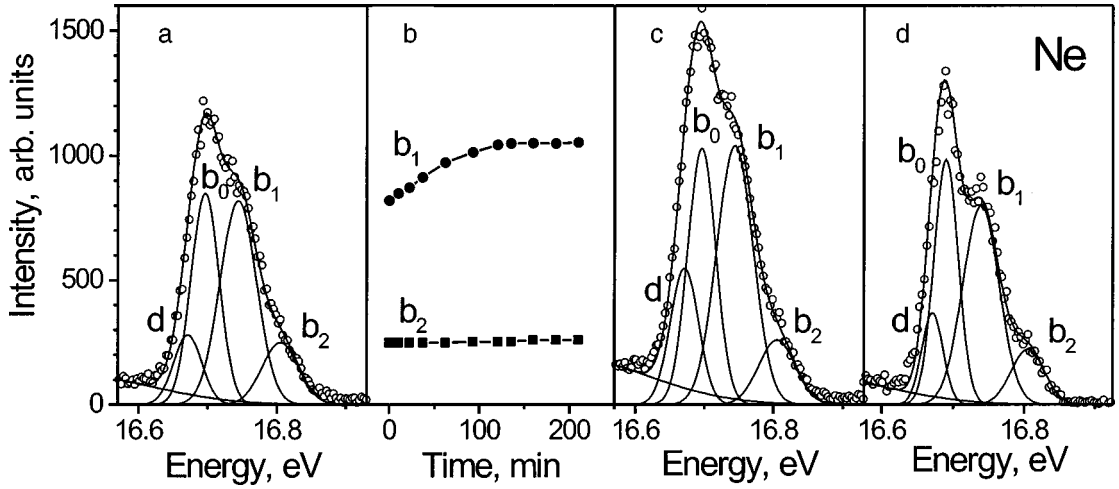

FIG. 2. Photoluminescence of solid Ne in the range of the $^3P_1 \rightarrow {}^1S_0$ transition (*b* band): (a) and (c)—the evolution of the *b* band upon irradiation with 20 eV photons, (b)—the dose dependence of the b_1 and b_2 components, (d)—the spectrum recorded after annealing of the sample at $T = 11.5$ K. The spectra were recorded at $T = 5$ K.

sorption coefficient the exciting light penetrated deep inside the sample and the A-STE centers were efficiently formed in the bulk. The temporal behavior of the luminescence was monitored at 5 K to rule out thermally stimulated processes. The sequence of spectra was measured during exposure to VUV light. The most intense *b* band was analyzed. The initial intensity distribution is shown in Fig. 2a and the final one in Fig. 2c. The positions and the widths of the components were obtained from a numerical fit of the band contour assuming a Gaussian shape of the components. The fitting was done taking into account the overlapping of the A-STE emission with a high-energy tail of the M-STE luminescence, shown in Fig. 2. The result of this treatment for the b_1 and b_2 components is shown in Fig. 2b as the corresponding points of the curves. Despite the fact that the $n = 2\Gamma(3/2)$ excitons are formed predominantly deep in the bulk, they reach the surface and are then trapped into the A-STE configuration with a subsequent desorption of the excited atom. The appearance of the b_0 component in the A-STE emission is in line with the results on the partial yield of the Ne atoms in the $^3P_1$ state.[24] The desorption is due to the formation of a microcavity (bubble) around the A-STE as a result of the prevailing repulsive interaction between the excited electron and surrounding atoms because of the negative electron affinity of solid Ne.[1] This so-called ''cavity ejection'' mechanism was studied in detail (see Ref. 2 and references therein). The width of the b_0 component related to the desorbing atoms is resolution limited. The positions and the widths of the b_1 and b_2 components are in perfect agreement with the data given in Ref. 23. These bulk components have analogs in the matrix-isolated Ar center spectra.[17] The *d* component may be tentatively assigned to the transition from the metastable $^3P_2$ state at defect sites or near the surface. Note that the transition from this state is strictly forbidden in a regular lattice. To the best of our knowledge the geometrical configuration of the centers that emit the peaks in the range of the $^3P_2 \rightarrow {}^1S_0$ transition has not been fully ascertained. Because of the long lifetime of this state and the negative electron affinity, the chance for the atom to desorb prior the radiation is very high.[25] For this reason the assignment of some emission lines as emissions from the surface centers in the $^3P_2$ state seems to be very unlikely. The efficient excitation of this emission in the range below the lowest bulk exciton band may also be due to excitation of some centers at defect sites, because the defect levels could be expected to occur quite close to the surface exciton band. Note that the *d* component has an analog in the matrix-isolated center spectra in the range of low concentrations.[17] The width narrowing and the decrease in intensity observed for the *d* component upon annealing (see Fig. 2d) seems to support the assignment of the *d* component as being related to the defect sites.

In order to get direct proof of the permanent lattice defect formation in the initially perfect lattice via the excitonic mechanism, let us consider the features in the range of the resonance transition $^3P_1 \rightarrow {}^1S_0$. This is just a transformation of the most intense *b* band on exposure to VUV photons in the range of the second term of the excitonic series well below the band gap energy. The shape of the *b* band after the cycle of irradiation is shown in Fig. 2c. A pronounced enhancement of the defect-related components b_1 and *d* was found. As for the b_2 component associated with the A-STE centers in the regular lattice, it remained unchanged. Figure 2b depicts the dose dependence of the b_1 and b_2 component intensity. The exposure time uncorrected for the synchrotron radiation pulse duration is in fact the real time of the measurements. The radiation-induced enhancement of the defect components clearly indicates the formation and accumulation of permanent lattice defects in solid Ne generated by the self-trapping of excitons into the A-STE states. A 30-min annealing of the samples at $T = 11.5$ K caused a decrease in the intensity of the defect-related components. The intensities of the b_1 and b_2 components were restored. The results obtained in the present experiments with selective excitation accord well with the results of experiments performed with electron beams.[17] Note that in these experiments a similar dose dependence was observed for the components of the transitions $^1P_1 \rightarrow {}^1S_0$ and $^3P_1 \rightarrow {}^1S_0$ (see Table I), which are dipole allowed in a cubic lattice. The similar dose dependences of the A-STE luminescence components found in the cases of superthreshold and subthreshold excitation by elec-

tron beams as well as selective excitation into excitonic states provide convincing proof of the excitonic mechanism of the point lattice defect formation.

The recent excited-state molecular dynamics studies[18,19] of the possible evolution of the A-STE states into stable lattice defects suggest a microscopic model of conversion from the A-STE to Frenkel pairs. The elastic deformation followed by the primary bubble formation due to the prevailing repulsive forces between the excited atomic center and surrounding atoms takes place within a very short time. It is interesting that an ultrafast expansion of the bubble was observed upon excitation of the Rydberg orbital of the NO impurity center in solid Ne.[26] Such primary bubbles with elastic deformation collapse once the electronic subsystem returns to the ground state. High local elastic stresses in the lattice can induce some plastic deformation during the lifetime of the excited state. Several cases of possible plastic deformation were examined. It was calculated that the energy levels of some of the bubbles accompanied by plastic deformation are at energies lower than that of the primary bubble. The lowest energies were found for a bubble with two vacancies in the first atomic shell. It was revealed that the second-nearest neighbor vacancy–interstitial pairs are formed and remain stable in the lattice after exciton annihilation. The estimated differences in energies of radiative transitions of the atomic centers in the primary bubble and in the bubble with plastic deformation, 54–66 meV, are in perfect agreement with the experimental value 60 meV obtained in the present study and with the results given in (Refs. 14 and 23) for the $^3P_1 \rightarrow {}^1S_0$ and $^1P_1 \rightarrow {}^1S_0$ transitions (see Table I). A quite similar process of electronically induced defect formation upon excitation of the Ar atoms in a Neon matrix has been observed experimentally[4] and considered theoretically.[18] To some extent the mechanism of lattice defect formation considered here resembles that in alkali halides, where the Frenkel pair formation is induced by the repulsive interaction between the excited electron of the STE and core electrons of the molecular ion pairs.[1]

It is a pleasure to thank Prof. A. K. Song for fruitful discussions. The authors (E.S. and A.O.) gratefully acknowledge the support of the DFG.

*E-mail: savchenko@ilt.kharkov.ua

[1] K. S. Song and R. T. Williams, *Self-Trapped Excitons*, Springer-Verlag, Berlin (1996).
[2] G. Zimmerer, Nucl. Instrum. Methods Phys. Res. B **91**, 601 (1994).
[3] I. Ya. Fugol', Adv. Phys. **37**, 1 (1988).
[4] E. V. Savchenko, A. N. Ogurtsov, and O. N. Grigo-rashchenko, Solid State Phys. **40**, 903 (1998).
[5] P. Feulner and D. Menzel, in *Laser Spectroscopy and Photochemistry on Metal Surfaces*, World Scientific, Singapore (1995), p. 627.
[6] M. A. Elango, *Elementary Inelastic Radiation-Induced Processes*, American Institute of Physics, New York (1991).
[7] N. Itoh and A. M. Stoneham, Radiat. Eff. Defects Solids **155**, 277 (2001).
[8] N. Schwentner, E.-E. Koch, and J. Jortner, *Electronic Excitation in Condensed Rare Gases*, Vol. 107 of Springer Tracts Modern Physics, Springer-Verlag, Berlin (1985).
[9] I. Ya. Fugol', Adv. Phys. **27**, 1 (1978).
[10] G. Zimmerer, in *Excited-State Spectroscopy in Solids*, Bologna, Corso (1987), p. 37.
[11] I. Ya. Fugol', E. V. Savchenko, and A. G. Belov, Sov. Phys. JETP Lett. **16**, 245 (1972).
[12] E. Schuberth and M. Creuzberg, Phys. Status Solidi B **71**, 797 (1975).
[13] O. N. Grigorashchenko, Yu. I. Rybalko, E. V. Savchenko, and I. Ya. Fugol', Fiz. Nizk. Temp. **8**, 886 (1982) [Sov. J. Low Temp. Phys. **8**, 447 (1982)].
[14] F. Coletti, J. M. Debever, and G. Zimmerer, J. Chem. Phys. **83**, 49 (1985).
[15] T. Suemoto and H. Kanzaki, J. Phys. Soc. Jpn. **49**, 1039 (1980).
[16] E. V. Savchenko, Yu. I. Rybalko, and I. Ya. Fugol', JETP Lett. **42**, 260 (1985).
[17] E. V. Savchenko, Yu. I. Rybalko, and I. Ya. Fugol', Fiz. Nizk. Temp. **14**, 349 (1988) [Sov. J. Low Temp. Phys. **14**, 220 (1988)].
[18] Chun-rong Fu and K. S. Song, J. Phys.: Condens. Matter **9**, 9785 (1997).
[19] K. S. Song and Chun-rong Fu, J. Low Temp. Phys. **111**, 645 (1998).
[20] R. Gaethke, P. Gurtler, R. Kink, E. Roick, and G. Zimmerer, Phys. Status Solidi B **124**, 335 (1984).
[21] E. V. Savchenko, T. Hirayama, A. Hayama, T. Koike, T. Kuninobu, I. Arakawa, K. Mitsuke, and M. Sakurai, Surf. Sci. **390**, 261 (1997).
[22] T. Hirayama, A. Hayama, T. Adachi, I. Arakawa, and M. Sakurai, Phys. Rev. B **63**, 5407 (2001).
[23] W. Laash, H. Hagedorn, T. Kloiber, and G. Zimmerer, Phys. Status Solidi B **158**, 753 (1990).
[24] T. Kloiber and G. Zimmerer, *Phys. Scrypta* **41**, 962 (1990).
[25] I. Arakawa, T. Adachi, T. Hirayama, and M. Sakurai, Fiz. Nizk. Temp. **29**, 342 (2003) [Low Temp. Phys. **29**, 260 (2003)].
[26] F. Vigliotti, L. Bonacina, M. Chergui, G. Rojas-Lorenzo, and J. Rubayo-Soneira, Chem. Phys. Lett. **362**, 31 (2002).

This article was published in English in the original Russian journal. Reproduced here with stylistic changes by AIP.